Assessment of 2D and 3D Image Characteristics of an Optical CT Scanner for 3D Dosimetry

---

Jarrad Begg

B. App. Sci. (App. Phys)

A thesis submitted in partial fulfilment of the requirements for the degree of Master of Applied Science (Medical and Health Physics)

School of Applied Sciences

College of Science Engineering and Health

RMIT University

Melbourne, Australia

August, 2013

DECLARATION

I certify that except where due acknowledgement has been made, the work is that of the author alone. The work has not been submitted previously, in whole or in part, to qualify for any other academic award. The content of the thesis is the result of work which has been carried out since the official commencement date of the approved research program.

Jarrad Begg

Date

SUMMARY

Developments in treatment techniques used in radiotherapy have resulted in highly individualised treatment dose distributions for cancer patients. The dose distributions are planned for conformity to individual patient treatment volumes and typically have steep dose gradients to reduce dose to nearby organs at risk. Quality Assurance (QA) of the individualised treatment plans is required to identify parts of the plan where the delivered and planned doses may differ. Point detectors (e.g., ion chambers, diodes) and two dimensional arrays (e.g., film, arrays of chambers or diodes) sample only a single point or plane in the dose distribution for verification against the planned dose distribution. Comparing measured dose in 1D or 2D to a distribution generated in a treatment planning system does not verify the whole 3D dose volume. Outside the sampled point or area, differences between the measured dose distribution and treatment plan may not be noticed during routine QA. Errors between the delivered and planned dose distributions can have adverse effects on the control of the patient's tumour, and could increase adverse effects in normal tissue.

Gel and plastic dosimeters have been developed to sample the entire 3D dose distribution. In general 3D dosimeters store the radiation dose distribution which can then be imaged and analysed using a number of techniques depending on the gel formulation used. Images of the dose distribution can be obtained via:

- magnetic resonance imaging (MRI),
- x-ray computed tomography (x-ray CT),
- ultrasound, or
- optical computed tomography (Optical CT)

Optical CT scanners have been of particular interest as they offer high spatial resolution in a relatively cost effective way.

Aim

Gel dosimetry is a method of measuring a dose distribution in three dimensions and requires an efficient accurate read-out approach. Optical CT has the potential to provide this. A number of commercial optical CT scanners are now available. However, there has not been a comprehensive review of procedures used for commissioning and QA of an optical CT scanner. Additionally, optical CT is an unfamiliar technique to clinical medical physicists. It is the aim of the present study to characterise the components and properties of the optical CT scanner and investigate procedures which could be used for commissioning or as part of an ongoing scanner quality assurance program.

Method

To investigate more time efficient methods of QA, some aspects of the characterisation were investigated using 2D projection and 3D reconstructed images. The characterisation of the Optical CT scanner involved:

- Measuring the light spectra of both LED light sources,
- Characterising the temporal constancy of the light sources after initially turning on the scanner,
- Investigating the CCD reciprocity and the influence of non-reciprocity on the reconstructed attenuation coefficient,
- Characterising uniform Polyurethane Opacity Reference Phantoms (PORPs) having a range of optical attenuation coefficients,
- Measuring and comparing attenuation coefficients of PORPs in both 2D projections and 3D reconstructed images,
- Measuring spatial resolution in both 2D projection and 3D reconstruction,
- Investigating CCD blooming and the influence on spatial resolution
- Investigating the uniformity of response for different types of uniform phantoms,
- Investigating the source and effect of scattered light on the measured attenuation coefficients of a reconstructed uniform phantom.

Results

Measured light source spectra have been compared to published attenuation/absorption spectra for PRESAGE™ and Fricke dosimeters. The attenuation/absorption spectra characterise the wavelengths of light that are most readily attenuated/absorbed by the dosimeters. The orange and red light sources inherent in the Optical CT scanner, designed for use with Fricke and PRESAGE™ dosimeters, have peak wavelengths of 598 and 642 nm respectively with a Full Width Half Maximum (FWHM) of 17.5 and 23 nm respectively. When combined with the filters in the optical CT scanner, the peak wavelengths shift to 595 and 625 nm respectively and the FWHM narrows to 11 nm for both the orange and red light source. The inherent light sources matched well with published absorption spectra for Fricke and PRESAGE™ dosimeters. The two LED light sources are polychromatic and thus will exhibit differential attenuation through the dosimeter and each wavelength will have a unique quantum efficiency in the CCD detector. Therefore the spread of wavelengths for the unfiltered and filtered light source is important. Using a filter reduces the variance in differential attenuation to 10.5 and 7.9 % across the FWHM of the filtered orange and red light sources respectively. The use of a filter reduces the variance in quantum efficiency to 3.0 and 3.7 % for the orange and red light sources respectively.

The light source intensity after switching on the optical CT scanner degraded exponentially over time. This indicated a warm-up time of approximately 2 hours is required before the relative change in light intensity from the light source over the time required to measure a gel is small. Uniform volumes, reconstructed from projection images acquired at different warm-up times, show that using a cold scanner can underestimate attenuation coefficients by up to 10 %. Using a scan where one set of projection images was acquired with a cold scanner, and the other set acquired with a warm scanner, will reconstruct an accurate 3D volume but with an increased level of noise.

The reciprocity law was investigated in the CCD to validate the method used to calculate optical density. If the law is not obeyed, then the calculated optical density will be dependent on the reference intensity measured by the CCD. Deviations from a linear response were observed for pixel values below ~5000 a.u. and above ~64000 a.u. The charge collection time was used to control the exposure of the CCD during acquisition of projection images, which were then used to reconstruct 3D volumes of a uniform object. The reconstructed attenuation coefficient was observed to change with CCD exposure.

Transmission measurements of the PORPs show that the phantoms have attenuation coefficients in the range between 0 – 1.8 cm^{-1} and 0 – 1.5 cm^{-1} for the orange and red light sources respectively. These attenuation coefficients were measured along the cylindrical axis of the PORPs in a reduced scatter geometry and were used as baseline attenuation coefficients for future comparison. Use of a known pathlength and reduction of scatter improved the accuracy of the measured attenuation coefficient. Measurements of the PORP attenuation coefficients were found to have good interday reproducibility and no dependence on orientation in the scanner. Profiles in 2D showed that the PORPs were light absorbing phantoms (rather than light scattering). Non-uniformities in the phantoms limited the effectiveness of the PORPs for characterising the attenuation coefficient accuracy.

The attenuation coefficient range measured in the 3D reconstruction was characterised for accuracy to the baseline values, signal to noise ratio and uniformity. The reconstructed values were observed to be up to ~17 % below baseline values in the range 0.1 – 0.68 cm^{-1} for the orange light source. For the red light source, differences up to 25 % relative to expected values were observed over the range 0.14 – 0.58 cm^{-1}. The noise in all regions for both attenuation coefficient ranges was below 1 %. Uniformity characterises the attenuation coefficient accuracy and noise throughout the entire dosimeter. The uniformity was compared via 5 volumes of interest (VOI). The VOI were at the top, bottom, left, right and centre of an axial slice. A validation of the method was performed with absorbing blue dye and water solutions. The uniformity measured using the 5 regions of interest showed good agreement with measured profiles. The PORP uniformity of the outer VOI (top, bottom, left and right) relative to the central VOI was within 5 % for the attenuation coefficient ranges described above.

The measured spatial resolution has a dependence on optical CT scanner set-up, CCD focus settings and CCD pixel size. As such, the spatial resolution requires characterisation for each scanner. In the 2D projection images, the preferred criterion of 50 % modulation at 1 lp/mm is only achieved at

positions closer than 45 cm from the CCD detector plane, which corresponds approximately to the centre of rotation of the sample holder.

Four resolution settings were available in the Vista™ Recon program; low, medium, high and extreme. The spatial resolution at the centre of a 3D reconstructed volume was 0.04, 0.12, 0.29 and 0.44 lp/mm for the low, medium, high and extreme resolution settings respectively. The spatial resolution was consistent within a radial distance of 12.5 lp/mm before dropping to a spatial resolution of 0.38 lp/mm at a radial distance of 15 mm.

Blooming of the CCD was observed to have two effects on the spatial resolution: i) a low overflow of charge causes the edge spread function (ESF) to shallow and the modulation transfer function (MTF) to decrease slightly, and ii) a high magnitude of overflow causes the ESF to sharpen and the MTF to increase. However, the ESF actually shifts across by 1 pixel and therefore was not accurately representing the real position of the edge.

The effect of scatter in 2D and 3D images was investigated using collimators to constrain the light entering or exiting the sample tank. Collimation at the entrance to the tank minimises light not originally incident on the CCD being scattered toward the CCD. Collimation at the exit minimises the detection of light scattered inside the specimen tank. The 2D projections and 3D reconstructions show that scattered light can influence the measured attenuation coefficient by up to 4 % even when an absorbing phantom is being used. The sources of stray light (either not originally incident on CCD and scattered toward, or light scattered inside the tank) were found to be approximately equal in magnitude.

Conclusions

The thesis has characterised properties of the optical CT scanner. Light spectra, CCD response, warm-up time, spatial resolution, response to light intensity, uniformity and the influence of scatter were all demonstrated to influence the accuracy of the optical CT scanner, with the light source/ filter combination and warm up time demonstrating the most significant impact. Phantoms for use as long term quality assurance tools were developed. Individual phantom attenuation coefficients were characterised and used to determine the stability of the phantoms over a period of time. Profiles measured from 2D projections and 3D reconstructions were measured and compared to absorbing solutions to determine uniformity and scattering properties. The results showed that the phantoms were not optimal for use as long term scanner quality assurance tools. Careful design and manufacturing procedures will be required to address potential problems such as uniformity of attenuation and minimisation of scattering. Additional problems, including independent validation of absorbance and refractive index matching, need to be considered prior to development.

The characterisation procedures presented here could constitute an acceptance testing procedure (or more likely a subset of the procedures might be considered necessary). Recommendations are made

for a set of quality assurance procedures, which include geometry calibration of the scanner, characterising the light source, verifying the CCD is functioning correctly, checking the reconstructed accuracy and verifying the reconstruction spatial fidelity.

Commissioning of an optical CT scanner should include an optimisation of the scanner geometry and lens settings, measurement of the spectra and temporal stability of the light source, measurement of CCD reciprocity, quantification of attenuation coefficient accuracy, uniformity and noise and measurement of spatial resolution. This work has shown that appropriate warm up times, light source and filter combinations and phantom material selection and manufacturing processors can significantly influence measured attenuation coefficient accuracy, uniformity and noise.

ACKNOWLEDGEMENTS

This thesis would not have been possible without the support and assistance of all the people at RMIT University and South West Sydney Cancer Services.

I would like to first thank all my supervisors over the course of the masters. You have all helped to guide me and I know I am a better physicist because of all of your influences.

Rick Franich for listening to me explain my thoughts and helping to shape them into coherent arguments.

Tomas Kron was always smiling and willing to take time out of his busy schedule to provide me with support and encouragement. Plus he likes ice hockey, what's not to like about him.

Thanks to Michael Taylor for always being a sounding board for ideas and random thoughts (I have lots of them) as well as providing some great (and not so great) background music.

Jamie Trapp took me under his wing, gave me good career advice, and helped me to start my career in Medical Physics (He *is* to blame for me being in this field!)

To Lois Holloway – Thank you so much for the help and hours of time spent trying to understand what my project was about.

Phil Wilksch deserves a heap of praise for his efforts in helping to investigate the components of the scanner and explain the optics involved.

Thanks should also go to Peter Johnston for being my supervisor (for a couple of months at least) when he already had too much work to do.

Thanks to Mrs May Whitaker for introducing me to a Linac and water tank during a tour of Peter Mac and for telling me about the wonderful world of Medical Physics.

Thank-you to all the staff at South West Sydney Cancer Services (SWSCS) for providing me with the time and understanding required to complete this thesis.

Thanks to my friends in Melbourne and Sydney, many of whom actually think I am working on a flux capacitor.

Amanda – Thanks for putting up with me over the last few years as I have finalised this thesis.

To my family:

Damo – You'll probably actually never read this acknowledgement, but you are always able to help me feel better when I am down and always able to bring me down when I am feeling good. I couldn't ask for a funnier, more awesome brother.

Mum – Thanks very much for all the support and encouragement over the years. Without your help I wouldn't have been able to do any of this. Sorry I moved to Sydney.

TABLE OF CONTENTS

1. INTRODUCTION

The aim of this thesis is to characterise an optical CT scanner to ensure optimal evaluation of 3D dosimeters. The light source has been investigated and assessed for compatibility with dosimeters and temporal stability. The CCD has been characterised for accuracy of response to light intensity. The scanner has been characterised for 2D and 3D attenuation coefficient accuracy, reconstruction accuracy over a large volume and spatial resolution. In addition the reconstruction has been investigated for scattered light artefacts.

1.1 Radiation Therapy

Radiation therapy (radiotherapy) uses ionising radiation to treat diseased tissue. The goal is to improve a patient's quality of life either through curative treatment of the cancerous tissue or, at minimum, palliative treatment providing symptom relief.

The process of radiotherapy starts with a patient consultation with a doctor where the patient is physically examined and patient anatomy and functional images are acquired. The diseased tissue and surrounding organs at risk are delineated by the Radiation Oncologist (RO) for treatment planning by a combination of physical examination of the patient and any anatomical and functional images acquired. A treatment is planned based on the dose required to achieve the clinical objective (curative treatment or palliation) and the dose constraints on the organs at risk. To maximise the chance of tumour control, a high dose of radiation to the tumour volume is required.

The dosimetric aim of the treatment is dependent upon the treatment technique. International Commission on Radiation Units and Measurements (ICRU) guidelines have been developed for conformal radiotherapy (reports 50[1] and 62[2]) and Intensity Modulated Radiotherapy (Report 83[3]). In conformal radiotherapy, the dosimetric aim is to achieve within +7 and – 5% of the prescribed dose to the Planning Target Volume (PTV). In IMRT, the dosimetric aim is to deliver a dose within 5 % of the prescribed dose for 85 % of the target volume sampled points in low dose gradient regions (less than 20 %.cm^{-1} in any direction)[3]. For high dose gradient regions (equal to or greater than 20 %.cm^{-1}) the use of a measurement of the distance-to-agreement is recommended. A distance to agreement of 5 mm for 85 % of sampled points is recommended[3]. Variations in the dose above or below the suggested tolerances can have an effect on the Tumour Control Probability (TCP) and the Normal Tissue Complication Probability (NTCP)[1].

In radiotherapy a compromise must be reached between irradiating the tumour volume to a high dose and trying to reduce the dose to the normal tissue surrounding the tumour volume. This is typically achieved by careful beam arrangements. A higher than expected dose to the normal tissue decreases

the NTCP. Compromising the dose to the tumour volume, to reduce the dose to the normal tissue, reduces the TCP. Emami et al[4] published a list of organ and tissue dose tolerances used to limit complications. Dose tolerance values have recently been reviewed in a series of publications that provide Quantitative Analyses of Normal Tissue Effects in the Clinic (QUANTEC)[5-25].

To reduce the dose to normal tissue and maintain the high dose to the tumour volume there has been an increase in individualised treatment techniques[26]. Techniques such as intensity modulated radiotherapy (IMRT)[27], high dose rate brachytherapy[28], stereotactic radiosurgery[29], and volumetric arc[30] treatments often have complex dose distributions that vary the dose deposited by large amounts over small distances. These treatment techniques conform the dose distribution more tightly to the planning target volumes than conventional treatment techniques.

Individualised treatment techniques can have very steep dose gradients between the tumour volume and the normal tissue. This clearly introduces a risk – i.e. deviation of the delivered dose distribution from the planned dose distribution could result in significant over-dosage of healthy tissue and/or under dosage of the tumour volume. This would reduce the likelihood of a positive patient outcome.

Differences between planned and delivered treatments may result in unplanned low dose to the tumour volume or an unplanned high dose to the normal tissue or vice versa[26]. This highlights the critical necessity for sophisticated quality assurance procedures to verify that the doses planned are consistent with those ultimately delivered. It is the principle aim of this thesis to contribute to the development of such sophisticated dosimetry.

1.2 Dosimetry

Dosimetry is the measurement or calculation of a dose deposited in a given medium, where dose is the differential energy imparted per unit mass. Dosimetry techniques are used to compare the planned (treatment planning system predicted) dose distribution to the measured dose distribution in a given volume[26]. For a complex dose distribution, measurement of the whole dose distribution would be preferential in evaluating if the dose has been deposited accurately[26]. Different dosimeters have been used to measure dose distributions. An ideal dosimeter would[31]:

- have an accurate and reproducible response that is independent of energy,
- measure the dose with a high spatial resolution,
- exhibit a linear response over a large dynamic range,
- not perturb the dose to the medium, and
- measure the dose distribution in three dimensions.[25]

Many different dosimetry techniques are used to assess treatment plans. Current point measurement devices include ion chambers and diodes. Thermo-luminescence devices are primarily used for in-vivo verification. Two dimensional (2D) planar measurement devices include film and arrays of chambers

or diodes[32-34]. Each individual measurement technique fulfils only some aspects of the ideal dosimeter described above. Negative attributes might include a large perturbation of the medium, low sensitivity to dose, resolution accuracy, water non-equivalence, energy dependence and differences between the phantom and the patient[35,36].

A disadvantage of the zero dimensional point dosimeters (or one dimensional when scanned) and 2D dosimetry measurement tools is that only part of the dose distribution is being sampled in an individual measurement[37]. The use of these techniques to validate the sampled dose distribution against the TPS[26] does not validate the entire 3D dose distribution. Furthermore, the finite volume of dosimeter gives rise to issues of volume averaging and may not accurately reflect the 'true' nature of the dose distribution in high-gradient regions. To fully and comprehensively measure a 3D dose distribution with these dosimeters would require a large number of measurements, which would be costly and time consuming.

The use of gels in the quality assurance process of individualised treatment techniques has the potential to yield high resolution, energy independent and three dimensional dosimetric information.

1.3 Gel Dosimetry and Evaluation Techniques

Gel dosimeters have been designed to measure dose distributions in three dimensions[26]. A gel dosimeter contains a radiation sensitive material throughout a gel matrix. This rigid matrix allows spatial dose information to be retained and read out later. There are numerous types of gel dosimeters with different radiation response mechanisms. The spin states of ions and molecules in the gel can change when irradiated[38]. Alternatively, polymerisation of the reactive material is induced by radiation[39-41]. The literature review in chapter 2 provides greater detail on gel and plastic dosimeters.

Depending on the active ingredient used, changes in the nuclear magnetic resonance[38,41], the x-ray attenuation coefficient[42-44], the ultrasonic properties[45-47] or the visible opacity[48-53] can be induced by radiation. To image these radiation induced changes, different imaging modalities such as magnetic resonance imaging (MRI)[38,41,54-56], x-ray CT[42,57], ultrasound[47,58] and optical CT[52,53,59-68] have been investigated. Section 2.2 of the literature review describes the advantages and disadvantages of each imaging technique.

Cone beam optical computed tomography is the focus of this thesis. A charged coupled device (CCD) is used to measure the light transmitted through a translucent dosimeter. Chemical changes in a dosimeter can cause light from the visible spectrum to be either absorbed or scattered when incident upon the dosimeter[51]. The difference in light transmission through unirradiated and irradiated dosimeters can be used to evaluate the optical density change due to irradiation[62] which can be related back to absorbed dose.

The measured dose distribution is effected by the accuracy and precision of the cone beam optical CT scanner[69] (herein termed the *"scanner"*). Differences between delivered and planned dose distributions could be missed due to uncertainties in the dosimetry measurement. As stated earlier, this could lead to under or over dosage of the tumour volume and adjacent tissues and either decrease the probability of tumour control and patient survival or increase the probability of acute and/or stochastic complications.

It is thus a critical necessity to characterise the properties of the scanner to ensure that the accuracy and precision of the measurements of dose distribution are known and maximised. A standardised approach for commissioning and QA protocols for this equipment has not been published.

1.4 Aim

The aim of this work was to investigate and characterise the properties of a Modus Medical Device Inc. Vista™ Cone Beam Optical CT scanner (Modus Medical Devices Inc., London, Canada) utilised for the imaging of gels. The main components to be assessed were the light source and the CCD. The accuracy of the reconstruction algorithm and influence of scatter were also investigated.

The light source was characterised by measuring the spectra of the two light sources inherent to the scanner and the temporal variation in light source intensity.

The measurement of the filtered and unfiltered light source spectra determines compatibility of the light source and different dosimeters, the influence of differential attenuation and quantum efficiency of the CCD at different wavelengths.

The variation in light source intensity after switching the light source on determines the warm-up time required for the optical CT to reach stable measurement conditions.

The CCD was characterised by measuring several parameters: the dynamic range of the attenuation coefficients from 2D projections and 3D reconstructions; the uniformity of the reconstruction; the spatial fidelity and linearity of response to light intensity.

The dynamic range of measurable attenuation coefficients was characterised by comparing the measured attenuation coefficient relative to known values, the signal to noise ratio and the uniformity of a set of polyurethane phantoms. Each phantom had a unique uniform opacity with the reference attenuation coefficient measured in geometry configured to minimise scattered light.

The spatial resolution in 2D and 3D was assessed by calculating the modulation transfer function (MTF). The spatial resolution dependence on the reconstruction settings was investigated to determine the optimal settings for use in the scanner. The change in MTF caused by overflow of charge from one CCD element to the next was also investigated.

Reciprocity of the CCD response to light intensity was used to validate the optical density calculation method used in this thesis. The reciprocity was characterised by measuring the pixel response of the CCD as a function of CCD charge collection time with a constant light source.

The source and influence of scatter on a projection and reconstructed volume was investigated by using collimating windows at the entrance and exit of the specimen tank.

1.5 Structure of Thesis

After this brief introduction, relevant literature is reviewed in chapter 2 with an emphasis on gel dosimetry, different types of Optical CT scanners and characterisation methods for Optical CT.

The materials and methodologies associated with characterisation are described in detail in chapter 3.

There are three main components to the work:

1. Characterisation of the imaging system,
2. Assessment of the projections from the cone beam optical CT, and
3. Assessment of 3D reconstructed images.

The three components are investigated in chapters 4, 5 and 6 respectively.

Chapter 4 investigates the basic components of the scanner, specifically, characterising the light source and the CCD. The spectrum of the light source was investigated for uncertainty caused by differential attenuation of light in the dosimeter and quantum efficiency of the CCD at different wavelengths. The temporal variation of the light source intensity during the initial warm-up of the optical CT scanner was evaluated for the magnitude of the effect on measurements performed during this time. The reciprocity of the CCD response to changes in light intensity affects the accuracy of the optical density measurement. The attenuation coefficients for uniform reference phantoms were determined via measurement in a geometry designed to minimise uncertainty due to scattered light and path length.

Chapter 5 focuses on the assessment of 2D projection images and consequently the information that can be derived from them. Chapter 6 investigates properties of the 3D reconstructed images. In chapters 5 and 6, attenuation coefficients of the reference phantoms were measured from 2D projection data, and from reconstructed 3D images. The values were compared to the attenuation coefficients obtained under reference conditions in chapter 4. The uniformity of response of the scanner was investigated in both 2D projection images and 3D reconstructed images. The measured spatial resolution of the 2D projection images and the 3D reconstructed images are presented in chapters 5 and 6 respectively. The influence of scatter on 2D projections and 3D reconstructions is investigated in chapters 5 and 6 respectively.

The minimum detectable light threshold and saturation limit of the CCD impose restrictions on the maximum and minimum optical densities that can be imaged with the scanner. Non-linear response close to these limits can lead to errors in the measured attenuation coefficients and the interpretation of dose. Variations in the linearity of the optical density response are investigated by comparing the 2D and 3D measured attenuation coefficients of specifically designed phantoms, to values obtained under

the well-known conditions in chapter 4. The practical working dynamic range is determined for both 2D projections and 3D reconstructed images in chapters 5 and 6 respectively.

The evaluated response of a uniformly attenuating phantom will be the same at all voxels inside a phantom. Therefore, differences in the response are caused by different path lengths through the phantom. This is due to the only difference in a uniform phantom is the path length through the phantom. The uniformity response of the scanner was investigated by imaging uniform phantoms. The effect of path length differences (through the typically cylindrical shaped phantoms) was observed in 2D projections. In 3D, the effects of scattered light on the ability to reconstruct a uniform object were quantified.

The spatial resolution of an imaging system is defined as the ability to distinguish between two points very close to each other. Poor spatial resolution may lead to the inability to image sufficient detail due to a blurring of the measured dose distribution. The spatial resolution of 2D projection images and 3D reconstructed images are investigated in Chapters 5 and 6 respectively.

Chapter 7 summarises and draws conclusions on the presented work. The chapter compares quality assurance methods and results using 2D projections and 3D reconstructions. Suggested characterisation tests are also discussed. Limitations of the work are presented as well as suggested items for future work.

2. BACKGROUND AND LITERATURE REVIEW

The background and literature review presented in this chapter cover the main types of 3D dosimeters used in clinical and research contexts, the different evaluation systems, the different types of optical CT scanners, the accuracy and precision of gel dosimetry and the tests performed to characterise a cone beam optical CT scanner. Gels and plastic dosimeters are used in radiotherapy to measure dose distributions in three dimensions. There is a strong argument for the routine implementation of 3D dosimeters as discussed in section 1.2. The different optical CT scanner designs and previous characterisation methods are described. The uncertainty of gel dosimetry, and the influence of the optical CT evaluation technique on accuracy and precision, is reviewed. As will be shown in the literature review there are a number of scanners and a large variety of characterisation techniques. This shows the importance of the characterisation process. However, there is not a single well defined procedure for characterising an optical CT scanner. The focus of this work is characterising the *cone beam* optical CT scanner for gel dosimetry and investigating characterisation techniques as part of a recommendation for ongoing quality assurance.

2.1 Gel and Plastic Dosimeters

Measuring a radiation induced change in a gel or plastic dosimeter is possibly the only true method for high resolution three dimensional integrating dosimetry. The radiation induced change may be the nuclear magnetic resonance (NMR) property of an ion[38,41,56], the x-ray attenuation coefficient[42-44], the acoustic properties of the gel[45-47] or the optical transmission of the gel[51].

As described in section 1.2, an ideal dosimeter is able to measure the dose:

- Accurately,
- Reproducibly,
- Over a large dynamic range,
- With a linear response,
- Independent of the dose rate,
- With “tissue equivalence” independent of energy, and
- With a high spatial resolution

Dosimeters may be characterised and compared by the properties listed above. Because an ideal dosimeter does not exist, compromises on the above properties are made when selecting a dosimeter. The required measurement influences which properties of the dosimeter are critical and which properties can be compromised. As an example consider using a parallel plate chamber for beam

profile and percentage depth dose measurements – the spatial resolution of the chamber perpendicular to the beam direction is critical for accurate profile measurements, but is not critical for PDD measurements.

The readout system can also impact upon the viable properties of the dosimeter and requires separate evaluation to assess which dosimeter and readout system will provide the best combination of the above properties.

3D dosimeters for optical (visible wavelength) readout can be divided into two broad categories; those that absorb light and those that scatter light. The main types of gel-based dosimeters are Fricke and polymer gels. The main type of plastic dosimeter is doped polyurethane, e.g., PRESAGE^{TM}. Polymer gels can be split further into hypoxic and normoxic sub-categories. The radiation induced change depends on the type of gel manufactured. Each type of gel has different advantages and disadvantages. The chemical make-up, reactions to radiation, and other properties are detailed below for each type of gel.

2.1.1 Fricke Gels

Fricke gels are based on the reaction of ferrous solutions to radiation discovered by Fricke and Morse[70]. They discovered that irradiated Ferrous ions, Fe^{2+}, change into Ferric ions, Fe^{3+}. Since the NMR relaxation times for the two ions are different, a quantitative difference from NMR measurements of control solutions and irradiated solutions was measured by Gore et al[38]. Gore et al[38] confirmed that the radiation induced change in the nuclear magnetic spin occurs for ferrous ions dissolved in a gelatine matrix. Chelating agents were then investigated to develop the solution into a gel[71,72].

Fricke gels comprise of Ferrous ions dissolved in water[38]. Gelatine or agarose is added as a gelling agent to bind the solution into a rigid matrix[72,73]. Sephadex and polyvinyl alcohol (PVA) have also been used as gelling agents[69]. The amounts used typically are 4-5 % by weight gelatine or 1 % by weight agarose[73]. Changes in the optical density for a non-doped Fricke gel are in the ultraviolet region[74]. The light transmission changes in the Fricke gel may be shifted into the visible spectrum with the addition of xylenol orange[51,75-78] making them suitable for optical readout.

Kelly et al[51] found a 2 % accuracy of the reconstructed optical attenuation coefficient from a Fricke dosimeter measured with a laser based optical CT scanner (see section 2.3.1 for description of laser based optical CT scanner). A 2 % reproducibility was measured for the dose response curve[51].

Fricke gels have shown a reaction completion time that varies depending on the concentration of the chemicals[51]. Changes in attenuation of approximately 0.0046 cm^{-1}/h, or 0.29 %/h, have been shown post-irradiation[51]. The reaction completion time increases with absorbed dose[51]. A limitation of Fricke gels is the diffusion of ions[75-81]. It was estimated that the Fricke gel requires imaging within two hours of irradiation for best results[80]. Chemicals such as xylenol orange have been shown to improve the

stability of the spatial dose distribution by reducing diffusion by a factor of four[74]. The amount of diffusion depends on the dose the gel is irradiated to and the initial Fe^{2+} concentration[74]. Additionally the Fricke gel requires storage in cool, dark areas to ensure no spontaneous reaction occurs causing a change in the NMR response or opacity of the gel[74].

The sensitivity of the Fricke gel is dependent on the initial Fe^{2+} concentration[74], how fresh the gels are[81] and the concentration of the chelating agent[73,81]. The sensitivity can be increased by using Benzoic acid[51], Sodium Chloride[72,73,81] or sugars[74]. When evaluating a Fricke gel dosimeter, the dose sensitivity is also dependent on the NMR frequency[74] or the optical wavelength[51,74]. Kelly et al[51] described a Fricke dosimeter with a linear response to dose between 0 and 10 Gy. The measurement wavelength was 543.5 nm. Fricke gel response was observed to be independent of dose rate[73,81].

The dosimetric response of Fricke gels is also dependent on the temperature of preparation[74]. Olding et al[82] investigated the optical CT scanner response with changing scan temperature. A change in light attenuation of 2.5 % /°C was observed for Fricke gelatine gel doped with xylenol orange.

Water (or tissue) equivalence is a typical requirement of dosimeters. This is because the dosimeter is designed to sample the dose with as minimal perturbation of the medium as possible. Significantly different radiological properties of the dosimeter will affect the measured dose[31]. The radiological properties of Fricke gels have been investigated via calculation of the physical density[83], effective atomic number[83,84], electron density[83], photon attenuation and absorption coefficients[85] and electron stopping and scattering powers[85]. Monte Carlo simulations of 6 MV and 6 MeV PDD curves were also used to investigate the photon attenuation and absorption and the electron stopping and scattering powers[85]. The results demonstrated the water and soft tissue equivalence of Fricke gel[74,83-85]. The tissue equivalence of Fricke gels is independent of energy for a large range of energies[74,83,84], with significant differences only present below 100 keV due to the strong Z dependence of the photoelectric interaction[74,84].

Fricke gels are easy to produce in a consistent fashion and can be used to determine the spatial dose information very quickly with a good tissue equivalence and a large dose range[74]. When doped with xylenol orange, the optical density changes induced by radiation in Fricke gels are in the visible region and can easily be imaged with Optical CT scanners[51-53]. Fricke dosimeters are accurate and reproducible[51] with no dose rate dependence[73,81] and minimal energy dependence[74,84]. The response of Fricke gels is affected by the ratio of the chemical components[51,72-74,81] and the temperature during fabrication[74] and evaluation[82]. The stored dose distribution is affected by the post irradiation diffusion of ferric ions[75-81]. Therefore the time between irradiation and evaluation is important[82]. For the interested reader a good review of Fricke gels is provided by Schreiner et al[74].

The diffusion of dose distributions measured with Fricke gels is a restrictive limitation, and polymer based gel dosimeters were introduced as an alternative.

2.1.2 Polymer Gel Dosimeters

Polymer gels are formed by monomers suspended in a gelatine matrix. When irradiated, the monomers polymerise to an extent proportional to the radiation dose[69]. Polymer gels can be split into two broad categories:

- *Hypoxic* polymer gels can undergo auto-polymerisation in the presence of oxygen and as such require an oxygen free environment[86,87]
- *Normoxic* polymer gels use an oxygen scavenger to restrict polymerisation and can be used in normal atmospheric conditions[40].

Both hypoxic and normoxic polymer gels react to radiation in the same way. Water molecule bonds are broken by radiation (radiolysis), which results in highly reactive atoms with unpaired electrons (free radicals) causing polymerisation reactions. The polymerisation of the monomers causes polymer chains to form. The polymer chains affect properties of the gel and this can be exploited for evaluation[88].

Magnetic resonance imaging (MRI) of polyacrylamide gel (PAG) dosimeters often uses the spin-spin relaxation rate (R_2). The R_2 response changes with radiation induced polymerisation, which is in turn a function of dose[69].

Optical CT imaging is possible due to the changing size of the monomers and polymers causing changes in the light scattering conditions. As the molecule size increases the amount of scattered light from the molecule increases. Increasing the dose essentially increases the opacity of the sample[89]. The process for scattering light, in both hypoxic and normoxic polymer gels, is Mie scattering – the scattering of light by particles roughly equivalent in size to the wavelength of light incident on the particle[69]. The disadvantages of scattered light are discussed in section 2.4

Details on the different evaluation techniques are presented in section 2.2.

A critical review of polymer gels was completed by Baldock et al[69]. A brief summary of hypoxic and normoxic gels is presented below.

2.1.3 Hypoxic Polymer Gel

Hypoxic polymer gels were the first type of gel developed that used polymerisation of monomers as a dose response mechanism. An early type of hypoxic polymer gel comprised N,N'-methylene bis-acrylamide (Bis), Acrylamide (AAm), Nitrous Oxide and agarose and was named BANANA[69]. This was refined to use gelatine as the chelating agent, AAm, Bis and Nitrogen. These gels have been called BANG™ (MGS Research Inc., Madison, CT, USA) gels[54].

Hypoxic polymer gels require a sealed oxygen free environment to ensure that oxygen does not induce auto-polymerisation[86,87]. Purging the solution of oxygen can be achieved by bubbling nitrogen through the solution during fabrication[86,87]. The solution is then transferred to air tight glass vials[86] or

anthropomorphic phantoms[87]. Glass vials are used because they are air tight, therefore stopping oxygen induced auto-polymerisation. Glass vials are not ideal due to a lack of tissue equivalence[40], less malleability[40], potential beam hardening[69] and potential refractive index mis-matches between glass and water when evaluating the dosimeter using an optical CT scanner[90]. Taylor et al[91] investigated the influence of glass walls on polymer gel calibration. The results showed differences less than 1 % relative to the expected dose in water as long as strict calibration conditions were used.

The MRI response from BANG™ gels, R_2, has been shown to be reproducible. The variation observed was less than 2 % up to 8 Gy[54]. BANG™ gel dosimeters were also shown to have a consistent opacity change compared to NMR relaxation times[54].

The radiological properties of hypoxic polymer gels have been investigated for atomic composition[50], measured density[50,92], electron density[50,92], average atomic number[50], effective atomic number[84,92], collisional, radiative and total electron interactions[85,93] and photon interaction cross-sections[85]. The investigations referenced above have shown that the radiological properties of hypoxic polymer gels are close to water or soft tissue. The radiological response was observed to have a small dependence on photon beam quality ($TPR_{20/10}$ between 0.620 – 0.781) and mean electron energy (3.6 – 14.9 MeV)[94].

De Deene et al[92] found the response for a hypoxic gel changed by up to 12 % over dose rates between 25 cGy/min up to 400 cGy/min. The response of BANG2™ gel (2nd Generation BANG™ gel, MGS Research Inc., Madison, CT, USA) was found to uninfluenced at dose rates of 80, 160, 240, 320 and 400 MU/min[94]. While both gels are hypoxic, one is unaffected by changes in dose rate, whilst the other is affected. The results cannot be compared directly because: i) different units of measurement were used to specify the dose rate[92] and ii) the formula for BANG2™ is not given and therefore it is not clear that these two gels are the same. Caution is required when using different dose rates due to the conflicting information on the influence dose rate has on dose response.

The influence of temperature on the MRI response at the time of evaluation and time of irradiation has been investigated[54,92]. No influence on the optical attenuation coefficient by temperature at the time of scanning has been communicated[69].

The relationship of the MRI response (R_2) and dose is dependent on the ratio of cross linker to monomer[92,95], the total concentration of the monomer[92] and the concentration of the gelatine[92]. The concentration of the cross-linker used in the gel has an effect on the optical density dose response[50]. The influence of total monomer and gelatine concentration on the optical density has not been communicated.

Diffusion in high dose regions and in steep dose gradients has been observed[54,87,92,96,97]. Monomers from outside the field diffuse into the irradiated volume. Once in the irradiated volume, the monomers interact with long lived macro-radicals[54,97].

The R_2 calibration curve has been observed to change with post irradiation time due to post irradiation polymerisation and the gelation process[92,98]. No influence on the optical density response has been communicated.

Hypoxic polymer gels have a good tissue equivalence[50,84,85,92,93] over a range of energies[94]. The dose response of hypoxic polymer gels is independent of the temperature at the time of irradiation[54,92]. Problems with hypoxic polymer gels include diffusion[54,87,92,96], temperature at the time of evaluation[54,92] and post irradiation polymerisation[98]. Hypoxic polymer gels are difficult to manufacture due to the requirement of an oxygen free environment[86,87]. Due to this requirement of an oxygen free environment, normoxic polymer gels were developed for use in normal atmospheric conditions.

2.1.4 Normoxic Polymer Gels

Normoxic polymer gels are similar to hypoxic polymer gels, but can be used in normal atmospheric conditions. Normoxic polymer gels use an oxygen scavenger, such as ascorbic acid[40,99], tetrakis hydroxy(methyl) phosphonium chloride (THPC)[100,101] or $CuSO_4$[100,102] to prevent oxygen induced auto-polymerisation and as such do not require an oxygen free environment. Hydroquinone is used as a free radical scavenger to react with free radicals to prevent free radical polymerisation[40]. Normoxic polymer gels can be split into two categories depending on the monomer. Fong et al[40] developed a normoxic polymer gel using methacrylic acid as the monomer. This type of gel was called MAGIC (Methacrylic and Ascorbic acid in Gelatine Initiated by Copper). De Deene et al[103] developed a normoxic polymer gel using acrylamide as the monomer. Different chemical formulations and concentrations of both types of normoxic polymer gel dosimeters have been investigated[101].

Normoxic polymer gels have been measured over a range of doses with a linear response to the varying dose[40,101]. Heard et al[104] measured the dose range for an acrylamide based normoxic dosimeter in a laser based optical CT. The reproducibility of the dose was as large as 20 % at 7 Gy. For lower dose regions a 5.5 % uncertainty in determining the optical density value has been observed[104]. For the same normoxic gel, Heard et al[104] observed an intra-batch reproducibility of the attenuation coefficient of 3.7 %. Post-irradiation polymerisation was reported by De Deene et al[98] to affect the dose response.

The radiological properties of normoxic polymer gels have been investigated for mass density[92], electron density[92], effective atomic number[84,92], mass attenuation coefficient[92] and the effective atomic number for collisional, radiation and total electron interactions[93]. Venning et al[105] determined the photon and electron interaction cross sections for a number of different formulations of normoxic gels. The interaction cross sections were calculated over an energy range of 10 keV to 20 MeV. Differences up to 3 % relative to water for the attenuation and collisional stopping power ratios were calculated in the Compton dominant energy range. The mass energy absorption ratios for all gels were within 2 % relative to water except below 100 keV where differences up to 6 % lower than water were observed[105]. The R_2 response of normoxic acrylamide based polymer gel shows no energy dependence.

For normoxic methacrylic acid based polymer gel, a small energy dependence, increasing with dose, was observed[92].

The MRI response of polyacrylamide based normoxic gels is independent for photon energies of 6 MV and 25 MV[92]. The MRI response of methacrylic based normoxic gels for the same energies is observed to have minimal energy dependence[92].

A 66 % difference in MRI response with varying dose rate was found for a methacrylic acid based normoxic gel dosimeter (8 % Gelatine, 6 % Methacrylic Acid, 2mM bis[tetrakis(hydroxymethyl)phosphonium]sulphate)[92]. The variance in dose rate was between 30 cGy/min and 400 cGy/min[92]. For the same range of dose rates, the MRI response for a polyacrylamide based gel dosimeter (6 % Gelatine, 3 % Polyacrylamide, 3 % N,N' – methylene-bis-acrylamide (bis), 5mM bis[tetrakis(hydroxymethyl)phosphonium]sulphate was observed to vary by ~5 %[92].

The sensitivity of the MRI response to dose for normoxic methacrylic acid polymer gels decreases with increasing ratio of cross-linker to monomer[92]. Increasing the concentration of methacrylic acid, without the use of a cross-linker, increases the sensitivity of the gel[92]. The sensitivity of the MRI response to dose for normoxic polyacrylamide gels increases with increasing ratio of cross linker to monomer, before the sensitivity saturates at a ratio of 50 % cross-linker to monomer[92]. Increasing the total concentration of polyacrylamide increases the sensitivity of the dose response[92].

Diffusion of monomers can influence the evaluation of the dose distribution[69]. Post-irradiation diffusion over time has been observed in methacrylic acid based normoxic dosimeters for doses above 10 Gy[92]. Post-irradiation diffusion in polyacrylamide based normoxic dosimeters has not been observed[92]. The diffusion has been observed for small regions with large changes in dose, and also in regions of high dose[69]. Diffusion has also been noted during the first few hours after irradiation[69].

Senden et al[101] observed a decrease in R_2 response with increasing temperature during evaluation scanning. De Deene et al[92] observed a dependence of temperature during irradiation for a methacrylic acid based dosimeter. During MRI scanning a 1 °C change in temperature was calculated to have a 5 % maximum dose error[92]. No dependence on temperature was observed for a polyacrylamide based dosimeter[92].

Normoxic polymer gels are relatively easy to manufacture compared to hypoxic polymer gels. Normoxic polymer gels are approximately equivalent to tissue and water and exhibit minimal energy dependence[92]. Normoxic polymer gels are, however, sensitive to the temperature during irradiation and evaluation, the dose rate and post irradiation polymerisation.

2.1.5 PRESAGE™ (Solid Polyurethane) Dosimeter

To overcome some of the problems associated with diffusion in gels and the refractive index mis-matches caused by either glass or plastic containers, Adamovics et al[39,48,106-108] developed a dosimeter comprised of a polyurethane matrix mixed with a radiosensitive, light absorbing, leuco dye[108]. The

dosimeter is ideal for optical read-out as it absorbs light, therefore eliminating the light scattering issues associated with polymer gels (discussed in section 2.1.2). PRESAGE™ consists of alkyl diisocyanate mixed with a solution consisting of a polyol, a leuco dye and a free radical initiator[39]. Free radical initiators used include chloroform, carbon tetrachloride, methylene chloride and tetrachloroethane[48]. Radiation acts as a catalyst to oxidise the leuco dye[48]. The sensitivity of PRESAGE™ is dependent on the concentration of the pre-mold mixture[109].

The optical response to dose is linear with an accuracy of ~1 % and an intrabatch reproducibility of <2 %[110]. The optical dose response stabilises within 2 days after being irradiated[110].

The optical density response has been investigated for dose range and dependence on the dose rate[48,49]. The optical density response indicates no dose rate dependence between 0.6-4.4 Gy/min for 145 kVp and 1-6 Gy/min for 6 MV[48]. The optical density response to dose is linear between 0-40 Gy[48,49].

Diffusion of the irradiated field over time was not exhibited by PRESAGE™ over the course of 2 weeks[48]. The stability of the dosimeter has been observed to decrease with increasing concentration of radical initiator[111].

The optical CT response of PRESAGE™ is dependent on the temperature during irradiation and post irradiation storage[112].

Brown et al[113] investigated the photoelectric cross-sections over an energy range of 10 keV to 20 MeV. The results showed the PRESAGE™ was not water equivalent. The effective atomic number and mass density were respectively ~17 % and ~10 % higher relative to water over the energy range investigated[113]. The Compton and photoelectric interaction probabilities were up to 55 % and 81 % higher relative to water respectively in the energy range 10 keV to 1 MeV[113]. Differences of less than 5 % for the photoelectric, Compton and pair production interaction probabilities were observed in the 1 – 20 MeV range[113]. Measurements by Adamovics et al[48] exhibited no energy dependence for 145 kVp, 6 and 18 MV, and 1.25 MeV.

PRESAGE™ dosimeters are sensitive to UV and blue light, which cause colouration of the dosimeter[107]. The refractive index of PRESAGE™ does *not* match water and requires a refractive index matching fluid for optical imaging[108]. The manufacturing process of PRESAGE™ takes approximately 48 hours[39,48]. The stability of the exposed portions of the PRESAGE™ have also been investigated by Adamovics and Maryanski[48] at different temperatures with no significant effect observed at different temperatures. Optical densities have been observed to change by approximately 4% per day (24hr) for samples stored in the dark at approximately 22°C. Adamovics and Maryanski[48] observed the rate of opacity change after irradiation can be slowed by storage in a refrigerator (at 2-8 °C) or under cooler temperatures (-20 °C).

PRESAGE™ is a containerless dosimeter that does not exhibit any diffusion[48] and has a response that is independent of dose rate[48,49] and energy[48,113]. PRESAGE is, however, not water or tissue equivalent and takes a long time to manufacture. The response is sensitive to the temperature during irradiation and post irradiation storage[112].

Table 2-1: Comparison of some different types of 3D dosimeters. Greater detail can be found in the relevant dosimeter sections in the text.

Property	***Fricke Gel***	***Hypoxic PAG***	***Normoxic PAG***	***PRESAGE^{TM}***
Chemical Makeup	Fe^{2+} Ions Gelatine/Agarose Xylenol Orange	N,N'-methylene bis-acrylamide Acrylamide Nitrous Oxide Gelatine	N,N'-methylene bis-acrylamide Acrylamide Nitrous Oxide Gelatine Oxygen and Free radical scavenger Methacrylic acid	Polyurethane matrix Leuco dye
Reaction	Fe^{2+} to Fe^{3+}	Free radicals from hydrolysis cause polymerisation	Free radicals from hydrolysis cause polymerisation	Oxidation of leuco dye
Optical Attenuation	Absorbing	Scattering	Scattering	Absorbing
Accuracy and Reproducibility	2 %	None communicated	~6 % uncertainty ~4 % reproducibility	~ 1 % accuracy <2 % intrabatch reproducibility
Post irradiation reactions	Varies depending on concentration of chemicals	No optical CT results communicated	Present	Present up to 2 days
Diffusion	High	In high dose regions and steep dose gradients	Present	None exhibited
Sensitivity dependencies	Dependent on chemical concentration, freshness of gel and wavelength of light used for evaluation	Dependent on ratio of crosslinker to monomer and total concentration of monomer	Dependent on ratio of crosslinker to monomer and total concentration of monomer	Dependent on concentration of pre-mold mixture
Dose Rate dependence	Independent	Some have shown dependence, whilst others have not	Dependent	Independent
Radiological properties	Water equivalent (2 %, 1 – 10 MeV)	Water equivalent (1 – 2 %, 1 – 10 MeV)	Water equivalent (1 %, 1 – 20 MeV)	Not water equivalent
Main limitations	Diffusion	Oxygen induced auto-polymerisation	Sensitive to temperature during irradiation and evaluation, dose rate and post irradiation polymerisation	Sensitive to UV + blue light Refractive index not matching water

2.2 Evaluation Techniques

The evaluation technique can affect the uncertainty and range of measurable dose which can limit the measured information. For example, film spatial resolution is theoretically limited by the size of the crystal grain size, however the film scanner's sampling resolution limits the measured information. The dosimetry system must be considered as a whole and characterising a method for dosimeter evaluation is essential for assessing the achievable accuracy and utility of the system.

As described above, radiation induced changes in a gel dosimeter can be evaluated by Nuclear Magnetic Resonance (NMR)[38,41], x-ray attenuation coefficient[42,44], propagation of ultrasonic sound[45-47] and the absorption[51-53] or scattering[50,69,89] of light. Some dosimeters are more suited to particular techniques used for readout of the radiation induced changes.

There are four major imaging techniques that have been investigated for the readout of gel dosimeters. MRI evaluates the magnetic resonance change between different ions caused by irradiation[38,40,41,55,56]. X-ray CT evaluates radiation induced electron density changes that affect the x-ray attenuation coefficient[42,57]. Ultrasound devices have been used to measure changes in the acoustic impedance due to irradiation[58]. Optical CT measures the change in optical transmission between an un-irradiated and irradiated gel[37,52,53,59-61,63-66,68,90,114-116]. A brief review of the advantages and disadvantages for Magnetic Resonance Imaging (MRI), x-ray CT, ultrasound and optical CT scanning is presented here. The principles behind the operation and the different types of optical CT scanners will be reviewed in greater depth in section 2.3. A summary of the advantages and disadvantages of the different evaluation techniques is presented in Table 2-2.

MRI involves changing the alignment of a molecule or ion relative to the direction of an applied magnetic field and measuring the time taken for the molecule or ion to relax back to the original alignment. The average relaxation rate of a sampled volume is affected by the type of compound the molecule has formed or the type of ion that has been formed. The mobility of the molecule or ion in the surrounding medium also effects the average relaxation rate[117]. In Fricke gels, radiation can induce a change in the ionisation state of Fe^{2+} ions as described earlier. This causes differences in NMR relaxation rates. In polymer gels the proximity of the hydrogen atom to a polymer chain, or position of the atom in a polymer chain, causes differences in the relaxation rate of the hydrogen atom. Hydrogen atoms located in a polymer will have a different relaxation rate compared to other bound states[117]. The expense and limited availability of MRI machines has led to the development of other techniques for the evaluation of gels[117].

X-ray CT of polymer gels has also been used to evaluate the radiation induced mass density change caused by polymerisation[42-44]. The dose response from gels imaged using an x-ray CT scanner is comparable to the response from an MRI machine[42]. The limitation of x-ray CT scanning is low dose sensitivity, which corresponds to a higher dose uncertainty[42]. Advantages of x-ray CT scanner over

MRI machines included scanner accessibility, quicker imaging time, higher spatial resolution and lower sensitivity to imaging temperature[42]. To allow complete oxygen diffusion through the irradiated gel, a post irradiation wait of 1 week is required prior to imaging[42]. This wait will change depending on the chemical composition of the gel and the size of the gel volume. The use of an x-ray CT scanner to image the gel causes radiation induced changes in the gel, which will eventually destroy the dose information stored, preventing further analysis[42].

Ultrasound scanning of the structural change of polymer gels and the resulting effects on the propagation speed and attenuation of ultrasonic waves has been investigated[45-47]. The technique measures dose by looking at changes in acoustic speed, acoustic attenuation and transmitted signal intensity[45-47]. PAG ultrasound dose response has been compared to the MRI dose response. The results show ultrasound has a larger dynamic dose range compared to MRI for similar formulations of gels[47]. The primary advantage of ultrasound imaging is the significantly lower cost compared to MRI[47]. Dose response uncertainties have been attributed to uncertainties in determining the acoustic parameters. In particular the noise in acoustic signals, loss of information when digitising the signal, sampling errors and scatter have been identified as sources of uncertainty[47]. The use of ultrasound for 3D dosimetry has not had as large an impact compared to optical CT scanning of 3D dosimeters.

An optical CT scanner measures the change in the transmission of light through the gel before and after irradiation. This imaging technique is the imaging modality of interest in this work. The advantages of using an optical CT scanner compared to MRI are low cost[66], quick acquisition speed of scans[114], high spatial resolution[114] and accessibility of optical CT[61]. Whilst there are a greater number of MRI units compared to optical CT scanners in Australia, the dominant use of an MRI unit is for clinical imaging. Clinical imaging generates a large income for an MRI operator from the patient health care system. A researcher using an MRI machine will be charged a similar amount of money that the operator would generate from clinical use. In addition, the machine and personnel to operate the machine will be hired outside normal working hours. This increases the cost to the researcher. An optical CT scanner purchased by a department costs a fraction of the cost of an MRI machine and will be easier to access. Disadvantages of gel dosimeter readout using an optical CT scanner are the light scattered within gel dosimeters, container walls and the artefacts associated with refractive index matching.[63] The walls of the gel container cause complications during optical CT imaging due to the mismatch in refractive indices of the container (either glass or plastic) and the gel[61]. When imaged optically the errors in measurement of optical density caused by scattered light can be as great as 30 %[69,118]. The wavelength of light sampling the dosimeter can influence the measured opacity[50,51,106]. This is because for different wavelengths of light there are different absorption or scatter cross-sections.

Table 2-2: Summary of advantages and disadvantages of MRI, x-ray CT, ultrasound and optical CT for evaluation of gel dosimeters

Imaging technique	*Advantages*	*Disadvantages*	*Ref*
MRI	First established technique. Principles well understood	Cost very high MRI machines not extensively available for research use in radiotherapy departments	[38,40,41,55,56]
X-ray CT	Already in most radiotherapy departments, easier access. Quick imaging time High spatial resolution Low sensitivity to imaging temperature	Cost high Low SNR High dose uncertainty Long wait after irradiation to image gel	[42]
Ultrasound	Low cost Portable Large dynamic range for attenuation vs. absorbed dose Large dynamic range for transmitted signal intensity vs. absorbed dose Large dynamic range for acoustic speed vs. absorbed dose	Low dose resolution due to: • Noise • Loss of information when digitising signal • Errors in sampling • Scattering effects	[47]
Optical CT	Low Cost Quick High Spatial Resolution compared to MRI	Problems with artefacts in reconstruction	[50,61,63,66,69,114,118]

2.3 Optical CT Evaluation

Optical CT scanning is a relatively new evaluation technique that was proposed for 3D gel dosimetry in companion papers by Gore et al[63] and Maryanski et al[50]. Different types of optical CT scanners have been developed and will be detailed below. The basic principle of an Optical CT scanner is the measurement of the change in opacity of a gel before and after irradiation. The scanning process is:

1. The light transmitted through an unirradiated dosimeter is collected at a particular incidence angle,
2. The dosimeter is rotated to a new angle and step 1 is repeated. This is repeated for a number of incidence angles
3. The dosimeter is removed from the scanner and used to undertake the desired dosimeter measurements
4. Steps 1 and 2 are repeated with the irradiated dosimeter and the same angles as used in step 2.
5. Tomographic reconstruction of difference image is undertaken

The method for calculating the optical density and attenuation coefficient is presented in section 3.2.2. A method for reconstruction is presented in section 3.4.

There are two main types of scanners. The first type of scanner uses a laser scanned across a dosimeter, with the transmitted light collected by a diode[63]. A second type of optical CT scanner uses a broad light source and CCD to capture projection images of the dosimeter. This method can be split into two types of CCD geometries. Doran et al[61] used a single light emitting diode (LED) and focusing optics to create a parallel beam of light across the gel specimen tank and Wolodzko et al[68] used a broad beam source and a CCD in a cone beam geometry. The type of scanner influences selection of the types of gels that can be imaged, and exhibits different optical density range, speed of scanning and spatial resolution of the images.

2.3.1 Laser Diode Scanner

In 1996 Gore et al[63] developed a tomographic optical density scanner. A monochromatic light source (He-Ne laser, 632 nm wavelength) was mounted in front of a travelling mirror, which linearly stepped across the face of a specimen tank, transmitting the laser light through the tank to another mirror, travelling in unison with the first mirror, which reflected the light toward a diode detector[63]. In figure 3 this system is shown with the incident beam being split between the mirror and a reference detector to provide a reference measurement of the laser intensity at any given time.

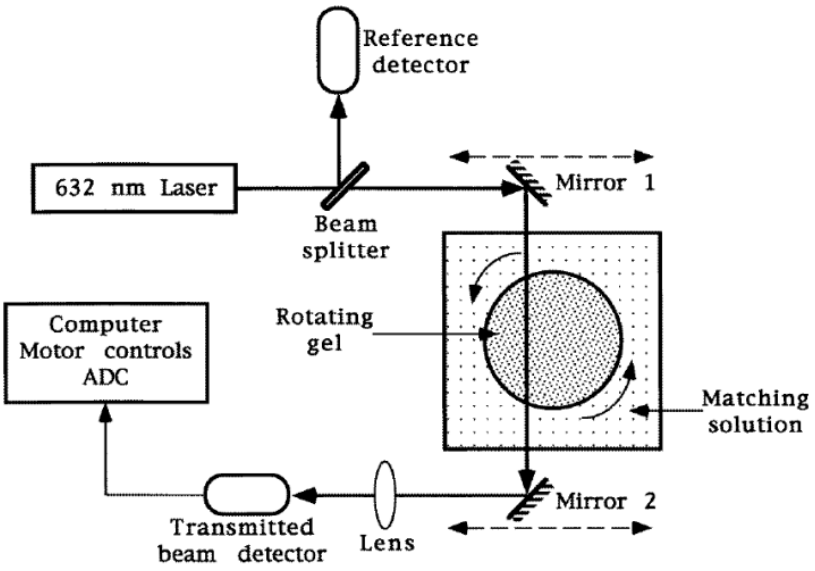

Figure 2-1: Laser diode Optical CT. (Image reproduced with permission from Gore et al, Radiation dose distributions in three dimensions from tomographic optical density scanning of polymer gels: I. Development of an optical scanner, Phys. Med. Biol., 41, 2695-2704 (1996)[63])

The laser was a narrow beam that was linearly stepped by the travelling mirrors across the sample before the sample was rotated. Projection profiles were obtained in 2-3 degree increments for 180°. The projection profiles obtained are then reconstructed using filtered back-projection. This scanner was modified by Oldham et al[37] to include an automatic vertical translation stage. Projections of different slices could also be obtained by the use of additional mirrors[63].

The scanner developed by Gore et al[63] used a diode with a sensitive area of 1cm^2 to detect the transmitted laser intensity. In order to minimise signal fluctuations due to non-uniform response across the detector a diffusing screen and converging lens were placed in front of the diode[63].

Modifications on the original design have been made to increase the speed of the sampling process. Van Doorn et al[119] and Conklin et al[120] incorporated rotating mirrors into the design of the scanner. Krstajic et al[121] used parabolic and galvanometer mirrors to raster scan a laser across a sample to acquire a slice. The mirrors are then adjusted to change the height of the laser on dosimeter and information for the next slice is acquired. Jirasek et al[122] modified the laser based design by using a lens to create a 60° fan beam. 320 photo detectors were arranged concentric to the focal point to detect the light.

2.3.2 Parallel Beam Optical CT Scanner

An optical CT scanner was developed by Doran et al[61] that contained a single light source, a lens system to produce a parallel light beam, a specimen tank and a secondary lens system to focus the light source onto a CCD. The light source used was a mercury lamp[61]. This provided a way to select an appropriate light source to use with a gel to provide the largest gel response and optical density range. The scanner was modified by Krstajic et al[65] to improve the imaging capabilities with new focusing optics and a high powered LED. A parallel beam optical CT scanner is shown in figure 2-2[65].

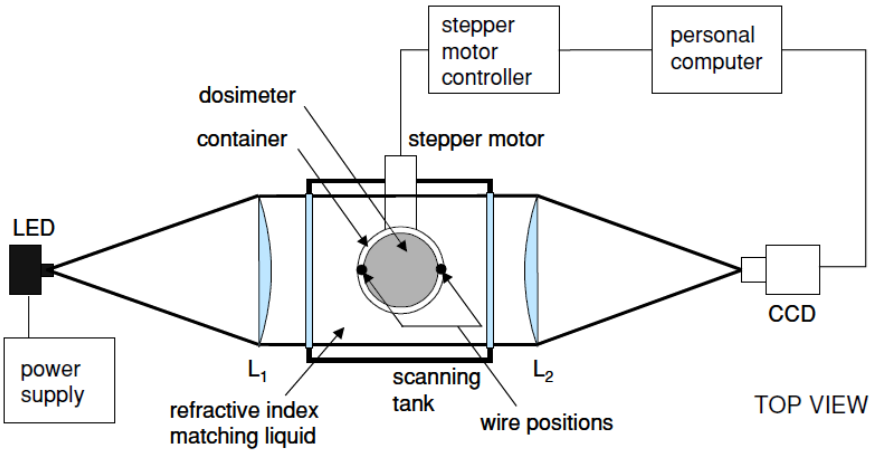

Figure 2-2: Parallel Beam Optical CT. (Image reproduced with permission from Krstajic and Doran, Focusing Optics of a parallel beam CCD optical tomography apparatus for 3D radiation gel dosimetry, Phys. Med. Biol., 51, 2055-2075 (2006) [65])

2.3.3 Cone Beam CCD Projections

Wolodzko et al[68] developed an optical CT scanner that comprised of a large light source, a diffuser screen, a specimen tank and a CCD (Figure 2-3). The light source had a broad spectrum (wavelengths 400 to 700 nm)[68]. The translucent diffuser panel provided a uniformly distributed light source[68]. The water tank was used to surround the vials of gel with a refractive index matching medium in order to

minimise reconstruction artefacts at the vial-air interface[68]. The installation of a turntable in the specimen tank allows the sample to be rotated by small increments to obtain different angles for projections[68]. The reconstruction was performed using mathematical algorithms developed for SPECT reconstruction that were based on the filtered back projection technique summarised in section 3.4[68].

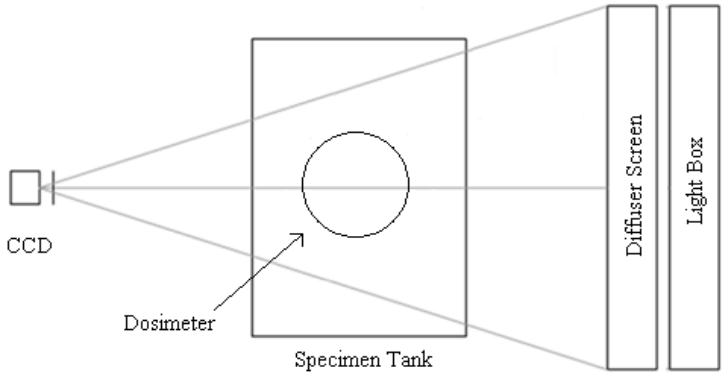

Figure 2-3: Cone Beam Optical CT scanner. Light is emitted from the LEDs in the light box, passes through the diffuser screen, through the dosimeter in the specimen tank and collected at the CCD.

The CCD used was 8-bit, 128x128 pixel matrix with a nominal pixel size of 0.78 mm[68]. The field of view of the detector at the centre of the specimen tank was 10 cm wide[68].

Jordan et al[123] expanded on the work by Wolodzko et al by using the same geometry but substituting the broad spectrum laser with a 35W low pressure sodium lamp. The Sodium lamp used had a spectral emission of 589.0 and 589.6 nm which the authors compared to a He-Ne laser (594nm light source)[123]. Jordan et al[123] showed that the sodium lamp was a good substitution for the broad beam used by Wolodzko et al.

The scanner at RMIT University investigated in this thesis was developed by Modus Medical Devices and is based on the work by Wolodzko et al[68] and Jordan et al[123].

2.3.4 Advantages and Disadvantages of Each System

Each evaluation system has different advantages and disadvantages depending on the properties of the scanner. Assessing the limitations of each technique influences the choice of dosimeter and scanner.

The scattering of light in an optical CT is extremely important. The influence of scattering is reviewed in section 2.4.3. All scanner types reconstruct the sample opacity assuming that the measured signal in each pixel is dependant only on the attenuation along the ray path from the source. Where scattering occurs in the sample, the measured signal is not necessarily only caused by attenuation. Some gel types, e.g., polymer gels, attenuate the light beam predominately by scattering rather than absorption. This can have a significant influence on the measured attenuation coefficients.

The translational laser based optical CT detects the lowest amount of scattered light compared to the other optical CT scanners. The disadvantage of the translational laser based optical CT scanner is the

long time required to acquire data for a reconstruction. The laser based technique has light incident and exiting the specimen tank along a single ray path. Any scattered light from the sample will be scattered away from the ray path between the light source and the detector. Therefore the scattered light will not be detected. Since the light is only incident on the sample along the ray path, there will be minimal amounts of scattered light, from other sections of the sample, being scattered into detector. Therefore, the detector predominately detects the attenuated light along the ray path between light source and detector. This allows laser based optical CT scanners to image scattering dosimeters, e.g., polymer gels.

The translational speed of the laser and diode results in a large amount of time required to acquire the information for a single projection[114]. Consequently, the scanning time may be significant for a large number of projections and the number of slices[63] when acquiring information for a reconstruction. The imaging time of a single 'slice' of gel is between 5 and 12 minutes with a full reconstruction taking up to 16 hours[114]. For dosimeters subject to diffusion of the spatial information, a long imaging time can change the spatial information collected and influence the apparent dose distribution. Newer designs of the laser based optical CT scanner, which eliminate the translational movement of the laser and detector, have shown shorter acquisition times[119-122].

Broad light source scanners (parallel and cone beam geometries), in general, provide a faster evaluation time when compared to the laser based scanners[62,114]. A disadvantage of the broad light source optical CT scanners is image artefacts caused by the scattering of light. Broad light source optical CT scanners are also susceptible to artefacts caused by refractive index inhomogeneities (Schlieren) causing light to refract[114]. The artefacts associated with imaging in a cone beam geometry will be reviewed in section 2.4.3. The major difference between the parallel and cone beam scanners is the light source's path across the specimen area. In parallel geometry the scanner utilises a narrow beam which is diverged into a broad light source at the entrance window and focused across the specimen tank by a lens. A second lens, on the exit side of the tank, converges the light onto a CCD. This setup results in parallel light paths across the specimen area. In contrast, cone beam geometry uses a broad, diffuse light source to illuminate the entire tank and has a small lens on the exit side of the tank. The use of a broad light source and small lens results in the light paths across the specimen tank forming a conical acceptance angle. The lens is used to change the direction of the converging light paths into parallel rays incident on the CCD. It has been hypothesised by Doran et al[114] that the parallel beam optical CT has better scatter rejection potential. This is because of the lens and CCD set-up.

Properties of the optical CT scanner, including speed of scan, types of gels that can be scanned and scattering artefacts, should be considered before a scanner is selected for use. A summary of the advantages and disadvantages of different Optical CT scanners is presented in Table 2-3.

Table 2-3: Development of Optical CT and advantages and disadvantages of each system

Optical CT Scanner	Year	Developed or Modified	Advantages	Disadvantages	Ref
Laser diode	1996	Developed by Gore et al[63]	High SNR[123] Can scan both scattering and absorbing gels[61]	Long acquisition time[62]	37,61-63,123
	2003	Vertical translation stage added by Oldham et al[37]	Able to scan different slices without needing to manually adjust measurement setup		37
	2005-2006	Van Doorn et al[119] and Conklin et al[120] added rotating mirrors to increase speed.	Faster scan time		119,120
	2007	Krstajic et al[121] used parabolic and galvanometer mirrors to raster scan laser	Faster scan time		121
	2009	Jirasek et al[122] added a lens to create 60° fan beam	Faster scan time	Lower scatter rejection	122
Parallel beam	2001	Developed by Doran et al[61]	Faster scanning time[62] Suited to evaluation of gels that absorb light[61]	Geometry detects large amounts of scatter compared to laser diode[61]	61,62,68,123
	2006	Krstajic and Doran[65] changed the focusing optics and used a high powered LED	Improved light emission spectra Improved focusing of light		65
	2009	Sakhalkar et al[109] modified with a larger field of view	Larger field of view		109
Cone beam	1999	Developed by Wolodzko et al[68]	Faster scanning time[62] Suited to evaluation of gels that absorb light[61]	Geometry detects large amounts of scatter compared to laser diode[61]	61,62,68,123
	2001	Jordan et al[123] replaced light source with low pressure sodium lamp	Improve light emission spectra		

2.4 Uncertainties in 3D Dosimeters

Properties of the dosimeter can affect the accuracy and precision of the measured dose. These uncertainties can be introduced during three different processes:

- Fabrication of the dosimeter,
- Set up and irradiation of the dosimeter and calibration phantoms, and
- Evaluation of the dosimeter.

The *accuracy* is the evaluation of the dosimeter's response to dose compared to the true value. The accuracy can be split into two components: *dosimetric accuracy*, related to dosimetric factors[69], and s*patial accuracy* associated with deviations in the spatial distribution of the delivered dose[69].

The *precision* is a measure of the reproducibility of the response and is influenced by variations in all the individual steps of the fabrication, irradiation and evaluation[69]. This can be split into two components: *dosimetric precision*, related to stochastic changes in the dosimeter[69], and *spatial precision* associated with spatial variations of properties that affect the measured dose[69].

2.4.1 Factors Affecting Uncertainty during Fabrication

Variations in the concentrations of the chemicals will influence the dose sensitivity[69], which can affect the outcome of the measurement if the batch has not been calibrated for dose. For Fricke gels the dose sensitivity is influenced by the concentration of ferrous sulphate (Fe^{2+})[74], chelating agent[73,81], benzoic acid[51], sodium chloride[71,73,81] and sugars[74]. The dose sensitivity of polymer gels is influenced by the ratio of cross linker to monomer[50,92,95], concentration of gelatine[92] and concentration of methacrylic acid and polyacrylamide in normoxic gel[92]. The sensitivity of PRESAGE™ is dependent on the ratios of leuco malachite green, the radical activator and the dissolution solvent[124].

De Deene et al[125] observed that the post manufacture temperature history of methacrylic acid based normoxic gel has an effect on the MRI response. Fricke gel dosimetric response has been observed to depend on the temperature of the gel during manufacturing[74]. Since the calibration phantoms and dose verification phantoms can be different sizes, the cooling rate is different between the different sized phantoms[69]. A systematic error may be induced between the response of the calibration phantom and the dose verification phantom[69]. Controlling the temperature history of the calibration and verification phantoms can reduce the maximum dose deviation of polyacrylamide based normoxic gels to less than 3 % relative to the dose maximum[125]. No studies at the present time have investigated the post manufacturing temperature history for optical CT scanner response of polymer gels[69].

Post manufacturing temperature history can also influence the precision of the dosimeter[69]. Stochastic variations in the controlled temperature will lead to variations in the measured dose related response[69]. If the cooling rate varies across the dosimeter, then the measured response will also vary depending upon position in the dosimeter.

Chemical instabilities affect the dosimetric accuracy[69]. The instabilities are caused by reactions of the gel formula with anything other than ionising radiation. An example of this is hypoxic gel's reaction to air. Chemical instabilities can also be caused by the incomplete setting of gels. De Deene et al[98] showed the gelation process (setting from liquid to solid) of hypoxic polymer gels influences the gel's unirradiated R_2 response. The amount of time required for the unirradiated response to stabilise depends on the gelatine concentration. Whilst this was observed for MRI, the fundamental cause of the effect is independent of evaluation technique.

Whilst highly reproducible gels can be manufactured, the uncertainty introduced during the fabrication process requires that either each batch of dosimeters must be calibrated individually, or inter-batch consistency must be measured. Table 2-4 shows the influence of different factors on the dosimetric and spatial accuracy and precision during the fabrication of 3D dosimeters.

Table 2-4: Factors influencing precision and accuracy during fabrication

Influenced Factor	***Source of Error***
Spatial Precision	Spatial variations in manufacturing temperature
Dosimetric Accuracy	Interbatch variation – Stochastic variations in chemicals effects dose sensitivity of each batch (Can be corrected by calibration of individual gel batchs)
	Discrepancies between calibration vials and phantoms due to different cooling rates
	Chemical stability of gel formula. Reactions to anything other than ionising radiation cause unwanted response in gel. E.g., hypoxic gel reaction to air
	Chemical stability of gels caused by incomplete setting of gel before irradiation.

2.4.2 Factors Affecting Uncertainty during Irradiation

A clinical linac beam should deliver the absorbed dose with an accuracy of 1.5 %[126] and a reproducibility of 0.5 %[127]. Variation in linac output needs to be considered when irradiating a 3D dosimeter.

De Deene et al[92] showed that typical variations in temperature during irradiation have no measurable effect on hypoxic polymer gels and normoxic polyacrylamide based gels. For normoxic methacrylic based polymer gels a temperature dependence during irradiation has been observed[92] which affects the dose sensitivity. The dose response of PRESAGE™ can change by a factor of 2 when changing the temperature from 5 to 30 °C during irradiation[112]. Variations in temperature which cause a change in dosimeter response will influence accuracy of a measurement.

The radiation induced chemical reactions in polymer and plastic gel dosimeters are stochastic in nature. The stochastic variation is known as radiochemical noise. Since this noise is on the molecular level, and most gel dosimetry evaluation systems use much larger voxel sizes, the influence on dosimetric precision is negligible[69].

Dose rate dependence also influences accuracy, due to the change in dose response calibration curve with a change in the dose rate. Dose-rate dependence is detrimental for a dosimeter because it could lead to a depth-dependent dose response[69]. A dose-rate dependence of the MRI response to dose has been observed in hypoxic polymer gels and normoxic methacrylic acid based polymer gels[92,128]. The MRI response of polyacrylamide based normoxic gels is independent of dose rate[92]. The optical density response of PRESAGE™ is independent of the dose rate[48]. No dose rate dependence has been observed for Fricke gels[81]. No dose rate dependence of the optical CT response is expected for hypoxic polymer gels[50].

Energy dependence is a key factor that could affect low energy radiation measurements that use a dose response calibration curve obtained using high energy radiation. This could lead to a systematic dose error in the measured dose distribution[69]. Energy dependence in hypoxic polymer gels was investigated by Novotny et al[94] and De Deene et al[92]. The energy dependence is small and not expected to influence dose distribution for external beam radiotherapy[69]. Polyacrylamide based normoxic gels were observed to have no energy dependence[92]. Methacrylic acid based normoxic gels were observed to have a small energy dependence[92]. The attenuation of light by PRESAGE™ was observed to be independent of energy used during irradiation[48].

Investigations of the radiological properties have shown that Fricke gels[83-85] and polymer gels[50,84,85,92,93] are close to water equivalent. Differences between water and the gels have been observed for very low energies. PRESAGE™ is less water equivalent[113] than Fricke or Polymer gels.

For hypoxic polymer gels glass or Barex® are often used as containers. This is because the glass or Barex® has a low permeability of oxygen. This is important because oxygen can cause changes to the gel[86,87]. The use of glass containers could affect the dose distribution[69]: Glass can contain heavy metals that could influence the incident beam[69]. Taylor et al[91] investigated the influence containers have on the absorbed dose and found relative differences within 1 % of the expected dose. Using PRESAGE™ eliminates the container as a source of measurement uncertainty.

Trapp et al[43] showed that radiation induces a change in the density of a polymer gel, which can cause a contraction of the volume of a polymer gel by approximately 1.5 %. The spatial resolution can be influenced by this contraction[43]. Depending on the time scale of this contraction, the dosimetric accuracy could be affected by changes to the set-up in position. If the contraction is dose dependent and is not uniform throughout the gel, then this can also cause spatial inaccuracies.

Phantom positioning errors can influence the spatial accuracy of the measured dose distribution[69]. In addition, errors in positioning calibration phantoms affects dosimetric accuracy and reproducibility

(dosimetric precision)[69]. Spatial precision is influenced by the positioning of dose verification phantoms[69]. Grebe et al[129] used stereotactic equipment to position phantoms within ±0.5 mm of the intended position. This error in the positioning can be applied to an IMRT dose gradient (to estimate the influence on *spatial precision and accuracy)* as well as 6 MV PDD curves (to estimate the influence on *dosimetric precision and accuracy*). ICRU Report 83[3] estimated dose gradients of a clinical IMRT field can be as large as 10 %/mm. Therefore with a lateral positioning error of 0.5 mm, the error in spatial precision and accuracy can be as large as 5 %. Using a typical 6 MV PDD (beam quality $TPR_{20,10}$ = 0.681), an error of 0.5 mm in longitudinal positioning is equal to a dose difference of less than 1.0 % relative to dose maximum at a depth of dose maximum. At a depth of 10 cm the error caused by a 0.5 mm error in positioning is less than 2 % relative to the dose maximum. A positioning error of the calibration phantoms contributes to the dosimetric inaccuracy. As shown in the calculation above the positioning error can lead to an approximate 2 % error in presumed dose to the calibration phantom when using a 6 MV beam. Table 2-5 shows an overview of different factors that influence uncertainty during irradiation.

Table 2-5: Factors affecting accuracy and precision during irradiation

Influenced Factor	*Source of Error*
Dosimetric Precision	Stochastic Variation in the delivered dose
	Variations in the temperature during irradiation
	Reproducibility of calibration phantom position
	Radiochemical Noise
Spatial Precision	Variations in phantom positioning
	Spatial temperature variations in combination with temperature sensitive dose response
Dosimetric Accuracy	Positioning error of the calibration phantom
	Dose-rate-dependent response
	Energy-dependent response
	Temperature dependence
	Tissue equivalence
	Wall effects of containers on dose distribution
Spatial Accuracy	Phantom positioning error
	Contraction of gel due to radiation

2.4.3 Influence on Measured Dose during Evaluation via Optical Methods

The influences listed here are caused by the dosimeter only. Section 2.5 reviews the influences of the optical CT scanner on 3D dosimeter evaluation. Baldock et al[69] determined that stochastic noise, voxel size and shape, imaging artefacts and temperature during scanning can influence the accuracy and precision of a gel dosimetry system. The noise and voxel size and shape are optical CT scanner dependent and are reviewed in section 2.5. The image artefacts caused by the 3D dosimeter itself include the scattering of light[37,63,130-134] and the refractive index mismatch[51,61,63]. Additional influences include the evaluation temperature[82], development of the dosimeter after irradiation[51,98,106] and diffusion[54,75-81,87,92,96].

The scanning temperature influences the transmitted light intensity for ferrous-benzoic xylenol (FBX) gel dosimeters[82]. The optical attenuation increases by approximately 2.5 % /°C. Olding et al[82] keep the dosimeter within 0.1 °C at the point of scanning to control this uncertainty. Hypoxic[54] and methacrylic acid based normoxic polymer gels[92] evaluated using MRI have shown a response that is dependent on the temperature during evaluation.

Image artefacts may occur due to scattered light reaching the detector. The method of calculating optical density in this thesis assumes all light entering the detector has followed a straight line from light source to detector. When scattered light enters the detector, it contributes to the intensity of light measured along the straight light path between light source and detector. This problem is particularly significant for polymers gels since the primary source of contrast is the scattering of light. The difficulty of optically measuring a light scattering object, whilst minimising the influence of scattered light, is well known[63]. Islam et al[132] and Xu et al[135] observed scatter artefacts when using polymer gels in laser based optical CT scanner. Optical Monte Carlo simulations by Oldham et al[37] confirmed that the artefact was caused by the scattering of light. Scattered light has been observed to influence the accuracy of the reconstruction of attenuation coefficients measured in a laser based optical CT scanner[90]. Bosi et al[130] used a funnel phantom to model the behaviour of optically scattering materials in a CCD based optical CT scanner. Obviously, scattered light artefacts are more pronounced when using a scattering based dosimeter like polymer gel, as opposed to using an absorbing gel like Fricke or PRESAGE™. The amount of scattering is dependent on the attenuation coefficient in the region of the sample, and the path length through the region[90]. Methods presented in the literature for the correction of scattering include:

- Quantitative model of cupping from light scattering phantoms[130,131],
- Monte Carlo first order approximation using Mie scattering theory[37],
- Averaging the stray light in the centre of a black disk blocking the central axis[136-138],
- Using a 2D array of beam stop disks to measure the stray light correction[139]
- Measuring the dependency on the diameter of the pin hole, of the light intensity through the pin hole relative to full scatter conditions[82]
- Using a grid of 2 mm diameter pin holes, to measure the ratio of light intensity through the pin hole relative to full scatter conditions at a number of different points. The results are then interpolated to calculate a correction for scattered light in a projection[82,133,138].

Scattering artefacts are best illustrated by considering the effect on the reconstructed volume of a uniform scattering sample or region. The effect in this case gives the name *"cupping artefact"* by which the artefact is known. "Cupping" occurs when the uniform opacity region in the reconstructed image, appears to be darker in the centre and brighter toward the edge of the sample. Cupping for a scattering phantom in a cone beam optical CT scanner has been observed to change the expected flat profile by the introduction of a concave or "cup" shape[59,130,131]. Cupping has been observed to increase

with the amount of scattering material[131]. Cupping artefacts are more pronounced for polymer gels. This is because the detection of the opacity change in polymer gels is predominantly through light scatter.

Al-Nowis and Doran[140] produced a cupping artefact in an absorbing phantom but were unable to identify the cause of the cupping artefact.

Image artefacts caused by a mismatch of the refractive indices can occur in two ways. The first type of artefact is caused by a mismatch between the dosimeter, container and surrounding medium. The second type of artefact is caused by mismatches in refractive index between different regions inside the gel.

A refractive index mismatch between the dosimeter, container wall and surrounding specimen tank liquid causes spatial and angular deflections of the light path through the dosimeter[63]. The refractive index mismatch also causes container wall reflection[63]. The addition of a high refractive index liquid to the liquid surrounding the dosimeter minimises the influence of the mismatch in the refractive index[51,61,63,90]. Doran et al[141] observed significant differences in the reconstructed wall thickness with a relative change of 0.2 % in the refractive index of the surrounding matching fluid. Glass containers used to stop auto polymerising of hypoxic gel will cause large differences between the refractive index of the gel, glass container and surrounding matching fluid.

Inhomogeneities in different regions inside the gel are known as *schlieren*[114]. Schlieren can be caused by temperature gradients in the dosimeter or incomplete mixing of the components of the dosimeter and/or matching liquid[114]. Schlieren cause the refraction of light and can appear as dark streaks in projection images[114]. Krstajic and Doran[121] postulate that schlieren have a larger influence in broad beam optical CT scanners compared to laser based scanners. This is due to broad beam scanners illuminating and imaging the whole volume at once as opposed to a laser based scanner only illuminating and imaging along a line. Any light refracted from schliere in the light path between the laser and diode will be reflected outside of the detector's sensitive area.

The basis for the reconstruction method used by the optical CT scanner, the attenuation of light along a straight path between the light source and detector, is affected by the detection of refracted and reflected light from outside the straight light source to detector path. The detection of refracted and reflected light could result in geometrical distortion[63] and image artefacts.

Ongoing radiation induced chemical reactions in a dosimeter after irradiation is a problem during evaluation. This raises questions about when to image because the measured intensity will depended on the time after irradiation. A total reaction completion time in Fricke gels has been observed[51]. Post irradiation polymerisation has been observed in hypoxic and normoxic polymer gels[98]. The light transmission of PRESAGE™ has been observed to change with time post irradiation[106]. Olding et al[82] estimated at 0.25 % increase in attenuation occurs during a 4-5 minute scan using a typical Fricke gel after the initial 30 minutes post irradiation.

Ideally the evaluation of a dosimeter in an optical CT would occur after the post-irradiation chemical reactions had stabilised. Waiting for the stabilisation of the chemical reactions causes a loss in the spatial accuracy and precision due to diffusion of the reactive elements (i.e. ions, monomers) of the dosimeter. Diffusion in Fricke gels is well known[75-81]. Maryanski et al[54] showed diffusion of monomers along regions of very high dose gradient and high doses for hypoxic gels. The diffusion is caused by unreacted monomers from an unirradiated area, diffusing across the high dose gradient and interacting with radicals that are still present in the irradiated area in the first hours after irradiation causing the response to continue to rise[142]. Post-irradiation diffusion has been observed for methacrylic acid based normoxic dosimeters[92]. No post-irradiation diffusion has been observed for polyacrylamide based normoxic gels[92] or PRESAGE[48].

The errors introduced by post irradiation development of the dosimeter and diffusion require a compromise to be reached between the development of the gel and limiting the diffusion. An imaging protocol is required that specifies the time before the data scan starts after irradiation[82].

Table 2-6 summarises the different factors that affect uncertainty during evaluation.

Table 2-6: Factors affecting accuracy and precision during evaluation

Influenced Factor	*Source of Error*
Dosimetric Precision	Stochastic noise from CCD
	Phantom positioning in scanner
Spatial Precision	Voxel size and shape
	Phantom positioning in scanner
Dosimetric Accuracy	Temperature during evaluation
	Scattering artefacts
	Refractive index mis-match
	Development of the dosimeter post-irradiation
	Post irradiation diffusion
Spatial Accuracy	Phantom positioning error
	Post irradiation diffusion

2.5 Characterisation of an Optical CT Scanner

The influence of the evaluation method on the accuracy of gel dosimetry requires the characterisation of the different components of the optical CT scanner. Individual components of the evaluation system have a large influence on the measurements obtained from a dosimeter[69]. In this thesis the different components of the Modus Medical Devices Inc. Vista™ Cone Beam Optical CT scanner have been characterised, to assess the impact on the overall dosimetric and spatial uncertainty of the reconstructed dose distribution. Previous characterisation methods of an optical CT scanner have been summarised in Table 2-7.

Table 2-7: Characterisation measurements from the literature for different types of optical CT scanners

Area of Characterisation	*Author*	*Optical CT scanner*	*Outcome of measurements*
Geometry Validation	Krstajic and Doran[65]	Parallel	Parallel geometry was valid
	Olding et al[133]	Cone beam	Cone beam geometry was valid
Evaluation parameters	Oldham et al[37] and Xu et al[134]	Laser based	Image quality effected by inadequate sampling, step size of laser and rotation increment of projections
Variation in light source intensity	Olding et al[82]	Cone beam	Light source required 1 -2 hours to stabilise after switching light source on
Wavelength of light	n/a	n/a	No published data has been presented on the spectra from cone beam optical CT scanners.
Non-Linear response of CCD	Van Doorn et al[119]	Laser based	Output variation in linearity was less than 2 % over optical density range of 0 – 1.
	Doran et al[61]	Parallel	Non-linear pixel response observed. Thought to be caused by low quality CCD
	Olding et al[133]	Cone Beam	CCD response was linear
	Krstajic and Doran[115]	Parallel	High Quality Test Target can be used to validate CCD response
Calibration of measured attenuation coefficient	Guo et al[143]	Laser based	Measured attenuation coefficients were linear compared to spectrophotometer
	Jordan and Battista[136]	Cone beam	Measured attenuation coefficients were linear compared to spectrophotometer
	Olding et al[144]	Cone beam	Scattering materials used for attenuation showed linearity between 0 – 0.15 cm^{-1}. Stable over time.
	Olding et al[133]	Cone beam	Linearity was observed for phantoms with uniform attenuation between 0 and 0.2 cm^{-1}
	Krstajic and Doran[115]	Parallel	Linearity of measure values compared to microdensitometer values between 0.125 and 1.425 OD. The range can be extended to 3.425 OD.
Calibration of CCD response to Dose	Wolodzko et al[68]	Cone beam	Linear optical CT scanner response over dose range of 1.5 – 9 Gy
	Papadakis et al[145]	Cone beam	Linear optical CT scanner response in dose range 0 – 20 Gy.
	De Jean et al[60]	Cone Beam	Used pencil beams to create dose response calibration curve. Linearity observed with two types of gels

Area of Characterisation	*Author*	*Optical CT scanner*	*Outcome of measurements*
Uniformity Measurements	Jordan and Battista	Cone Beam	Scattering assessed
	Olding and Schreiner[82]	Cone Beam	Used to assess scatter from surrounding matching fluid. No large impact observed
	Olding et al[133]	Cone Beam	Used to assess effect of absorbing and scattering solutions on reconstructed attenuation coefficients.
	Jirasek et al[122]	Laser based (Fan Beam)	Used to investigate pixel response in a projection
	Doran et al[61]	Parallel	Validated the use of a correction scan Observed ring artefacts
	Krstajic and Doran[115]	Parallel	Used to investigate the propagation of noise from projections to reconstructed images
	Oldham et al[90]	Laser based	Observed ring artefacts
Spatial Resolution	Gore et al[63], Oldham et al[37], Guo et al[143], Kelly et al[51], Van Doorn et al[119], Islam et al[132], Krstajic et al[64]	Laser based	Sub-millimetre spatial resolution achievable
	Krstajic et al[115]	Parallel	Sub-millimetre spatial resolution achievable
	Olding et al[133], Papadakis et al[145]	Cone Beam	Sub-millimetre spatial resolution achievable
Axis of rotation	Gore et al[63]	Lased-based	Influence on spatial resolution. Vista™ Recon software takes into account
Filtration used during reconstruction	Gore et al[63]	Laser based	Difference in FWHM of reconstructed pin between different filters
	Wolodzko et al[68]	Cone beam	Loss of resolution as filters frequency cut-off and widths/order were changed to reduce noise
Geometric Distortion	Oldham et al[90], Guo et al[143]	Laser based	No distortion observed
	Olding et al[133]	Cone beam	Minimal distortion observed

2.5.1 Cone Beam Geometry Validation

Krstajic and Doran[65] described the light detected in a CCD pixel as part of a bundle of rays travelling in a two cone shapes (one diverging from the object, the other converging on the CCD) with both cones sharing a common base The light travelling in a straight line at the centre of the cone is known as the "chief ray". The light rays in the cone shape that are focused by the lens back to a sharp point with the chief ray, are known as "marginal rays". The spread of marginal rays forms an acceptance angle. The bundle of light rays in the cone beam geometry can be visualised in figure 2-4. The angle between two opposed marginal rays is known as the acceptance angle, α.

The size of the ray bundle (i.e. the acceptance angle) is affected by the focal length, the f-stop, the depth of field and distances between light source, imaging volume and detector[133]. A smaller acceptance angle reduces the effect of stray light[65,133], but decreases the light collecting efficiency[133] and increases sensitivity to refractive index mismatches[65].

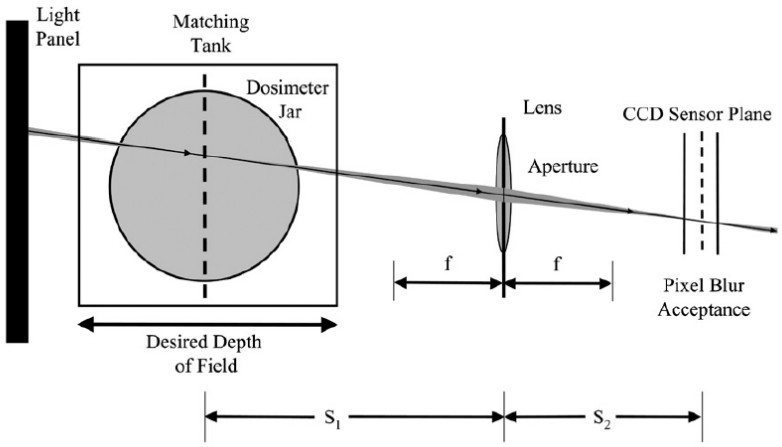

Figure 2-4: Light ray bundle in cone beam geometry. The spread of marginal rays around the chief ray forms an acceptance angle. This is visuallised along the ray line above as the grey around the central black line. The focal length, f-stop, depth of field and distances between light source, imaging volume and detector all influence the size of the acceptance angle. Reducing the size of the acceptance angle reduces the effect of stray light, but reduces collecting efficiency and increases refractive index mismatches. (Image reproduced with permission from Olding, T., O. Holmes, and L.J. Schreiner, Cone beam optical computed tomography for gel dosimetry I: scanner characterization. Physics in Medicine and Biology, 2010. 55: p. 2819-2840).

Olding et al[133] compared the light intensity through a 1 mm diameter hole to an open field illumination as the camera lens aperture was changed. A range of f-numbers between f4-f6.7 were observed to have pinhole-to-open field percentage intensities above 90 %. For a constant f-number (f5)the pinhole-to-open field percentage intensities were measured for a range of pinhole apertures between 1 - 10 mm[133]. The percentage intensities ranged from 91 % to 99 % with increasing aperture size. A percentage intensity of 99 % indicates most of the light collected is within a cone with a base diameter of 10 mm and a vertex angle of ~0.9°.

Measuring the light collected in a certain diameter cone was extended to the entire 2D projection to determine the percentage of detected light that was in the preferred light cone at each point in the projection image. The light collected in a preferred cone was measured by a regularly spaced grid pattern of 2 mm diameter pin holes. A bi-cubic spline interpolation between these points is used to calculate a 2D map of percentage light intensity with the resulting map indicating how much of the detected light is in the preferred light cone. A calculated percentage light intensity above ~95 % for most areas of the projection image indicated good conformance of the detected light with the preferred light cone[133].

Olding et al[82] used the 2D map of the ratio of pinhole-to-open field values to correct for scatter in the projections.

2.5.2 Evaluation Parameters

Oldham et al[37] investigated the influence of scanner parameters on reconstructed images of a finger phantom in a laser based optical CT scanner. A finger phantom is created by setting a gel in a container with test tubes in the gel forming "fingers". The fingers are then backfilled with gel doped with an opaque ink or scattering medium. The image quality was investigated by varying the number of analogue to digital conversions (ADC), the spatial increment between line integrals through the dosimeter and the angular increment between projections[37]. Xu et al[134] also investigated the number of samples and number of projections for a laser based optical CT scanner. The results showed image quality is significantly compromised by inadequate sampling and step size of the laser across a projection. Decreasing the rotational increment and increasing the number of projections acquired decreases streaking and image noise in the reconstructed image.

2.5.3 Variation in Light Source Intensity

The light intensity of LEDs depends on the temperature of the LED[146]. Therefore as the LED "warms up" the light intensity will change. Olding et al[82] measured the light intensity as a function of time after turning on a cone beam optical CT scanner. Thomas et al[147] published similar measurements for a parallel beam optical CT scanner. Variations in the light intensity after turning on the scanner have an effect on the intrascan optical density in the projections acquired during the 'warm up' period[82]. This has an effect on the reconstructed attenuation coefficients, as there can be a significant difference in light intensity during the time required to acquire all the projections in a scan. The normalisation used in the Vista™ Recon software only accounts for inter-scan variations in the light intensity[82].

The light source in a cone beam scanner required 1-2 hours to stabilise after turning on the light source[82]. After this time the variation of the light source is less than 1 % over time. This difference can be accounted for by the software normalisation.

The results from Thomas et al[147] indicate that a 45 minute warm-up period is required for the parallel beam optical CT scanner.

2.5.4 *Wavelength of Light in Optical CT Scanner*

Light attenuation by the dosimeter (either absorption or scattering) has a dependence on light wavelength[50,51,107,148,149]. Wavelengths with a large change in transmission as a function of dose have a high sensitivity to changes in dose. Using a wavelength that matches the peak attenuation in a gel will increase the sensitivity of the dose measurement.

Beam hardening is a well-known artefact in x-ray CT[150]. A spread of wavelengths causing differential attenuation through a dosimeter was observed to affect the measured attenuation coefficient by ~12 %[151]. A monochromatic light source reduces the uncertainty due to differential attenuation. From a practical point of view a monochromatic light source is often not possible. Jordan and Battista[136] suggested spectral hardening could occur for very strongly attenuating samples, but also noted that spectral hardening is not dominant at the 1 % transmission level. A narrow band pass filter and a dosimeter with a uniform absorption over the spectral width of the light source has been suggested to minimise uncertainty due to spectral hardening[136]. The full width half maximum (FWHM) can be used to characterise the spread of wavelengths from the light source.

2.5.5 *Response of the Detector to Light Intensity*

Non-linear response of the detector to light intensity can affect the calculation of the optical density[114] (see section 3.3 for optical density calculation method). Ideally, a CCD has a linear photometric response[152]. Non-linear response can be caused by low quality CCDs. Using high quality CCDs can eliminate this problem[114].

Stochastic noise from the CCD affects the dosimetric precision and is caused by thermal detector noise, which is caused by electrons on the chip being freed by thermal vibration[115]. Thermal noise cannot be compensated for because of the rapid and random nature of the noise. Cooling the CCD or averaging multiple images reduces this noise[115]. Thermal noise could have a large impact on the optical density measurable, due to low signal being affected by an unfavourable signal to noise ratio. As long as the signal to noise ratio is kept high, then the thermal noise will not have a significant influence on the measured dose. Therefore, characterisation of the dynamic range of the detector pixel values is required to ensure thermal noise does not affect the measurements.

Linearity of CCD has generally involved measuring the change in photodiode or CCD output as the light intensity has been modulated. Some methods used to verify the linearity of the response include neutral density filters[119], two crossed polaroids[61] and phantoms containing various concentrations of food dye [132,135]. Depending on the device measured the results have either shown a linear response (CCD, Orca 1024 BTII, Hamamatsu Photonics, Japan, part C4742-98-26KAG[115] and UDT PIN13D high responsivity PIN photodiode[119]) or a non-linear response (CCD, RS Components Ltd, Corby, UK, catalogue number 208-0200)[61]. These results show that the CCD linearity is dependent on the scanner and therefore should be measured during scanner characterisation measurements[115].

The response of a CCD (Dragonfly2 DR2-HIBW, Point Grey Research, Richmond, BC, Canada) in a cone beam optical CT to mean transmitted light intensity was measured by varying the charge collection time of the CCD between 0 – 100 ms[133]. A highly linear response was observed above ~6500 a.u (about 10 % of the camera full scale intensity. However, these results did not investigate the CCD response at higher light intensities and also did not investigate the influence non-linearity has on optical density measurements. These aspects will be investigated in this work.

2.5.6 Reconstructed Attenuation Coefficient Accuracy

Accuracy of the reconstructed image can be measured by comparing reconstructed and known attenuation coefficients[116]. Phantoms comprised of known attenuation coefficient and pathlength are used to assess the optical measurement independent of the uncertainties associated with dose delivery[82]. The known attenuation coefficient may be determined using a spectrophotometer, or equivalently, by using the light source and detector of the scanner in a collimated low-scatter configuration.

Guo et al[143] created a "layer cake" phantom designed for the quality assurance of a laser based optical CT scanner. A layer with cylinders of known geometry and attenuation was included for comparison measurements between reconstructed attenuation coefficients and independent spectrophotometer values. The linearity over a 0 – 2 optical density range had a coefficient of determination of 0.9917.

Jordan and Battista[136] measured the attenuation coefficients of a set of absorbing gel dosimeters with individual uniform attenuation coefficients in a cone beam optical CT scanner. The results were compared to the values from a spectrophotometer. Quantitative agreement (< 2 % difference) indicates no large instrumental or reconstruction errors.

Olding et al[144] developed an acrylic base with columns or "fingers" of latex to create a phantom used for characterising the attenuation coefficient reproducibility over a long period of time . The concentration of latex in each finger was kept constant. The concentration for different fingers was varied between 0 – 0.4 g/L. The measurement of attenuation was constant over a period of 7 months. Linearity was observed between 0 – 0.15 cm^{-1}.

Olding et al[133] also developed a set of uniform phantoms with a different concentration of absorbing dye in each phantom. A correlation between attenuation coefficients, in a dynamic range of 0 and 0.2 cm^{-1}, measured in a spectrophotometer and an Optical CT scanner was observed. The attenuation coefficients were measured in the reconstructed image from a cone beam optical CT scanner using a wavelength of 591 nm[133]. The wavelength of 633 nm was not used to calculate the linearity because only two sample points were within the 0 to 0.2 cm^{-1} range. The absorbing phantom had a diameter of 8 cm[133].

The reported measurements show that reconstruction attenuation coefficient accuracy can provide information for the given optical CT scanner. However, the information is dependent on properties of

the phantom such as pathlength and opacity. Therefore, measurements of the accuracy of attenuation coefficients obtained from reconstructed images relative to known values should be determined for each scanner with phantoms similar to the types of 3D dosimeters that will be used routinely. The differences in measurement methodology demonstrate that there is no preferred method to characterise the accuracy of the reconstructed attenuation coefficient. Thus, the accuracy of attenuation coefficients from reconstructed images relative to known values can be determined provided the known attenuation coefficient in a region is uniform and the pathlength is known.

2.5.7 Uniformity

Measurements of a large uniform sample can be used to measure accuracy and noise over a large volume, visualise the effect of scatter, verify scatter reduction methods and corrections and determine if the CCD is operating correctly. Uniformity measurements can also be used as part of ongoing quality assurance as a quick evaluation of a number of parameters in the optical CT scanner. This section gives examples of uniform phantoms use in the literature followed by a summary of their use in this thesis.

A uniformity layer was included in the "layer cake" phantom[143] The layer was created from polyurethane to match PRESAGE™ dosimeters.

Jordan and Battista[137] used uniformity measurements to measure and correct for scattered light in a cone beam optical CT scanner. Uniform phantoms were also used to investigate the response of the detectors across a slice in the projection.

Olding and Schreiner[82] used uniformity measurements to measure the influence of scatter from the refractive index matching medium surrounding the dosimeter. The results showed that stray light from outside the dosimeter changes the mean attenuation coefficient in the inner 90 % of the gel by less than 0.5 %.

Olding et al[133] measured the uniformity through scattering and absorbing uniform solutions to assess the effect of absorption and scattering on the reconstructed attenuation coefficients. In addition the impact of the jar walls was assessed by measuring the uniformity of a projection image with and without a jar in place.

Jirasek et al[122] measured the uniformity in a projection through an empty tank to investigate the variation in pixel response in a fan beam optical CT scanner.

Doran et al[61] reconstructed an empty tank to investigate the constancy of the light field and therefore the validity of using a correction scan. The ratio of the standard deviation to the mean was investigated with variations of 1 % observed. No systematic variations were observed. Krstajic and Doran[115] have also used the ratio of the standard deviation to the mean to investigate the propagation of noise from projections to reconstructed images.

Ring artefacts are caused by a feature not associated with the dosimetry sample being present in every projection. The feature could be from a bubble or scratch on the specimen tank glass, a non-linear response to light intensity from a pixel, or a non-response from a pixel (i.e. dead pixel). Ring artefacts have been observed in both laser [90] and CCD[61] based optical CT scanners. Uniform phantoms have been used to evaluate ring artefacts[61,90].

In this study uniformity phantoms have been used due to their ease of manufacturing and efficiency in characterising large volumes. Measurements similar to those in the literature are used to check the functionality of the optical CT scanner. Additionally, a proposed uniformity index is investigated as quality assurance tool.

2.5.8 Spatial Resolution

The spatial resolution is a measure of the ability of an imaging system to measure large attenuation changes over small distances, and reflects the *reproducibility* of changes over a small distance in an optical CT scanner *(spatial precision)*[69]. Gore et al[63] observed the spatial resolution in a laser based optical CT scanner was limited by the laser width, alignment of the mechanical rotation axis with the central column of pixels, the backlash of moving the laser forward and backward and the filtration used during reconstruction. In a cone beam optical CT scanner the CCD model, aperture settings for the camera, distance between the CCD imaging plane and position of interest, alignment of the rotation axis to the central pixel in the projection and filtration during the reconstruction will affect the resolution. The alignment of the rotation axis is described in section 2.5.9. The filtration used in optical CT reconstruction is described in section 2.5.10. Methods and results for measuring spatial resolution are described here.

Methods for measuring the spatial resolution typically involve calculating the modulation transfer function (MTF) from an image of a thin wire[37] or sharp edge[119], measuring the light intensity through a MTF test pattern with increasing frequency[115] and mathematical simulation of the optics in the optical CT[115]. A MTF test pattern is a series of light and dark opacities with a decreasing distance between the lines (see MTF calculation methodology in section 3.5 for an example of this pattern). The test pattern is used to measure the ability to distinguish between lines as the frequency increases. The methodology to measure and calculate the MTF is presented in section 3.5.

In a laser based optical CT scanner the spatial resolution has been characterised in terms of the full width half maximum (FWHM) of the laser[119,132], the FWHM of a profile across a reconstructed capillary tube containing ink[63,], the MTF and FWHM of a 0.25 mm diameter steel wire[37] and the reconstruction of a 0.8 mm diameter wire in a number of radial positions[51]. Guo et al[143] measured the FWHM of a wire in a layer in the "layer cake" phantom. All the results indicate that the spatial resolution is between 1 mm and 2 mm. Krstajic et al[121] measured the spatial resolution using a high quality test target (HQTT) in a newer design of the laser based optical CT scanner. The results indicate

sub millimetre spatial resolution. They employed the same approach to measure the spatial resolution in a parallel beam optical CT scanner[115]. The results indicate sub mm spatial resolution. A simulated spatial frequency was also modelled[115]. The differences between the modelled and measured spatial resolution indicate that the limiting factor for spatial resolution is the sampling.

In a fan beam optical CT scanner, the spatial resolution was determined by the measurement of the MTF across a wire. The results indicate a spatial resolution of 0.25 mm, which is in the order of the reconstruction grid size of 0.22 mm/pixel (note that the spatial resolution was actually reported as "0.25 mm/pixel" featuring a possible typographical error in the units)[122].

Olding et al[133] measured the spatial resolution of a cone beam optical CT scanner in 2D projection using a sinusoidal MTF test pattern. The results indicated 50 % modulation were 3.2, 2.5 and 1.8 lp/mm for detector to test target distances of 49.9, 57.5, and 65.1 cm respectively[133]. Papadakis et al[145] measured a MTF in a reconstructed image in an in-house built cone beam optical CT scanner. The MTF was calculated from a profile across a 360 μm diameter optical fibre. The reconstruction image was calculated from 360 images with a step size of 1° between projections. The CCD had an acquisition area size of 640 x 480 pixels. However Papadakis et al[145] did not indicate the reconstruction resolution and the distance between the test target and the CCD. The MTF results indicate a modulation greater than 10 % down to a value of 1.1 $lp.mm^{-1}$.

2.5.9 Mechanical Axis of Rotation Alignment

Gore et al[63] observed that the spatial resolution was limited by the accuracy of the alignment of the centre of rotation for a laser based optical CT scanner. Accurate knowledge of the centre of rotation is crucial because the reconstruction algorithm uses these co-ordinates to as a common point for the different projection images, which is then used to align the sinogram data. For the Vista™ cone beam scanner, the centre of the projection is a common point for all projection images. The correction method in the Vista™ Recon software is used to correct the alignment of the middle column of pixels in the camera and the axis of rotation of the turntable[153]. This offset is applied to all images in order to align the axis of rotation to the centre of the projections.

2.5.10 Filtration used in the Reconstruction of Images

The spatial resolution is influenced by the filter used. Gore et al[63] observed a difference in the reconstructed FWHM of a pin using Ram-Lak and Shepp-Logan filters.

In a cone beam optical CT scanner, Wolodzko et al[68] used both Hann and Butterworth filters, with varying frequency cut-offs and filter widths (Hann) and orders (Butterworth). The results demonstrated a loss of resolution as the filter's frequency cut-off and widths/order were changed to reduce noise.

2.5.11 Geometrical Distortion

Geometrical distortion will influence the spatial accuracy and precision. Refractive index mismatches between the dosimeter and the surrounding medium have been observed to result in the geometrical distortion[90]. Oldham et al[90] investigated the geometrical distortion of a needle phantom in a laser based optical CT scanner. The reconstructed optical CT scanner image was compared to the "Gold Standard" X-ray CT scanner image with no geometrical distortion observed. Olding et al[133] investigated geometric distortion in a cone beam optical CT scanner using a pin phantom with pins arranged in spiral shape, and the results indicated minimal amounts of distortion[133].

2.6 The Need for the Measurements in this Thesis

The measurements in this thesis have been used to characterise different properties of the cone beam optical CT scanner for the evaluation of 3D dosimeters. Key areas of assessment are:

- Cone beam geometry validation
- Light intensity as a function of time
- Spectral output compatibility with 3D dosimeters
- Projection and reconstruction attenuation coefficient accuracy and dynamic range
- Projection and reconstruction spatial resolution
- Effect of scatter on the projection and reconstructed image
- Geometrical distortion

The cone beam geometry has been investigated previously[133]. The result indicated that using a lens with an f-stop between f4 and f6.7 maximises the light intensity detected along a ray path from the light source to the CCD, therefore minimising the influence of scattered light. A valid cone-beam geometry is dependent on the focal length, the f-stop, the depth of field and distances between the light source, imaging volume and detector[133]. Therefore the validation of the cone beam geometry is a property of the components of the cone beam optical CT scanner and requires characterisation for each individual optical CT scanner. This was not reported in this work due to the measurement method and results previously being communicated by Olding et al[133].

The spectral output of the light source affects the selection of gel dosimeters that are suitable for evaluation in the optical CT scanner (see section 2.5.4). A measurement of the spectrum is used to characterise the light source wavelength. Also, future proposed dosimeters can be compared against this (in terms of their absorption properties) to determine suitability for evaluation using the optical CT scanner.

The LED light intensity is known to vary as a function of LED temperature[146]. Varying light source intensity will affect the measured attenuation coefficients (see section 2.5.3). Therefore a measurement of the light intensity as a function of time is required to characterise the influence of the varying light

intensity on the evaluation of 3D dosimeters and to define the warm-up time for scanner usage protocol. This type of measurement has been used previously to investigate the warm-up time of a scanner[82]. The measurement is repeated here to verify a warm-up period and to investigate the effect on attenuation coefficient from measuring dosimeters during the warm-up period.

CCD linearity measurements have been communicated previously, which have either investigated different equipment[61,115,119,132,135] or only investigated low intensity regions[133]. This work investigates the whole CCD response range with an emphasis on characterising linear regions and the influence non-linearity has on the measured attenuation coefficient.

In order to characterise the accuracy and dynamic range of the attenuation coefficients measured in the optical CT scanner, a set of uniform phantoms were developed (see section 3.2.1). The uniform phantoms require independent assessment of individual attenuation coefficients. The phantoms can then be used to compare attenuation coefficients derived from both projections and reconstructed images. Scattering properties of the uniform phantoms have also been assessed and compared to scattering and non-scattering phantoms.

Previously in a cone beam optical CT the projection and reconstructed spatial resolution has been measured by different authors[133,145]. The projection spatial resolution is a function of the distance between the test target and the CCD[133] and is therefore dependent on the scanner set-up. As such the spatial resolution should be characterised for individual scanners. In addition, this thesis investigates if a correlation exists between the projection and reconstructed spatial resolution. If a correlation exists, then ongoing quality assurance may be simplified to a single projection acquisition rather than the acquisition of a large number of projections and the reconstruction into a 3D volume. The charge integration time of the CCD was also investigated for influence on the spatial resolution.

Light scatter has been shown previously to affect measurements in an optical CT scanner[37,63,90,130,132,134]. The influence and source was investigated in both projections and reconstructed volumes.

The geometrical distortion requires characterisation for any effect the reconstruction algorithm has on the spatial precision. No geometric distortion has been observed in a laser based optical CT scanner[63]. The spatial distortion in cone beam optical CT scanners has been measured. The results indicated that minimal geometrical distortion occurs[133]. The spatial distortion is a property of the reconstruction algorithm and as such will not vary from scanner to scanner. Therefore this measurement has not been performed in this thesis.

The measurements presented in this thesis have been selected to characterise the scanner. Whilst some measurements have been performed in the literature, they have either been performed for other types of optical CT scanners, or are dependent on scanner set-up and therefore individual to a scanner. Measurements have also been presented to investigate alternative techniques for performing quality assurance.

3. APPARATUS, MATERIALS AND MATHEMATICS COMMON TO ALL EXPERIMENTS

This chapter describes the major apparatus, materials and mathematical procedures fundamental to each of the individual investigations. The materials and methodologies for particular experiments are discussed separately in the individual chapters which address each experiment. The key piece of equipment described is the optical CT scanner recently purchased by RMIT University. The optical CT scanner is the focus of the present study.

Several phantoms have been developed for the purpose of this investigation including:

- Polyurethane Opacity Reference Phantoms (PORPs)
  - A series of uniform, solid phantoms that feature a range of attenuation coefficients which are stable over time
- Uniform gelatine phantoms
  - These exhibit light scattering during readout
- Uniform solutions of dye and water
  - These exhibit a range of optical densities which absorb light without scattering during readout.

Mathematical methods presented relate to the calculation of:

- Optical density
- Attenuation coefficients
- Image reconstruction, and
- The Modulation Transfer Function

3.1 The Optical CT Scanner at RMIT University

The commercially developed scanner purchased by RMIT University was the Modus Medical Devices Inc. Vista^{TM} Cone Beam Optical CT scanner as shown in figure 3-1 (Modus Medical Devices Inc., London, Canada, www.modusmed.com). In this thesis the Cone Beam Optical CT scanner will be referred to as *the scanner* where appropriate.

The scanner is a 3D imaging system designed for use with gel dosimeters. The scanner utilises transmitted light to determine the attenuating properties of the material placed between the light source and CCD. To measure the change in light transmission due to absorbed dose, the dosimeter is scanned before and after irradiation. The components and dimensions of the scanner are shown in figure 3-2.

The scanner consists of a:

- Light source
- Diffuser screen
- Specimen tank
- Filter holder
- Lens
- Charge Coupled Device (CCD)

Figure 3-1: Modus Medical Inc. Vista™ Cone Beam Optical CT scanner (the scanner) purchased by RMIT University. The properties of the scanner are characterised in this thesis to determine the scanner's influence on the uncertainty in measured dose distributions.

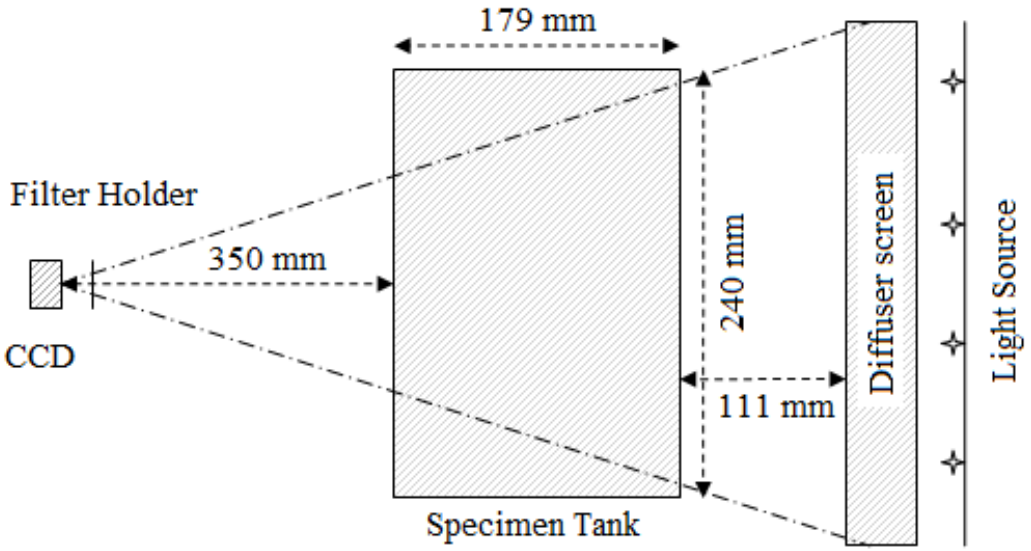

Figure 3-2: Schematic of the scanner. The light source comprises two separate arrays of orange or red LEDs. The diffuser screen scatters light across the specimen tank. The specimen tank comes in two sizes each with different fields of view through the respective tank. The filter holder contains amber and red narrow band pass filters to be used in conjunction with the matching light source. The CCD used is a 1st generation Dragonfly (Point Grey Research, Richmond, BC, Canada, www.ptgrey.com).

The light source consists of two separate arrays of Light Emitting Diodes (LEDs). The nominal wavelength of light for the two sources is 590 nm (orange light source) and 633 nm (red light source). Choice of light source is given because different dosimeters will have different peak absorbance wavelengths[50,51,107,148,149].

The specimen tank is used to contain the index matching fluid used so that light rays are not refracted at interfaces between air, container or dosimeter.

The filter holder contains both amber and red narrow band pass filters. The appropriate filter is used with the corresponding light source when evaluating a dosimeter. The narrow band pass filter is used to decrease the spectral bandwidth of the light entering the CCD[136]. The addition of a filter contributes some reflected stray light which can be minimised by tilting the filter[136].

A key component of the scanner is the CCD which is used to measure the light transmitted through the sample. The CCD used is a 1st generation Dragonfly (Point Grey Research, Richmond, BC, Canada, www.ptgrey.com). The sensitive component of this model is a 1/3" Sony CCD Model Number ICX204AL (Sony Corporation, Tokyo, Japan) with an array of 1024 x 768 pixels[154]. Spectral response of the CCD is shown in Figure 3-3. The square pixel size is 4.65 µm. Each CCD pixel measures a charge proportional to the total integrated light flux incident on the pixel during the acquisition period[155]. The CCD is a single channel (i.e. monochrome) 16-bit detector with a range of response levels between 0 and 65535 (total of 2^{16} = 65536 response levels). This corresponds to a theoretical maximum optical density range of 4.8 OD units if the maximum difference in response levels is used to calculate the optical density (see optical density calculation method in section 3.3). Ideally the response of the CCD to different light intensities will be linear[152]. If the calculation method presented in section 3.3 is used to measure the optical density and attenuation coefficients, then a non-linear response to light intensity limits the dynamic range of optical density values.

Geometrical setup and calibration was per the method described in the manual from Modus Medical Devices Inc[156].

Modus Medical Devices Inc. supplied 3 programs with the scanner. The Vista™ Scan program was used to acquire projection images and control the sample rotation. The Vista™ Recon program was used to reconstruct the projection images into a 3D dataset. The Vista™ View program was used to view data.

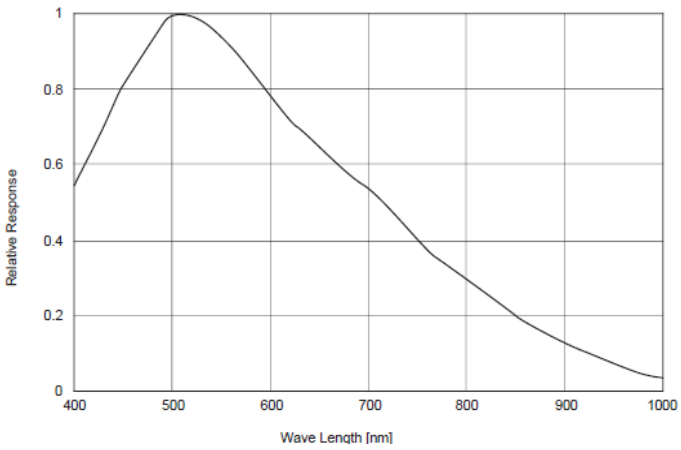

Figure 3-3: Spectral sensitivity characteristics of CCD. Relative response excludes lens and light source characteristics. Data from CCD manufacture documentation[154].

3.2 Phantoms used in this Work

As described earlier, the scanner measures a difference in light transmitted through the unirradiated and irradiated dosimeter. To simulate unirradiated and irradiated dosimeters, different types of phantoms were created. In this thesis a *reference* phantom is an untinted phantom and a *data* phantom is a tinted phantom. A reference phantom is used to simulate an unirradiated dosimeter, whilst a data phantom is used to simulate an irradiated dosimeter. Each type of phantom has properties similar to a type of gel or plastic dosimeter. The phantoms require a measurement of individual phantom attenuation coefficients, the range of attenuation coefficients and the attenuation coefficient step size between individual phantoms. The phantoms can then be used to characterise the scanner.

3.2.1 Polyurethane Opacity Reference Phantoms (PORPs)

To simulate absorbing plastic phantoms, a set of calibration phantoms, with individual uniform opacities, was developed at RMIT University by Kirsten Zuurmond and Leah McDermott[157]. A total of 20 phantoms were created as uniform, stable, long term calibration tools. Individual phantoms attenuate different amounts of light creating a set of phantoms with a range of attenuation coefficients. The measurement of the phantom attenuation coefficients is presented in chapter 4. For each phantom a rigid polyurethane casting was manufactured using pre-polymers diisocyanate and polyol (Crystal Clear 206, part A and B, Rowe Trading Company, Richmond, South Australia, http://www.rowetrading.com.au/). The cylindrical phantoms are 78 mm in diameter and 20 mm thick. The attenuation coefficient of each individual PORP was created by adding a different amount of black tint (So-Strong® liquid urethane colorant, Smooth On, Easton, Pennsylvania, http://www.smooth-on.com/). A non-tinted phantom is used as the "reference phantom". The difference in light transmission between the non-tinted and tinted phantoms is used to calculate optical density. A holder was manufactured to stack the phantoms in the scanner. This allowed the stacking of 5 cylinders in a projection image (Figure 3-4).

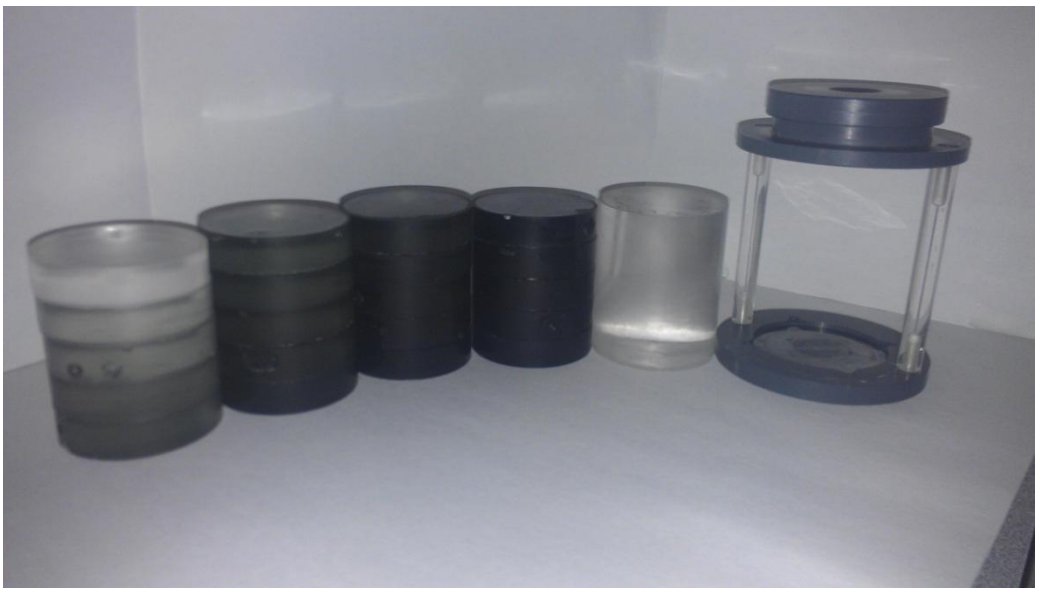

Figure 3-4: A) Polyurethane phantoms of various opacities. 20 PORPs were manufactured with a diameter of 78 mm and a thickness of 20 mm. A reference PORP (second from right) was also manufactured to be the same diameter but with a height of 100 mm. On the far right of the image is the PORP holder which allowed the stacking of 5 PORPs.

3.2.2 Gel and Water Phantoms

To investigate the influence of light scattering by samples being imaged, phantoms were created with different light scattering properties.

The first type of phantom was created to simulate a polymer gel base. The gelatine base is used in the manufacturing of a large variety of polymer gels in the literature (e.g., BANG™ polymer gels[54], normoxic polymer gels[40], or Fricke gels[38]). The scattering of light limits the use of a polymer gel in an Optical CT scanner[69,130]. Scattered light from the gelatine base gel increases uncertainties in measured attenuation coefficients. The phantom was created by mixing a uniform solution of 5 % by weight gelatine and 95 % by weight water at a temperature of 50 °C. The solution was allowed to cool and set into a gel.

The second type of phantom consisted of blue dye mixed with water. The dye solution was created to absorb light, similar to the methods of light attenuation in Fricke gels and PRESAGE™ dosimeters. The properties of Fricke gels and PRESAGE™ have been discussed in sections 2.1.1 and 2.1.5 respectively. Light absorbing dosimeters scatter a minimal amount of light. Using a light absorbing dosimeter will reduce image artefacts caused by scattered light. Individual light absorbing phantoms were created by mixing different amounts of dye and water together. The dye used was blue food colouring. The dye concentration in each phantom was created using the following process:

1. 1 mL of dye was added to 1 litre of water. This solution was then used as a base solution to create the phantoms. The volume of water was calculated by weighing an empty beaker and adding 1 kg of water to the beaker.

2. 1 – 45 mL of the base solution was added to separate containers of 1 L of water (measured as per part 1). The concentrations were calculated via equation 1, where C1 is the original concentration of the dye in the water (0.1 %), V1 is the volume of liquid removed from the base solution (1 – 45 mL), V2 is the volume of liquid that sample base solution is added to (1 L) and C2 is the concentration of the new solution. The final fractional concentrations of the dye in each jar are in Table 3-1.

$$C_1V_1 = C_2V_2 \qquad (1)$$

The uncertainty in the measuring of the dye or a solution in the pipette was 3 µL. The uncertainty in the weighing of 1 L of water was ± 0.05 g. Equation 2 was used to calculate the uncertainty in the concentration of the solution. The uncertainty was first calculated for the dye concentration in the base concentration solution. The uncertainty in the base concentration solution was then used in the same equation to calculate the uncertainty of the concentration in the final solutions.

$$\Delta C_1 = C_1\left(\frac{\Delta V_1}{V_1} + \frac{\Delta C_2}{C_2} + \frac{\Delta V_2}{V_2}\right) \qquad (2)$$

Table 3-1: Dye concentration of absorbing phantoms. The phantoms were created by combining 1 mL of dye with 1 L of water to form a base solution, then sampling the volume in column 2 and combining with 1 L of water to form solutions with fractional concentrations given in column 3. The concentration was calculated by equation 1. The uncertainty was calculated via equation 2.

Dye Solution	Vol. of base solution sample (mL)	Fractional Dye Concentration (%)
1	1	$1 \times 10^{-4} (\pm 6 \times 10^{-7})$
2	5	$5 \times 10^{-4} (\pm 3 \times 10^{-6})$
3	10	$1 \times 10^{-3} (\pm 6 \times 10^{-6})$
4	15	$1.5 \times 10^{-3} (\pm 9 \times 10^{-6})$
5	20	$2 \times 10^{-3} (\pm 1 \times 10^{-5})$
6	25	$2.5 \times 10^{-3} (\pm 2 \times 10^{-5})$
7	35	$3.5 \times 10^{-3} (\pm 2 \times 10^{-5})$
8	40	$4 \times 10^{-3} (\pm 2 \times 10^{-5})$
9	45	$4.5 \times 10^{-3} (\pm 3 \times 10^{-5})$

3.3 Optical Density

The term *Optical Density (OD)* is sometimes used to describe the attenuation of light along a total path length or the attenuation of light per unit path length. In this thesis it will be used to describe the *change in attenuation of light caused by the attenuation of light along a total light path*. The OD is an extrinsic property of the material, meaning it is measured over the entire sample. To measure the change in attenuation, the light intensity is first measured prior to the dosimeter being irradiated, I_0, then after the dosimeter has been irradiated, I. Theoretically, all points along the light path should *not* have changed between the two measurements. Therefore, the change in light intensity is attributed to changes in the dosimeter attenuation between the first and second scan. In the case of 3D dosimetry, changes in the dosimeter attenuation property are due to dose. The difference in the light attenuation property is proportional to the dose.

The *attenuation coefficient*, μ, is used to describe the total loss of light intensity due to absorption and/or scattering per unit pathlength d. The attenuation coefficient is an intrinsic property of the sample, meaning it is independent of how much of the material is present. When the loss in light intensity is only cause by absorption then the term *absorption coefficient* can be used. The term *extinction coefficient* has also been used to define the loss in light intensity due to attenuation (e.g., Bosi et al[118]). The distinction between optical density and attenuation coefficient is important in the understanding of the information from projection or reconstructed images.

For the measurement of the optical density or attenuation coefficient, equations 3 to 5 have been used. The equations are derived from the Beer-Lambert law which relates the attenuation of light by a medium to the intensity of light measured before and after the medium[158]. Equation 3 describes the intensity based on attenuation coefficient of a unit length sample, μ_i, through a number of identical sized unit length samples, d_i, along a total path length. The sum over all attenuation coefficients for all segments, i, is used to calculate the new intensity, I, based on the original intensity, I_0. As the segments of material decrease in thickness, the number of segments increases toward infinity and the sum of attenuation multiplied by path length is replaced by an integral of the attenuation along a path length. Figure 3-5 depicts the segments of attenuation and segment sizes used in equation 3.

$$I(d) = I_0 e^{(-\sum_i \mu_i d_i)} = I_0 e^{\left(-\int_{sample} \mu(y) dy\right)} \qquad (3)$$

In equation 4; I_0 is equivalent to the measured intensity of the light source prior to irradiation, I, is equivalent to the intensity of light after the same sample has been irradiated and the optical density, OD, is equal to new intensity divided by the original intensity.

$$OD = \frac{I}{I_0} = e^{\left(-\int_{sample} \mu(y) dy\right)} \qquad (4)$$

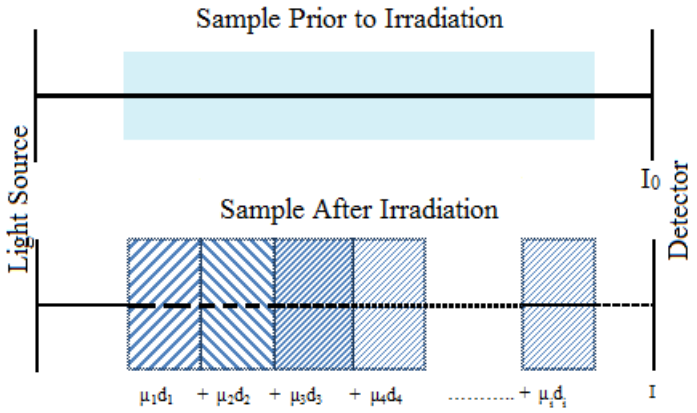

Figure 3-5: Calculation of optical density. The light intensity through the sample is measured prior to irradiation, I_0, and after the sample has been irradiated, I. If the light path is broken up into multiple small volumes, with each volume having a uniform attenuation coefficient, μ, over a path length d, then the summation of all attenuation coefficients results in the total loss in light intensity. The new intensity, I, is calculated via equation 3 and the optical density is derived by equation 4.

3.3.1 Measurement of μ for Uniform Phantoms in 2D Projections

The attenuation coefficient of a uniform phantom with known path length can be calculated from a transmission measurement via equation 5, where OD was defined above, μ is the attenuation coefficient and d is the total path length. The assumption in this equation is the attenuation of light is even throughout the path length and the path length is well known.

$$\mu = \frac{-\ln OD}{d} \qquad (5)$$

3.3.2 Uncertainty of Attenuation Coefficient measured in 2D Projections

The uncertainty in the attenuation coefficient is evaluated in a two-step process. First, the uncertainty in the optical density is evaluated. This value is then combined with the path length uncertainty.

The uncertainty in the measured optical density in a projection for a uniform phantom can be calculated by equation 6. The equation combines the variance in the light intensity in the original image, σ_{I_0}, and the variance in the light intensity through the translucent sample, σ_I. The variance in the light intensity is calculated by measuring the standard deviation of the intensity values in a region of interest around a point. The variance in the light intensity was calculated by the square of the standard deviation of the intensity values in a region with approximately constant intensity.

$$\sigma_{OD}^2 = \left(\frac{\partial OD}{\partial I}\right)\sigma_I^2 + \left(\frac{\partial OD}{\partial I_0}\right)\sigma_{I_0}^2 \qquad (6)$$

Using equation 4 to calculate the partial derivatives, simplifies equation 6 into equation 7.

$$\sigma_{OD}^2 = \left(\sigma_I\left(\frac{1}{I_0}\right)\right)^2 + \left(\sigma_{I_0}\left(\frac{-I}{{I_0}^2}\right)\right)^2 \qquad (7)$$

The uncertainty in the attenuation coefficient, σ_μ, is calculated by combining the uncertainty in the optical density (σ_{OD} from equation 7) with the uncertainty in the path length, σ_d, through the sample, as shown in equation 8. Evaluation of the partial derivatives using equation 5 results in a simplification of equation 8 into equation 9. Because this calculation of the attenuation coefficient is based on a uniform phantom, the uncertainty of the attenuation coefficients presented here is only valid for phantoms with a constant attenuation over the entire path length of the sample. The uncertainty is calculated for the measurements of the attenuation coefficients from 2D projection images. For the 3D reconstructed images, the standard deviation is used as a measure of the uncertainty in each volume of interest.

$$\sigma_\mu^2 = \left(\frac{\partial \mu}{\partial OD}\right)^2 \sigma_{OD}^2 + \left(\frac{\partial \mu}{\partial d}\right)^2 \sigma_d^2 \qquad (8)$$

$$\sigma_\mu = \sqrt{\left(\left(\frac{-1}{OD}\right)\sigma_{OD}\right)^2 + \left(\left(\frac{\ln OD}{d^2}\right)\sigma_d\right)^2} \qquad (9)$$

3.3.3 Dynamic Range

Qualitatively, the 'dynamic range' is the range of values over which a change in attenuation coefficient results in a (one-to-one) change in measured optical density. The dynamic range is often specified as a ratio – in this case, the ratio between the largest and smallest measurable attenuation coefficient with a high level of accuracy and low noise.

3.4 The Reconstruction Process

In general, samples are not uniform and the attenuation coefficients in individual regions (i.e. voxels) along a light path are not known. Therefore the process used in equation 5 cannot be used in the calculation of attenuation coefficients. To calculate the attenuation coefficient of an individual point in the sample, the inverse radon (*Iradon*) transform[159] is used. The 3D images in this thesis have been reconstructed using the Iradon transform that is part of the Vista™ Recon program.

The Iradon transform is used to calculate attenuation coefficients for individual voxels in a 3D matrix. The function uses the total attenuation along a number of paths that pass through each voxel at various angles. The function deconvolves the information from the different paths into the attenuation coefficients for the voxels in a region of interest. The following steps describe a simplified Iradon process for a laser based optical CT scanner. Doran et al[114] gave a detailed description of the process.

1. The optical density along a path through a translucent sample is calculated by comparing the difference in measured light intensity through an unirradiated and irradiated sample (equation

4). This is repeated for a number of parallel paths to form a profile of the light intensity through a slice of the dosimeter from a particular angle[114]. An example of the measurement of a profile of attenuation coefficients from a particular angle, before rotating to a new angle is shown in figure 3-6.

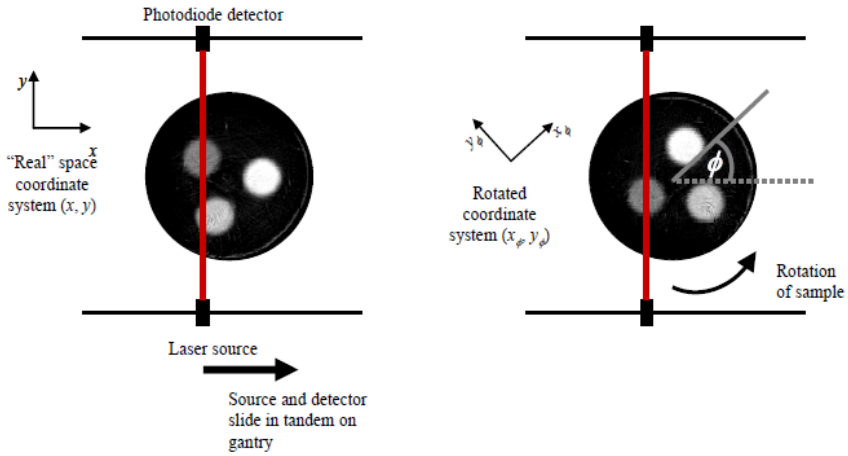

Figure 3-6: Measurement of a profile of optical density values before rotating to a new angular position and acquiring optical density values from a different angle. The optical density is calculated through a slice for a particular angle before the sample is rotated to a new angle, and the optical density is acquired from the new angle. Equations 10 to 13 convert the measured intensity at the new angle to the co-ordinate system of the first angle. (Image reproduced with permission from S Doran, The History and principles of optical computed tomography for scanning 3-D radiation dosimeter: 2008 update, Journal of Physics: Conference Series - 5th International Conference on Radiotherapy Gel Dosimetry[114]).

2. The sample is then rotated by an angle, φ. This forms a new angle to acquire the light transmitted through the slice of the sample (see figure 3-6). Equation 10 can be used to calculate the attenuation of the light at a single point on a profile in the original reference co-ordinates. This calculation is repeated for all points on a profile. Equations 11 to 13 change the co-ordinates from the rotated to the original co-ordinate system[114].

$$I_\phi(x) = I_0 e^{(-\int \mu_\phi(x,y)dy)} = I_0 e^{(-\int \mu(x_\phi,y_\phi)dy)} \quad (10)$$

$$\mu_\phi(x,y) = \mu(x_\phi, y_\phi) \quad (11)$$

$$x_\phi = x\cos\phi + y\sin\phi \quad (12)$$

$$y_\phi = -x\sin\phi + y\cos\phi \quad (13)$$

3. The measured intensity profiles are plotted according to position, x, and angle of acquisition, φ. The matrix formed is known as a 'sinogram'. Equation 14 calculates the intensity of a point at position (x, φ) in a sinogram as defined by Doran et al[114] for optical computed tomography, where: $\lambda_\varphi(x)$ is the intensity at point (x, φ) in the sinogram, $\int_{sample} \mu(x_\phi, y_\phi)dy$ is the change

in attenuation along a path length and $I_\varphi(x)$ is the light intensity calculated in equation 10. A single point in a plane will be mapped to a sinusoidal curve in the matrix. This can be visualised in figure 3-7. $\lambda_\varphi(x)$ is equivalent to calculating the optical density as per equation 4.

$$\lambda_\phi(x) = \int_{sample} \mu(x_\phi, y_\phi)dy = -\ln\left(\frac{I_\phi(x)}{I_0}\right) \qquad (\ 14\ )$$

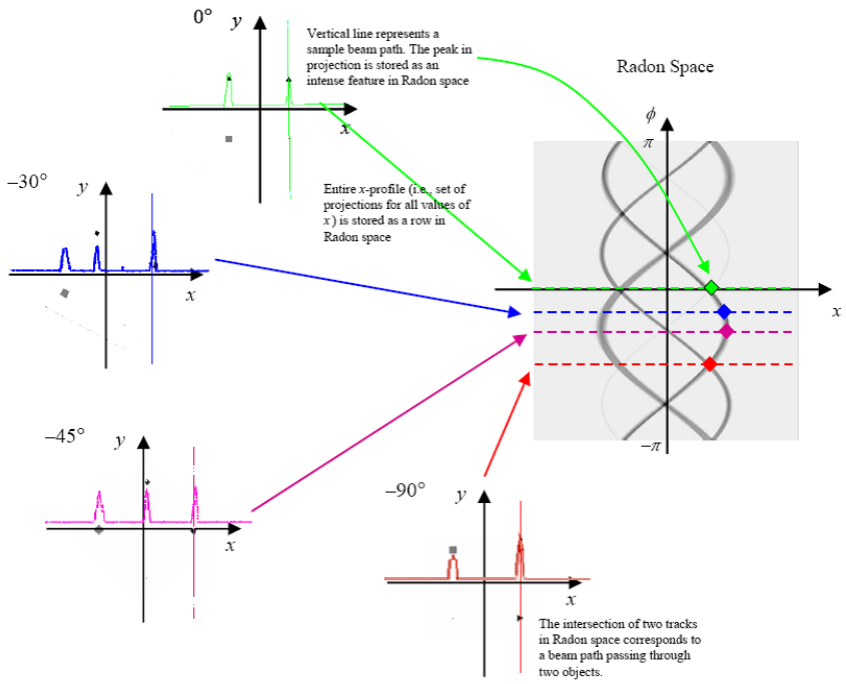

Figure 3-7: Creation of a sinogram. Measured optical density at a position on the profile, x, for a particular angle, φ, are plotted on the sinogram. The optical density at each coordinate (x, φ), relates to the measured attenuation at that particular point on the profile. (Image reproduced with permission from S Doran, The History and principles of optical computed tomography for scanning 3-D radiation dosimeter: 2008 update, Journal of Physics: Conference Series - 5th International Conference on Radiotherapy Gel Dosimetry[114]).

4. The spatial and angular information from Radon space (optical density profiles plotted against projection angle of the profile) can be used in an Iradon transform to calculate attenuation coefficient at a position in real space. The Iradon transform is analogous to projecting the measured profiles of attenuation at different angles onto a real space region. The profiles are positioned so that the angle the profiles were measured at is used to position the projection of the particular profile back across the region (see Figure 3-8). The attenuation coefficients from each angular projection sum to form the attenuation coefficient at the real space position[114]. This is known as back projecting the profiles.

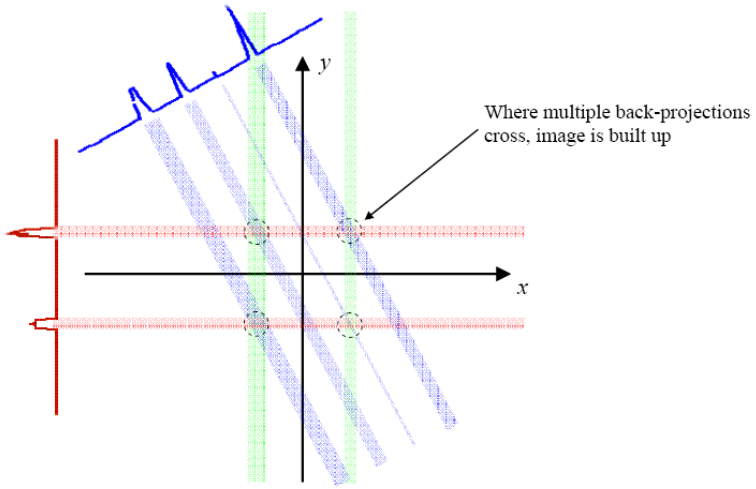

Figure 3-8: Back projecting the projection profiles. Profiles are back projected across the sample space. At each point in the sample space, the summation of the intensities from all angles is used to calculate the intensity at the particular point. (Image reproduced with permission from S Doran, The History and principles of optical computed tomography for scanning 3-D radiation dosimeter: 2008 update, Journal of Physics: Conference Series - 5th International Conference on Radiotherapy Gel Dosimetry[114])

When a reconstruction uses a large source and small detector the geometry changes from light rays being parallel to light rays converging in a cone geometry. The use of a large source and small detector is the opposite of the method used in conventional x-ray CT scanner geometry, but the principle of calculation is the same.

The cone beam geometry uses an extension of equal-spaced fan beam geometry[160]. In equal-spaced fan beam geometry, a point in a projection can be specified relative to the reconstruction axis by s and β. The distance between the reconstruction axis and the intersection of a ray with an imaginary detector plane is the variable s, where the imaginary detector plane is parallel to the actual detector plane and intersects the reconstruction axis. The actual and imaginary detector planes are related to each other via a magnification factor. β is the angle between an iso-ray and the real space y-axis, where the iso-ray is a line from the source, through the reconstruction axis to the centre of the actual detector. A point in fan-beam geometry is corrected into parallel beam geometry by trigonometry based on the variables s and β[161].

In a cone beam geometry, a fan beam is tilted out of mid-plane of the fan beam geometry into a different plane in the cone beam. This plane is then reconstructed as if part of the mid-plane of another fan-beam geometry. A correction for this tilt is applied. The final value of each voxel is the sum of all tilted fan beams passing through the voxel[160].

3.5 *Modulation Transfer Function*

The detection system requires characterisation in terms of the ability to distinguish contrast changes over small distances. This is known as the spatial resolution. An indication of spatial resolution is the Modulation Transfer Function (MTF) curve. The MTF describes the ability of an imaging system to reproduce a small object with a high level of contrast. The MTF can be measured from images of regular "bar" patterns or from the Fourier transform of a line spread function.

The simplest way to visualise the MTF is to consider the regular "bar" pattern and the shape of the light intensity profile formed by the pattern. In the pattern, the bars (and open light transmitting spaces between bars, or openings) decrease in width whilst increasing in number per unit distance. The light intensity profile varies in a sinusoidal pattern. As the frequency of the sinusoid increases, the amplitude of the sinusoid decreases. As the magnitude between maxima and minima on the sinusoid decreases (i.e. a decrease in contrast between the high light intensity opening and low light intensity bar), the ability to distinguish between two bars is reduced. A bar pattern, with decreasing distance between bars, and the measured light intensity across the pattern are shown in Figure 3-9.

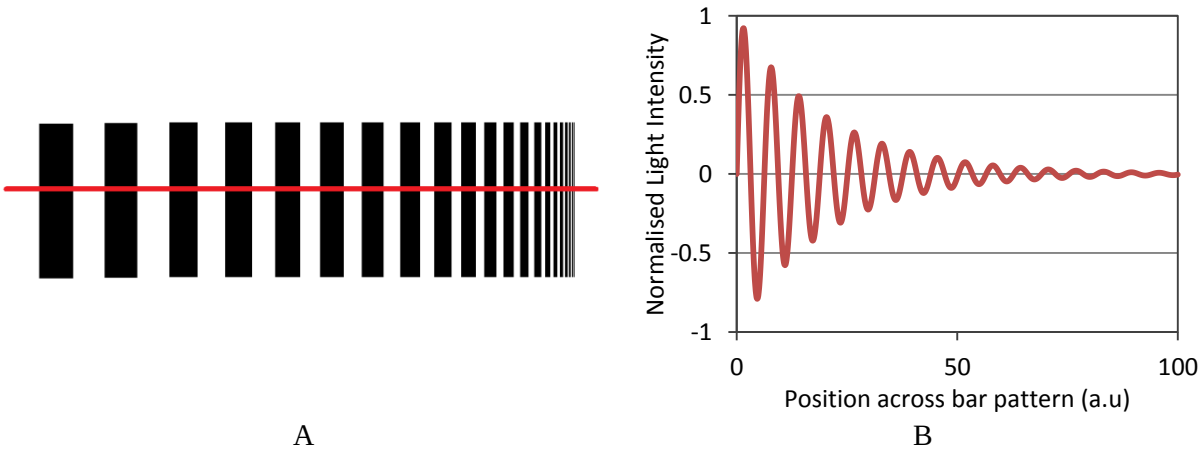

Figure 3-9: A) Sinusoidal bar pattern with decreasing distance between bars, and B) measured light intensity across the bar pattern

The MTF can also be calculated from a line spread function (LSF), the image of an infinitesimally thin line, using a Fourier transformation[152]. The LSF is, in turn, the derivative of the Edge Spread Function (ESF), which is easily measured by a profile across the edge of a sharp object. An ESF is used because the finite width of the attenuating material, used to create a line spread function, influences the measurement of the line spread function[152]. Equation 15 shows the derivation of the MTF from the LSF.

$$\text{Line Spread Function} = \frac{d}{dx}\ \text{Edge Spread Function(x)}$$

$$\text{MTF} = F[\text{LSF}] \qquad (\ 15\ )$$

A Fourier transform uses the super-position of sine and cosine trigonometric functions with varying frequency and amplitude, to reproduce the line spread function[162].

In this thesis MATLAB® (The Mathworks Inc., Natwick, USA) was used to acquire profiles across the edge of the sharp object in the 2D projections or 3D reconstructions (Figure 3-10 A). The sharp object was used to simulate a high contrast change over a small distance. Microcal™ Origin® (Microcal Software, Inc., Northampton, MA, USA) was used to calculate the Line Spread Function from the Edge Spread Function (Figure 3-10 B and C). The Line Spread Function was Fourier transformed to calculate the MTF curve (Figure 3-10 D).

The MTF curve relates the decrease in ability to distinguish the individual lines in a line pair (Y-axis in figure 3-10 D), as the number of line pairs per unit distance is increased (X-axis in figure 3-10 D). Characterisation of the MTF for both projection and reconstructed images is an important tool in assessing the level of detail that can be evaluated using the scanner.

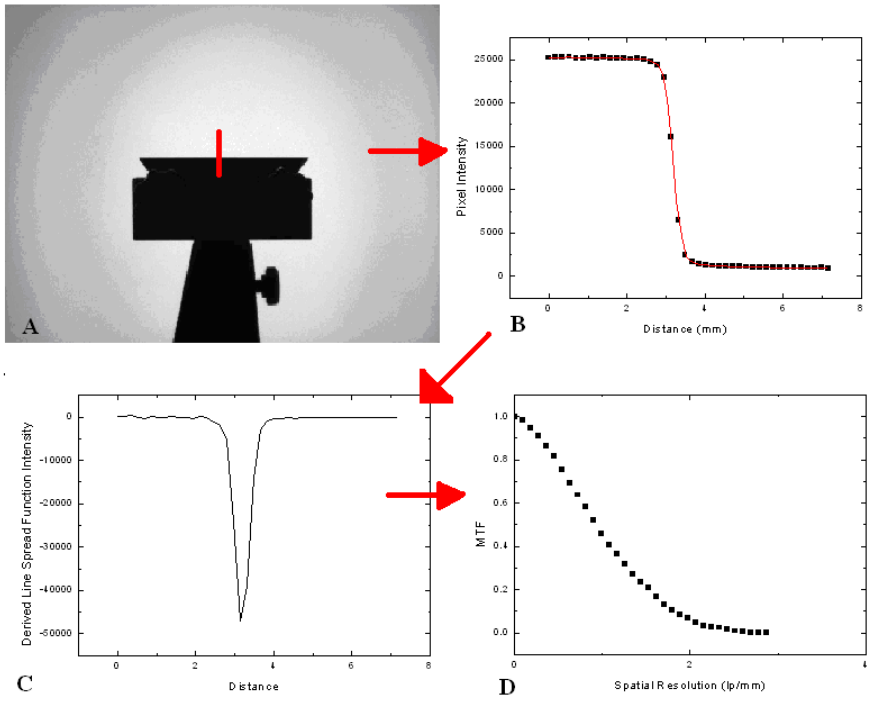

Figure 3-10: Calculation of the modulation transfer function process. A) Edge profile acquired across razor. B) Interpolation of curve of edge spread function (Red line). C) Calculation of the line spread function from the edge spread function. D) Fourier transform of line spread function to calculate modulation transfer function curve.

4. CHARACTERISATION OF THE SCANNER SETUP

4.1 Introduction

In the literature (see section 2.4 and 2.5) it has been observed that the optical CT evaluation of a dosimeter can be influenced by:

- Scanner acquisition parameters
- Scattered light
- Wavelength and intensity of the light source
- Response of the detector to different light intensities
- Detector spatial resolution
- Mechanical axis of rotation alignment
- Cone beam geometry
- Filtration used in reconstructed images, and
- Geometrical Distortion

The aim of this chapter was to characterise the light source and CCD of the Vista™ Cone Beam Optical CT scanner (the scanner) for effects on accurate evaluation of a dosimeter. In addition, attenuation coefficients for a set of uniform phantoms were measured to establish baseline values for future constancy and reproducibility studies. The phantoms measured were the Polyurethane Opacity Reference Phantoms (PORPs) described in section 3.2.1.

Both the orange and red light sources were evaluated by measuring each light source's spectrum and stability of light intensity after switching the scanner on. The influence of the light source stability on a reconstructed image of a uniform phantom was also investigated.

Both light sources were characterised to determine the spectra, evaluate the match between the peak light and dosimeter absorbance wavelengths, assess the impact of adding a filter and determine the influence of spectral hardening caused by differential attenuation at different wavelengths across the FWHM of the peak wavelength. The CCD spectral response to different wavelengths was also investigated.

The temperature of the environment surrounding light emitting diodes (LEDs) is known to influence the light source intensity[163]. Two separate investigations[133,147] have determined different warm-up times for LEDs used in different scanners. No information has been published on the temporal stability of the LED light source in the scanner used in this work. As such, a "warm-up" time was determined for the type of LED used in the scanner.

The change in light intensity after the light source was switched on can influence the measured optical density. Using an unstable light source to evaluate a dosimeter could decrease the accuracy of the reconstructed attenuation coefficients. Reconstruction of a uniform phantom, from projection images acquired at different times after activation, investigates the impact of the light source intensity change on measured attenuation coefficients.

CCD response to light intensity is required to be linear in order for the method used to calculate optical density to be valid. The reciprocity law is a relationship between the light intensity, the charge integration period and the lens aperture. The law means charge integration time can be used as a surrogate for light intensity. The response of the CCD to charge integration time was evaluated to investigate the range of pixel values from the CCD for which a linear response exists. To investigate the influence of non-linear response on the reconstructed attenuation coefficient, a uniform phantom was scanned and reconstructed with a range of initial light intensities.

Attenuation coefficients of the Polyurethane Opacity Reference Phantoms (PORPs – see section 3.2) were measured in a parallel beam geometry. These results are used as baseline values in subsequent chapters to evaluate the accuracy of attenuation coefficients measured in both 2D projections and reconstructed volumes.

A summary of the measurements described in this chapter is presented in Table 4-1.

Table 4-1: Measurements used to characterise the imaging system of the optical CT scanner. These provide information on the light source or the CCD. In addition, the baseline attenuation coefficients of the PORP were measured.

Measurement	***Reason for measurement***
Spectra of available light sources	Provide suitability of evaluating different 3D dosimeters Quantify the influence of the filter on the light intensity and the light spectra Investigate differential light attenuation and CCD spectral response
Temporal variation of light source intensity after initial activation	Establish a recommended “warm up” time to minimise uncertainty in optical density measurement
Uniformity using an unstable light source	Determine the significance of an unstable light source on the reconstructed uniformity
CCD response to light intensity	Evaluate the response of the CCD to light intensity and therefore the validity of the optical density calculation method
Uniformity with different charge integration times	Determine the influence of non-linear behaviour in the CCD response on the reconstructed attenuation coefficient.
Baseline attenuation coefficients of PORPs	Used for evaluation of attenuation coefficient accuracy in subsequent chapters

4.2 Spectra of the Available Light Sources

The scanner has two available light sources comprising LEDs of nominal wavelength 590 nm (orange) and 627 nm (red) both of which are not truly monochromatic (GVA Lighting, Mississauga, Ontario, Canada). Two light sources are present so that multiple types of 3D dosimeters could be evaluated. Each light source consists of an array of LEDs (one 4 x 3 and one 5 x 3) mounted on the rear wall (Figure 4-1). The diodes emit light onto a diffuser screen, which scatters unpolarised light across the specimen tank. The array of diodes in combination with the diffuser screen creates a broad light source. The broad light source and small detector with a focusing lens forms the cone beam geometry which lends its name to the type of scanner.

Figure 4-1: LED light source in the Vista^{TM} Cone Beam Optical CT scanner (Modus Med Inc., London, Ontario, Canada) showing alternative strips of orange and red light sources (nominal wavelength 590 and 627 nm respectively). Light sources are mounted on the rear plate and shine directly at the diffuser screen.

Measurement of each light source's spectra: i) determines the difference between the measured and nominal peak wavelength, ii) quantifies the efficiency of the band pass filter and iii) investigates the influence of a polychromatic light source, specifically looking at preferential light attenuation and the CCD spectral response.

As discussed in section 2.5.4, the attenuation of light by a gel dosimeter is dependent on the wavelength of light[50,51,107,148,149]. The change in attenuation coefficient at a particular wavelength is an important consideration when selecting a light source. A larger change in dosimeter dose response will result in a greater light intensity change. Consequently, smaller differences in the attenuation coefficient can be measured. This will decrease the uncertainty in the measured attenuation coefficient. The dose response is defined as the change in attenuation coefficient as a function of dose (cm^{-1} Gy^{-1}). Ideally, the best dose resolution is achieved by matching the peak wavelength of the light source, to a dosimeter's wavelength of maximum dose response. A difference between the nominal and measured peak wavelength could influence the achievable dose resolution. The measured light source and dosimeter attenuation spectra were compared to determine the change in attenuation, and therefore the effect on dose resolution, caused by a difference between the nominal and measured peak wavelength.

The filter reduces the full width half maximum (FWHM) of the light source spectrum. It should be noted the filter does not change the light source from polychromatic to monochromatic. The

transparency of the filter will affect the intensity of light reaching the CCD camera. As such, the efficiency of the band pass filters used for each light source is quantified.

The combination of a polychromatic light source (either filtered or unfiltered) and dependence of the attenuation on the wavelength of light gives rise to *differential attenuation* – i.e. the attenuation of light at different rates dependent on the wavelength. This is analogous to beam hardening observed for X-ray sources. For an initial light source with a uniform light intensity for all wavelengths incident on a medium with a wavelength dependent attenuation, the light exiting the medium will exhibit a lower intensity at wavelengths near the peak attenuation wavelength of a dosimeter. This results in differences in detected light intensity depending on wavelength, which can cause inaccurate reconstructions[151]. Figure 4-2 is a simple diagram depicting this process. The process is more complicated if the incident light intensity at each wavelength is not equal and if there are ray paths of different lengths through the sample.

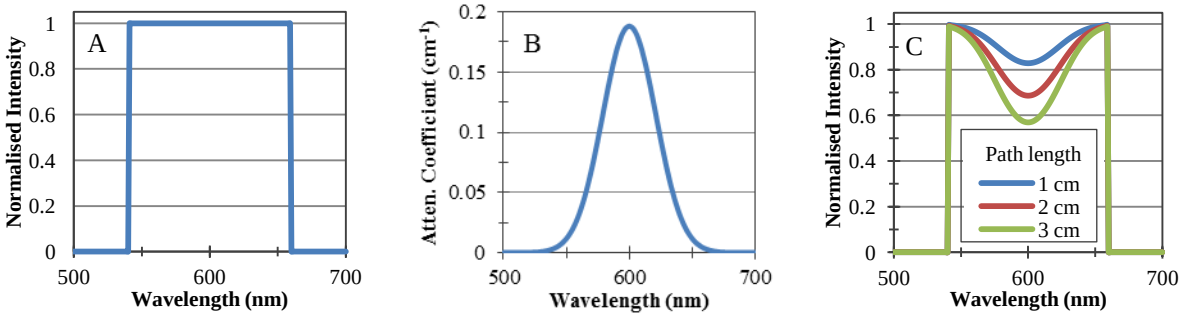

Figure 4-2: A) Normalised light intensity incident on phantom. B) Phantom's wavelength dependent attenuation. C) Normalised light intensity after passing through three individual phantoms with different path lengths.

Thomas et al[151] investigated the influence of differential attenuation on the reconstructed attenuation coefficient and found large differences between a polychromatic LED light source (FWHM ~25 nm) compared to a monochromatic laser (FWHM ~0.1 nm). Correction factors have been developed to compensate for differential attenuation[151], but the use of a filter to narrow the FWHM was observed to be an effective solution[147]. The narrower FHWM of the filtered light source resulted in the dosimeter dose response being approximately uniform across the range of wavelengths in the narrower peak of the light source[147]. The work presented by Thomas et al[147,151] investigated 3W Red LEDs (manufacturer identified as Leutron Vision Inc., Burlington, MA from an investigation of the same optical CT scanner by Sakhalkar et al[164]) and the dose response of PRESAGE™ relative to a 633 nm light source.

The LEDs in the scanner investigated in this work were from a different manufacturer and could exhibit different spectra compared to those characterised by Thomas et al. As such, the spectrum of each light source was measured and the dose response for Fricke and PRESAGE™ dosimeters were compared. Fricke and PRESAGE™ were chosen for comparison because the dosimeters are absorbing and therefore uncertainty is not introduced due to scattering. In addition these dosimeters are commonly used. A Fricke dosimeter was compared to the orange light source and PRESAGE™ was compared to the red light source.

Thomas et al[151] also investigated the dependence of the CCD's response on wavelength. This was also assessed for the CCD used in the scanner to complete the characterisation of the effect of the polychromatic light source measurements.

4.2.1 Measurement of the Spectra

An ILT900R spectroradiometer (International Light Technologies, Peabody, MA, USA, serial number: RPS9002947) was used to measure the spectra of both light sources (orange and red) in the scanner. The spectroradiometer has an absolute radiance response in μW/cm^2/nm/sr traceable to the National Institute of Standards and Technology (NIST, http://www.nist.gov/index.html). The spectroradiometer was positioned between the CCD and the filter. The filter was removed from the light path for the unfiltered measurement. The consistency of the measurement position allows the comparison of the absolute radiance between the unfiltered and filtered spectra.

From the spectra acquired, the peak wavelength and spread of wavelengths (as described by the FWHM) were determined. The shift in the peak wavelength between filtered and unfiltered light was also determined. The light source was switched on 2 hours prior to the measurement to allow the scanner sufficient warm-up time (see section 4.3 for further details on scanner warm-up).

The addition of a filter to a polychromatic light source, combined with the dose response from a dosimeter can have two effects. First, the shift of the peak wavelength can change the dose response at the peak (Figure 4-3 A). This was measured for both light sources and the corresponding dosimeter. The change in dose response between the peak wavelengths is denoted by Δ_p. Secondly, the narrowing of the FWHM can cause the variation in dose response across the FWHM to decrease (Figure 4-3 B), and is denoted by Δ_{FWHM}. The variation of the dose response across the FWHM will affect the significance of differential attenuation between the unfiltered and filtered light source. The attenuation spectra were obtained from Kelly et al[51] and Thomas et al[151] for Fricke and PRESAGE™ respectively. Both light source spectra are plotted on graphs with wavelength on the abscissa, light intensity on the primary ordinate and dose response on the secondary ordinate.

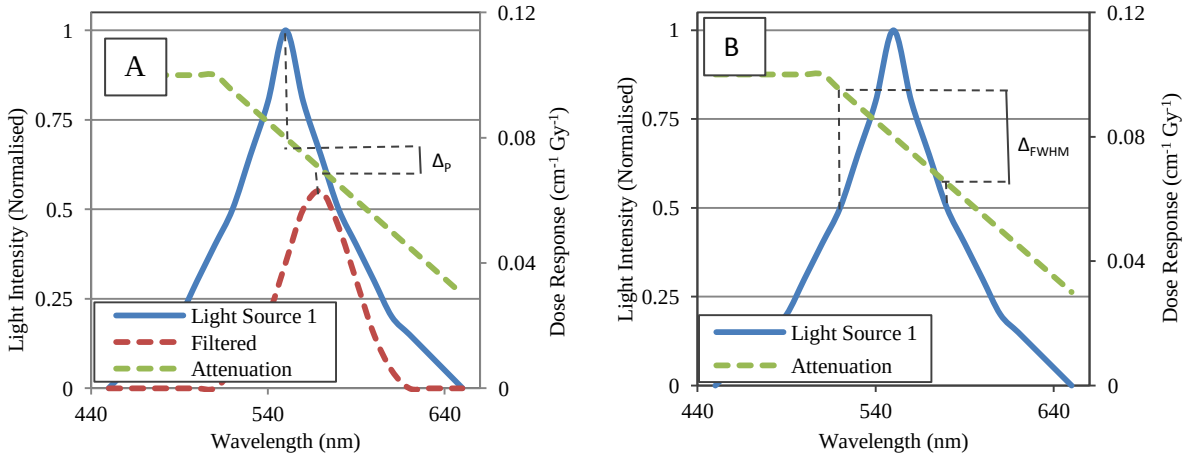

Figure 4-3: A) The change in dose response at the peak wavelength, Δ_p, caused by the addition of a filter. B) Variation of the dose response across the FWHM of a peak, Δ_{FWHM}.

The spectral response of the CCD used in the scanner (Model ACX204AL, Sony Corporation, Japan) was assessed across the orange and red light source peaks. Similar to the method described above used to assess the variation in dose response across the FWHM, the spectral response across the FWHM was determined for the unfiltered and filtered light and was denoted by Δ_{CCD}. The spectral response was determined from graphs of the CCD's response to wavelength in the manufacturer's documentation.

4.2.2 Measured Spectra Results

The wavelength spectrum for the unfiltered orange light, shown in Figure 4-4 A, had a peak wavelength of 598 nm and a FWHM of 17.5 nm. When the filter was inserted between the light source and spectroradiometer the peak wavelength changed to 595 nm and the FWHM narrowed to 11 nm.

The change in dose response of Fricke gel at the peak wavelength (Δ_p) was 3 %. The variation of Fricke gel's dose response across the FWHM (Δ_{FWHM}) for the unfiltered and filtered orange light source was 0.03 and 0.02 cm^{-1} Gy^{-1} respectively. These were differences of 21 % and 10.5 % respectively. The variation in CCD spectral response is not shown on the same graph for simplicity. The variation was 4.8 % and 3 % for the unfiltered and filtered light source respectively.

Figure 4-4 B shows the red light had a peak wavelength of 642 nm and a FWHM of 23 nm. When the red filter is used, the peak is 635 nm and the FWHM narrows to 11 nm.

The shift of the peak wavelength caused an increase in dose response for PRESAGE^{TM} (Δ_p) from 0.032 to 0.038 cm^{-1} Gy^{-1}. This was a percentage difference of 16 %. The percentage difference of the dose response across the FWHM (Δ_{FWHM}) was 46 % and 7.9 % for the unfiltered and filtered light source respectively. The percentage difference in CCD spectral response (Δ_{CCD}) was 8.0 % and 3.7 % for the unfiltered and filtered light. A summary of the observed changes in dose response and CCD response is shown in Table 4-2.

Table 4-2: Summary of the peak and FWHM of the unfiltered and filtered light sources. The change in dose response caused by the change of the peak wavelength by the addition of a filter was larger for the red light source relative to the change for the orange light source. The variation across the FWHM for the dose response and spectral response of the CCD was observed to decrease with the addition of a filter.

Light Source		***Peak***		***FWHM***		
		Value	Dose response change between peaks (Δ_p)	Value	Variation in dose response(Δ_{FWHM})	Variation in Spectral Response of CCD (Δ_{CCD})
		(nm)	(%)	(nm)	(%)	(%)
Orange	Unfiltered	598	3 %	17.5	21	4.8
	Filtered	595		11	10.5	3.0
Red	Unfiltered	642	16 % difference	23	46	8.0
	Filtered	635		11	7.9	3.7

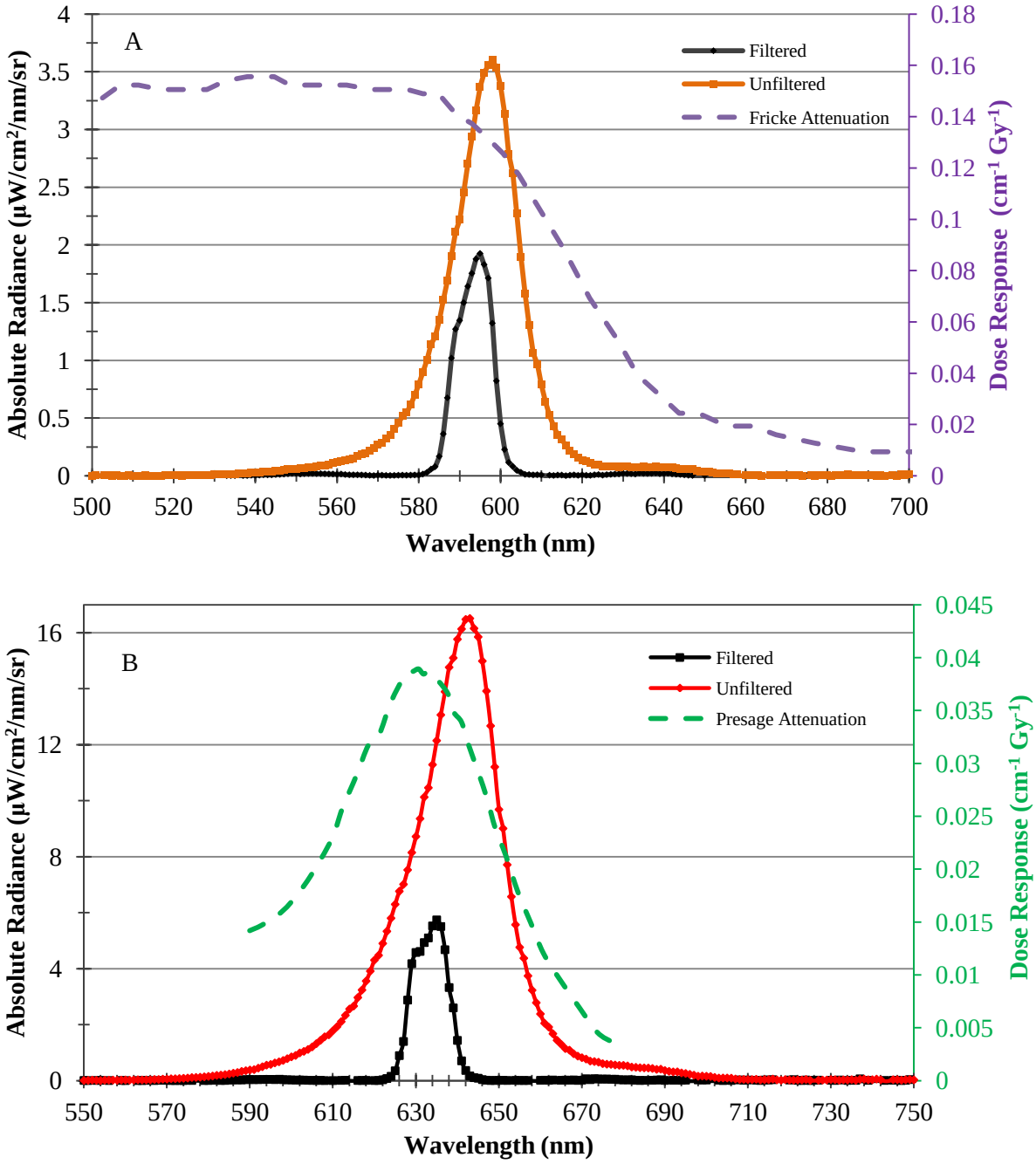

Figure 4-4: Unfiltered and filtered spectra for the A) orange light source and B) red light source. The spectra were measured in absolute radiance (µW/cm^2/nm/sr). The details on the peak wavelength and FWHM for the unfiltered and filtered spectra measured for the orange and red light source are in Table 4-2. The dose response of Fricke gel and PRESAGE™ are plotted on the secondary ordinate in A and B respectively. This shows how each dosimeter's dose response varies over the spectrum of the LEDs. The attenuation spectra of the dosimeters were obtained from Kelly et al[51] and Thomas et al[151] for Fricke gel and PRESAGE™ respectively.

4.2.3 Discussion

The orange and red LED spectra show a difference in the peak wavelength between the unfiltered and filtered spectra. The difference in peak wavelength was caused by a mismatch between the peak wavelength of the light source and the peak transmission wavelength of the band pass filter. The FWHM of the peak in both the orange and red spectra narrows due to the addition of a filter.

A 3 % difference in the dose response was measured for the peak wavelength of the orange unfiltered and filtered light source. This difference is less significant than the difference in variation of the dose response caused by the addition of a filter (21 % variation reduced to 10.5 %). Therefore, the main function of the orange filter is to narrow the wavelength spectrum, thereby reducing the effects of differential attenuation. For the red light source the dose response increases with the addition of the filter whilst reducing the variation of dose response across the FWHM. Thus, the role of the filter is to better match the light spectrum to the maximum dose response of the dosimeter and to narrow the wavelength spectrum. The larger dose response of the filtered red light will result in a reduction of the uncertainty of the measured attenuation coefficient.

The change in light intensity through the filter was expected. The light intensity loss will affect the maximum intensity measured by the CCD which can be compensated for by adjusting the detector settings. For some scanning geometries, the light intensity loss cannot be compensated despite adjusting the detector settings to acquire the maximum amount of light. This limits the maximum light intensity detected, which limits the optical density range that can be measured.

Comparison of the LED spectra and the spectral response of the CCD (see section 3.1) shows the spectral response of the camera decreases with increasing wavelength across the peaks of the orange and red light sources. The magnitude of the change in spectral response across the FWHM was smaller than the change in dose response across the FWHM of the filtered light source. However, the variation in spectral response could still increase uncertainty in the measured light intensity. This is because wavelength dependent attenuation (beam hardening) through a sample will change the spectrum. Therefore the spectrum incident on the CCD will be sample dependent. Therefore, spectral dependent response of the CCD contributes uncertainty in the total measured light intensity and is an important consideration when selecting the detector to be used in conjunction with the light source.

For 3D plastic dosimeters, the unfiltered and filtered peak wavelengths for the orange light (597 nm and 595 nm respectively) are appropriate for use with leuco crystal violet micelle hydrogel which has a maximum absorption at 590 nm[148]. A spectrum of the dose response was not available and as such no further analysis of the differential attenuation was performed.

BANG™ type polymer gels have a maximum dose response in the blue end of the spectrum[50], indicating the difference observed with dose at both 595 and 635 nm will not be as large as the response at 450 nm. Therefore the light sources in this scanner are not optimal for measurement of this form of BANG™ gel.

For both the orange and red light source, the observed change in attenuation and spectral response of the CCD across the FWHM of the filtered light source will have an impact on the accuracy of the detected light intensity. The effect will be smaller relative to the change in attenuation and spectral response observed for unfiltered light.

4.3 Stability of Light Intensity after turning on the Light Source

As described in section 4.2, the light source in the scanner consists of two independent 4x3 matrices of LEDs (one matrix for orange, the other for red), behind a diffuser screen.

The temperature of the surrounding environment is known to affect the intensity of an LED light source[163]. Two groups have presented stability measurements of light intensity after initial activation for a cone beam[82] and parallel beam[147] optical CT. The cone beam LED manufacturer was not stated. The parallel beam LEDs are 3W red LEDs from Leutron Vision Inc. (Burlington, MA, USA)[164]. The results indicated a large difference in the recommended time required to reach a stable light intensity output (2 hours vs. 45 minutes respectively).

The LEDs used in the scanner investigated in this work were from GVA Lighting (GVA Lighting Inc., Mississauga, Ontario, Canada) and had nominal wavelengths of 590 and 627 nm.

Due to difference in suggested warm-up times and no published information on the LEDs used in the scanner, the stability of the LED's intensity after activation was measured to determine a suitable warm-up time.

4.3.1 Light Source Intensity Measurement

Light source intensity was measured with a photodiode and amplifier/reader located in the specimen tank near the central light source to CCD axis. The photodiode used was a United Detector Technology silicon photodiode type PIN-10DP (UDT Instruments, San Diego, CA, USA). The photodiode has a circular sensitive area of 1 cm^2. The amplifier connected to the photodiode was a Terahertz Technology Inc. PDA-750 photodiode amplifier (Oriskany, NY, USA, s/n: 10029). The digital resolution of the readout was 0.01 μA. No uncertainty in the photodiode measurement was given in the manual.

An instantaneous current output from the photodiode was measured as an indication of the intensity of the light source as a function of time. The amplifier provided a digital readout of the measured current from the photodiode. The light intensity was measured for 4 hours initially at 1 minute between readings, then at less frequent intervals as the current stabilised. The offset of the amplifier, measured with no incident light source (i.e. the dark current), was adjusted to 0 μA prior to the acquisition of the light intensity change over time. Both available light sources in the scanner were investigated.

4.3.2 *Results*

The absolute photodiode current output for both light sources reduces with time, indicating that the light intensity decreases with time after activation. The maximum rate of change in light intensity was measured just after switching on the light source (t = 0). As time increases, the rate of change in the light intensity decreases. Figure 4-5 A and B show the light intensity measured over time since activation (t = 0) for the orange and red light sources respectively.

The orange and red light sources have an initial absolute current of 27.6 and 57 µA respectively, reducing to 19.68 and 52.01 µA after 2 hours. The rate of change in the measured current at 2 hours was 0.005 and 0.003 µA/min for the orange and red light source respectively. The change in absolute current per minute was given because acquisition times are generally in the order of 5 – 10 minutes. The percentage change in the measured current at 2 hours relative to the initial intensity was 29 and 9 % for the orange and red light sources respectively.

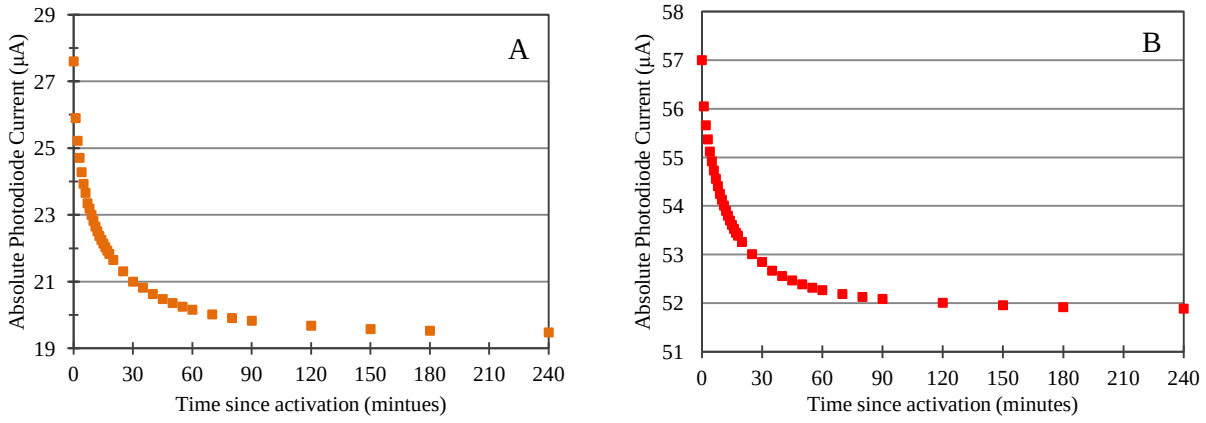

Figure 4-5: Change in light source intensity with time since switching on the A) Orange and B) Red light sources. The initial rate of change in the light source intensity is relatively large compared to the change in intensity at 120 minutes.

4.3.3 *Discussion*

The decrease in light intensity was expected due to the increase in temperature as the light source warms-up. Light intensity of LEDs has been observed to decrease with increases in temperature[163].

The impact of the changing light intensity on the evaluation of a 3D dosimeter can be described by the change in light intensity over a 5 minute period. This length of time was used because the time required to measure 420 projections in the scanner is ~5 minutes. Over a 5 minute period after initially turning on the scanner, the light intensity changes by 13.2 % and 3.6 % relative to the initial light intensity at t = 0, for the orange and red light sources respectively. At 2 hours the variation in light intensity relative to the initial light intensity was 0.1 % and 0.03 % over a 5 minute period. The difference is caused by the orange light source having a larger absolute change at 2 hours relative to the red light source. The larger absolute change could be caused by different responses to temperature by the orange and red LEDs[163].

A change in the light intensity over the time taken to complete a rotation of the dosimeter will cause the measured attenuation coefficient accuracy to decrease and the uncertainty in the measured optical density to increase. Waiting for a smaller change in light intensity will reduce uncertainty.

The change in light source intensity at 2 hours after activating the light source indicates that a recommended time of ~2 hours will be sufficient to warm-up the orange and red LEDs.

Olding et al[82] published the measured light intensity over time using a photodiode for a cone beam optical CT scanner. The warm-up time indicated in the current study is consistent with the published value. Olding et al[82] have used this to develop an evaluation protocol which stipulates a 2 hour warm up period.

Thomas et al[147] have published light source stability results using 3W Red LEDs in a parallel beam optical CT scanner. The results showed that the LED light stabilised after approximately 45 minutes. The manufacturer of the LED light source was different from the LEDs used in this work and thus was not expected to match.

4.4 Influence of Stability on Measured Uniformity

Warm up times of the LED light sources have been suggested in the literature[133,151], but the significance of not allowing the light source to reach a stable intensity output has not been investigated. The effect of a changing light intensity on the uniformity was investigated by comparing profiles measured from a reconstructed uniform phantom acquired with the scanner at different times since activation of the light source.

4.4.1 Method

Projection images of an undyed and dyed phantom, representing pre and post irradiation dosimeters respectively, were acquired and reconstructed for different scenarios (see Table 4-3). The different measurement scenarios represent the state of the scanner (either warm or cold) when the projection images were acquired. The reference scan is analogous to a pre-irradiation scan, whilst the data scan is analogous to a post-irradiation scan. A scanner which was allowed to warm up for at least 2 hours is designated as being in a warm state, whilst a cold scanner is the state immediately after activation unless otherwise stated.

The data reconstructed from reference and data scans both acquired with a warm scanner (scenario 1) was repeated over a number of days to determine reproducibility.

The reference phantom was a jar filled with water. The data phantom was made from water and blue dye (fractional concentration of blue dye: 1×10^{-3} %). Water was used as the refractive index matching fluid. 342 projection images were acquired for both the pre and post irradiation scans. A constant shutter time of 40.6 ms was used for all image acquisitions. All reconstructions were performed by

using the Vista^{TM} Recon software (Modus Med Inc.), which uses a Hamming filter (A = 0.540, B = 0.460). The time taken to acquire 342 projections was ~4 minutes.

ImageJ (National Institute of Health, USA) was used to average 10 profiles from a single slice across the diameter of the reconstructed phantom. This was repeated for 10 slices in the centre of each reconstruction (slices 122 to 131 of a 256 slice reconstruction). A volume of interest (VOI) between voxel positions -70 to 70 around the centre of the reconstruction was analysed for the mean and standard deviation of each scenario. The VOI was limited to voxels with a minimum distance of 1 cm from the container walls. Differences outside the VOI were influenced by container wall artefacts or fluctuations in noise outside the jar.

Table 4-3: Projection acquisition scenarios used to investigate the influence of light intensity stability on uniformity. The reference and data phantoms were a container of water and a blue dye solution respectively.

Scenario	*Reference Scan*	*Data Scan*
1	2 hours warm up	2 hours warm up
2	Immediate after activation	Immediate after activation on the next day
3	Immediate after activation	2 hours warm up
4	2 hours warm up	Immediate after activation
5	Immediate after activation	Immediately after Pre-irradiation scan

4.4.2 Results

The inter-day reproducibility was evaluated by comparing profiles measured from reconstructions of projections acquired using scenario 1 (i.e. warm scanner state for both reference and data projection acquisition). Figure 4-6 A shows a plot of the reproducibility measurements for the central 150 voxels surrounding the centre of the reconstruction. The VOI mean and standard deviation were 0.1027 ± 0.0005, 0.1033 ± 0.0008, 0.1026 ± 0.0005 for day 1 – 3 respectively.

A comparison between profiles measured from a reconstructed uniform phantom acquired using scenarios from Table 4-3 is presented in Figure 4-6 B. The mean and standard deviation of the VOI for each scenario is presented in Table 4-4.

In general, the uniformity of the reconstructions created using projections acquired with the scanner in a cold state was worse compared to the reconstructions acquired when the scanner was warm. The difference was usually increased noise (indicated by a larger standard deviation) and was most notable at the centre of the reconstruction volume.

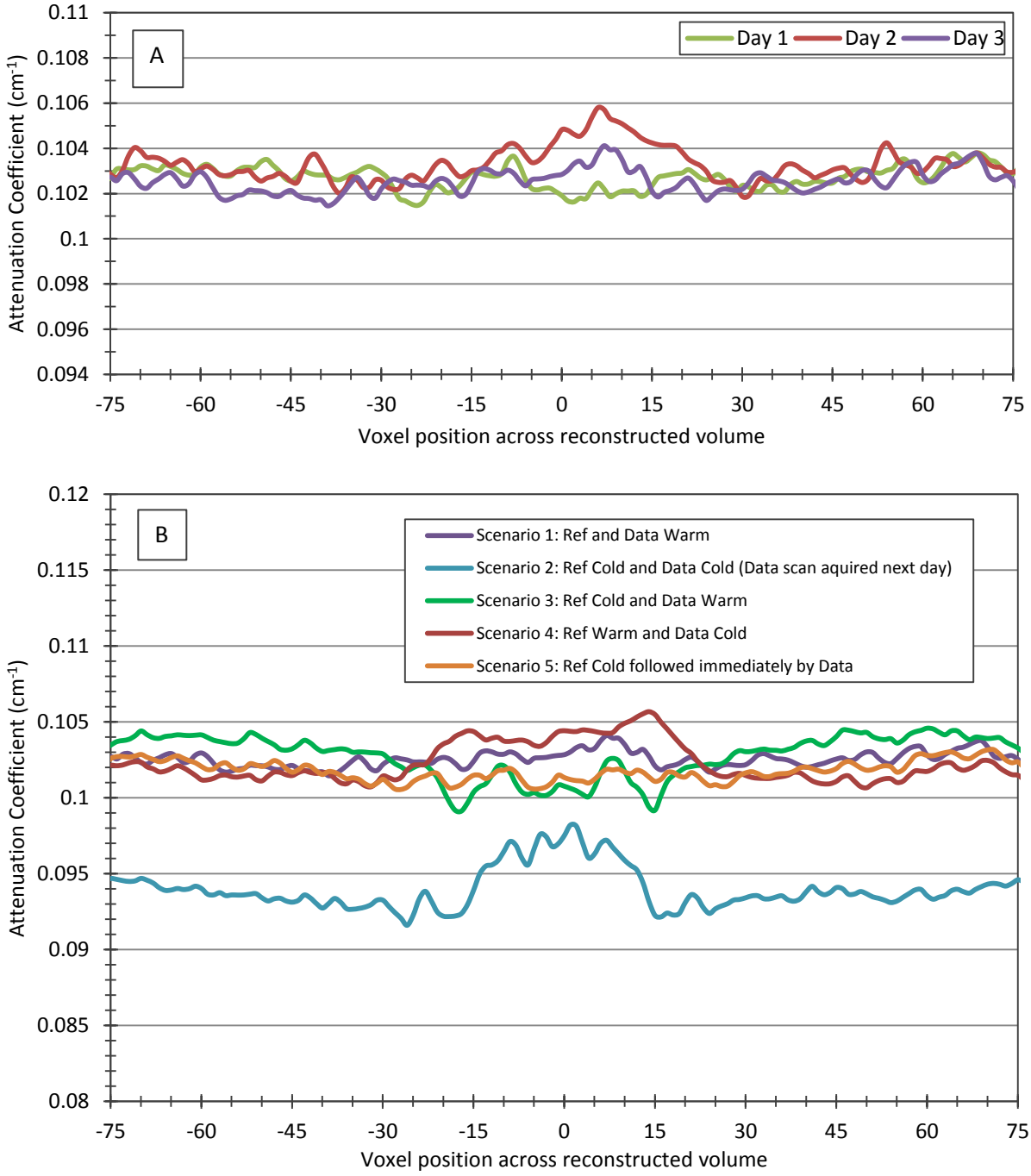

Figure 4-6: A) Reproducibility of reconstruction of a uniform phantom with both the reference and data scan acquired with a warm scanner. B) Comparison of uniformity profiles for the different acquisition scenarios in Table 4-3. The cold reference and data projection images measured on separate days showed significant decrease in the measured attenuation coefficient relative to the other scenarios.

The use of projections with one acquisition in a cold scanner state, and the other in a warm scanner state does not significantly influence the mean measured attenuation coefficient, however, an increase in noise was observed. In the voxel region -20 to +20 the profile drops for scenario 3 (ref cold, data warm) or rises for scenario 4 (ref warm, data cold). A cupping artefact was more noticeable for scenario 5 (ref cold followed immediately by data scan).

Table 4-4: Accuracy and standard deviation across the central region of the profiles (-70 to +70 voxels around the central voxel). A mixture of cold and warm scanner states for either the pre or post scan results in a comparable measured attenuation coefficient but a larger standard deviation. Acquisition of both the reference and data projections using a scanner in a cold state results in a reduced attenuation coefficient and a large standard deviation.

Scenario	***Attenuation Coefficient*** (cm^{-1})	***Standard Deviation*** (cm^{-1})
1 (Reference and Data Warm)	0.1026	0.0005
2 (Ref cold – Data cold on the next day)	0.094	0.001
3 (Ref cold, Data warm)	0.103	0.002
4 (Ref warm, Data cold)	0.102	0.001
5 (Ref cold - post immediate)	0.1027	0.0006

4.4.3 Discussion

The reconstructed phantom acquired using a warm scanner was observed to be reproducible within ± 0.0008 cm^{-1} within a single scan, and an inter-day reproducibility within ± 0.0004 of the mean over 3 days. This result is similar to the inter-day precision observed for an absorbing phantom by Olding et al[133] and confirms that our scanner is reconstructing with a similar level of reproducibility.

The central voxel region's drop and rise (scenario 3 and 4 respectively) and observed cupping (scenario 5) is most likely due to the pathlength through the phantom compounding the influence of the light source intensity decrease on measured attenuation coefficient.

As determined in section 4.3, the light source intensity decreases with time after the light source was switched on. The light source reached a stable output after ~ 2 hours. The results in this section show that using a scanner in a cold state will affect the measured accuracy and noise. The most significant difference occurs when the scanner was used to acquire the pre and post irradiation projection images on separate days immediately after switching on the light source. The scenario 2 results (ref and data acquired with a cold scanner on separate days) were repeated twice to confirm the observed result. Both results were significantly below the measured values observed for the other scenarios, indicating the observed result was reproducible and was not caused by an error in the measurement.

A theoretical example demonstrating how the decrease in light source intensity influences both the measured attenuation coefficient and the standard deviation is described below.

If a light source with decreasing intensity was used to acquire data, then the reference intensity (I_0) would be sampled at a higher intensity relative to the intensity present during the sampling of the data intensity (I). E.g., if a uniform 1 cm phantom with an attenuation coefficient of 0.5 cm^{-1} was sampled with a stable intensity, then the optical density (I/I_0) is 0.606 (or I = 60.6 and I_0 = 100 a.u). However, if the I_0 measurement was sampled earlier, when the intensity was 5 % higher, then the measured intensity (I) would still be 60.6 a.u, but the reference intensity (I_0) will be 105 a.u, and therefore the optical density would be 0.578, a decrease in optical density of ~4.8 %, which results in a calculated

attenuation coefficient of 0.55 cm^{-1}. This example demonstrates the influence both the reference and data projection light intensity has on measured optical density and consequently the attenuation coefficient.

The observed increase in noise indicated by the standard deviation is due to the variation in the light intensity used to acquire the pre and/or post irradiation projection images. Having a large variation in the intensity measuring a single point over the time required to rotate the dosimeter in the scanner, will result in a larger variation in the measured optical density. This was shown by the calculation of the uncertainty in optical density.

A theoretical example of this can be described by considering a uniform phantom comprising a non-attenuating material surrounding a 1 cm diameter cylinder with an attenuating material of 0.5 cm^{-1}, with the attenuating material offset from the central axis. A 1 cm diameter cylinder is chosen so that as the phantom rotates, the path length through the attenuating material will be constant. This is depicted in Figure 4-7.

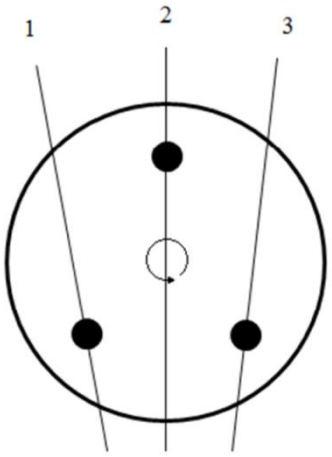

Figure 4-7: Depiction of the 3 calculation path lengths through a single point as the phantom rotates. The calculation of the optical density along each path only relies on the reference (I_o) and data (I) intensity measured for each path length. The variation in optical density measured with both stable and changing light sources was calculated based on the intensity change observed for the red LED in section 4.3. The second and third positions correspond to points 1.66 and 3.33 minutes into the scan. The data scans for the same point used the light intensity at 5, 6.66 and 7.33 to calculate the intensity measured through a uniform attenuating medium of 0.5 cm^{-1}.

The rotation of the phantom through a full 360° was assumed to be 5 minutes, therefore the intensity of the light source was measured at times of 0, 1.66 and 3.33 minutes for paths 1 – 3 through the reference phantom. Time equal to 0 is the starting point of the scan and is either 0 or 2 hours for the unstable and stable measurement respectively. For the measurements through the data phantom, the initial intensity was calculated at times 5, 6.66 and 7.33 minutes after t = 0. These initial intensities were then used in conjunction with the attenuation of the medium to calculate the measured intensity after the light passes through the dosimeter. The decrease in red light intensity from section 4.3 was used to calculate the light intensity along each path. The light intensity (in arbitrary units) was

normalised to the intensity along the first path length in the reference phantom. Optical density and uncertainty were calculated as per the method in section 3.3. Table 4-5 shows a large variation in optical density measured for a changing light source relative to the variation of optical density observed for a stable light source. This theoretical example shows how the noise increases due to a changing light source as observed in the uniform profiles.

Table 4-5: Reference and Data light intensities and the calculated optical density. The light intensity of the red LED at 2 hours was used for the stable calculations, whilst the light intensity after initially activating the light source was used for the changing light source. The variance in the optical density for the changing light source leads to an increased amount of noise in the reconstructed image.

Position	***Stable Light Source***			***Changing light source***		
	Ref Intensity (I_0)	Data Intensity (I)	OD	Ref Intensity (I_0)	Data Intensity (I)	OD
1	100	60.65	0.607	100	58.4	0.584
2	100	60.64	0.606	97.9	58.1	0.593
3	99.99	60.64	0.606	96.9	57.8	0.596
Range	0.01	0.01	0.001	3.1	0.6	0.012

4.5 Charge Integration and the Reciprocity Law

The optical density equation defined in this thesis (see section 3.3) relies on a linear response of the CCD to light intensity. However, the opto-electronic conversion taking place in a CCD response is related to the spectral exposure, $H(\lambda)$, which is a measure of the exposure at a given wavelength[165]. The spectral exposure is proportional to the spectral radiance, $L_e(\lambda)$, charge integration time, t, and inversely proportional to the square of the aperture size, N. The spectral radiance is a measure of light intensity at a certain wavelength[165]. The spectral exposure is shown in equation 16, where k is a factor used to account for the effective or irradiated sensor area, lateral magnification and spectral transmittance of the zoom lens as well as the spectral transmittance of the atmosphere[165].

$$H(\lambda) = \frac{kL_e(\lambda)t}{N^2} \qquad (16)$$

The intensity of light transmitted through a dosimeter is related to the exposure by keeping the time and aperture size constant during a measurement[165].

The objective of this section was to measure a range of pixel values where the CCD response is proportional to light intensity and therefore the method for calculating optical density was valid. The CCD response was measured in a projection image as a pixel value which has arbitrary units.

Evaluation of the CCD response to light intensity would ideally use a method that varies the light intensity incident on the CCD whilst keeping the charge integration time and aperture size constant. In practice this method is not simple, and methods of varying the light intensity introduce additional uncertainties. For example, inserting absorbers such as neutral density filters introduces uncertainties associated with the absorption coefficient, thickness and spectral response of the neutral density filter itself.

From equation 16 it can be observed that the exposure can be changed by varying the charge integration time and keeping the spectral radiance and aperture size constant.

Using equation 16, if the spectral exposures are equal, $H_1(\lambda) = H_2(\lambda)$, then:

$$L_{e_1} = mL_{e_2}\,, \quad m = \left(\frac{N_2}{N_1}\right)^2 \frac{t_1}{t_2} \qquad (\ 17\ )$$

Equation 17 shows that if the constant (m) is not equal to 1, then the same spectral exposure can be measured for different spectral radiance, provided the aperture size and charge integration time between the two exposures is changed. This is known as the reciprocity law and has previously been validated for CCDs[165]. The electronic shutter time offset controlled the method for determining the actual shutter time. The method for calculating the actual shutter time for the CCD used in the scanner could not be determined from the manufacturer's specifications.

The reciprocity law was used in this work by varying the charge integration time and keeping the aperture size and light intensity constant. Therefore, a change in the charge integration time should result in a proportional change in the CCD pixel value. A non-proportional change in the pixel value is a result of the CCD not collecting a proportional amount of charge relative to the change in charge integration time. A non-proportional response limits the dynamic range of the CCD, therefore limiting the optical density range that can be measured. Mullikin et al[152] have previously used the charge integration time to characterise the photometric response of CCDs.

4.5.1 Method

Projection images were acquired from Vista™ Scan for charge integration period between 0.0 and 85.9 ms. The specimen tank was left empty and the scanner was allowed > 2 hours to warm up to allow stabilisation of the light source intensity. The gain of the CCD was set to 0. The red light source was used in the investigation. A dark image was acquired with the LED light switched off and subsequently subtracted from all data projections before analysis. The mean and standard deviation of a 10 x 10 region of interest (ROI) in the centre of the projection was measured using ImageJ. The area of the ROI was chosen so as to represent an averaging of pixel values as part of the reconstruction process and is approximately equivalent in size to the ROI used by Olding et al[133] for a similar measurement. The position of the ROI in the projection image represents a light path along the central axis.

Pixel values were used as a measure of the exposure. They were unsigned 16 bit integer greyscale values and were measured from projection images obtained from the Dragonfly 2 DR2-HIBW camera (Point Grey Research Inc., Richmond, BC, Canada) using a ICX204 CCD chip (Sony Corporation, Japan). Therefore a value of 0 (Black) is the minimum and 65535 (white) is the maximum greyscale value. The exposure of the CCD was controlled by the charge integration period or "shutter time" of the CCD. The "shutter time" is a software control setting that defines the integration time of the collected charge before the CCD pixels discharge during readout and is named after the analogous function in a conventional camera that controls film exposure time with a physical shutter.

4.5.2 CCD Response

A linear CCD response to charge integration time was observed in the pixel value range between 0 and ~64000 a.u (Figure 4-8). The maximum value was limited to 64000 a.u because some pixels in the ROI saturate at longer charge integration times, which caused a deviation from a linear response. Uncertainty in the pixel value was calculated via the method described in section 3.3. The error bars represent a ±1 standard deviation around the mean value.

Magnifications of the region below 20000 a.u and above 60000 a.u are used to show changes from linearity (Figure 4-8 B and C respectively).

A linear fit was applied between 0 – 64000 with the coefficient of determination equal to 0.994. The equation used was 966.7t + 1034.6, where t is the integration time. A non-linear fit was also applied ($at^2 + bt + c$), with the a, b and c coefficients equal to -1.6, 1074.7 and 62.7 respectively and t defined as above. The coefficient of determination for the non-linear fit was 1.

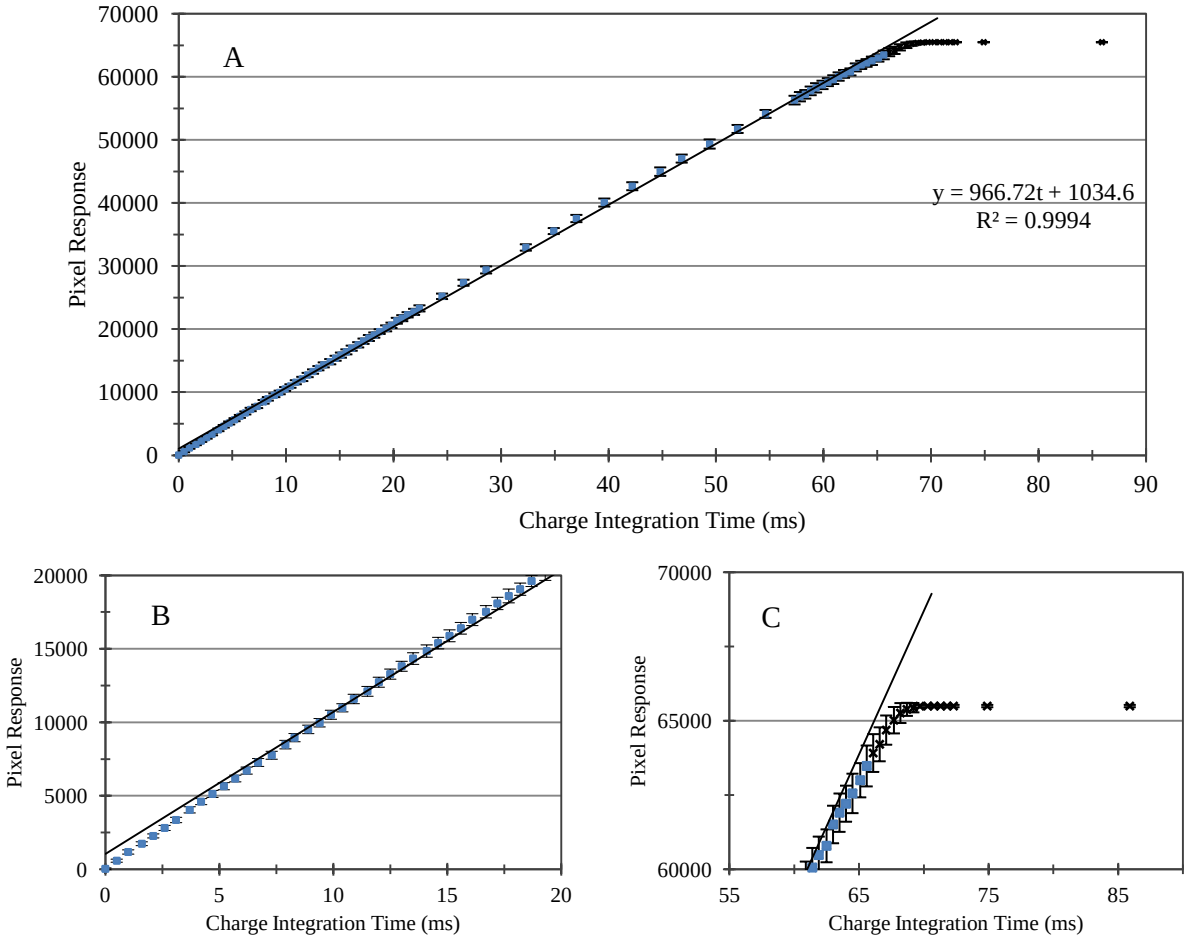

Figure 4-8: A) The mean pixel response of the 10 x 10 pixel ROI with various charge integration times. A line of best fit was fitted to the pixel response between charge integration times of 0 and ~65 ms. The coefficient of determination (R^2) was 0.9994. The black crosses represent CCD pixel values that were not included in the calculation of the linear fit. The error bars represent a ±1 standard deviation uncertainty, which was calculated from the standard deviation of the pixel values in each ROI . B) Data from part A below pixel values of 20000 a.u. C) Data from part A above 60000 a.u. In both B and C the linear fit from A is plotted. The linear fit demonstrates the deviation from linearity observed for pixel values below ~5000 and above ~64000.

4.5.3 Discussion

The results indicate that the response of the CCD is approximately linear with charge integration time. Thus, by the reciprocity law, the CCD response is linear with light intensity. However, the CCD response is not *perfectly* linear and therefore different initial light intensities through a dosimeter will result in a different measured optical density. An investigation of the uniformity of a reconstructed phantom with different acquisition settings is presented in section 4.6.

Both the linear and polynomial curves of best fit show a high linear correlation. The linear fit has a high coefficient of determination indicating a highly linear relationship. The polynomial fit has a R^2 value of 1, and a very small non-linear term (-1.6). The small non-linear term indicates the CCD response to light intensity is highly linear.

Deviation from linearity was observed below ~5000 a.u and above ~64000 a.u. The slight non-linearity observed at low and high light intensities (Figure 4-8 B and C respectively) was due to the charge generated in the CCD not being proportional to the light incident on the CCD. A linear fit between 5000 and 64000 gives an equation of 959.2t + 1385, where t is the charge integration time, and a coefficient of determination of 0.9995. The fit of this trend line for this region shows a slight improvement in linearity of the CCD response to charge integration time, but the response is still not perfectly linear.

Olding et al[133] measured the linearity of response for a different CCD. A departure from linearity was indicated for pixel values below 10 % of the camera full scale intensity. This departure from linearity was at a similar level to the departure observed in the CCD measured in this work.

CCD response to light intensity has only been tested for this type of CCD and should be independently verified for each CCD.

4.6 Influence of Non-linearity of CCD Response to Exposure on the Attenuation Coefficient

The calculation of attenuation coefficients relies on the linear response of the CCD to light intensity. As observed in section 4.5, the CCD response was approximately linear for the pixel values between ~5000 and 64000. If the response was perfectly linear, then the initial intensity (I_0 in section 3.3) should not influence the reconstructed attenuation of a uniform phantom. This is because according to the definition of optical density a change caused by an attenuating material will be the same irrespective of the magnitude of the initial intensity. The slight non-linearity of the CCD response will influence the reconstructed attenuation coefficient. The objective of this section was to determine the influence of non-linear response on the reconstructed attenuation coefficient.

4.6.1 Method

The uniform phantom used in section 4.4 (water and dye solution, fractional dye concentration 1 x 10^{-5} %) was scanned with varying initial (I_0) maximum pixel values. Because the uniform phantom

will provide constant attenuation, the reconstructed image should be the same if the CCD response is linear. Profiles were measured across the reconstructed phantom using the same method as described in section 4.4 (10 profiles across the diameter of a phantom per slice, total of 10 slices, all averaged together). Similar to section 4.4, only the central part of the phantom was investigated to eliminate errors due to container walls and small numbers outside the container.

The exposure was controlled by the charge integration time of the CCD. Projection images were acquired at charge integration times ranging between 10 – 65 ms. As described in section 4.5, the charge integration time controls the exposure of the CCD provided light intensity and aperture size is kept constant. The reciprocity law shows that this technique will measure an equivalent exposure to the value measured when light intensity is changed and the charge integration time and aperture size are kept constant. If the CCD response to light intensity is not linear, then the reconstructed images acquired with different initial intensities will not be the same.

4.6.2 Results

Figure 4-9 shows a number of profiles measured from a reconstructed uniform phantom, which was scanned at different charge integration times. The mean attenuation coefficient and standard deviation calculated from the voxels in the region between -75 and 75 around the central axis are shown in Table 4-6.

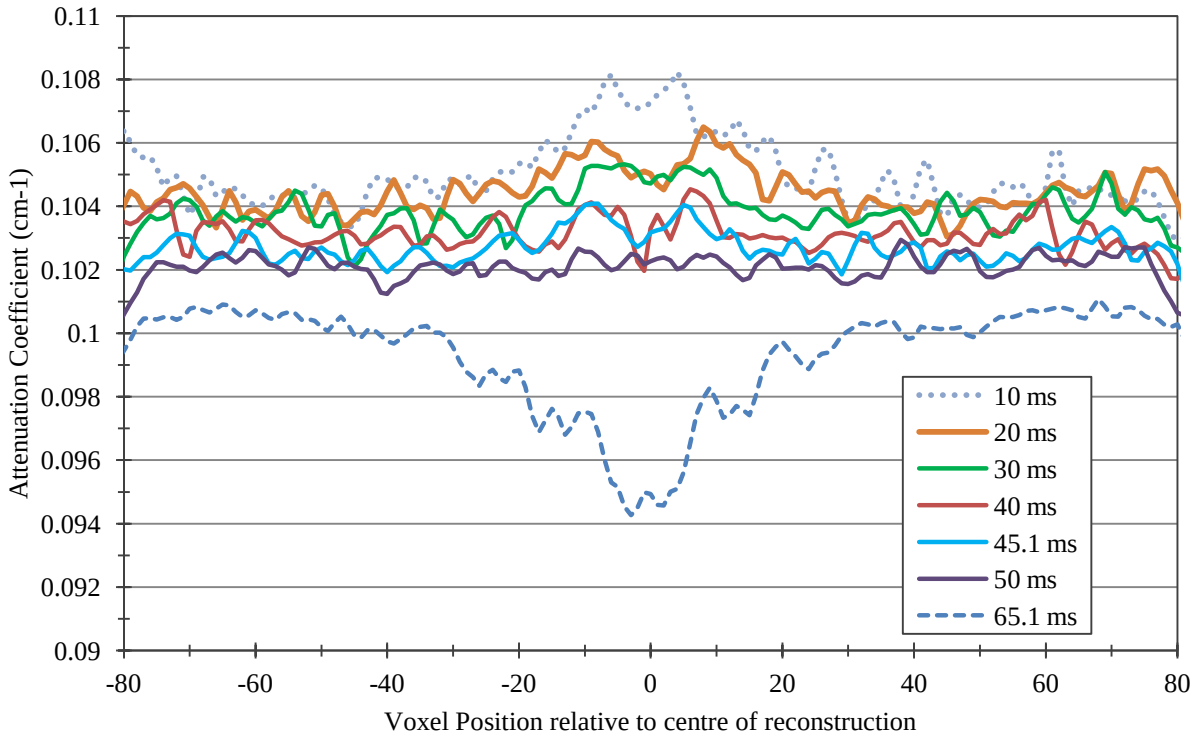

Figure 4-9: Variation in profiles measured in a uniform phantom with reference and data scans acquired at different charge integration times. The measured profile for 65 ms exhibits saturation artefacts which cause the dip in the centre of the profile. The profiles measured from volumes reconstructed using projection images acquired using charge integration times of 40, 45 and 50 ms were uniform within ± 1 % of the mean value. For profiles measured with shorter charge integration times (10 – 30 ms) the profiles indicate a less accurate and nosier reconstruction. The 10 ms profile shows a significant rise in the central region.

Table 4-6: Mean and standard deviation of profiles acquired with varying charge integration times. The profiles were acquired across the central -80 to +80 pixels of a uniform absorbing phantom.

Charge integration time (ms)	*Mean (cm^{-1})*	*Standard Deviation (cm^{-1})*
10	0.105	0.001
20	0.1045	0.0007
30	0.1039	0.0007
40	0.1032	0.0005
45.1	0.1027	0.0005
50	0.1022	0.0003
65.1	0.099	0.002

4.6.3 Discussion

The profiles indicate that the uniformity of volumes reconstructed from projection images acquired with charge integration times of 40, 45.1 and 50 ms were similar in magnitude and standard deviation. The measured attenuation increases as the charge integration time decreases due to the non-linear response of the CCD (measured in section 4.5). Due to the slight curvature of the response, measuring the same amount of attenuation with different initial pixel values will result in a slightly higher or lower attenuation coefficient observed for the 10, 20 and 30 ms (higher) and 65.1 ms (lower) profiles.

The measured attenuation rises in the centre relative to the outer regions for the 10 and 20 ms profile. This is due to the longer path length through the central region of the phantom causing the measured pixel value to be lower than the region for which linearity between the light intensity and CCD response is measured (below ~5000 a.u.). The pixels toward the edge of the phantom have a shorter pathlength and therefore have a higher light intensity relative to the central pixels. This rise also causes the standard deviation of the voxel attenuation coefficient to be larger relative to the 40, 45.1 and 50 ms measurements.

The drop in attenuation in the central region for the 65 ms reconstruction was due to the very high pixel values in the original reference (I_0) projections. The pixel values were above 64 000 a.u where deviation from linearity of the CCD response to light intensity has previously been observed (see section 4.5). The very high pixels combined with the non-linear response results in a lower calculated optical density. The path length through the centre of the phantom magnifies the influence of the curvature in the CCD response. Therefore, the optimal integration time for this sample can be seen to be 50 ms. This example demonstrates that integration time can be selected for individual samples to provide optimum linearity, uniformity and reduced noise.

4.7 PORP Baseline Attenuation Coefficients

The PORPs were used in 2D projections and 3D reconstructions to measure the range of measurable attenuation coefficients (see section 3.2.1 for details on the PORPs). Reference attenuation coefficients

of the PORPs were measured here to evaluate the accuracy of coefficients measured later from projections and reconstructions. The reference attenuation coefficients were measured in the cone beam optical CT scanner with a collimated window size of ~1 cm2. The collimated geometry served to reduce the scattered light. This was critical due to the PORPs not having an optically flat surface – i.e. the surface of the PORP was not flat within 1 wavelength of the light source. A non-flat surface will affect the refraction and reflection of the light rays through the phantoms. Positioning the PORPs in the low scatter geometry shown in Figure 4-10 will reduce the error introduced by a non-flat surface.

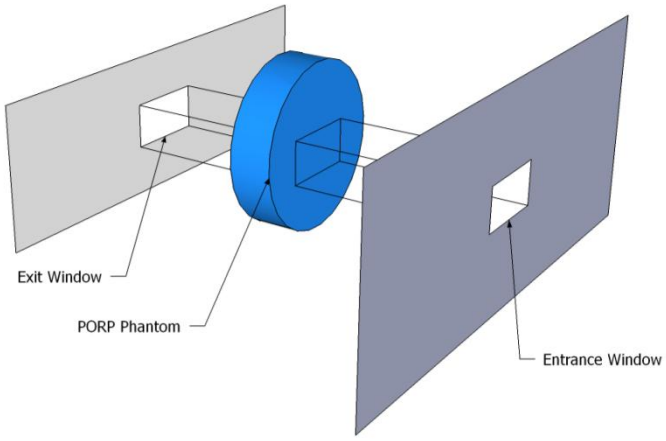

Figure 4-10: Low scatter geometry. The light path was along cylindrical axis of a PORP. The small entrance and exit window were used to collimate the light. The PORP was measured along the cylindrical axis to simplify the light path through the PORP to a single distance.

4.7.1 Characterisation Method

The measurement technique uses the ratio of light intensity through tinted and untinted PORPs to calculate the optical density, which is divided by the path length to calculate the attenuation coefficient. The attenuation coefficients and uncertainty were calculated via equations 4, 5 and 8 in section 3.3. The reference intensity projection (I_0 in equation 4) was measured through an untinted phantom. The intensity projection (I in equation 4) was measured for each individual PORP to calculate the attenuation coefficient relative to the reference. Images acquired from the CCD with the light source turned off were used as background noise images and were subtracted from both the I_0 and I projection images before the optical density was calculated. Both light sources were used to characterise the PORPs as the attenuation coefficients for orange and red light are expected to be different.

The light intensity was measured by collimating the light entering and exiting the specimen tank using black cardboard with a 1 cm^2 hole cut in the centre. The dynamic pixel value range of the scanner was adjusted by reducing the gain and exposure to minimum values, and adjusting the shutter time so that the mean pixel value through the reference PORP was ~62000 a.u for the red light. For the orange light source, the shutter time was adjusted to the maximum time, but the maximum pixel value achievable (~50000 a.u) was less than the desired value. As shown in section 4.5, a pixel value of

~64000 a.u was desired as the maximum pixel value because this value will provide the largest range of pixel values with a high level of linearity with light intensity. Using a lower maximum pixel value limits the maximum attenuation coefficient that can be measured. The cylindrical axis of each PORP was aligned with the light path so that the length was constant. Figure 4-10 shows the setup of the PORP in the scanner.

ImageJ was used to measure the light intensity through each PORP after subtracting a dark image. The dark image was a CCD image without a light source turned on. This image serves to capture some random fluctuations in the CCD. The total area across the 1 cm^2 window was used to determine the measured light intensity through the PORPs (see Figure 4-11 A). This technique was used because the PORPs are not purely absorbing and some scatter occurs, which causes a doming of a profile across the window. Figure 4-11 B shows the doming for 3 of the profiles across different PORPs and highlights how positioning of a small region of interest could influence measurements. Since the transmitted light intensity will be a convolution of a transmission and a scattering profile, calculating the total integral of measured intensity in a region of interest encompassing the whole window will be more conserving of the transmitted light and less sensitive to scattered light. Positioning and size of the pixel region (70 x 65 $pixel^2$) was kept consistent for light intensity measurements and was used to calculate the total integral of measured intensity.

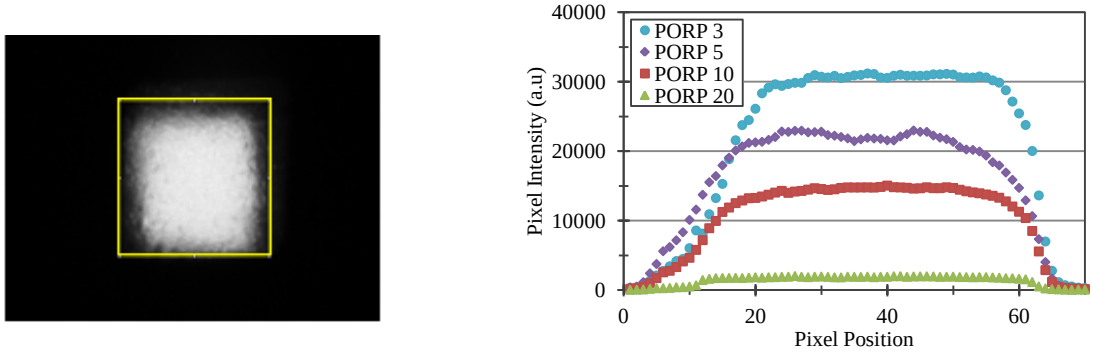

A B

Figure 4-11: A) Area used to measure the total integral of measured light intensity. B) Pixel response across the opening for four PORPs with different attenuation coefficients. The difference in the curvature highlights the influence of scattered light on the measured light intensity.

The scanner was allowed > 2 hours to warm up to account for light intensity fluctuations during warm up of the scanner (see section 4.3).

The reproducibility of the attenuation coefficients, and hence the stability of the PORPs, was evaluated using the red light source over a 3 year period. The 2009 attenuation coefficient data was acquired with a larger field size (2 x 2 cm^2) and as such required a larger region of interest during analysis (120 x 120 $pixel^2$).

The measurement of the PORP attenuation coefficient in the scanner using a collimated window was selected for use instead of a spectrophotometer because, as shown in section 4.2, dosimeter attenuation

and CCD response has a dependence on wavelength of light. The spectrophotometer's light source would not match the light source inherent in the scanner and could introduce uncertainty in the attenuation coefficient due to different spectra between the two systems. Using the scanner's light sources to measure the attenuation coefficient of the PORPs will avoid uncertainty introduced by differences in spectra.

The uncertainty in the methodology was investigated by 2 separate measurements:

1. Light intensity has been observed to vary slowly over a long period of time after the initial warm up of the scanner was completed[82]. The influence of a slowly varying light intensity was investigated by placing the untinted PORP in the scanner and acquiring projections every five minutes for 30 minutes without moving the PORP. 30 minutes was chosen because this was the time required to measure the light intensity through the remaining PORPs.
2. The consistency of the positioning of the PORP (in particular the alignment of the cylindrical axis to the light path) was evaluated by repeating the untinted PORP measurement after every 5th light intensity measurement through a tinted PORP (total number of repeats 5 over the course of the measurement).

For both uncertainty measurements, the mean and standard deviation was calculated.

4.7.2 Baseline Attenuation Coefficients

The attenuation coefficient of each PORP, for both light sources, is shown in Figure 4-12. The first PORP is not plotted as this is the untinted reference PORP and by definition has an attenuation coefficient of 0. The range of attenuation coefficients was between 0 and 1.8 cm^{-1} for the orange light source. For the red light source, the range of attenuation coefficients was between 0 and 1.5 cm^{-1}. These attenuation coefficients were measured in 2012.

Attenuation coefficients acquired using the red light source in 2009 were plotted to show the consistency of the measured attenuation coefficient over a long period of time. The coefficient for PORP number 20 was not plotted due to the data not being acquired. The results show an agreement within ± 8.0 % in the attenuation coefficient range between 0.2 – 1.25 cm^{-1} (PORPS 5 – 18), except for PORPs 5, 12 and 13 (0.22, 0.53, 0.57 cm^{-1} respectively). PORPs with an attenuation coefficient below 0.2 cm^{-1} (PORPs 2 – 4) and above 1.29 cm^{-1} (PORP 19) show differences greater than ± 8.0 %.

The mean integrated intensity for seven measurements over 30 minutes exhibited a standard deviation of ± 0.7 % (data not shown here). The variation in the total integrated value was not systematic.

The mean integrated intensity measured through the untinted PORP after every five tinted PORPs exhibited standard deviations of ± 2.7 % and ± 3.7 % for the orange and red light source respectively This is a much large contribution to uncertainty than time dependence alone.

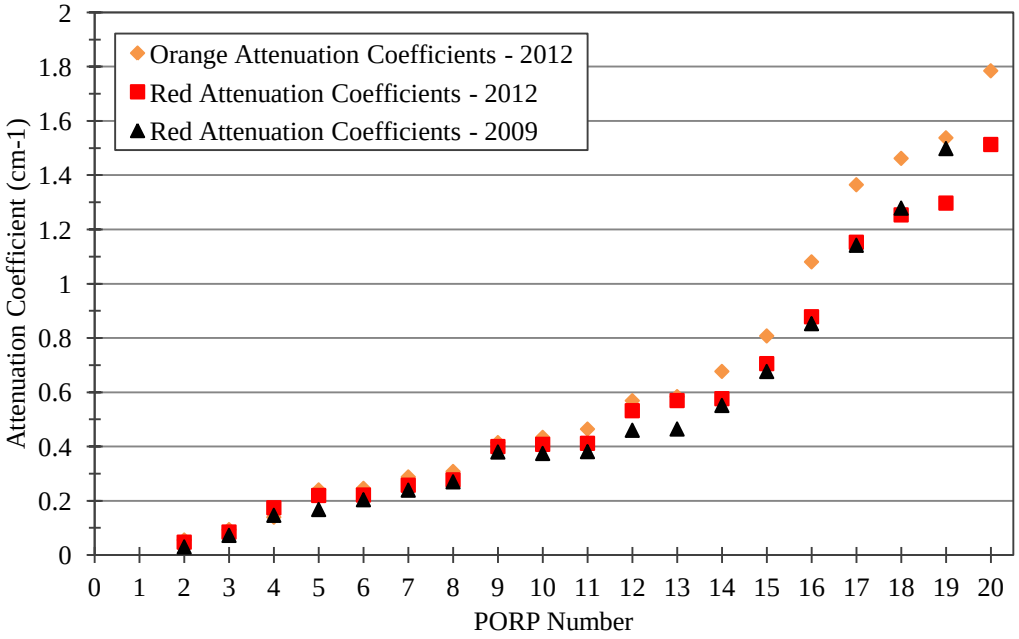

Figure 4-12: Orange and Red attenuation coefficients measured in parallel beam geometry. The Red light data from 2009 does not contain information on PORP number 20. PORP number 1 is not plotted because the phantom was untinted and acted as a reference for the measurement of the other PORP's attenuation coefficient.

4.7.3 Discussion

The baseline attenuation coefficients of the PORPs for both light sources was used to compare attenuation coefficients measured from 2D projections and in 3D reconstructions. The attenuation coefficient of each PORP is expected to be different for the orange and red light source due to a dependence on wavelength of the PORP's absorption coefficient.

The reproducibility of the red attenuation coefficients was within ± 8.0 % over the attenuation coefficient range of 0.2 – 1.25 cm^{-1}. An uncertainty of ± 8.0 % is approximately equal to the positioning uncertainty which will be discussed below. The difference between the 2009 and 2012 attenuation coefficients measured for PORPs 5, 12 and 13 could potentially have been influenced by scratches and bubbles affecting the uniformity of the PORP's, which would affect the measured light intensity through the PORPs. Eliminating non-uniformities could reduce the variation observed between the 2009 and 2012 attenuation coefficients. The difference between the attenuation coefficients measured in 2009 and 2012 for PORPs 2 - 4 was also very high. This discrepancy is due to the very small numbers being compared (e.g. 0.03 to 0.04 for PORP 2) and therefore a small difference has a large percentage difference.

The use of maximum pixel intensity level of ~50000 for the orange light source will not affect the measured attenuation coefficients because the intensity is within the linear range of the CCD response. However, limiting of the maximum pixel value will influence the maximum optical density that can be measured. Therefore, to use the full dynamic range of the CCD, the shutter speed should be set to give a value of ~64000 (see section 4.5).

The measured variation in light intensity with time will affect the uncertainty in the measured values. However, the greatest contribution to uncertainty will come from the positioning of the PORP. It should be noted that due to the long period of time required to measure positioning uncertainty, the variation in light intensity could influence these values. The large uncertainty caused by positioning could be corrected by using a more robust positioning device.

Using a more robust position device and eliminating non-uniformities in the PORPs could reduce the uncertainty in the measured attenuation coefficient toward the level of uncertainty introduced by the light intensity variation (± 0.7 %).

4.8 Summary of the Investigations

The measured peak wavelengths for the unfiltered orange and red light sources were 597 and 642 nm. When the filters were added, the peaks changed to 595 and 635 nm respectively. The change in peak wavelength reduced the uncertainty of the measured attenuation for PRESAGE^{TM} with the red light source, whilst the uncertainty remained approximately constant for Fricke measured with the orange light. The addition of a filter caused the FWHM to narrow from 18.5 to 11 nm and 23 to 12 nm for the orange and red light sources respectively. The drop in light intensity associated with the addition of filters was not expected to significantly affect the measured attenuation accuracy because camera settings can be adjusted to compensate. The narrowing of the FWHM also reduced the change in attenuation across the spectrum of each light source. This reduces the influence of differential attenuation and therefore increases the accuracy.

The light source intensity was observed to decrease after switching on the light source due to the increase in temperature of the environment containing the LED. The rate of change in light source intensity decreased with time since activation. A warm-up time of 2 hours was required to reach stable output intensity for the orange and red light sources.

The variation of the light source intensity after switching the scanner on, was observed to cause a decrease in accuracy and increase in noise of the reconstructed uniformity if the warm-up time wasn't used.

The CCD response to charge integration time was almost linear. Reconstruction of a uniform phantom acquired at different charge integration times showed that the slight non-linearity observed would still influence the reconstructed attenuation coefficient. The measurement is only valid for this type of CCD and should be independently verified for different CCDs.

The measured attenuation coefficients for the individual PORPs were used as a reference to characterise the accuracy of the attenuation in both 2D projections and 3D reconstructions presented in chapters 5 and 6 respectively. For the orange and red light sources a range of 0 – 1.8 and 0 – 1.5 cm^{-1} respectively, was measured. The reproducibility of the PORP's attenuation coefficient over a three

year period using a red light source was ~8 %, but could have been influenced significantly by positioning of the PORPs. This accuracy would not be acceptable for long term scanner quality assurance, however the problem is most likely related to issues with the manufacturing of the PORPs. The results indicate the PORPs have potential as a long term quality assurance phantom provided improvements are made in the manufacturing process.

This chapter shows that attenuation coefficients can be influenced by the light source and filters, response of the CCD to the light source, linear response of the CCD to light intensity and time after switching on the scanner. Accuracy of the reconstructed attenuation coefficient was shown to improve via appropriate selection of the light source, filters and CCD, as well as adherence to warm up protocols. Improved accuracy in the reconstructed attenuation coefficient will result in improved accuracy and increased confidence in patient quality assurance results.

5. ASSESSMENT OF PROJECTIONS IN CONE BEAM OPTICAL CT

5.1 Introduction

The quality of the 3D data from an optical CT is dependent on reliable acquisition of 2D projections used to reconstruct the data. Therefore, an accurate, high spatial resolution, 2D measurement of the opacity change is required. Projection images could also be used for quality assurance (QA) measurements of different properties of the scanner. Their use for QA could potentially decrease the amount of time required for QA whilst improving the accuracy of the measurements. A comparison between parameters measured in 2D projections and 3D reconstructions is presented in the next chapter.

The aim of this chapter is to measure the 2D projection characteristics of the Vista™ Cone Beam Optical CT scanner (the scanner). This is achieved by characterising: i) the measurable optical density range, ii) spatial resolution of the projection images, iii) the effect of charge integration time on the spatial resolution, and iv) the influence stray light has on projection images.

PORPs were used to measure the absorption properties of the scanner. The PORPs were designed for use as a long term, stable, uniform phantom. Absorbance profiles from PORPs were compared to a uniform absorbing phantom made from a dye solution known to be a non-scattering absorber to determine if significant amounts of scattering were present and what effect this has on projection images.

For uniform phantoms, the attenuation coefficient can be determined from a single projection image if the path length through the sample is known. A comparison of attenuation coefficients measured in the reference geometry (see section 4.7), 2D projections and 3D reconstructed volumes (see next chapter), determines the accuracy of measured attenuation coefficients against known attenuation coefficients. This provides an opportunity to assess the usability of the projection in determining if a reconstruction will be accurate. For an irradiated sample with a more complex dose distribution, a quick check of the pixel values measured in a projection could determine if the opacity is either too high or low for an accurate measurement. In addition the potential use of 2D projection images as a fast constancy check of known attenuation coefficients was evaluated.

The ability of the scanner to measure large changes in a dose distribution over small distances can be characterised by the spatial resolution. The spatial resolution in 2D projections affects the reconstructed image and hence the reconstructed voxel size and shape[69]. Previous methods of quantifying spatial resolution in projection images have involved the use of high quality photographic test patterns[133]. In a cone beam geometry, the measured spatial resolution over the diameter of a

dosimeter is important in quantifying the maximum achievable resolution. Spatial resolution should be measured over the dosimeter diameter in both the parallel and perpendicular direction relative to the CCD – light source axis. This ensures the dosimeter is sampled with the required spatial resolution.

Increasing the total charge accumulated in a CCD pixel well can introduce blooming – i.e. an overflow of charge from a pixel into a neighbouring pixel[166]. The overflow could potentially influence the measured edge spread function across a sharp high contrast boundary, therefore affecting the spatial resolution. Measurements of the spatial resolution for different charge integration times were used to qualify the impact of blooming on the spatial resolution.

The influence scatter has on the projection image is also investigated. Artefacts caused by scattered light have previously been described in the literature (see section 2.4.3). 2D projection data is acquired in a cone beam geometry, which is more susceptible to scattered light relative to fan beam and laser-diode geometries (see section 2.3 for description of different geometries). To investigate the influence of scattered light on measured results, profiles were measured across phantoms for a full cone beam and a 'reduced scatter' geometry. The reduced scatter geometry approximates a fan beam geometry. This geometry uses collimation to prevent scattered light from reaching the detector.

Table 5-1: Measurements used to assess the projection from a cone beam optical CT scanner. These provide information on the presence of scattering in the PORPs, the measurable attenuation coefficient range, spatial resolution, the effect of charge overflow in the CCD on the spatial resolution and the influence of scatter on measurements.

Measurement	*Reason for measurement*
Scatter assessment of PORPs	• Determine suitability of PORPs for use as an absorbing phantom to characterise attenuation coefficient range
Attenuation Coefficient	• Measure the attenuation coefficient range of both Red and Orange light in 2D projection images. • Compare to reconstruction attenuation coefficient measurements
2D Spatial Resolution	• Measure the spatial accuracy of the projections • Compare to reconstruction spatial resolution measurements • Investigate the influence blooming has on the spatial resolution
Scatter artefacts in 2D projection	• Investigate the influence of scatter on the projection images

5.2 Assessment of Scattering in PORPs

Polyurethane opacity reference phantoms (PORPs) were described in section 3.2 and were characterised for individual attenuation coefficients in section 4.7 using a narrow beam geometry to constrain the path length through the sample. They were designed to be light absorbing quality assurance phantoms used to measure the reproducibility of attenuation coefficient measurements over time.

The objective of this section is to validate the PORPs as a non-scattering, uniform phantom. This was achieved by comparing the absorbance profiles of PORPs and blue dye phantoms acquired via projection images with modelled absorbance profiles assuming only absorption and no scattering.

Differences between absorbance profiles for non-scattering and scattering solutions have been previously observed with a flattening of the profiles observed for scattering phantoms[167]. The blue dye phantoms are absorbing solutions and serve as a baseline for validation of the model. PORPs with various uniform attenuation coefficients were measured to characterise the absorbance over the optical density range of the scanner.

5.2.1 Method

Reference and data projection images of blue dye comparison phantoms (herein known as the comparison phantoms) and four PORPs were acquired in the scanner. The reference phantoms for each phantom were a jar of water and a PORP with no tint respectively (Figure 3-4 shows the reference PORP). The comparison phantoms were described in section 3.2 and had blue dye fractional concentrations of $5.0\text{x}10^{-6}\pm8.0\text{x}10^{-8}$, $1.0\text{x}10^{-5}\pm1.6\text{x}10^{-7}$, $2.0\text{x}10^{-5}\pm3.2\text{x}10^{-7}$ and $3.5\text{x}10^{-5}\pm5.6\text{x}10^{-7}$ %. The baseline attenuation coefficients of the four PORPs were 0.042, 0.15, 0.24 and 0.38 cm^{-1} (measured in section 4.7). Projection images of the PORPs were acquired and absorbance profiles calculated via equation **Error! Reference source not found.**, where I_0 and I are the reference and data ixel values respectively.

$$A = -\ln\left(\frac{I}{I_0}\right) \qquad (18)$$

Image J was used to sample intensity profiles 10 pixels in height across the full projection image (i.e. the value at each position on the profile was an average of all 10 pixels at said position). All projections were acquired in a specimen tank filled with water. Red light was used and the scanner was allowed to warm up for 2+ hours to ensure a stable light intensity. An example of a projection image used to acquire profiles is shown in Figure 5-1. The example also shows causes of artefacts such as air bubbles and overlap (discussed in detail later).

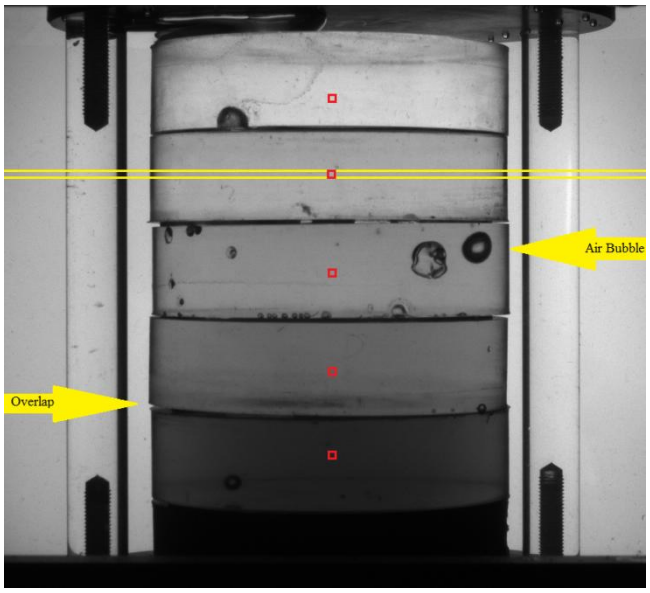

Figure 5-1: Projection image showing profile measurement across 2D projection (yellow lines) and example regions of interest (red squares). Profiles and ROIs were measured avoiding causes of artefacts such as air bubbles and overlap regions. The perspex rods at the side of the holder are also shown.

A model was developed using a method similar to Bosi et al[131]. The model assumed the phantoms were acquired using a parallel beam geometry and that the comparison phantom and the PORPs were positioned symmetrically around the centre of the projection image. The model used known diameters of the phantoms (comparison phantoms = 92 mm, PORPs = 78 mm). To convert the diameter into pixels, a conversion factor was used to scale the modelled diameter to the width of a phantom in the projection from which the profile was taken. Adjustment of this value was acceptable because the conversion factor varies with distance from the CCD camera and the focal plane does not necessarily coincide with the rotational axis. This will be discussed in further detail in section 5.4. The final values used in the model were 0.16 and 0.17 mm/pixel for the comparison phantoms and PORPs respectively.

The conversion factor was used to convert pixel position into distance, which was then used, in conjunction with the radius of the phantom, to calculate the half length of the chord. This relationship can be seen in Figure 5-2 where C is the chord length, d is the distance of the chord from the centre of the phantom and r is the radius of the phantom.

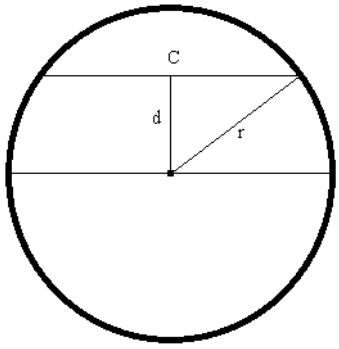

Figure 5-2: Chord calculation for use in absorbance model. C is the chord, d is the distance between the centre of the phantom and the chord and r is the radius of the phantom.

The chord length was used in equation 19 to calculate the absorbance along the chord where C(d) is the chord length at distance d from the centre of the phantom, A(d) is the absorbance along the chord path and μ is the absorbance in cm^{-1}.

$$A(d) = C(d)*\mu \qquad (19)$$

Absorbance values for the model were taken from measurements in section 4.7 for the PORPs, and by normalising to measured profiles for the comparison phantoms. For two of the PORPs a small adjustment of the attenuation coefficient was necessary to renormalise the profiles and enable comparison between modelled and measured curvatures. Table 5-2 shows the fractional concentration of the comparison phantoms and independently measured attenuation coefficients of the PORPs with the attenuation coefficient used in the model to adjust the profile to match the measured profile.

Table 5-2: Comparison phantoms and PORPs used to assess scattering and the attenuation coefficients used to model the phantom absorbance.

Phantom	*Concentration/Measured attenuation coefficient*	*Attenuation coefficient used in Model*
Comparison 1	$5.0x10^{-6}\pm8.0x10^{-8}$ %	0.045 cm^{-1}
Comparison 2	$1.0x10^{-5}\pm1.6x10^{-7}$ %	0.11 cm^{-1}
Comparison 3	$2.0x10^{-5}\pm3.2x10^{-7}$ %	0.21 cm^{-1}
Comparison 4	$3.5x10^{-5}\pm5.6x10^{-7}$ %	0.35 cm^{-1}
PORP 1	0.042 cm^{-1}	0.042 cm^{-1}
PORP 2	0.15 cm^{-1}	0.15 cm^{-1}
PORP 3	0.24 cm^{-1}	0.26 cm^{-1}
PORP 4	0.38 cm^{-1}	0.4 cm^{-1}

5.2.2 Results

Figure 5-3 A and B show the measured and modelled absorbance profiles for the comparison phantoms and PORPs respectively. The comparison phantoms were observed to have a similar curvature as the modelled absorbance. Some mismatch between the measured and modelled profile is observed at the edge of the comparison phantom. The PORPs have a similar curvature to the modelled absorbance in the centre of the phantom, however a mismatch between the modelled and measured profile was observed toward the edge of the PORP. A visual comparison of the noise in the profiles indicates that the PORPs are noisier relative to the comparison phantoms.

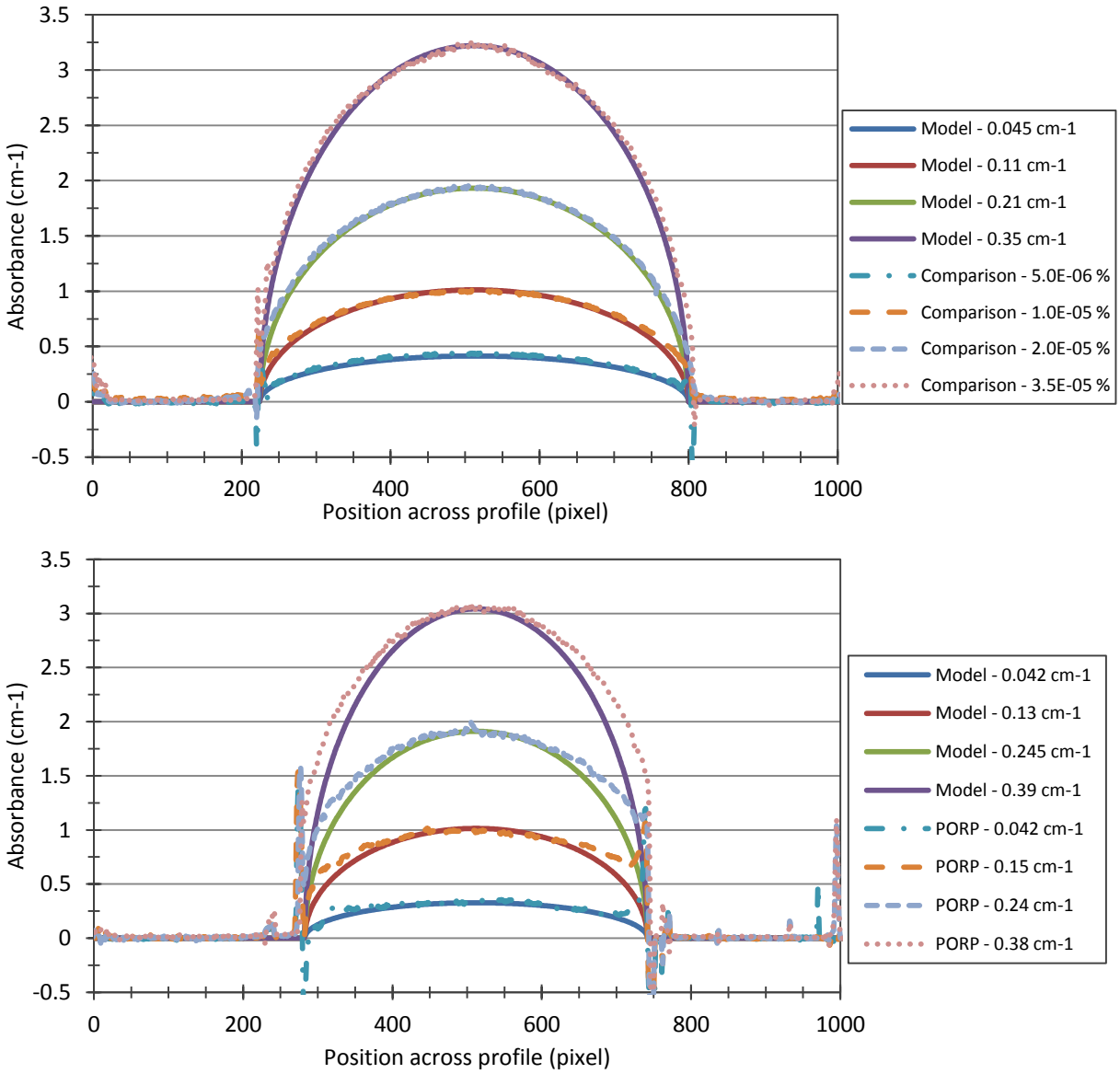

Figure 5-3: Measured and modelled profiles for comparison phantoms (A) and PORPs (B). Good agreement between the measured and modelled was observed for the comparison phantoms, whilst the PORPs were only in good agreement toward the centre of the phantom.

5.2.3 Discussion

The curvature of the absorbance profiles measured for the comparison phantoms is similar to the model with only small differences observed which are attributed to the assumption of parallel beam geometry. However, the differences are minor and the model is similar enough to illustrate the profile shape of a purely absorbing phantom. Differences at the edge of the container were most likely related to the relatively high amount of reflectance at the edge of the container caused by differences in the refractive index between the container wall and both the surrounding medium and the dyed liquid[63].

The curvature of the measured profiles from the PORPs is similar to the modelled curvature. However, wall artefacts were observed to be larger for the PORPs relative to the comparison phantoms and were

most likely due to a mis-match in refractive index between the PORPs and surrounding material. This mis-match has been shown to cause wall artefacts[63]. A flattening of the curvature of the measured relative to the modelled profiles has been linked to increased scatter[167]. If truly absorbing phantoms are needed, liquid dye should be used. As these may not be suitable as long term standards PORPS will need to be used. Measurements with the PORPs should be restricted to the central region where curvature differences are small. Alternatively, a refractive index matching solution should be used when acquiring the PORPs.

The amount of noise in the PORP profiles relative to the comparison phantoms could be caused by scattering from inhomogeneities in the PORPs. Attenuation coefficient measurements of the PORPs will be affected by this noise which could cause larger uncertainty in the measured coefficient. Limitations of the PORPs caused by non-uniformities were previously discussed in section 4.7.

Small peaks in absorbance were observed for the PORP measurements outside the actual phantom at pixel positions across the projection of ~250 and ~790. The small peaks in absorbance are due to the Perspex rods used in the PORP holder (observed in Figure 5-1). The peaks are not expected to affect the profiles measured in the projection images because the rods are to the side of phantom. However, in 3D measurements the rods may cause some artefacts.

The comparison phantoms and PORPs both exhibit an absorbance curvature similar to the model at the centre of the respective phantoms. As such, the PORPs can be used for future measurement of attenuation coefficients provided the attenuation coefficient is measured in the centre of the phantom.

5.3 Projection based Attenuation Coefficient Measurements

The cone beam geometry allows the sampling of multiple PORPs quickly. The projections could be used as a replacement for fully reconstructed volumes during quality assurance measurements. Measuring each PORP's attenuation coefficient in 2D projections could save time and potentially simplify the quality assurance process.

The attenuation coefficients of individual PORPs were measured in section 4.6 using a collimated beam geometry to provide a baseline value. Attenuation coefficients are measured here in the cone beam geometry and compared to the baseline measurements for accuracy and adverse effects due to sample curvature or off-central-axis measurement. Accuracy within 3 % relative to the baseline was used to determine a usable range of attenuation coefficients[67]. The cone beam geometry is used for routine evaluation of 3D dosimeters.

5.3.1 Acquisition of Attenuation Coefficients from a Projection

Reference (I_0) and data (I) projections were acquired and used to calculate the optical density for a total of 20 PORPs using both light sources (see section 3.3 for details on optical density and

attenuation coefficient calculations). Dark projections were subtracted from the reference and data images before the calculation. The scanner was given an appropriate amount of time to warm up. The CCD gain was minimised when collecting the projections. Shutter time was adjusted to provide a maximum pixel value of ~60000 a.u and ~55000 a.u for the orange and red light sources respectively. The camera shutter time was adjusted to limit the maximum pixel outside of the dosimeter to below the level of saturation. Saturation of the CCD pixels near the edge of a dosimeter could cause blooming toward the darker pixels inside the dosimeter (see section 5.5 for more detail on blooming). Limiting the pixel value measured outside the dosimeter has the unintended consequence of reducing the maximum pixel that can be measured at the centre of the dosimeter (normally the location of longest path length and highest attenuation). Reducing the maximum pixel limits the maximum attenuation coefficient that can be measured.

In the cone beam geometry five PORPs were stacked on top of each other and placed into the specimen tank filled with water for the data image. This set up is shown in Figure 5-1. The transmitted light intensity was measured through an untinted reference PORP with the same cylindrical length as a stack of five tinted PORPs.

Image J was used to calculate the mean pixel value and standard deviation of a region of interest (ROI) with an area of 100 pixels. Examples of the 5 ROIs in a projection image of a stack of PORPs is shown in Figure 5-1. The area of the ROI was placed in the centre of the PORP which was shown in section 5.2 to have a similar curvature of absorbance as modelled profiles and thus relatively unaffected by light scattering or mis-matches in refractive index between the PORPs and the surrounding medium. Additionally, this region minimised the curvature of the sample across the ROI and therefore the path length through the dosimeter was considered constant. The positioning of the ROI avoided air bubbles and overlap between adjacent PORPs, which were visible in the projection as a darker region between two lighter regions. Both the non-uniformities and overlap between PORPs are indicated by arrows in Figure 5-1. The ROI area was large enough to have confidence in the mean and standard deviation.

The optical density was measured in a path across the diameter of the disks and corrected for path length as per section 3.2.2. The path length through the phantom depends on position in the projection. Placement of the ROI at the centre of the rotational axis of the PORPs means that the diameter of the PORP (7.8 cm) can be used in the calculation of the path length in the cone beam geometry.

The position of the ROI centre relative to the pixel at the mid-point of the projection (384) was calculated. The height of the middle pixel in the projection is at the horizontal mid-plane of the cone beam geometry. The number of pixels per centimetre was calculated by measuring the number of pixels in a stack of 5 PORPs, which has a known height of 10 cm. Due to the cone beam geometry, the distance from the CCD to the point of measurement will change the number of pixels in a 10 cm distance. The highest and lowest part of the PORP in the image were easily identifiable (see lines in

Figure 5-4 A). Due to conebeam geometry, the highest and lowest part of the PORP were at the closest part of the PORP to the CCD. Since the PORPs were centred on the rotation axis, the radius of the PORP could be subtracted from the source to axis distance to calculate the distance between the CCD and the closest part of the PORPs. Trigonometry was used to calculate the angle of the light path from the CCD to the ROI relative to the central CCD to light source axis (Figure 5-4 B). This angle was then used, along with the diameter of the PORP to correct the path length through the PORP. The corrected path length was then used in the calculation of the attenuation coefficient.

The uncertainty in the attenuation coefficient was calculated by combining the uncertainty of the optical density and uncertainty of the path length through the dosimeter as described in section 3.3.

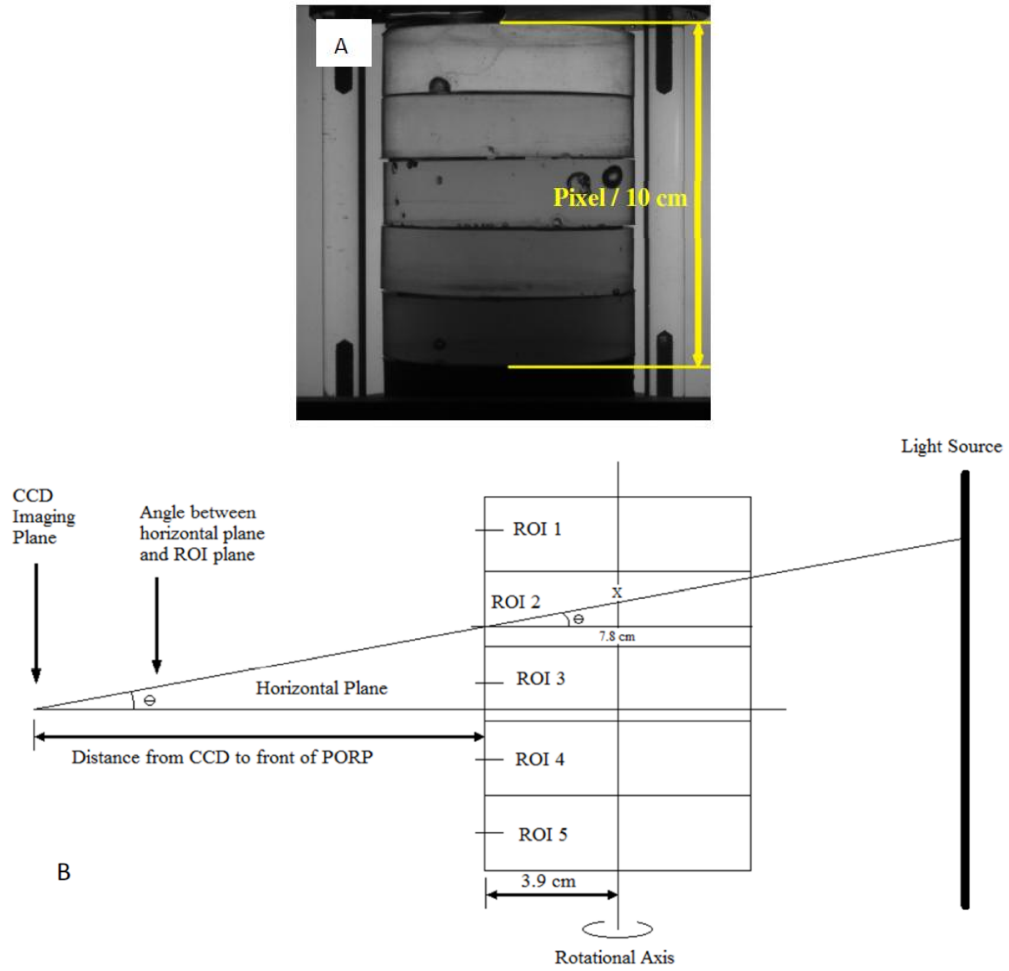

Figure 5-4: Calculation of the path length through the PORP. A) Measuring the pixels per centimetre at the front face of the PORP. This is used to calculate the distance between the horizontal plane and the middle of the ROI, which in turn can be used to calculate the pathlength through the PORP based on the diameter of the PORP (B).

5.3.2 Results

Figure 5-5 shows the attenuation coefficients measured in the cone beam geometry compared to the baseline values measured previously in the parallel beam geometry (Section 4.6). The line of identity represents perfect agreement between attenuation coefficients in the cone beam geometry relative to

the parallel beam geometry. A high level of agreement can be observed in the range between 0 – 0.53 cm^{-1} and 0 – 0.45 cm^{-1} for the orange and red light sources respectively.

Saturation of the CCD response causes a deviation from the line of identity above approximately 0.55 cm^{-1} and 0.45 for the orange and red light sources respectively. Maximum values of attenuation were measured at 0.7 and 0.6 cm^{-1} for the orange and red light sources respectively.

The uncertainty in the measured attenuation coefficient, calculated as per the method in section 3.3, was observed to increase as the PORP opacity increased.

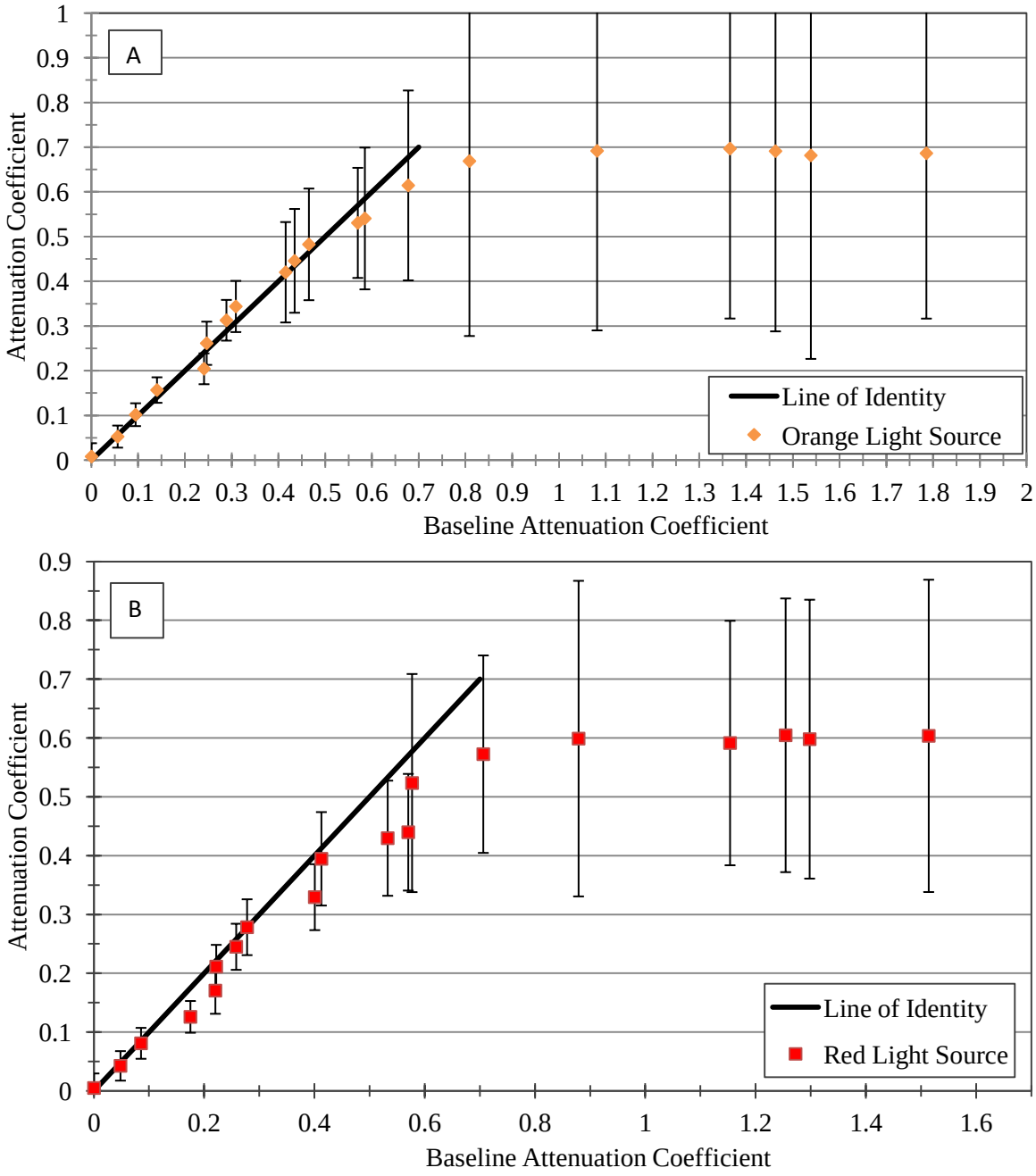

Figure 5-5: Comparison between reference and cone-beam attenuation coefficients measured with the A) Orange light source and B) Red light source. For the orange light source (A) the line of identity indicates accuracy between the baseline and measured attenuation coefficients between 0 – 0.5 cm^{-1}. For the red light source (B) the line of identity indicates accuracy between 0 – 0.45 cm^{-1}. The error bars were based on ± 1 standard deviation calculated as per the method in section 3.3.

5.3.3 Discussion

The line of identity indicates the measured attenuation coefficients are accurate compared to the baseline values up until ~0.53 and ~0.45 cm^{-1} for orange and red light respectively. The deviations from the line of identity for the orange and red light sources were due to non-uniformities in the PORPs.

Saturation of the attenuation coefficient occurred at ~0.55 and ~0.45 for the orange and red light sources respectively. These values were measured using 7.8 cm diameter phantoms. Therefore across a 1 cm path length the maximum attenuation coefficients measurable, before saturation affects the accuracy, is 4.1 and 3.5 cm^{-1} for the orange and red light sources respectively. This is only valid if no other attenuation occurs along the path between the light source and the CCD. The values are the maximum net OD measurable in the scanner.

The differences in accuracy observed for the orange light source at low attenuation coefficients were due to a small difference between the measured and baseline attenuation coefficient resulting in a large percentage difference because the measured attenuation is very small.

Saturation of both the orange and red attenuation curves is caused by the measured charge at the CCD being low for highly attenuating PORPs. When the measured charge is in the same order of magnitude as the CCD's inherent noise, increasing the attenuation coefficient will not result in a decrease in measured charge. Therefore, the calculated optical density (I/I_0) will be the same even with increasing attenuation resulting in a saturation of the attenuation curves as observed in Figure 5-5.

The difference in the saturation point for the orange and red light sources was caused by the absolute level of light transmitted through the PORP, being a different fractional amount relative to the absolute level of light transmitted through the reference PORP. A higher transmittance of light through the reference PORP results in larger dynamic range of measurable attenuation coefficients. Section 4.5 showed the maximum pixel value should be limited to ~64000 a.u. The maximum pixel value will predominately be at the edge of the dosimeter with lower pixel values measured in the centre of the dosimeter, due to the longer path length which attenuates light through the dosimeter. This restricts the pixel value in the centre of the dosimeter which limits the range of optical densities that can be measured. Increasing the shutter time to increase the light detected through the middle of the dosimeter can have adverse effects. Whilst increasing the shutter time will increase the reference projection's pixel value, and therefore increases the range of optical densities measurable, the drawback is that the collected charge in the open field can be very high and 'blooming' or an overflow of the CCD elements can occur[140]. Consequently, the exposure of the dosimeter to radiation will need to be scaled to provide an opacity range consistent with the attenuation coefficient range of the scanner.

A comparison of the attenuation coefficients from 2D projection and 3D reconstructions will be presented as part of the discussion in the next chapter.

5.4 Projection based Spatial Resolution

Measured dose distributions using 3D dosimeters will predominately have large dose gradients over small distances. Therefore, 3D dosimetry requires a high resolution evaluation of the dosimeter[67].

Spatial resolution is a measure of the ability to distinguish high contrast edges. This is important because it characterises an optical CT scanner's ability to measure changes in the dose distribution.

Spatial resolution has been measured previously in the literature, for a range of different types of scanners, using projections[115,119,133] and 3D reconstructions[37,63,145,168]. The advantages of projection based measurements include being able to measure over a depth of field in the scanner and the measurement is relatively quick. However, a projection measurement does not sample the reconstructed image and therefore does not take into account pixel binning and the corrections applied by filters during the reconstruction process.

The achievable spatial resolution is also dependent on CCD model, aperture settings and the alignment of the dosimeter rotation axis with the central pixel on the projection image (see section 2.5). Since a large number of different combinations of the above factors are possible, the spatial resolution requires measurement for each individual scanner. The CCD model used for this work was the Sony CCD Model Number ICX204AL and was described in section 3.1.

The objective of this section is to characterise the projections' spatial resolution in 3 planes. Each plane was a different distance from the CCD and orientated perpendicular to the light source to CCD axis. The measurement positions in each of the 3 planes cover the diameter of the dosimeter in the direction perpendicular to the light source to CCD axis. This establishes the spatial resolution at different positions over the depth of field required for reconstruction of a 3D dosimeter. These measurement positions are required because as shown in Figure 5-6, a VOI radially distant from the centre of the reconstruction axis is sampled with a varying spatial resolution dependent on the distance from the CCD imaging plane to the point of interest.

Oldham et al[67] suggested a criterion of less than 1 mm^3 for spatial resolution. Therefore, in a projection image, the modulation is required to be greater than 50 % at a line pairs per millimetre value of 1 to satisfy the sub-mm criterion. The 50 % modulation value is commonly used to define the spatial resolution and is the spatial frequency at which the measured contrast between two objects decreases to 50 % of the actual contrast.

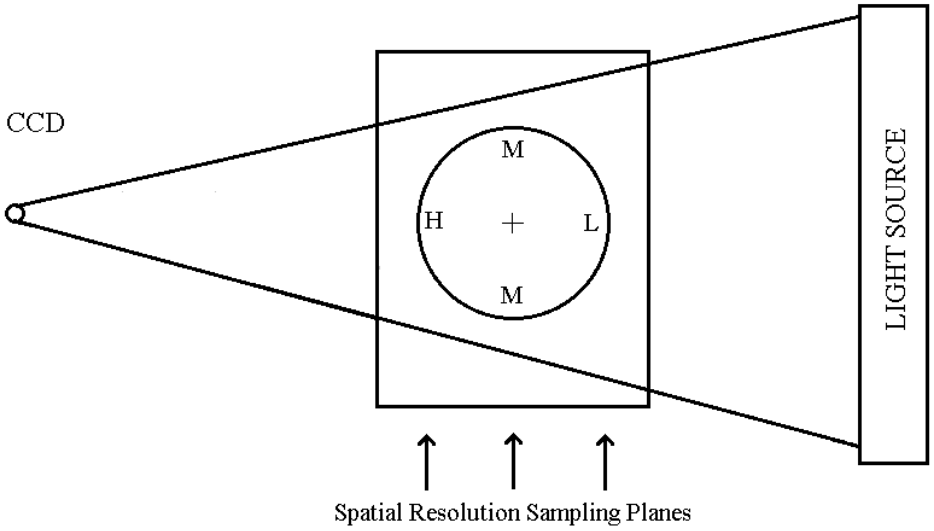

Figure 5-6: Varying spatial resolution for a volume of interest (VOI) radially distant from the axis of rotation in the centre of the phantom. H = High spatial resolution. M = Medium spatial resolution. L = Low spatial resolution. The rotation of a VOI results in the sampling of dosimeter detail at low and high resolution. The spatial resolution sampling planes are shown at distances over the depth of field required to acquire projection data.

5.4.1 Method

The calculation of spatial resolution in projection images follows the methodology presented in section 3.5. A sharp razor's edge was placed into a holding device to produce an edge function. The razor was positioned parallel to the horizontal pixel direction for the vertical spatial resolution calculations. The razor was then rotated 90° to align the razor with the vertical pixel direction for the horizontal spatial resolution calculations.

Projection images of the razor edge were measured at distances from the CCD imaging plane of 40.0 ± 0.2, 45.0 ± 0.2 and 51.2 ± 0.2 cm (Measurement planes A, B and C respectively in Figure 5-7). This is a distance of 11.2 ± 0.2 cm over the central region of the specimen tank. These positions encompass the depth of field required to measure both the PORP (diameter ~7.8 cm) and blue dye phantom (diameter ~9.2 cm).

At all three distances the razor edge was moved from right to left as viewed in the projection image (1 – Right, 2 – Centre, 3 – Left). The right and left measurement positions were not symmetrical about the central axis due to the size of the measurement equipment and the limited space available in the specimen tank. The off-axis positions allow the comparison of the edge response function away from the central light path. The individual distances to the measurement points were within the uncertainty of the central axis distance. This is because the position to CCD distance is much larger relative to the off-axis distance (approximately 40 – 50 cm vs 4 – 5 cm); therefore the angle formed by the central axis and measurement point is small. As such, the distance of the measurement position to the lens along the central axis was used for the correction of pixel size for all three positions in each of the 3 planes.

A transparent calibration grid, with black lines spaced at even 1 cm distances, was used to calculate a ratio of pixels to millimetres at the measurement positions. The ratio was then used to convert the acquired edge spread from each measurement position, into a function of distance. The ratio is required because a comparison to other CCDs with different pixel sizes is not possible if the spatial resolution is not measured as a function of distance.

The MTF was compared between different positions and distances via the 50 % modulation value. The red light source was used in the investigation.

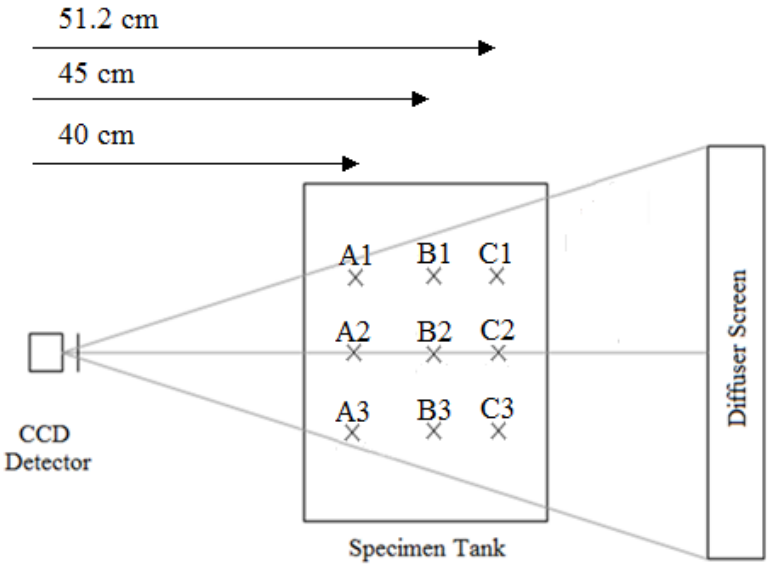

Figure 5-7: Razor positions for the measurement of spatial resolution. Measurement positions are at planes labelled A, B and C corresponding to distances of 40.0 ± 0.2, 45.0 ± 0.2 and 51.2 ± 0.2 cm from the CCD imaging plane and shifted from left to right in the projection image labelled position 1, 2 and 3 respectively. The razor was aligned parallel to the horizontal and then the vertical pixel direction in the projection image, to measure the spatial resolution in each direction. The measured edge profile function was used to calculate the MTF for each position as described in the methodology (section 3.5). Image not to scale.

5.4.2 Projection Resolution

Figure 5-8 shows the vertical spatial resolution at the measurement positions in Figure 5-7. A comparison of the vertical spatial resolution measured along the central axis for the different CCD to measurement plane distances is shown in Figure 5-8 D.

Figure 5-9 shows the horizontal spatial resolution measured at the same positions and the same comparison along the central axis. From both the horizontal and vertical comparisons it can be observed that the maximum 50 % modulation value is found along the central axis. The 50 % modulation value changes across the projection image, but varies by a larger amount in the CCD to light source direction. The horizontal spatial resolution along the left hand side of the projection (side 1) decreases in modulation value for very low line pairs per millimetre and will be discussed in the next section. The 50 % modulation values at each measurement position are shown in Table 5-3.

Table 5-3: 50 % modulation values for measurement positions in Figure 5-7.

Position	*A1*	*A2*	*A3*	*B1*	*B2*	*B3*	*C1*	*C2*	*C3*
Horizontal (lp/mm)	1.1	1.3	1.5	0.7	0.9	0.9	0.5	0.6	0.6
Vertical (lp/mm)	1.2	1.5	1.2	0.8	0.9	0.8	0.5	0.6	0.5

A comparison between the horizontal and vertical spatial resolution along the central axis (Row 2) at all distances is shown in Figure 5-10. The graph shows good agreement at positions close to the light source and in the centre of the tank. The difference between the horizontal and vertical spatial resolution was largest at the measurement position closest to the detector. From the comparison of the central axis MTF curves it was observed that the spatial resolution increased as the object was moved closer to the detector. As the angle off-axis was increased (i.e. the measurement point off axis was moved closer to the CCD, thus from plane C to A) a larger discrepancy between the central axis and off axis 50 % modulation value was observed. For the furthest point (51.2 cm, plane C) the difference between the central axis and off axis was ~16 %, whilst for the closest point (40.0 cm, plane A) the difference between the central axis and off axis 50 % modulation value was ~20 %.

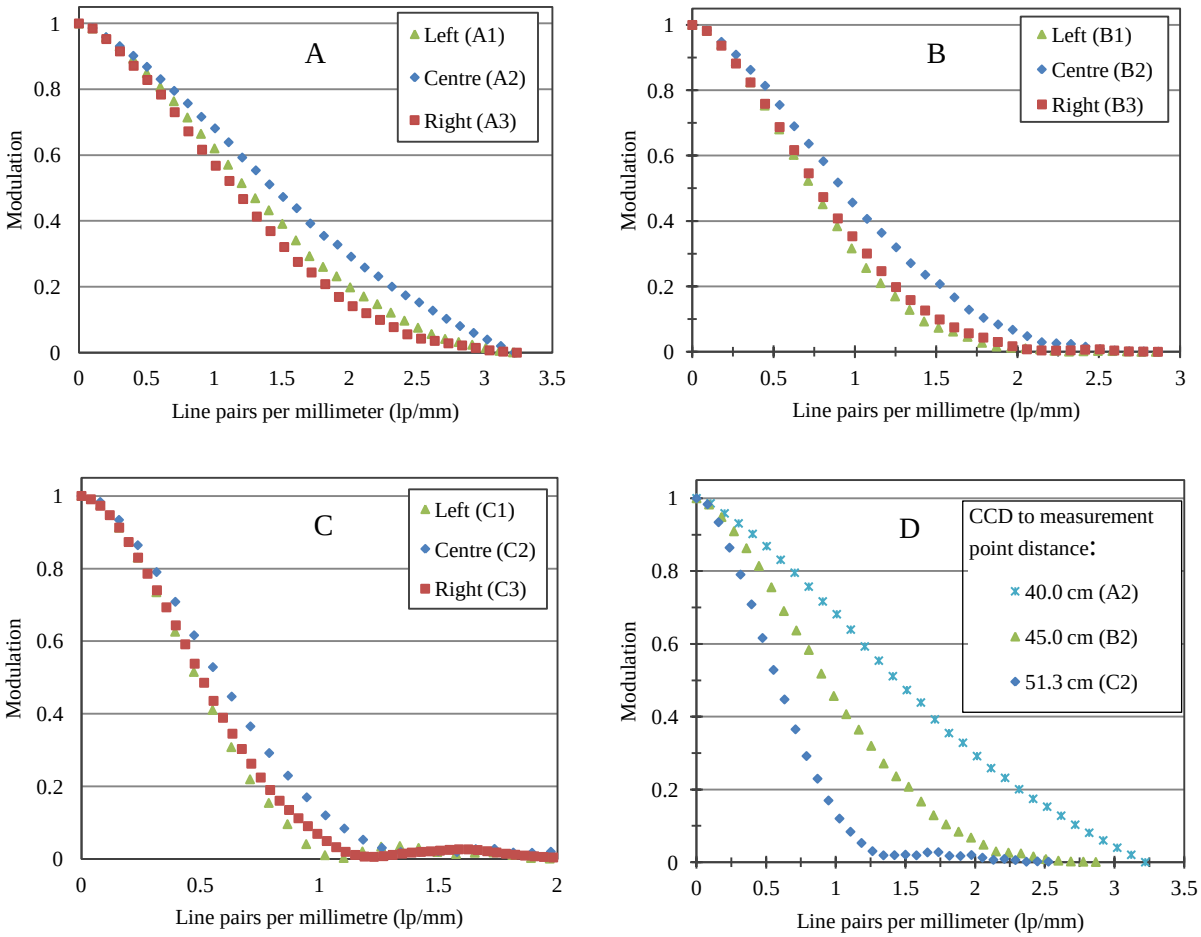

Figure 5-8: Vertical spatial resolution across projection at 40, 45 and 51.2 cm from the CCD image plane (A, B and C respectively). Graph D shows a comparison of the vertical spatial resolution along the central axis. The central axis data illustrates the increases in spatial resolution as the razor was moved closer to CCD. The difference in the MTF curves between the left, centre and right of the projection image is detailed in the discussion.

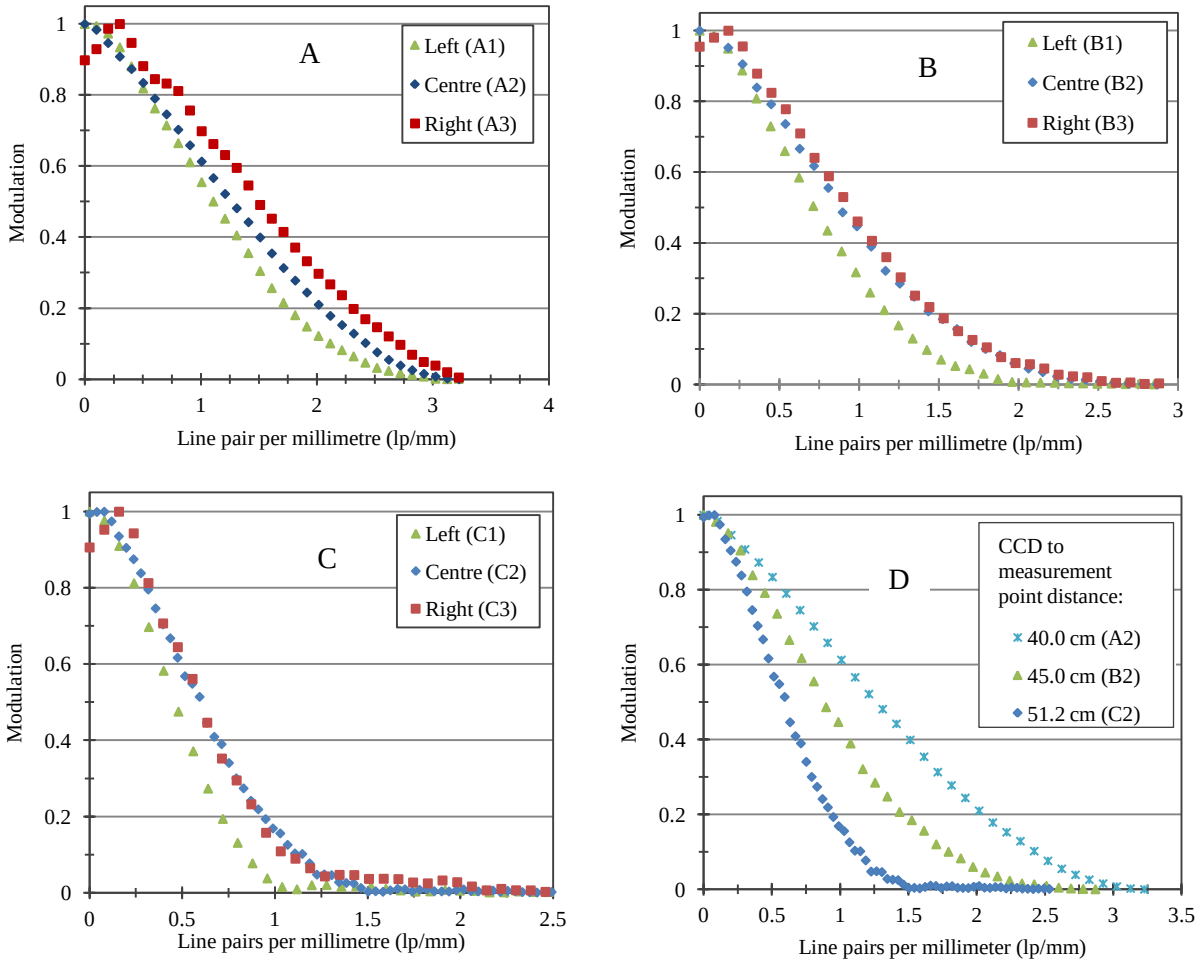

Figure 5-9: Horizontal spatial resolution across projection at 40, 45 and 51.2 cm from the CCD image plane (A, B and C respectively). Further details on the low modulation values for low spatial resolution in the left side of the projection (Row 3) and the difference between the left, centre and right MTF curves can be found in the discussion. Graph D shows a comparison of the horizontal spatial resolution along the central axis. The central axis data illustrates the increases in spatial resolution as the razor was moved closer to CCD.

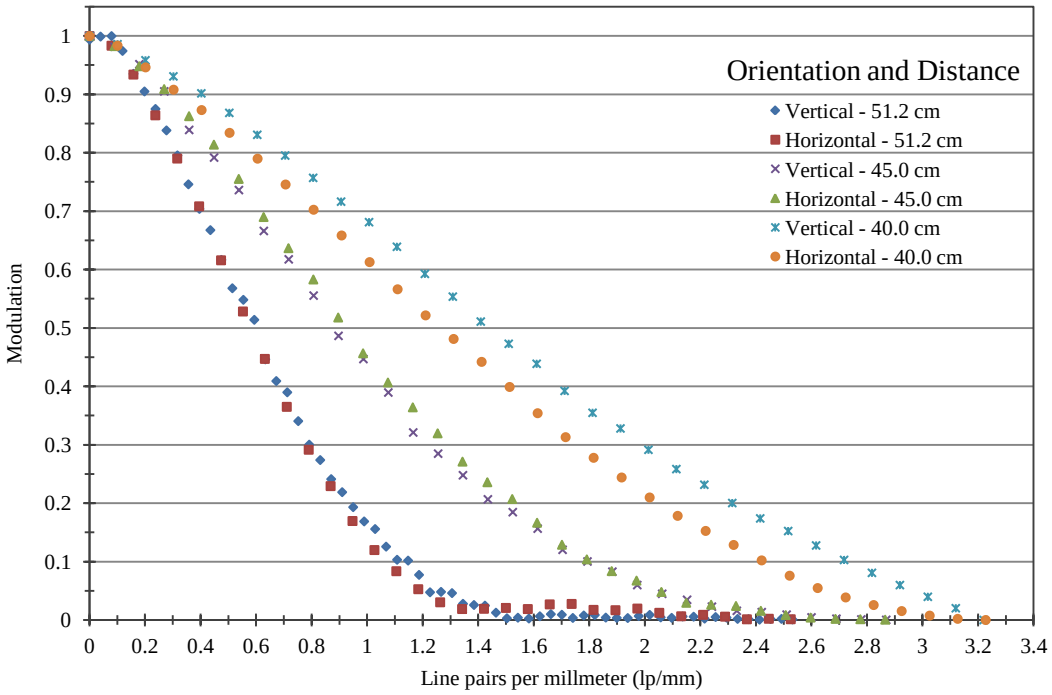

Figure 5-10: Comparison of horizontal and vertical spatial resolution along central axis. Data has already been presented. This graph illustrates the agreement between the horizontal and vertical spatial resolutions and the increase in spatial resolution as the measurement position is moved closer to the CCD.

5.4.3 Discussion

Moving the razor closer to the CCD changes the distance from the detector to the measurement point and results in an approximately linear increase in the 50 % modulation value (Figure 5-11). The measured 50 % modulation values were only above 1 lp/mm for distances less than ~ 45 cm. Therefore the scanner in the measured geometry was not optimal for acquiring projection images which are then reconstructed and used to evaluate dosimeters. To optimise the scanner, the aperture settings and the distance between the CCD detector and the centre of rotation require adjustment. A sub-mm spatial resolution in the 2D projection image, for measurement points across the entire diameter of the dosimeter, is considered optimal for acquisition.

The projection based MTFs change between the central axis and off-axis position. The movement of the object closer to the imaging plane has two effects on the measurement position off axis: (i) The percentage increase in the distance between the CCD image plane and the off central axis point, relative to the CCD to central axis point, will be larger for measurement points closer to the CCD, thus making the drop in irradiance due to radial distance a larger factor, and (ii) The angle between the central axis and the measurement point increases.

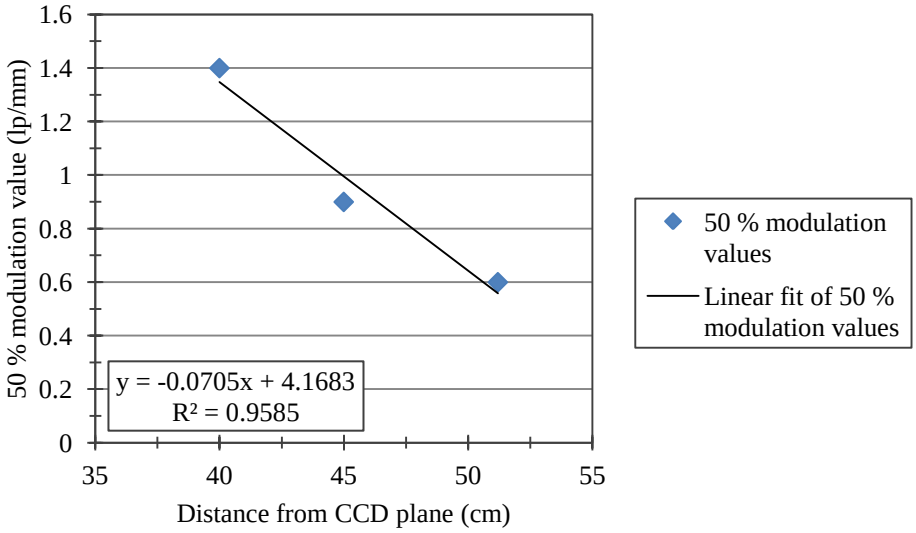

Figure 5-11: Linear relationship between 50 % modulation value and the distance from the imaging plane. The extrapolated fit is almost linear (R^2 = 0.9585). Using the linear fit equation, a change in the distance of approximately 0.2 cm (equal to the difference between off-axis and central axis distances) will only result in a difference in the MTF of ~0.02 lp/mm. This change in MTF does not explain the difference in 50 % modulation value observed between the central and off axis positions.

Using the linear relationship calculated for the central axis in Figure 5-11, the difference in the distance along the off axis line relative to the central axis (~0.2 cm) will result in only a 0.02 change in 50 % modulation value. The difference between central and off axis 50 % modulation values is significantly larger than this. Therefore the source of the discrepancy is not due to the increase in distance from the CCD.

A potential reason for the difference between the central and off axis spatial resolution could be due to the lens system being non-ideal. In non-ideal lens systems, aberrations can cause changes in the sharpness of an image and a loss in high spatial frequency information[169]. The most likely form of aberration, which would cause the observed results, is pin-cushioning. Pin-cushioning distorts the image by increasing the magnification as the distance from the optical axis increases[169] (i.e. a point spread function will be spread across more pixels relative to the projected image on the central axis).

Whilst this is a theorised explanation, angular dependence of the spatial resolution of a CCD has not been reported in the relevant literature to the best of the author's knowledge. Further measurements are required to confirm spatial resolution angular dependence.

The discrepancy between the horizontal and vertical MTF curves indicates a difference in the horizontal and vertical CCD pixel size. The CCD pixel specifications[154] suggest the CCD chip has square pixels, which should result in an equal MTF at the same distance. Figure 5-10 shows the horizontal and vertical MTF are equal along the central axis at the measurement planes close to the detector and in the centre of the water tank. The difference in the horizontal and vertical MTF curve could potentially be introduced by aberrations in a non-ideal lens system[169].

The left and right 50 % modulation values (sides 1 and 3 in Table 5-3) were different from each other due to the different distances from the central axis for each side. The difference in distance from the central axis for each side was due to the size of the measurement equipment and the limited space in the specimen tank.

The lowering of the modulation in the horizontal MTF along the left hand side, near spatial frequencies approaching ~0 lp/mm, is an artefact caused by the position of the razor edge. The razor was positioned with the sharp edge closest to the side of the projection. Theoretically the calculation of the MTF requires only the pixel values of the edge response function. In practice extra pixel values on either side of the edge response are also used for the integration to a line spread function and Fourier transform. As can be observed in Figure 5-12 A, the open field pixel response were not uniform in the high intensity region for the measured profile. Replacing the pixels which had a decreasing response with a theoretical profile consisting of constant pixel response results in a MTF without the lowering of the modulation near ~0 lp/mm (Figure 5-12 B).

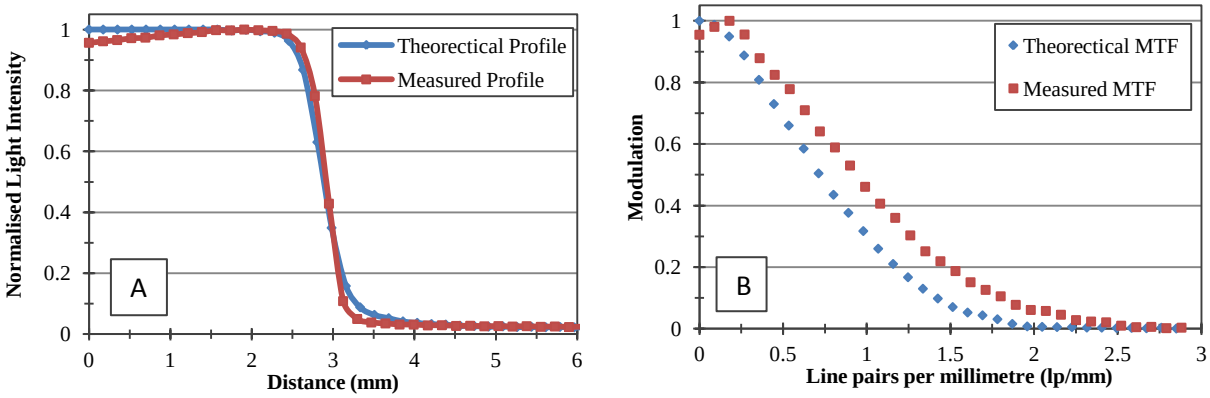

Figure 5-12: A) Edge response function with measured and theoretical high intensity pixel values. Values have been normalised for the purpose of graphing. B) The MTF curves calculated for the respective profiles.

The spatial resolution for a Vista™ cone beam optical CT scanner has previously been measured using a MTF test pattern[133]. The camera system used by Olding et al[133] was the 2/3" Dragonfly 2 model DR2-HIBW (Point Grey Research, Richmond, BC, Canada, www.ptgrey.com), and is different from the acquisition system used in this thesis (Dragonfly 1 with a Sony 1/3" ICX204 CCD). In addition the distances from CCD imaging plane to the measurement point were different. A comparison between calculated 50 % modulations at a similar distance (~50.0 cm) shows the result in this thesis, 0.6 lp/mm, was less than the 1.8 lp/mm reported by Olding et al[133]. This indicates that the newer camera and optimised focus and lens system used by Olding et al[133] improves the spatial resolution substantially.

Subsequent to the measurements presented in this work the CCD was changed to the Dragonfly 2 Model due to a failure in the original CCD.

5.5 *Effect of Charge Integration Time on the Spatial Resolution*

CCD's generate electrons proportional to the incident light on each pixel. As the total integrated charge is increased, the probability of the electrons overflowing from a pixel into neighbouring pixels increases. This process is known as blooming[166].

As described in section 5.4, spatial resolution is the ability of a system to resolve a high contrast object (e.g., a wire or edge). High contrast objects will have high pixel values neighbouring low pixel values. Overflow from the high intensity region to the low intensity region may have consequences for the spatial resolution.

A theoretical example of different amounts of blooming and the influence on edge spread functions (ESF), and consequently the modulation transfer function (MTF) is shown in Figure 5-13. The uncertainty is measured in terms of how accurate the ESF is reproduced to the correct position (accuracy) and the reproduction of the ESF relative to an ideal ESF (precision).

Figure 5-13 A shows how a CCD collecting charge without blooming will measure an edge spread function as shown in Figure 5-13 D. Since no blooming is occurring, the measured edge spread function will be an accurate and precise reproduction of the edge. A charge overflow of low magnitude will only cause a small rise in collected charge in the next few pixels across the razor edge. The small overflow will cause the pixel response underneath the razor to increase slightly (Figure 5-13 D – Low Blooming). The ESF will still be in the correct position but will be different from the ideal ESF. Therefore the response will be accurate but imprecise. A very high collected charge in the pixel aligned at the razor edge, causes an overflow of charge into the pixels measuring the low charge behind the razor as shown in Figure 5-13 C. If the overflow is sufficiently high, then the measured charge in the pixels next to the edge will also be high (Figure 5-13 D – High Blooming). The ESF measured will be sharp like an ideal ESF, but will be positioned away from the actual edge position. Thus the measured ESF may be precise but will have low accuracy.

The objective of this section was to measure the spatial resolution as the charge integration time of the CCD was changed. Charge integration time was used to control the exposure of the CCD in section 4.6. As charge integration time is increased the magnitude of blooming will increase.

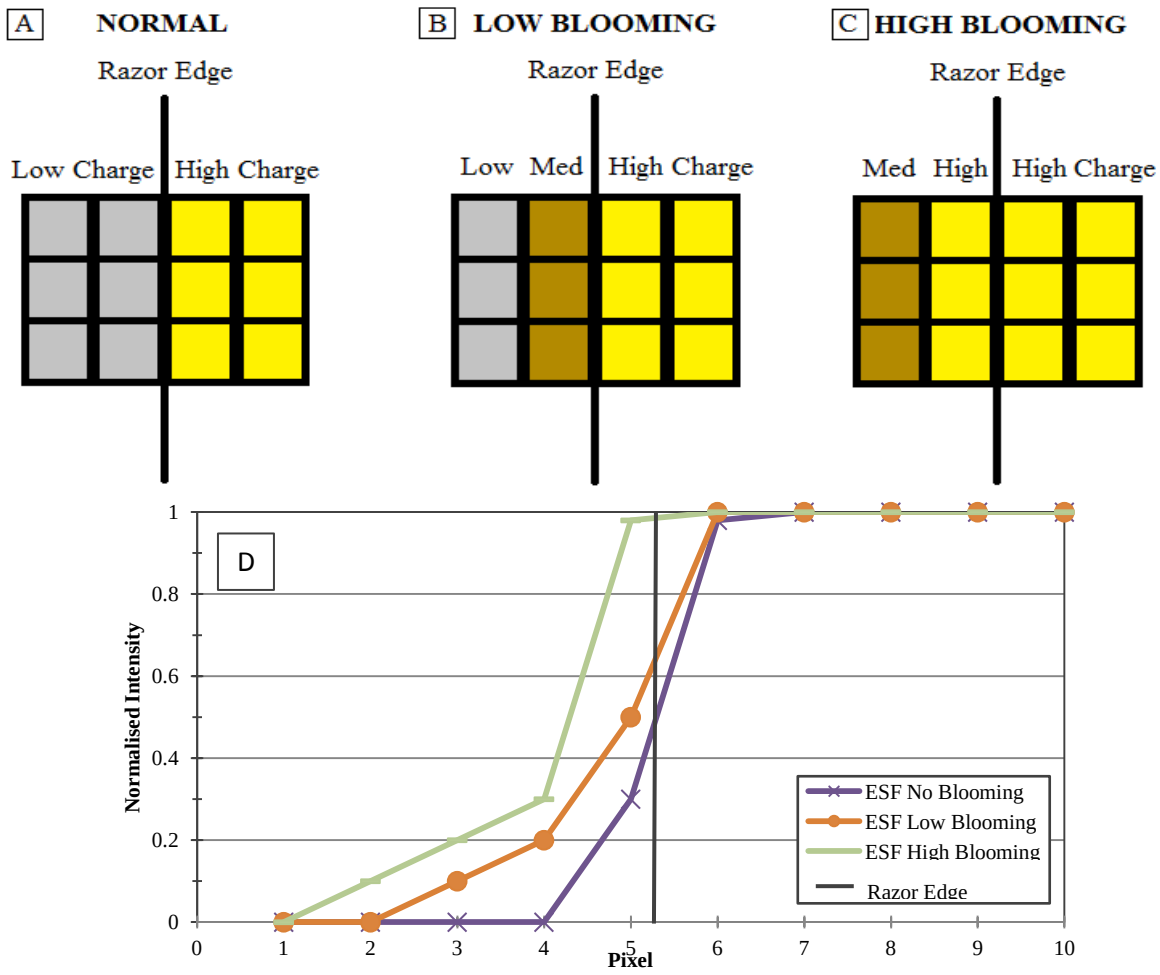

Figure 5-13: Process of blooming and its effect on spatial resolution. A) Normal charge detection over a razor edge. B) Low level of blooming over a razor edge. C) High amount of blooming over a razor edge. D) The edge response function expected in each situation described in A, B and C with a razor edge positioned between pixel 5 and 6 at the location of the half height (50 % value) of the ESF that exhibits no blooming.

5.5.1 Method

Similar to the method used to measure the modulation transfer function in section 5.4, a projection image of a razor edge was acquired to measure an ESF. The ESF was then differentiated to form a point spread function PSF. A MTF was calculated from a Fourier transform of the PSF.

The razor edge was placed in the centre of the specimen tank at the position of the rotational axis (distance from imaging plane 55 cm). This position is not consistent with Figure 5-7 due to a change in scanner geometry between when the spatial resolution in section 5.4 was acquired and the blooming measurements in this section were acquired. The position of the razor was constant whilst the charge integration time of the CCD was varied between 10.4 ms and 133.2 ms. Profiles were acquired in the same position for each charge integration time using ImageJ. The profile was re-scaled from pixels to millimetres via the same method as used in section 5.4.

The CCD used in this section is the Dragonfly 2 DR2-HIBW (Point Grey Research, Richmond, BC, Canada, www.ptgrey.com) with a Sony ICX204 CCD array (Sony Corporation, Tokyo, Japan). This CCD was used due to a failure of the original CCD (Dragonfly 1).

5.5.2 Results

Figure 5-14 shows the influence blooming has on an edge response function, used to calculate the MTF in Figure 5-15. The apparent location of the razor edge position was measured at the half height (50 % value) of the edge response function via a linear interpolation between the two closest points. Table 5-4 shows the distance of the half height position relative to the half height position measured from the ESF with the lowest charge integration time (10.4 ms). The profiles collected for charge integration times below 30.2 ms overlap and exhibit no blooming. The half height position for these ESF are approximately the same. For the charge integration times between 50.5 and 80.1 ms, the profiles exhibit a slight blooming via an increase in the pixel position between 1.1 – 1.3 mm which results in a shift of the half height. At the longer charge integration time of 133.2 ms, blooming causes a high collected charge on the pixel at a position of ~1.1 mm. The resulting profile is sharp but the half height is offset left by ~0.15 mm.

Table 5-4: Offset distance of half height of edge response function for different charge integration time relative to 10.4 ms charge integration time.

Charge Integration Time (ms)	Offset distance of half height relative to position of 10.4 ms half height (mm)
20.3	0.00
30.2	0.00
40.6	0.00
50.5	0.01
60.4	0.04
70.8	0.08
80.1	0.10
133.2	0.15

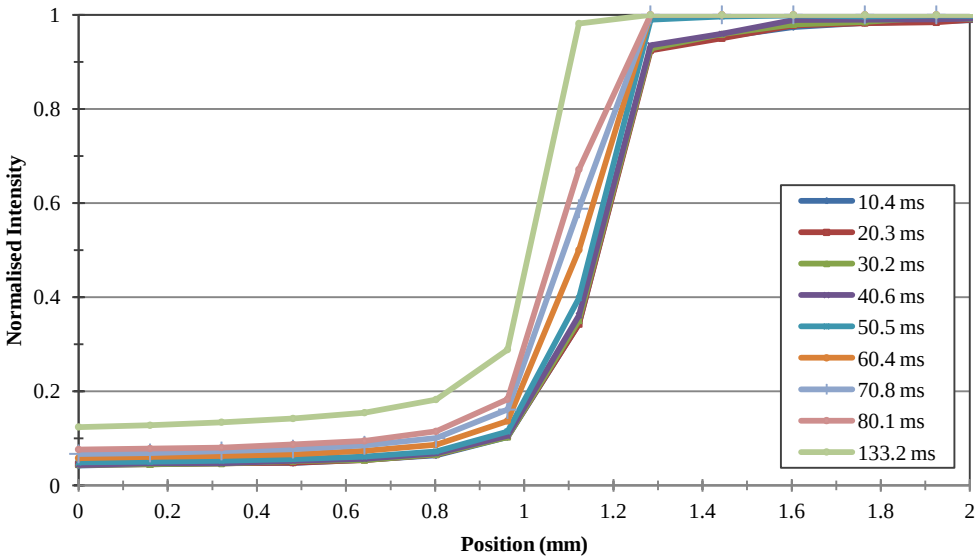

Figure 5-14: Edge spread functions used to calculate the corresponding MTF in Figure 5-15. The effects of blooming were observed on profiles with a charge integration time ≥ 60.4 ms. For ESF at charge integration times of 40.6 and 50.5 ms a slight increase due to a low magnitude of blooming was observed.

Figure 5-15 shows the MTF for each charge integration time calculated from the MTF in Figure 5-14. The measurements for the charge integration times between 10.4 and 50.5 ms show no significant change in MTF. The modulation transfer functions for times between 60.4 and 80.1 ms exhibit a small change at higher spatial frequencies. At a time of 133.2 ms the MTF significantly increases.

The change in 50 % modulation values for the different charge integration times is shown in

Table 5-5. The 50 % modulation values were constant for the measurements between charge integration times of 10.4 to 60.4 ms. Above this, the 50 % value was observed to decrease for the 70.8 and 80.1 ms charge integration times. The 50 % value was observed to increase at a charge integration time of 133.2 ms.

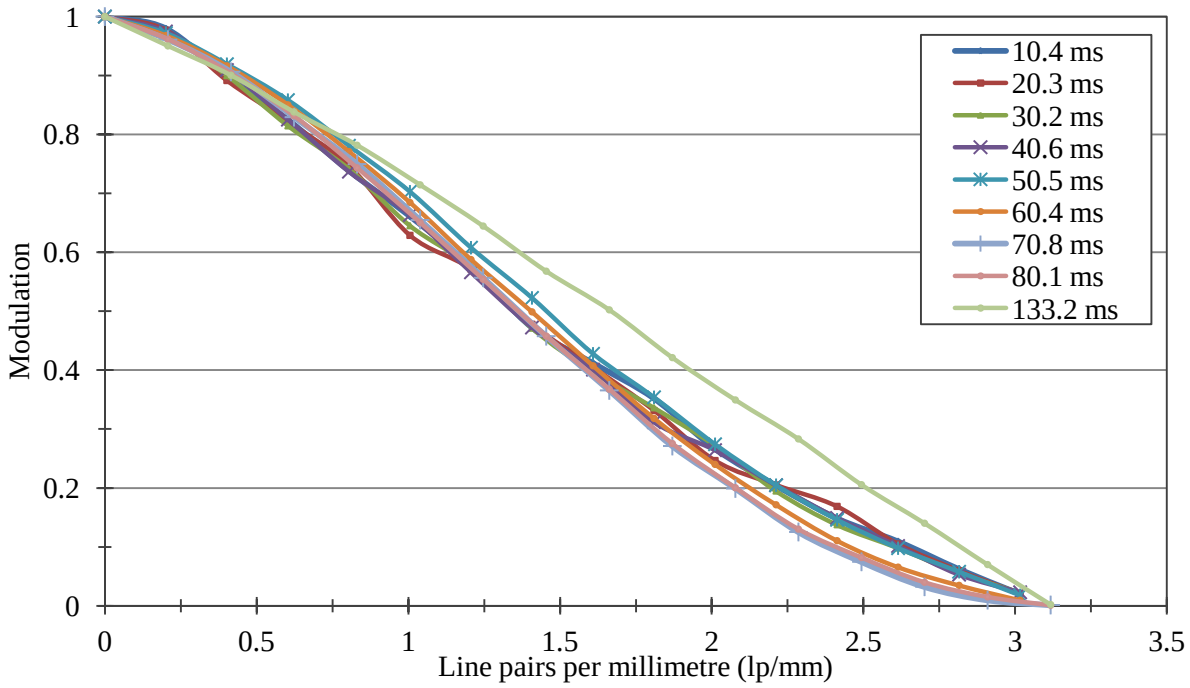

Figure 5-15: Modulation transfer function measured for different charge integration times. The MTF for charge integration times between 10.4 and 50.5 ms was approximately the same.

Table 5-5: 50 % modulation values measured for different charge integration times. The 50 % value is constant until ~70.8 ms where the value decreases slightly, before increasing significantly at a charge integration time of 133.2 ms.

Charge Integration Time	*50 % Modulation value*
10.4	1.4
20.3	1.4
30.2	1.4
40.6	1.4
50.5	1.4
60.4	1.4
70.8	1.3
80.1	1.3
133.2	1.6

5.5.3 Discussion

Blooming of charge from one pixel element to the next can have a range of effects on the edge spread function as shown in Figure 5-13, which will then influence the MTF derived via Fourier transform.

As described in section 3.5, a Fourier transform uses the super-position of sine and cosine trigonometric functions with varying frequency and amplitude, to reproduce a point or line spread function[162]. Different shaped line spread functions will be formed by the differentiation of the different ESF in Figure 5-15.

ESF measured at charge integration times between 10.4 and 50.5 ms resemble the *no blooming* example in Figure 5-13. As such, the measured ESF will have a high accuracy and precision. The calculated MTF and 50 % modulation value for these times were shown not to change. The half height position for the ESF at charge integration times between 20.4 – 50.5 ms is not different relative to the half height position measured for the ESF measured at a charge integration time of 10.4 ms.

ESF measured for charge integration times between 60.4 and 80.1 ms are not as sharp relative to those between 10.4 and 50.5 ms. The ESF resemble the *low blooming* example in Figure 5-13. The ESF measured with charge integration times between 60.4 and 80.1 ms are similar in position to the profiles collected with shorter charge integration times, but do not have the same shape. Therefore the ESF are accurate in position relative to the ESF with no blooming but will be imprecise because of the small increase in charge collected underneath the razor, which affects the shape of the ESF This is supported by the half height position for these ESF being different relative to the 10.4 ms charge integration time half height by between 0.04 and 0.10 mm, which is below the 0.16 mm resolution of the CCD. The MTF calculated for charge integration times between 60.4 and 80.1 ms were observed to drop in modulation at higher spatial frequencies (Figure 5-15) and the 50 % modulation values for the 70.8 and 80.1 ms curves also decreased.

The ESF measured at a charge integration time of 133.2 ms was affected by a large magnitude of blooming, which caused pixels behind the razor edge to saturate. The ESF resembled the *high blooming* example given in Figure 5-13. The ESF was sharp, but the position of the half height was offset by 0.15 mm from the half height measured for the 10.4 ms ESF. This is approximately equal to the 0.16 mm resolution of the CCD and indicates that the positional accuracy of edge is low. Due to the sharper ESF measured at a charge integration time of 133.2 ms, the corresponding line spread function would require a greater modulation at higher frequencies during Fourier transform. The increase in modulation value at higher frequencies in the MTF and the increase in the 50 % modulation value indicate this.

The MTF curve at a charge integration time of 133.2 ms highlights a problem with measuring the spatial resolution using this method. The ability to resolve small features *appears* to be better with a higher charge integration time, but the decrease in accuracy of where those features are resolved is worse and not indicated by the graphing of the MTF.

5.6 Influence of Scatter

Scattered light in the optical CT scanner can significantly affect the measured uniformity[37,132,135] and attenuation coefficient[37,63,90,130-132,135]. The influence of scattered light and corrections has been reviewed in section 2.4.3. Scattered light not only occurs from polymer gels[130-132,135] but also from optical components in a scanner[114]. The method used to measure optical density assumes detected light at the CCD is travelling in a straight line from the light source. Scattered light from paths other than the straight path between the CCD and light source will increase the detected light at the CCD. This will underestimate the attenuation of the sample.

Figure 5-16 shows some different light paths and how scattered light along each is a problem. Path A is a straight path between the light source and detector. The measured change in light intensity along this path between a pre and post irradiation evaluation of a dosimeter is used to calculate the optical density along that path as defined in this work. Path B shows light not originally directed toward the detector being scattered toward the detector. The scattering can occur in the medium or outside the medium (e.g., from an internal surface of the specimen tank). This type of scattering artificially increases the detected light intensity at the CCD. Path C represents light originally travelling toward the detector in a straight line scattered toward a different point in the detector. Whilst this represents attenuation along the original light path, the scattered light toward the detector will contribute to the intensity of light detected along another path. The optical density calculated along the original light path will be correct, but along the other path the optical density will be incorrect. This is more common in scattering dosimeters. Path D shows light scattered away from the detector. Along this light path the measured optical density will be correct provided no scattered light from other light paths artificially increases the measured intensity.

This section compares "reduced" and "full" scatter geometries. The reduced scatter geometry uses collimation, at the entrance and/or the exit window of the specimen tank, to approximate a fan beam geometry. Whilst fan beam geometries are not scatter free, the reduction of the acquired data from a large area to a smaller area, reduces the impact of scatter. The full scatter geometry is the cone beam geometry used for most measurements.

The objective of this section is to determine whether scattering contributions can be observed, even when using a light absorbing sample. This will indicate whether there is a substantial scattering effect arising from the scanner components including the sample tank. Using the reduced and full scatter geometries investigates the contribution of the different types of scatter in Figure 5-16 to the overall projection image. The level of scatter should be remembered when deciding if another factor affecting uncertainty is significant. This section is not designed to quantify a correction factor for scattering, which has been covered in the literature[133,138,144].

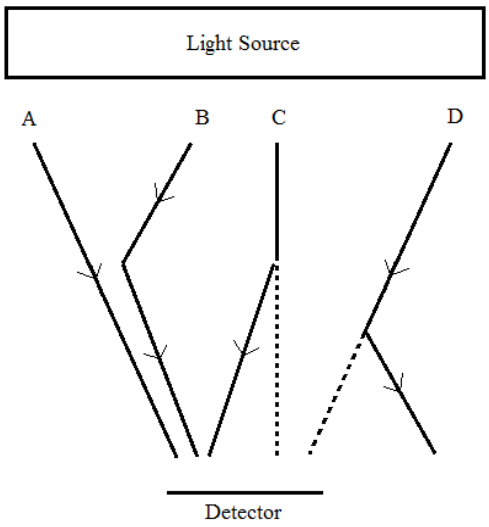

Figure 5-16: Different paths from light source to detector that contribute to scattered light. The different light paths represent how scattered light can contribute to the measured light intensity. A description of each light path is in the text. Image not to scale.

5.6.1 Method

The light absorbing uniform phantom used in section 4.4 (water and dye solution, fractional dye concentration 1 x 10^{-5} %) was scanned in the reduced and full scatter geometries to investigate the contribution of light scattered within the specimen tank from sources other than the sample. Black cardboard was used as a collimating window frame at the entrance and exit windows of the specimen tank. The cardboard completely covered the front and rear of the tank except for the entrance or exit windows. The entrance window is closest to the light source, whilst the exit window is closest to the CCD. The cardboard was positioned so that the cone beam geometry was reduced to approximate a fan beam. The exit window was set to 11 mm and the entrance window was slightly larger (18 mm), so that the acceptance angle of light collimated separately by the front and rear window was equivalent.

The configurations of the window were:

i) Collimation of the **entrance** window – Designed to reduce the volume of the specimen tank illuminated (see Figure 5-17 A). Detected stray light at the CCD is scattered *out of* the open light field region (light path C from Figure 5-16). Light not originally incident on the detector, which would be scattered toward the detector, has a lower probability of being detected (light path B from Figure 5-16).

ii) Collimation of the **exit** window – Designed to restrict the light scattered in the specimen tank from reaching the detector (see Figure 5-17 B). Stray light detected at the CCD has been scattered *into* the open light field region (light path B from Figure 5-16). Light scattered from the tank toward the CCD has a lower probability of reaching the detector (Light path C from Figure 5-16).

iii) Collimation of **both** windows – Designed to restrict the light detected at the CCD to direct light from the light source (see Figure 5-17 C) and is analogous to a fan beam scanning geometry described earlier. Light not originally incident on the detector which is scattered toward the CCD and light scattered in the tank have a lower probability of reaching the detector. (Both light path B and C from Figure 5-16). This setup is used as a reference geometry for comparisons (herein referred to as the full collimation geometry)

iv) No collimation of either window – The scanner is left in normal acquisition conditions and all scattered light paths are detected. The uncollimated geometry is shown in Figure 5-16. All light paths will be detected.

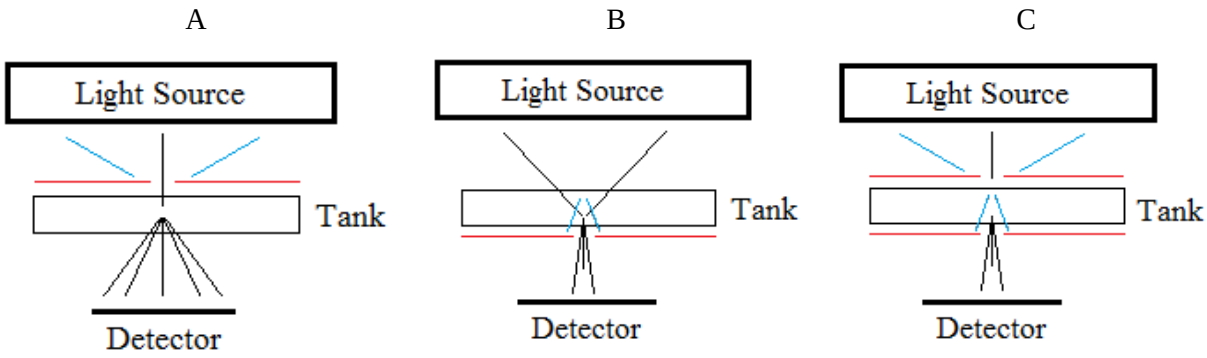

Figure 5-17: A) Collimation of light source before the entrance window (Red lines are collimation windows). Scattered light not originally incident on detector has lower probability of being scattered back onto the detector relative to open cone beam geometry (represented by blue lines between light source and tank). Scattered light generated in tank was still detected. B) Collimation of light source after exit window (Collimation represented by red lines). Scattered light from inside the tank has lower probability of being detected relative to cone beam geometry (blue lines inside the tank). Scattered light not original incident on detector but scattered inside the tank toward the detector is still detected. C) Collimation of both the entrance and exit (Red lines). Scattered light from inside the tank and light not originally incident on detector (blue lines) both have lower probability of being detected. All diagrams not to scale.

The red light source (633 nm) was used to acquire projections of a water filled jar (used as the undyed phantom) and the previously described light absorbing phantom (used as the dyed phantom - see section 3.2 for details on the manufacture of the phantoms). The dyed phantom was previously used as a comparison phantom in section 5.2. An example of the acquisition area is shown in Figure 5-18. The CCD settings were optimised for the undyed phantom in an uncollimated geometry so that the collected light was below saturation. The CCD settings were kept constant for measurements made with different window collimations. The scanner was allowed sufficient time to warm-up as per stability conditions described in section 4.3.

ImageJ was used to measure 10 profiles from the projection image, which were averaged together to reduce random noise. The position of the measured profiles in the projection image was the same for each window combination. A ratio of the profiles acquired through the dyed phantom relative to the

undyed phantom was used to calculate absorbance profiles as per the method described in section 5.2. Absorbance profiles were used instead of the raw profiles to account for differences in light intensity between non collimated and collimated geometries. Introduction of a collimation device will reduce any scatter if present. Changes in lateral scattering properties will cause a flattening of absorbance profile curvature[131]. Changes to the contribution of scatter from outside the slice to the measured slice will reduce measured light intensity. A ratio of the absorbance profiles acquired with different collimation set ups relative to the full collimated set up was used to investigate the magnitude of scatter in each geometry and if a difference in the curvature of the profile was observed.

The width of the collimating windows was larger than the size of the collected profiles (see yellow lines in Figure 5-18). The large field size was used to ensure that adequate signal was measured. For thinner collimation widths, the amount of light detected was significantly affected by low signal to noise ratio. These results are not shown.

Mean and standard deviations of the ratios of the absorbance were calculated for the central 300 pixels of the measured profiles. The central values were used to avoid artefacts caused by the container walls. A comparison of the mean and standard deviation was used to investigate the difference in light intensity and noise caused by the differences in measurement geometries.

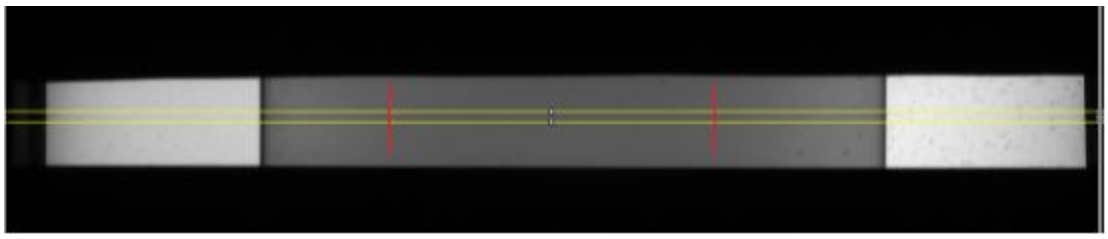

Figure 5-18: A collimated projection image showing the upper and lower profiles (yellow lines) which bound 10 profiles used to calculate an average profile. The mean and standard deviation were calculated in the central 300 pixels of the average profile (between red lines).

5.6.2 Results

Figure 5-19 shows the measured absorbance across the entire window for the various collimation geometries. The observed difference is minimal between different geometries, however a slight decrease in absorbance can be observed for the full scatter geometry. The difference in absorbance between different geometries is better visualised by calculation of the ratios of measured absorbance for the entrance and exit only geometries and the uncollimated geometry relative to the collimated geometry (Figure 5-20). The ratio was calculated over the central 300 pixels. The ratio does not have a curvature over the 300 pixel range investigated and as such was valid for use in calculations of the mean and standard deviation of the observed differences.

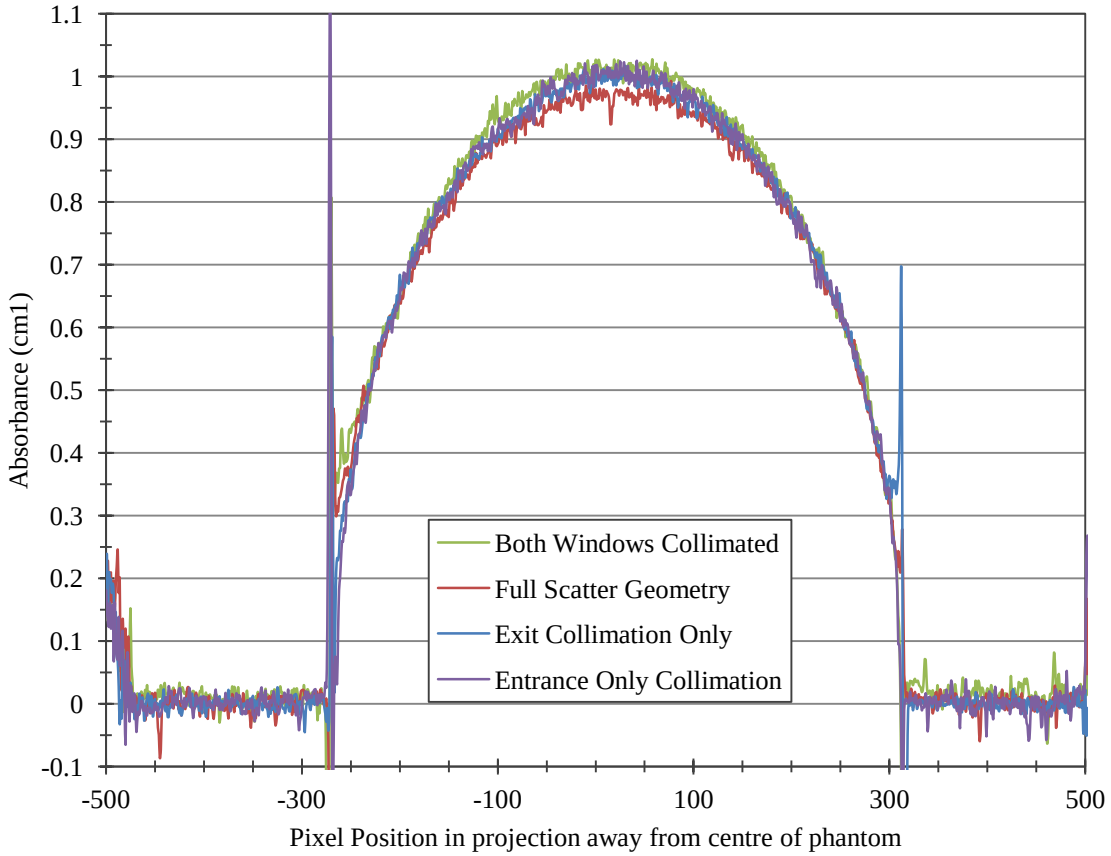

Figure 5-19: Absorbance profiles for different collimation geometries. The absorbance measured for the full scatter geometry and entrance and exit only collimation was less than the absorbance measured for the full collimation geometry.

The optical density measured for the full scatter geometry was lower relative to the optical density measured when collimation was applied to the entrance and/or exit window. Applying light collimation at either the entrance or exit window reduces the light intensity by similar magnitudes (see Figure 5-20).

The mean values calculated for the ratio show percentage differences of 1.7 %, 2.0 % and 4.1 % respectively for the entrance only, exit only and full scatter geometries relative to reference geometry. The standard deviation of the ratio was 1.6 % for the entrance collimation only geometry. A standard deviation of 1.4 % was measured for both the exit only and full scatter geometries.

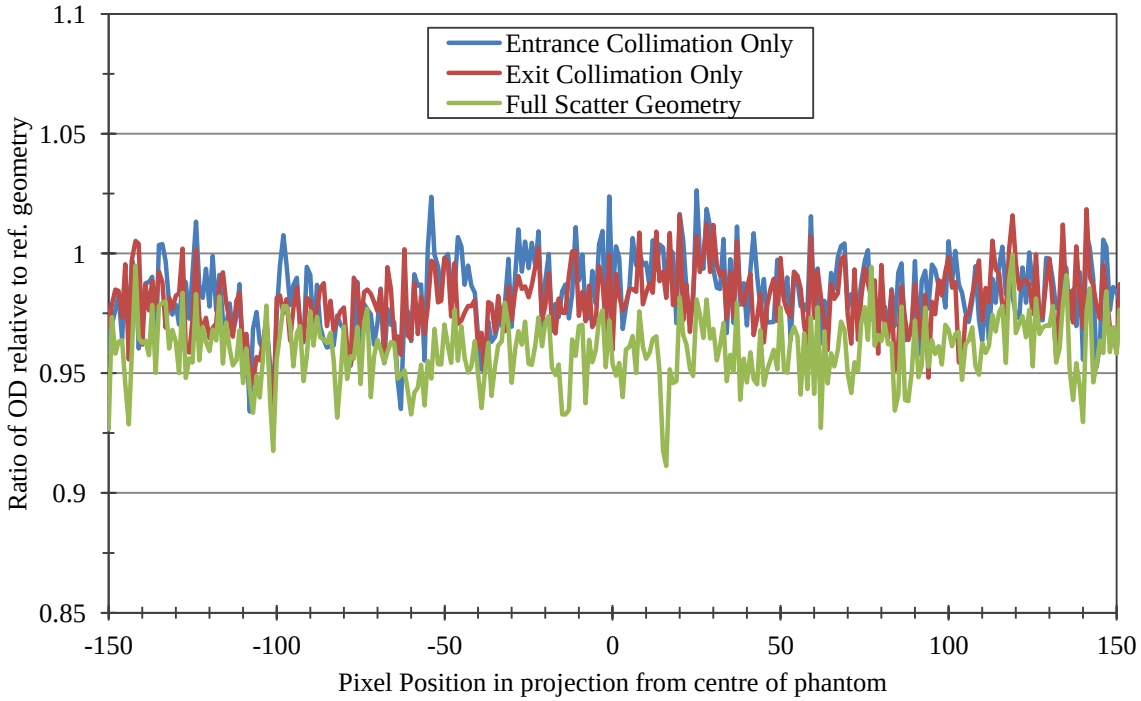

Figure 5-20: Ratio of optical density measured in different collimation geometries relative to the reference geometry. The measured optical density is lower relative to the full collimated geometry for the full scatter geometry and both the entrance or exit only collimation configurations.

5.6.3 Discussion

As attenuation of light increases, the impact of scattered light increases. Therefore the impact of scattered light for the different window collimations with no scattering material (i.e., an undyed phantom) is expected to be similar. This is because the intensity of direct light in these projection images is high. However, when a scatter material is placed between the light source and the CCD, the intensity of light reaching the CCD is low and therefore the impact of scattered light will be more significant. If more scattered light reaches the detector, then the measured absorbance will be underestimated as shown in Figure 5-20. Since optical density is a ratio of the light intensity with and without attenuation material, a higher optical density indicates a larger attenuation. A lower measured absorbance indicates scattered light has artificially increased the measured light intensity. This leads to a smaller optical density measurement, which is observed for both the entrance and exit only collimation and the uncollimated geometry relative to the full collimation geometry.

Figure 5-19 and Figure 5-20 show that collimation of the entrance and exit windows of the specimen tank reduces the light intensity measured relative to the uncollimated geometry. This drop in intensity is most likely due to a reduction in the amount of scattered light directed toward the detector. The magnitude of the change in absorbance indicates that scattered light from the water tank contributes up to 4 % to the measured light intensity. This is similar in magnitude to the estimated contribution of scattered light made by Olding et al[133] via calculation of the difference between attenuation coefficients measured in a spectrometer and in a 2D conebeam geometry.

The measured difference in the profile from collimating either the entrance or exit window is of a similar magnitude. This indicates that scatter is contributed approximately equally from light not originally directed towards the detector being scattered toward the detector (light path B in Figure 5-17) and light originally incident on the detector, scattered in the specimen tank toward other areas of the tank (light path C in Figure 5-17).

The absorbing phantom or container could potentially contribute some scatter. However, the absorbing phantom does predominately absorb light and as such a conservative estimate of ~4 % scattered light contribution from the water tank is valid.

Scatter corrections via the collimation of light have been previously published[133,138,144] and have been described in section 2.4.3. 2D scatter correction methods have been presented by Olding et al[133,144] and Jordan and Battista[138].

Babic et al[170,171] and Olding et al[82] have previously used cardboard to block the side of projection images at the edge of phantoms. Their results showed that no difference was observed for an absorbing solution using this technique. Collimating the measurement window could improve accuracy and uniformity, however as described by Olding et al[82], collimating windows do not allow the use of the normalisation region which can correct for differences in light intensity between reference and data images.

5.7 Summary of the Investigations

The work presented in this chapter investigated the absorbing properties of the PORPs by comparison to blue dye phantoms, the measurable range of attenuation coefficients using the PORPs, the spatial resolution of the projection images and the influence of scattered light on 2D projection images obtained from the scanner.

A comparison of absorbance profiles acquired from absorbing phantoms to modelled profiles shows a similar curvature. When the modelled profiles are compared to the measured PORP profiles the flattening of the curvature for the PORP profiles indicate that the PORPs are not entirely absorbing. Wall artefacts were observed in the PORP profiles and could significantly affected the measured profile. A similar curvature was observed between the modelled and measured profiles in the centre of the phantom. This result should be remembered when measuring the attenuation coefficient of a PORP with an optical CT scanner. Noise in the PORP profiles indicate less uniformity in the PORPs relative to the blue dye phantoms. A solution of absorbing dye and water showed good agreement with the model relative to the PORP phantoms.

The attenuation coefficient range which can be measured with the PORPs was linear between 0 – 0.5 and 0 – 0.45 cm^{-1} for the orange and red light sources respectively. Above these values saturation influenced the measured attenuation coefficients. Large uncertainty in measured attenuation

coefficients was a limiting factor in the use of the PORPs in the 2D projections for ongoing quality assurance. A high precision method of determining reference attenuation coefficients could reduce the uncertainty in the measured cone beam values. A comparison of the 2D and 3D attenuation coefficients is presented as part of the discussion in the next chapter.

The spatial resolution for the optical CT scanner has been measured to be greater than 0.5 lp/mm at distances less than ~46 cm from the CCD, which corresponded to approximately the cylindrical axis of rotation. The result means that the scanner's setup was not optimal for evaluating dosimeters with sub-mm spatial resolution. The discrepancy between MTF curves and 50 % modulation could be caused by lens aberrations. From these measurements the dosimeter should be positioned so that the nearest edge of the dosimeter is at approximately 46 cm from the CCD imaging plane. This can be achieved by increasing the distance between the central rotation axis and the CCD. The spatial resolution obtained in the 2D projections is compared to the 3D reconstruction in the next chapter.

Blooming or overflow of the charge from a CCD pixel into a neighbouring pixel was observed to affect the measured spatial resolution. Depending on the severity of the overflow, the spatial resolution can either decrease or increase (low and high blooming respectively).Blooming can also cause an apparent increase in the resolving ability of the scanner. However, closer inspection shows the location of the edge response function to be shifted and therefore the edge was not resolved at the correct location. This result highlights the limitations in simply graphing the MTF without understanding the imaging system.

The measured amount of scatter present was approximately 4 % using the full cone beam geometry and 2 % when either the entrance or exit of the specimen tank was collimated with black cardboard. This indicates that stray light was contributed to equally by scatter from light originally incident on the detector which was scattered toward a different part of the detector, and light not originally incident on the CCD being scattered toward the detector.

The measurements in this chapter showed the PORPs were not truly absorbing, spatial resolution was insufficient for complex treatment quality assurance, spatial resolution could be influenced by blooming artefacts in the CCD which cause an inaccuracy in the position of measured edges and scattered light caused an underestimation of attenuation in projection images by up to 4 %. Optimisation of the optical CT geometry and limitation of the CCD charge integration time can be used to improve the spatial resolution and limit the influence of blooming. Scattered light in the projection image could be reduced by the use of light collimating windows. However, collimating windows reduced the field of view used to acquire projection images and would have to be considered in conjunction with field size considerations.

6. ASSESSMENT OF 3D RECONSTRUCTED IMAGES

6.1 Introduction

The aim of this chapter was to characterise the reconstructed images obtained from the Vista™ Cone Beam Optical CT scanner (the scanner). This will be achieved by assessing the measurable range of reconstructed attenuation coefficients using PORPs, spatial fidelity and influence of scatter. This chapter also compares the measured results with similar measurements from 2D projections (Chapter 5). The work presented is used to determine the most efficient and accurate method for performing ongoing quality assurance on the optical CT scanner. Table 6-1 summarises the work in this chapter.

Reconstructed attenuation coefficients were assessed for accuracy, noise and uniformity. These results were used to determine a range of measurable attenuation coefficients for the PORPs. Accuracy defines the ability to relate a measured attenuation coefficient to a known value. Noise affects the ability to distinguish between different attenuation coefficients. Uniformity of the reconstructed image is used to quantify the accuracy and noise over a large volume.

A secondary objective behind the evaluation of accuracy, noise and uniformity using the PORPs, was to determine the suitability of these phantoms for long term quality assurance measurements.

The spatial fidelity of the reconstructed volume was measured for different resolution settings and at different radial distances from the centre of the rotation. This established the ability of the scanner to reconstruct with a high spatial resolution. The 2D and 3D results were compared to determine the most efficient method of measuring and assessing spatial resolution for QA purposes.

Collimation of the entrance and exit window size affects the light collected in the projection image and, as demonstrated in section 5.6, effects the amount of scattered light detected. The influence of light scatter on the uniformity of a reconstructed volume was evaluated.

Table 6-1: Measurements used to characterise the reconstructed volume of the optical CT scanner.

Measurement	*Reason for measurement*
Reconstructed attenuation coefficient accuracy, noise and uniformity	• Determine the range of reconstructed attenuation coefficients with a high accuracy relative to known value and low noise • Uniformity characterises the accuracy and noise in a large volume. • Evaluate suitability of PORPs as long term quality assurance tools
Spatial Fidelity	• Determine resolution limits for different reconstruction settings
Scattered light influence on reconstruction	• Investigate the influence of scatter on the reconstruction attenuation coefficients

6.2 3D Reconstruction Attenuation Coefficients

Two important properties of the optical CT scanner can be characterised by measurement of the reconstructed attenuation coefficient. First, the accuracy of the reconstructed attenuation coefficient relative to a known value has an impact on dose evaluations. The known attenuation coefficient can be related to a dose. An inaccurate measurement of the reconstructed attenuation coefficient relative to a known value, results in dose being mapped to the reconstructed attenuation coefficients inaccurately. Therefore an under or over dose might be missed. Secondly, the amount of noise in the reconstruction limits the ability to resolve differences in the attenuation coefficient. Low noise in the reconstructed value improves contrast resolution.

Attenuation coefficient accuracy and noise can be used to check the long term consistency of measurements in the scanner. The attenuation coefficient is dependent on the light source and the CCD functioning normally. Abnormal functionality of the light source or CCD will incorrectly reconstruct the attenuation coefficient. Problems with the light source include non-stability of the light intensity over the measurement time and changes in the light source spectra. A change in the CCD quantum efficiency could cause changes to the measured attenuation coefficient.

The aim of this work was to measure a range of attenuation coefficients with high accuracy and low noise for the orange and red light sources in the scanner, using the PORPs. The measurement of attenuation coefficients using the PORPs is important due to the similarity of the PORPs to plastic dosimeters such as PRESAGE™. Oldham et al[67] suggested an accuracy greater than 3 % relative to known values of attenuation coefficient, and noise less than 1 % as a requirement for dosimetric verification. Knowledge of the range of attenuation coefficients measured using PORPs which meets this criteria means the dose response of 3D plastic dosimeters can be tailored or the delivered dose scaled, to suit the range of coefficients.

A secondary objective was to evaluate the potential of the PORPs for use as long term quality assurance (QA) tools. The PORPs were described in section 3.2. Baseline attenuation coefficients of PORPs were measured in parallel beam geometry in section 4.6.

Olding et al[133] have previously published an attenuation coefficient range between 0.0 – 0.2 cm^{-1} for an absorbing solution using a 9.2 cm diameter phantom and an orange light source. An agreement within 3 % and SNR greater than 100 was measured over the 0.06 – 0.18 cm^{-1} attenuation coefficient range[133]. The results were based on the same CCD and model of the scanner but were measured with a different type and sized phantom, which affects the measurable range of attenuation coefficients. This is because the net optical density is dependent on opacity of the medium and path length through the medium. This in turn affects the maximum attenuation coefficient that can be measured.

Since the PORPs have a different diameter and were evaluated for use as a long term consistency tool, the accuracy and noise of the reconstructed attenuation coefficient for the orange and red light sources was evaluated.

6.2.1 *Measurement of Reconstruction Attenuation Coefficient*

Reference, data and dark projection images were acquired in the Vista™ Cone Beam Optical CT scanner. Twenty PORPs were stacked five at a time inside the scanner, similar to the measurement method used to acquire the 2D projection based attenuation coefficients in section 5.2. The reference projections were acquired using a uniform, non-tinted plastic phantom which was the same height as a stack of five tinted PORPs (~10 cm). 410 projection images were acquired of the reference phantom and the PORPs (angular increment of ~0.88° between projections). Projection images were acquired with both the orange and red light sources.

Reconstructed volumes were calculated using the high resolution setting on the Vista™ Recon software. A Feldkamp backprojection technique[160] with a Hamming filter (A= 0.540, B = 0.460) was used during the reconstruction. This created a 256 x 256 x 256 voxel volume with 0.125 mm^3 voxels (0.5 x 0.5 x 0.5 mm). The attenuation coefficient of each voxel was calculated during the reconstruction process. The voxel value is the attenuation coefficient multiplied by the *data multiplier factor*. The factor scales the reconstructed voxels for display purposes[172] and was set to a value of 500.

The reconstructed volumes of the PORPs were analysed in image J. The mean and standard deviation were measured in a volume of interest (VOI) at the centre of each PORP. The VOI used was 10 x 10 x 10 voxels (total 1000 voxels).

The accuracy of measured attenuation coefficient was evaluated by comparison to the baseline value for each PORP. Accuracy was calculated via equation 20 which compared the attenuation coefficient in the central VOI, μ_{CVOI}, to the baseline attenuation coefficient, μ_B, measured in section 4.7. The signal to noise ratio (SNR) in the central VOI was used to determine if the noise criterion (<1 %) was satisfied, with the signal to noise ratio being defined as per equation 21, where μ_{VOI} and σ_{VOI} and the mean and standard deviation of the volume of interest respectively. To achieve this criterion the SNR needs to be greater than 100 (i.e. a ratio of 100:1). Measured central VOI attenuation coefficients are plotted against the baseline attenuation coefficient and line of identity to show the deviation from unity.

$$Accuracy = \frac{(\mu_{CVOI} - \mu_B)}{\mu_B} * 100 \quad (20)$$

$$SNR = \frac{\mu_{VOI}}{\sigma_{VOI}} \quad (21)$$

6.2.2 *3D Reconstruction Attenuation Coefficients*

Table 6-2 shows the accuracy of the measured voxel value relative to the baseline value as well as the SNR for both the orange and red light source. Large differences in both the accuracy and SNR due to non-uniformities were calculated for some of the PORPs. Non-uniformities were identified by visual inspection of the reconstructed data, with a non-uniformity deemed to have an influence if the streaking artefact affected either accuracy or SNR. Some samples appeared to have large differences in

attenuation coefficient or high amounts of noise, which could not be explained by inhomogeneities in the samples. PORP responses that were influenced by non-uniformities in the phantoms have been lightened in colour and italicised. Non-uniformities were observed for PORPs with a baseline attenuation coefficients of 0.094, 0.24, 0.25, 0.29 and 0.42 cm^{-1} using the orange light source, a baseline attenuation coefficients of 0.085, 0.22, and 0.57 cm^{-1} using the red light source. PORPs below the dotted line were beyond the dynamic range of the scanner.

Table 6-2: Baseline vs measured attenuation coefficient accuracy and SNR for the orange and red light source. The values are plotted in Figure 6-1. The measured voxel value has been corrected by the data multiplier factor to be expressed as an attenuation coefficient. PORP responses that were influenced by non-uniformities have been lightened in colour and italicised. Measured attenuation coefficients below the dotted line were beyond the dynamic range of the scanner.

Orange Light				***Red Light***			
Baseline Attenuation Coefficient	Measured Attenuation Coefficient	Accuracy	SNR	Baseline Attenuation Coefficient	Measured Attenuation Coefficient	Accuracy	SNR
(cm^{-1})	(cm^{-1})	(%)		(cm^{-1})	(cm^{-1})	(%)	
0.0	0.006	-	10	0.0	0.008	-	17
0.055	0.049	-11%	102	0.048	0.042	-13%	116
0.094	*0.10*	*6.4%*	*141*	*0.085*	*0.086*	*1.18%*	*60*
0.14	0.14	0.0%	305	0.17	0.12	-29%	314
0.24	*0.20*	*-17%*	*448*	*0.22*	*0.16*	*-27%*	*206*
0.25	*0.24*	*-4.0%*	*350*	0.22	0.20	-9%	677
0.29	*0.28*	*-3.4%*	*505*	0.26	0.23	-12%	506
0.31	0.33	6.5%	582	0.28	0.27	-3.6%	872
0.42	*0.38*	*-9.5%*	*364*	0.40	0.31	-23%	503
0.43	0.45	4.7%	537	0.41	0.36	-12%	171
0.46	0.46	0.0%	444	0.39	0.37	-5.1%	606
0.57	0.51	-11%	462	0.47	0.41	-13%	721
0.58	0.53	-8.6%	460	*0.57*	*0.43*	*-25%*	*273*
0.68	0.59	-13%	221	0.58	0.50	-14%	138
0.81	0.58	-28%	194	0.71	0.50	-30%	553
1.1	0.59	-46%	285	0.88	0.51	-42%	161
1.4	0.58	-59%	53	1.2	0.53	-56%	361
1.5	0.59	-61%	76	1.3	0.53	-59%	94
1.5	0.61	-59%	440	1.3	0.55	-58%	84
1.8	0.66	-63%	185	1.5	0.57	-62%	394

Figure 6-1 A and B shows the VOI mean voxel value measured for each PORP against the baseline attenuation coefficient for orange and red light sources respectively. From the graph it can be observed that a deviation from a linear relationship occurs at a measured signal of ~0.6 and ~0.5 cm^{-1} for the orange and red light source respectively. On both figures a rise in the attenuation coefficient was noticed in the saturation region. The rise occurs above baseline values of 1.3 and 1.1 cm^{-1} for the orange and red light sources respectively.

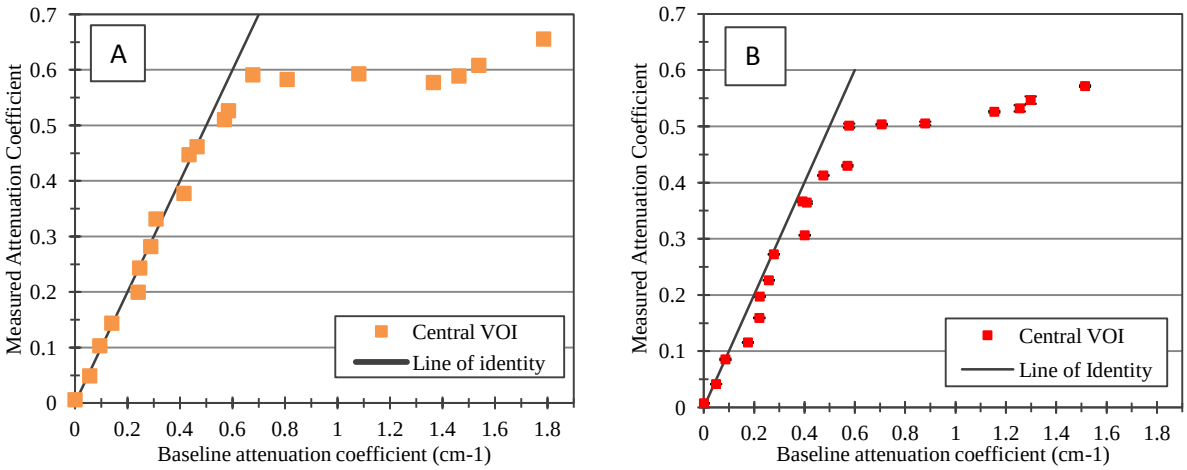

Figure 6-1: 3D attenuation coefficient relative to the baseline attenuation coefficients for each PORP measured using the orange and red light source (A and B respectively). The line of identity is plotted in each figure and shows a linear trend in both light source for baseline attenuation coefficients between 0 – 0.68 cm^{-1} and 0 – 0.58 cm^{-1} for the orange and red light sources respectively.

The results show that central VOI attenuation coefficients measured with the orange light source were within 3 % of baseline values for two PORPs (with baseline attenuation coefficients of 0.14 and 0.46 cm^{-1}).However, it can be seen that the majority of the PORPs (17 of 20) have a signal to noise value greater than 100 which corresponds to noise value less than 1 %. For the red light source, the central VOI was within 3 % of the baseline value for only one PORP (baseline attenuation coefficient of 0.085 cm^{-1}). Similar to the orange light, the majority of PORPs (16 of 20) had a SNR greater than 100.

For the orange light, 9 of 13 measured attenuation coefficients, in the baseline value range between 0.0 – 0.68 cm^{-1}, were within 10 % and the remaining 4 of 13 were within 10 – 17 % of the expected value. 3 of 13 measured attenuation coefficients were higher than expected, with another 2 equal to the expected value. The remaining 8 measured attenuation coefficients were below the expected value.

For the red light, 4 of 13 measured attenuation coefficients, in the baseline value range between 0.0 – 0.58 cm^{-1}, were within 10 % of the expected value and 5 of 13 were between 10 – 14 % lower than the expected value. The remaining 4 were greater than 14 % lower than expected. Accuracy was not calculated for a baseline attenuation coefficient of 0.0 cm^{-1}, hence a total of 13. All attenuation coefficients were below the expected value when measured with the red light source except for the measured attenuation coefficient at a baseline value of 0.085 cm^{-1}.

6.2.3 Discussion

The results indicate a proportional increase in reconstructed attenuation coefficient relative to an increasing baseline value for both the orange and red light source with a maximum measurable attenuation coefficient of ~0.6 and ~0.5 cm^{-1} respectively. Since it is difficult to accurately determine from the graphs the point at which the deviation from a linear relationship occurs, the highest opacity

PORPs with a measured attenuation coefficient within 13 % and 14 % of the expected value, for the orange and red light source respectively, were chosen to represent a maximum measurable signal. For the orange light source the measurable range was between 0.0 – 0.68 cm^{-1}, whilst for the red light source, the measurable range of baseline attenuation coefficients was between 0.0 – 0.58 cm^{-1}.

The orange light source showed slightly greater accuracy relative to the red light source. From a total of 14 PORPs in the baseline attenuation coefficient range between 0.0 – 0.68 cm^{-1} for the orange light source, 2 of 14 PORPs were within 3 % of the expected value and 7 of 14 PORPs were within 3 - 10 % of the expected value. For the red light source, in the baseline attenuation coefficient range between 0.0 – 0.58 cm^{-1} only 1 PORP (0.09 cm^{-1} baseline attenuation coefficient) was within 3 % and 5 PORPs were within 3 - 10 % of the baseline value. A correlation of the data points to a linear line of best fit (forced through 0) over this range shows a coefficient of determination (R^2) of 0.981 and 0.970 for the orange and red data respectively. This suggests a similar linear trend for both sets of data. The gradient of the line of best fit was 0.930 and 0.844 for the orange and red light source. The gradient can be used to compare the data to the line of identity (gradient = 1). This analysis shows the orange data to be closer to the line of identity relative to the red data. This can be observed in Figure 6-1 A and B which shows a closer grouping of the orange data points around the line of identity relative to the grouping of the red data points around a similar line.

The difference between baseline and reconstructed attenuation coefficients could be attributed to non-uniformities, such as bubbles in the PORPs, introduced during the manufacturing process. During transmission measurements for the baseline attenuation coefficients, care was taken to position the PORPS to avoid air bubbles in the transmission path. During the reconstruction process, air bubbles outside the region of interest can influence the measured attenuation coefficient through streaking artefacts which are caused by the refractive index mis-match between the PORP and the air in the bubble. The effect on the reconstructed image is shown in Figure 6-2. The streaking artefact can have two effects: 1) introduce noise into the VOI and therefore influence the SNR, 2) lower the overall attenuation value in the VOI and affect the accuracy of the measured attenuation coefficient relative to a baseline value. The first effect is caused by large variations in measured attenuation coefficient within a VOI. The second influence requires an understanding of the size of streaking artefacts and the VOI size shown in Figure 6-2. Streaking artefacts and VOIs show a similar size, which means an artefact could potentially lower the mean attenuation coefficient in the VOI without influencing the standard deviation of the VOI.

PORPs measured with the orange light source with attenuation coefficient accuracy better than 3 %, did not have attenuation coefficient accuracy within 3 % when measured with the red light source. Similarly, the one PORP measured with the red light source with an attenuation coefficient accuracy better than 3 % did not have the same level of accuracy when measured with the orange light source. Because samples were removed between measurements with different light sources and placed into the

holder in different positions for the two light source measurements, the impact of bubbles and other non-uniformities on the VOI could be different for the two measurements. Additionally, the baseline attenuation coefficient measurements contains a long term reproducibility, positioning and light variation uncertainty in the order of 8 %, 3 % and 1 % respectively (see section 4.7) which could also influence the comparison accuracy between measured and baseline values.

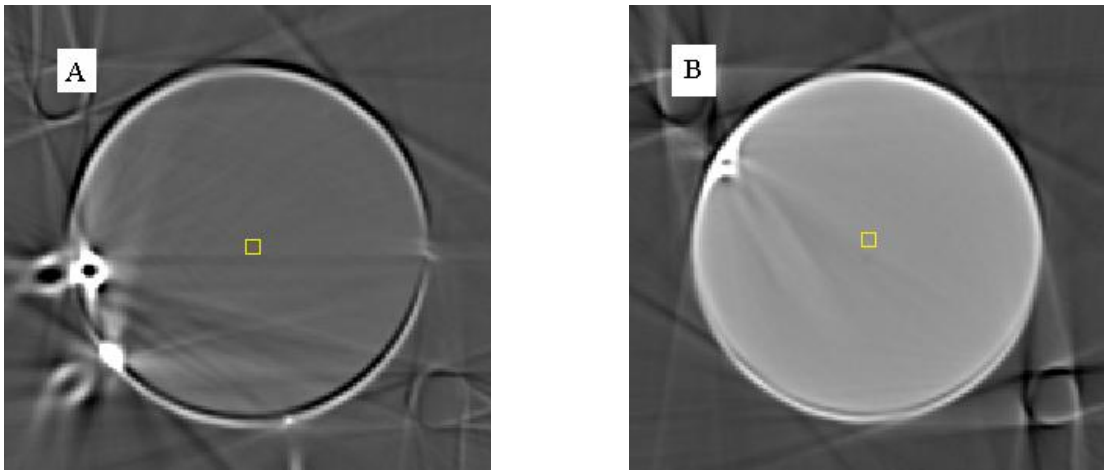

Figure 6-2: Worst case (A) and typical (B) example of streaking artefact caused by air bubbles in PORP. The refractive index mismatch between the air and PORP causes the streaking. The centre VOI is shown for comparison of the streaking artefact and VOI size.

Differences observed for attenuation coefficients below ~0.1 cm^{-1} could be due to small differences in the reconstructed and baseline values being large relative to the low attenuation coefficients. This could effectively limit the measurable range of attenuation coefficients for the PORPs to between 0.094 – 0.68 cm^{-1} and 0.085 – 0.58 cm^{-1} for the orange and red light sources respectively.

The SNR measured in the range between 0.094 – 0.68 cm^{-1} and 0.085 – 0.58 cm^{-1} for the orange and red light sources respectively indicates a noise level below 1 % is achievable. This corresponds to a high contrast resolution.

To determine if these ranges are sensible, the range of optical densities measurable using the CCD can be calculated based on a realistic range of pixel values and compared to the range of optical densities calculated using an attenuation coefficient range of 0.094 – 0.68 cm^{-1} and 0.085 – 0.58 cm^{-1} (orange and red light source respectively). The optical density measurable by the CCD can be calculated by the ratio of the minimum to maximum pixel value (i.e. 1:65536), or an OD range of ~11 (calculated via equation 22). Thresholding and saturation of the CCD response affects the minimum and maximum pixel value respectively. Assuming noise limits the minimum useful pixel value to ~1000 and saturation limits the maximum to ~64000 (section 4.5), the range of optical densities measurable is between 0.06 and 4.2 (I/I_0 = 60000/64000 and 1000/64000 respectively). Using an attenuation coefficient range of 0.094 to 0.68 cm^{-1} over the diameter of a PORP (7.8 cm), results in an OD range between 0.73 to 5.3 (0.094 cm^{-1} x 7.8 cm and 0.68 cm^{-1} x 7.8 cm respectively). For the OD range 0.085 – 0.58 cm^{-1}, the OD range is 0.66 to 4.5.

$$Net\ OD = \mu d = -\ln\frac{I}{I_0} \qquad (22)$$

Calculation of the measurable optical density range is important. From the values we can determine the maximum optical density that can be measured before saturation will influence the measured signal. Calculation of the range of measurable optical densities can also allow comparison between attenuation coefficient ranges measured with different diameter uniform phantoms. It is important to note that for gel dosimetry measurements, the maximum optical density does not have to be evenly spread over the entire pathlength and that the majority of attenuation can occur over a small distance provided the overall attenuation along the pathlength does not exceed the maximum measurable optical density. The maximum of the OD range from these calculations are larger than the expected value of 4.2 which indicates that the maximum and minimum useful pixel values may be slightly different to the assumed values used in the calculations above. An example of this is that if the minimum usable pixel value was changed to 500, then the maximum measurable optical density would change to 4.9.

Olding et al[133] presented a range of attenuation coefficients for the orange light source that could be measured accurately (< 3 %), with minimal noise (<1 %), between 0.06 – 0.18 cm^{-1} over a sample diameter of 9.2 cm, which represents a OD range between 0.55 to 1.6. The data for the red light source published in the same body of work did not contain enough data points to calculate a range of attenuation coefficients with a linear response. The linear OD range presented is smaller than the range measured in this work. The difference could be caused by a difference in the accuracy criterion. At a maximum of 0.18 cm^{-1}, the results are within 3 % of the spectrophotometer measured values[133]. Our work chose a maximum value with less accuracy as a maximum attenuation coefficient. Investigation of the data presented by Olding et al[133] shows a data point with an error in the order of 25 % of the expected value at a reference value of ~0.5, however they did not discuss this at all. This is similar to the accuracy observed in our data. When this attenuation coefficient range (0.06 – 0.5) is used, the OD range (calculated with a sample diameter of 9.2 cm) becomes 0.55 – 4.6. This is similar to the range of OD values measured in our work and the dynamic OD range measurable with the CCD.

As stated earlier, non-uniformities in the PORP phantoms affected the measured reconstruction accuracy and the baseline values. Some of the non-uniformities are air bubbles and scratches on the PORP surface. The dominant artefact caused by the air bubbles was streaking. The method used by Olding et al[133] used a uniform solution in a spectrophotometer as a measurement of the baseline attenuation coefficient. This measurement technique is less susceptible to bubbles. The method used in these experiments was an analysis of the accuracy and noise of an experimental set-up that could be used for quality assurance using a single set of samples indefinitely which cannot be done with liquid samples.

In Figure 6-2 it can also be observed that the edges of the reference and data PORP were not properly aligned. This artefact could have two main sources of error; (i) the reconstruction axis offset was not

measured properly, or (ii) the placement of the PORPs in the holder was not accurate. The reconstruction axis was identified early in the process as a potential source of error and was corrected for. However, the placement of the PORPs in the holder was not robust and errors in position could be introduced. The edge artefact is not expected to significantly influence reconstruction accuracy at the centre of a reconstructed volume.

Saturation of both light sources occurs above 0.68 and 0.58 cm^{-1} for the orange and red light source respectively. At this point the transmitted light intensity is approximately equal to the background noise inherent in the CCD. As explained in section 5.3, attenuation coefficient saturation occurs when the difference between non attenuated and attenuated light intensity is large and the transmitted light intensity is approximately equal to the background noise.

The 2D process of acquiring attenuation coefficients has the advantage of less scanning time, resulting in less time for QA of the optical CT scanner and more time performing treatment QA measurements. The advantage is lost due to the high level of noise in the 2D projections making their use for routine QA unfeasible. Using reconstructed volumes of uniform phantoms was the most accurate method of measuring accuracy of the attenuation coefficient relative to baseline values due to the lower level of noise. The lower noise for 3D images could be attributed to the "binning" of pixel values in a projection image prior to reconstruction. Binning is the process of averaging a region of pixels into one value to represent the region[139], which improves the SNR and decreases reconstruction time.

The secondary objective of this work was to evaluate the PORPs for long term consistency measurements. The PORPs did not have the required accuracy for use as a long term QA tool. However, the low level of noise suggests that the PORPs could be used for long term QA provided there is better quality control during the manufacturing process.

6.3 Uniformity of Attenuation Coefficients in a Reconstruction

Uniformity of reconstructed values can be used to check the accuracy and noise over a large volume, which defines the relationship to known attenuation coefficients and the contrast resolution respectively (see section 6.2). Uniformity measurements can also be used to check the consistency of the light measurement over a period of time. The objective of this section was to measure the uniformity and therefore evaluate the reconstruction voxel accuracy and noise away from the central rotation axis. The results will also be used to characterise the PORPs as a quality assurance tool.

Previously uniformity measurements have been used to investigate stray light[133,136,137] which has an influence on the measured uniformity of an absorbing phantom. This was especially noticeable for highly absorbing phantoms, causing bowing of the constant profiles expected from measurements of uniform phantoms[133,137].

Four volumes of interest (VOI) were defined at peripheral locations and one at the centre of a reconstructed volume to quantify the accuracy and noise. The accuracy of the peripheral VOIs was measured relative to the centre, whilst the noise was measured in all five VOIs. The use of the VOI allows a quick numerical comparison of the constancy over a period of time. The VOIs method employed in this work is similar to consistency of uniformity measurements used in x-ray CT scanners.

6.3.1 Method

The PORPs were evaluated and reconstructed in section 6.2. Briefly, the PORPs were reconstructed from 410 projection images of both the reference and data phantoms. The reference PORP was a clear plastic cylinder 10 cm in length. Each individual PORP had a height of 2 cm and a unique attenuation coefficient. The PORPs were stacked 5 at a time into the scanner. Vista^{TM} Recon was used to reconstruct 0.5 mm^3 voxels using a Hamming filter (A = 0.540, B = 0.460) with a volume size of 256 x 256 x 256 voxels.

Volumes of interest (VOIs) were identified at the top, bottom, left and right of the reconstructed phantom volume (as shown in Figure 6-3). These volumes were collectively referred to as the *outer VOIs*. The mean and standard deviation in each outer VOI was measured for PORPs with an approximately linear attenuation coefficient range between 0.085 – 0.58 and 0.094 – 0.68 cm^{-1} for the red and orange light source respectively. The VOI positions were selected to be symmetrical around the central VOI and away from the interface between adjacent PORPs (see overlap artefact in Figure 5-1 on page 85). The size of each VOI was 10 x 10 x 10 voxels (125 mm^3). This is identical to the VOI used in the measurement of the attenuation coefficients at the centre of the VOI. Therefore comparisons of attenuation accuracy and noise can be made between the outer and central VOI. The accuracy was calculated relative to the central axis reconstructed attenuation coefficient.

To validate the VOI method, solutions of different concentrations of dye and water were scanned and VOIs were compared to profiles measured across the reconstructed images of the solutions. The dye solutions were used to provide a set of results which would be observed in ideal circumstances. This is because dye solutions are known to be uniform and absorbing. The measured profiles were 10 pixels wide and measured over 10 slices. The position of the profile used to measure each phantom was selected to pass through the left, centre and right VOI. Therefore a comparison of profiles and these VOIs was presented. A comparison through the top, centre and bottom was not presented as the uniform phantom is radially symmetric.

Both the orange and red light sources were used in the investigation of the accuracy and noise in the PORP. The VOI method was validated with the red light source.

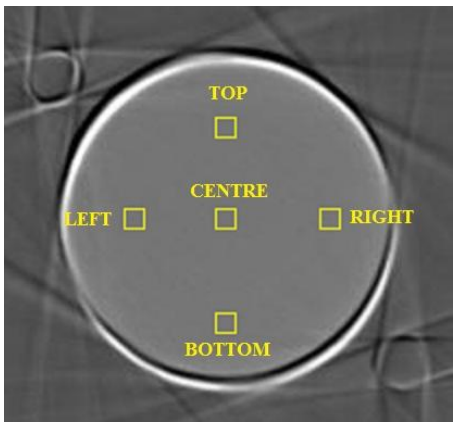

Figure 6-3: Axial slice from a uniform absorbing phantom showing the position of the outer and central VOIs used to investigate uniformity for all PORPs. The size of each VOI was 10 x 10 x 10 voxels (125 mm^3). The mean and standard deviation were measured in order to compare accuracy and noise (via SNR) relative to the central VOI.

6.3.2 Results

To validate the VOI method, the measured profiles across a number of phantoms tinted using an absorbing dye was compared to the differences in the VOIs in Figure 6-4. As can be seen in Figure 6-4 A, some wall artefacts were observed and bowing artefacts affect the high dye concentration profiles. The solutions with a concentration of 1.0 x 10^{-5}, 1.5 x 10^{-5}, 2.0 x 10^{-5} and 2.5 x 10^{-5} % have profiles that appear flat (Figure 6-4 A) and have a VOI accuracy within 2 % (Figure 6-4 B). Figure 6-4 B shows a 2 – 2.5 % difference between the outer and central VOI at an absorbing dye concentration of 5.0 x 10^{-6} %. Differences of ~5 % were observed at concentrations of 3.5 x 10^{-5} and 4.0 x 10^{-5} %. A difference of ~10 % was observed at a concentration of 4.5 x 10^{-5} %.

A comparison between the outer VOIs relative to the central VOI, measured using the PORPs, for the orange and red light sources is shown in Figure 6-5 and Figure 6-6 respectively. Data measured at 0.24 cm^{-1} with the orange light source (Figure 6-5) and at 0.22 and 0.57 cm^{-1} with the red light source (Figure 6-6) are close to measured data from other PORPs.

The orange light source's outer and central VOIs show agreement within 5 % over a PORP baseline attenuation coefficient range of 0.094 – 0.68 cm^{-1} (Figure 6-5 A). Values below 0.14 cm^{-1} show large inaccuracies and a low SNR. VOI's with a difference of greater than 5 % in the attenuation coefficient range 0.14 – 0.6 cm^{-1} were observed for the right, left and bottom VOI for the PORP with a baseline attenuation coefficient of 0.24 cm^{-1}, the bottom VOI for the 0.58 cm^{-1} PORP and all VOI for the 0.68 cm^{-1} PORP.

From Figure 6-5 B, the SNR in the attenuation coefficient region 0.14 – 0.6 cm^{-1} was above 100 for all VOIs, except for the left VOI for the 0.24 cm^{-1} PORP and the bottom VOIs for the 0.24 and 0.58 cm^{-1} PORPs.

Figure 6-6 A shows the red light source accuracy. The outer VOI were within ± 5.0 % of the central VOI in the attenuation coefficient range 0.085 – 0.58 cm^{-1}. Differences greater than 5.0 % were

observed for the left and bottom VOI of the 0.22 cm^{-1} PORP, the top and left VOI of the 0.28 cm^{-1} PORP, the top, left and bottom VOI of the 0.39 cm^{-1} PORP, the bottom VOI of the 0.41 cm^{-1} PORP, the left, right and bottom VOI of the 0.57 cm^{-1} PORP and all VOI for the 0.58 cm^{-1} PORP.

From Figure 6-6 B it is observed that the SNR was above 100 for all VOI in the attenuation coefficient range between 0.15 – 0.58 cm^{-1} except for the left VOI for the 0.22 and 0.41 cm^{-1} PORPs, the bottom VOI for the 0.22 cm^{-1} PORP and the right VOI for the 0.57 cm^{-1} PORP.

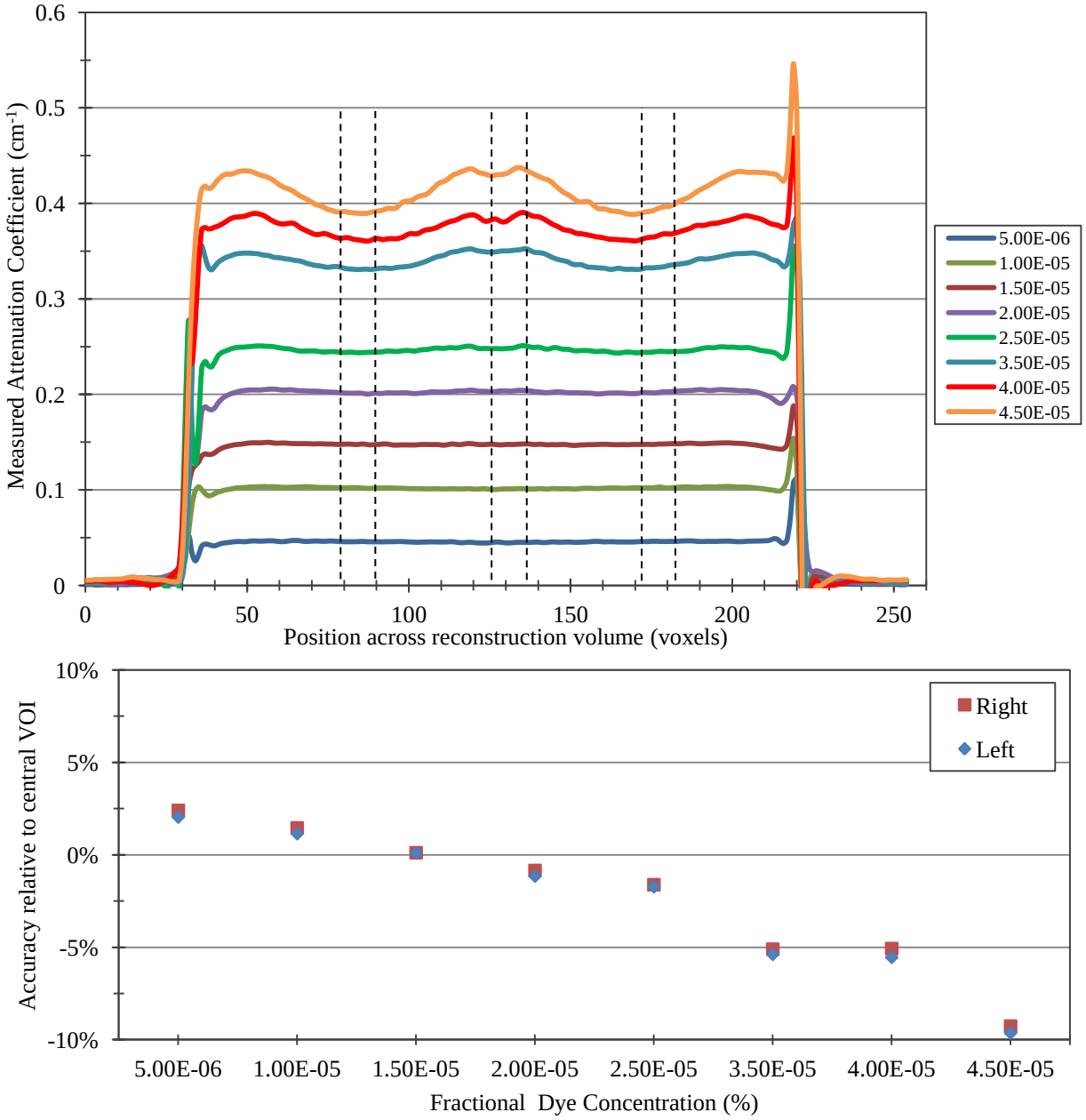

Figure 6-4: A) Profiles acquired across uniform phantoms with the corresponding VOI positions. The left and right VOI were used to calculate the accuracy relative to the central VOI (B). This is used to indicate the uniformity of the reconstructed image.

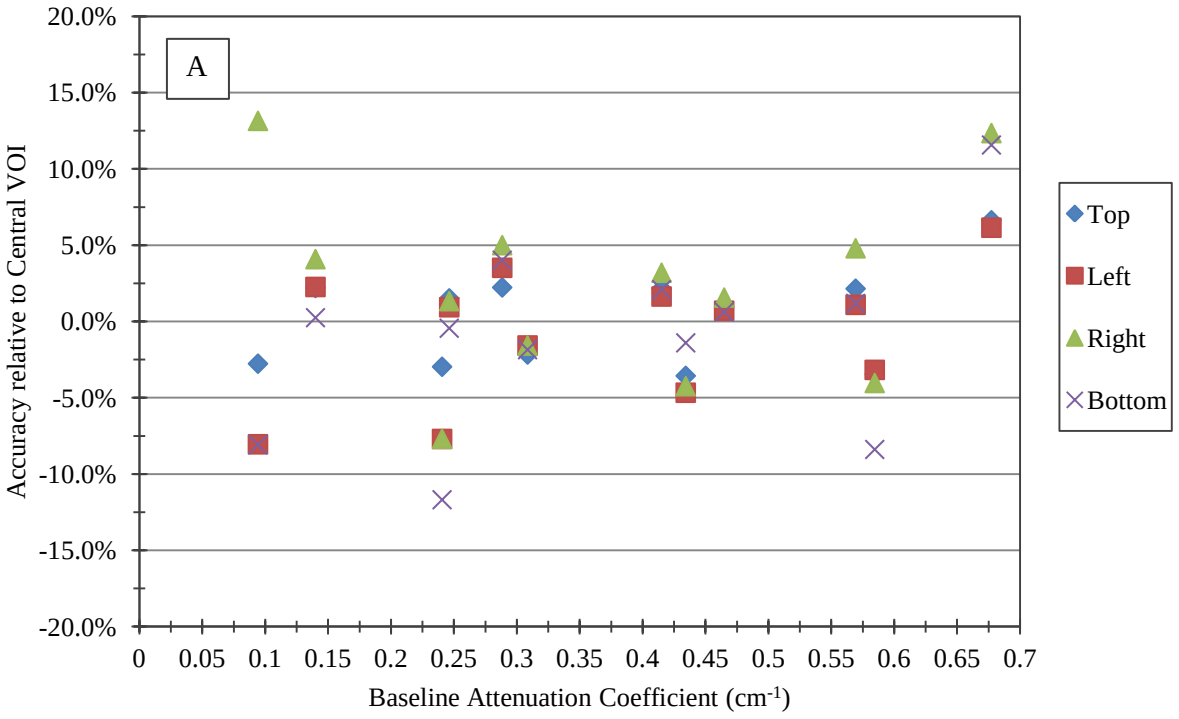

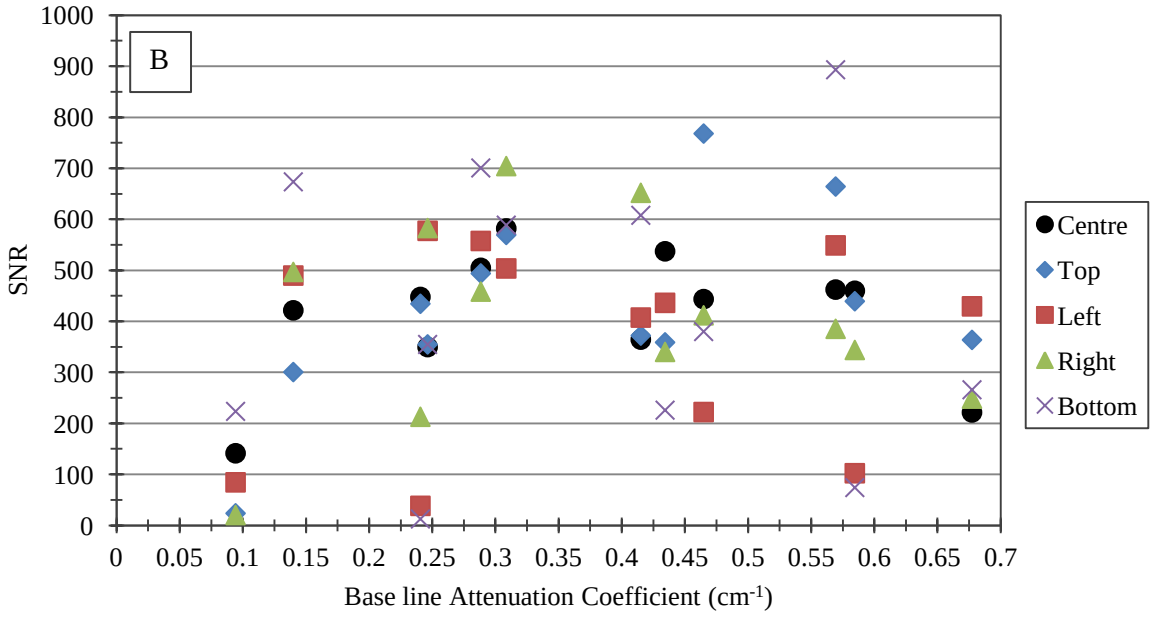

Figure 6-5: A) Outer VOI accuracy relative to the central axis for the orange light source measured using the PORPs. The accuracy shows agreement within ±5.0 % over an attenuation coefficient range 0.14 – 0.58 cm^{-1}. B) The SNR for each VOI was above 100 for all VOI in the attenuation coefficient range described. Values outside 5 % accuracy and above 1 % noise (below 100 SNR) were due to non-uniformities in the PORPs.

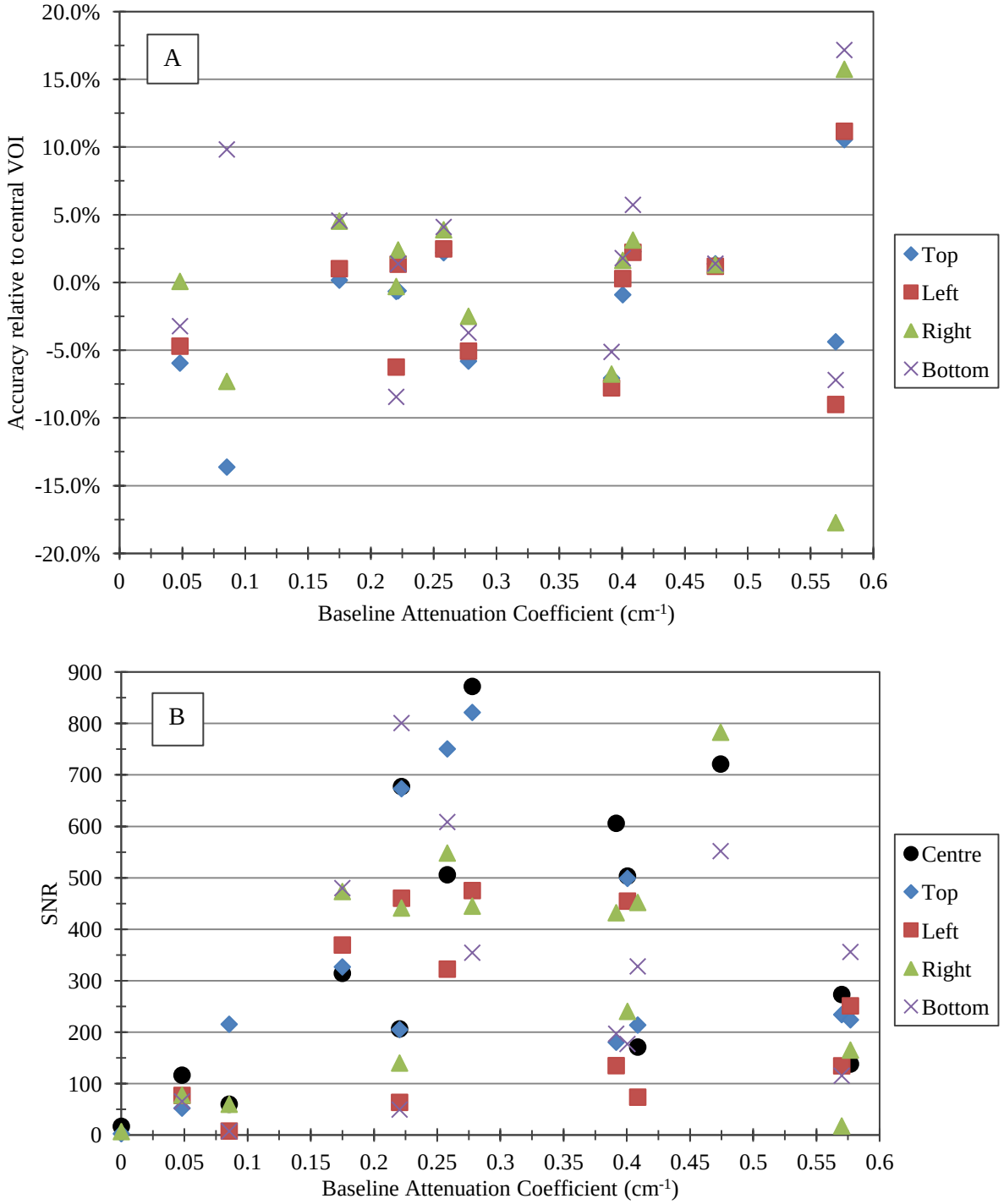

Figure 6-6: A) Outer VOI accuracy relative to the central axis for the red light source measured using the PORPs. The accuracy shows agreement within ±5.0 % over an attenuation coefficient range 0.17 – 0.47 cm^{-1}. B) The SNR for each VOI was above 100 for all VOI in the attenuation coefficient range described. Values outside 5 % accuracy and above 1 % noise (below 100 SNR) were due to non-uniformities in the PORPs.

6.3.3 Discussion

The uniformity of the profiles used to validate the VOI method indicates ratios within 2 % between the outer and central VOI for a flat uniform reconstruction. The results highlight how the uniformity of a reconstructed image can be reduced to a comparison of the mean voxel attenuation coefficient in VOIs from different regions in the phantom. This potentially eliminates the requirement of measuring profiles, plotting the profiles and then comparing the profiles. The accuracy of outer relative to central VOI could be compared to baseline values to indicate changes in uniformity over a period of time with increased efficiency relative to the profile plotting method. A study on the reproducibility of this measurement is required to characterize this technique which is similar to a method used in x-ray CT[173].

Drawbacks to this technique include large inaccuracies for low attenuation coefficients and false positives where a profile is not constant but the VOI are within the expected accuracy of each other. For low concentration solutions, the observed profile appears flat, but the calculated percentage difference can be large. Similar to the inaccuracies observed for low attenuation coefficients relative to known values in section 6.2, small differences in small values are relatively large.

The grouping of the outer VOIs measured for each PORP suggests a high accuracy between the outer VOI. This result and the high accuracy between the outer and central VOI observed for the absorbing dye and water solutions, indicates that the observed percentage differences in the outer VOI relative to the central VOI for the VOI measured with PORPs are potentially caused by an artefact. The PORPs were scanned in water which has a different refractive index compared to polyurethane (the primary ingredient in PORPs). A refractive index mismatch has been shown to cause artefacts[63]. As observed in section 5.2, a profile from an absorbing model does not accurately represent a similar profile acquired through a PORP which was acquired in water with the observed differences between the model and the PORP increasing with distance from the central axis. As such the difference between central and outer VOI could increase because of this. The close grouping of the outer VOI indicates that the PORPs could potentially have accuracy within 2 % if refractive index mis-matching is the source of this artefact. Refractive index mis-matching would cause a systematic shift in the outer VOI relative to the central VOI, with the difference increasing with attenuation coefficient. This is because the actual profile always underestimates the model profile (see section 5.2), which would result in a systematic shift, and the difference between model and measured profile appears to increase with attenuation coefficient. The results presented here do not show a systematic error or degradation in the accuracy, prior to the decrease in accuracy caused by saturation of the signal at a baseline attenuation coefficient of ~0.6 cm^{-1}.

Some differences between the outer and central VOI, measured for the PORPS with the orange and red light sources, were due to streaking from the Perspex rods, air bubbles and wall artifacts due to misalignments between the reference and data PORPs. Non-uniformity artefacts were described and

examples given in section 6.2.3. Once the inaccurate and noisy VOIs caused by non-uniformities were removed, the VOI method showed agreement between the outer VOI and central VOI within 5.0 % and a high SNR over the baseline attenuation coefficient range 0.094 – 0.58 cm^{-1} and 0.085 – 0.47 cm^{-1} for the orange and red light sources respectively.

Olding et al[133] measured the attenuation coefficient of an absorbing solution with a 3 - 4 % accuracy relative to reference values over the range 0.06 – 0.18 cm^{-1} for more than 60 % of the volume of a 9.2 cm diameter, cylindrical container. The SNR is this region was greater than 100. The measurable attenuation coefficient range in the current system is expected to be different due to the different diameters of the phantom used. The results from the absorbing dye solutions are truly homogeneous and indicate uniformity can defined by an agreement between outer and central VOI within 3 %. The observed accuracy of the outer relative to central PORPs indicates that if care is taken to minimise the impact of air bubbles, non-uniformities and refractive index mis-matches, then a level of 3 % accuracy should be achievable.

6.4 3D Reconstruction Spatial Resolution

Spatial resolution is a measure of how accurately a high contrast change can be evaluated as the distance between two high contrast objects is reduced. The spatial resolution of a cone beam scanner has previously been determined for projection images[133] and 3D reconstruction volumes[145]. The spatial resolution has a dependence on source to axis distance, the CCD and focal length of the lens. A scanner can have many combinations of these properties and therefore each scanner requires measurement during the characterisation of the scanner.

6.4.1 Method

A PORP phantom implanted with 10 metallic wires in a spiral pattern was acquired and reconstructed in the scanner. The wire had a diameter of 25 µm. 410 projections were acquired of the PORP wire phantom. The non-tinted phantom, used in the attenuation and uniformity measurements previously, was used as a reference for this work. The presented method is similar to the spatial resolution measurement presented for CT scanners[173].

The scanner in this work had a CCD to central axis distance of 55.3 cm and a 2/3” Computer M1212-MP2 lens (CBC Group, Tokyo, Japan).

The scanner was allowed a sufficient warm-up time and the shutter speed was set so that the maximum pixel value was ~64000. The reconstruction used the Vista™ Recon program and a Hamming filter (A = 0.540, B = 0.460) to reconstruct a volume for each of the settings in Table 6-3.

The reconstructed volume was imported into ImageJ and 5 profiles, placed in a spoke pattern, across each of the wires were used to calculate an average point spread function (PSF). The 5 profiles were

registered to each other via alignment of the maximum pixel value. This was designed to smooth out the digitisation of the point spread function caused by the finite size of the voxels. The profiles avoided changes in intensity caused by artefacts from neighboring wires where possible.

Table 6-3: Differences between various reconstruction resolutions. For each increase in the reconstruction resolution settings: the number of voxels in each slice increases by a factor of 4, the number of slices doubles, the memory required increases by a factor of 8 and the voxel size decreases by a factor of 8.

Reconstruction Setting	*Axial slice size (Voxels)*	*Number of slices*	*Reconstruction memory*	*Voxel size (mm)*
Extreme	512 x 512	512	512 Mb	0.25 x 0.25 x 0.25
High	256 x 256	256	64 Mb	0.5 x 0.5 x 0.5
Medium	128 x 128	128	8 Mb	1 x 1 x 1
Low	64 x 64	64	1 Mb	2 x 2 x 2

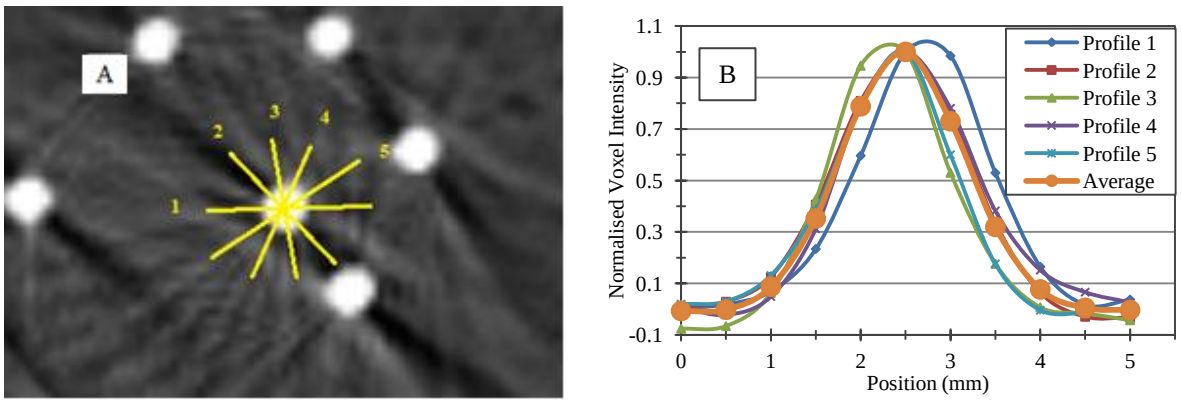

Figure 6-7: A) 5 profiles acquired across the point spread function from a wire. B) The profiles were aligned according to maximum pixel value and an average point spread function (PSF) calculated. Lines have been included to aid the eye. A Fourier transform was then applied to the PSF to calculate the modulation transfer function.

The PSF was used to calculate the MTF. Due to the wire having a finite width and not being a delta function, the MTF of the wire potentially needs to be de-convolved from the measured MTF. However, it was shown in x-ray CT scanners that provided the wire diameter was sufficiently small relative to the sampling interval, then the correction applied will be within the measurement error[174]. The wire diameter used in our scanner was 25 µm, which was much smaller than the sampling interval of 0.25 mm. Thus, the measured MTF of the wire was used and a correction to de-convolve the finite wire diameter was not applied.

According to Nyquist theory, the sampling of the point spread function should be twice the cut-off frequency[174]. The cut-off frequency is the maximum frequency that can be measured without a reduction in signal[175]. Since the voxels have a finite size of 0.25 mm (i.e., sampling frequency of 4 mm^{-1}), the cutoff frequency is defined as 2 cycles/mm (i.e. 1 lp/mm). Therefore, the number of pixels sampled across the FHWM of the peak spread should be approximately 8 (2 x 4 voxels). Practical measurements have shown that a total of 5 – 6 pixels in the FWHM of the PSF were sufficient to calculate the MTF in reconstructed volumes from x-ray CT scanners[174].

6.4.2 Spatial Resolution

The same slice from a low, medium, high and extreme reconstruction setting is shown in Figure 6-8. Care was taken to use the default window and level settings. However, the point of the figure is to display the level of detail achievable with the different resolutions.

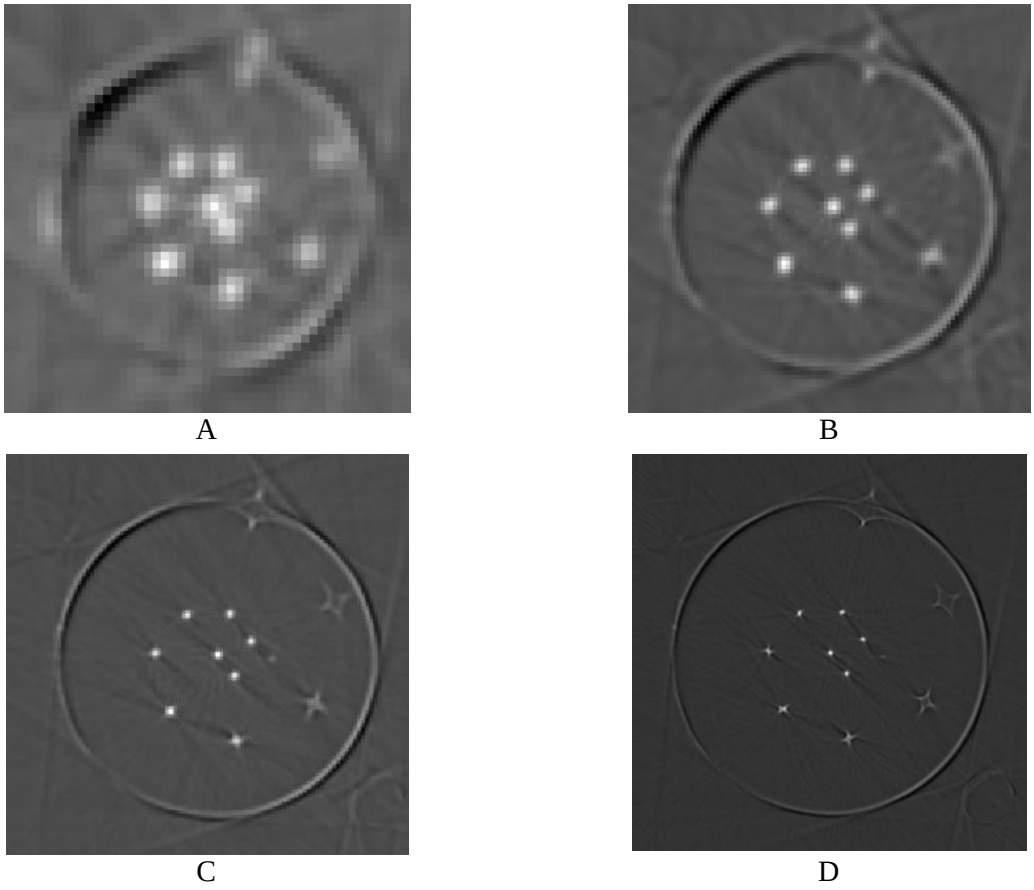

Figure 6-8: Central slice from low (A), medium (B), high (C) and extreme (D) resolution reconstructions. The image displays the increasing amount of detail observed as the reconstruction setting was changed.

Point spread functions measured across the central wire and the calculated MTF for each of the resolution settings in Table 6-3 are shown in Figure 6-9 A and B respectively. The FWHM of the PSF was observed to decrease as the voxel size was decreased. This indicates that the spatial resolution improves as the voxel size decreases. 50 % modulation values of 0.04, 0.12, 0.29 and 0.44 lp/mm were calculated for the low, medium, high and extreme resolution settings respectively.

Streaking artefacts were observed around all wires, with the magnitude of the artefact increasing with radial distance (Figure 6-10). The PSF measured at each radial distance between 0 and 15 mm (Wires 1 – 6) is shown in Figure 6-11 A. Individual profiles measured at larger radial distances were not Gaussian in shape due to streaking artefacts and therefore did not accurately represent a point spread function. However, when averaged together a Gaussian shape can be observed. An example of the average profile measured for the wire at position 7 is shown in Figure 6-11 B. The PSF measured for the wire at position 10 was not Gaussian in shape. Therefore no MTF could be calculated at this position.

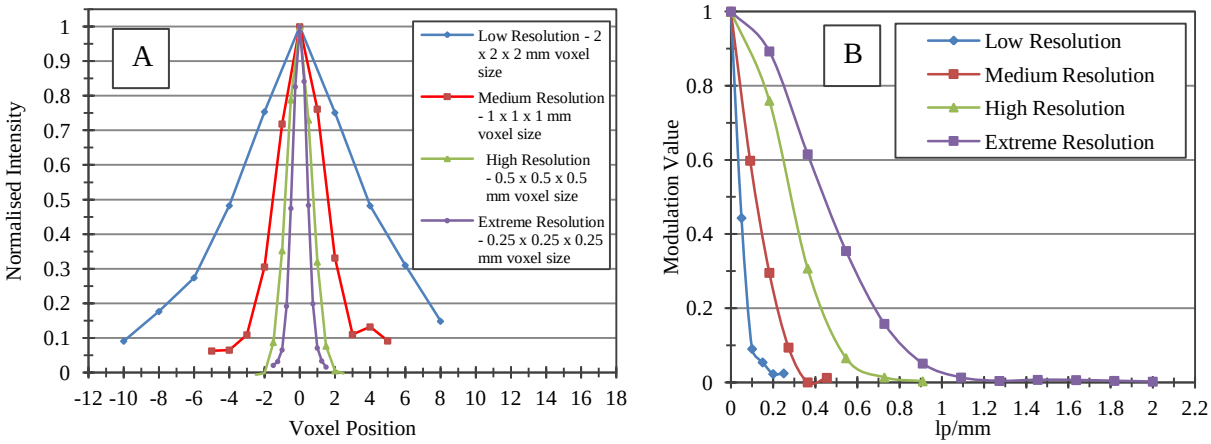

Figure 6-9: A) Point Spread Functions measured for the different resolution settings. Lines have been added to aid the eye. The decrease in FWHM indicates an increasing spatial resolution. (B). MTF calculated for the different resolution settings.

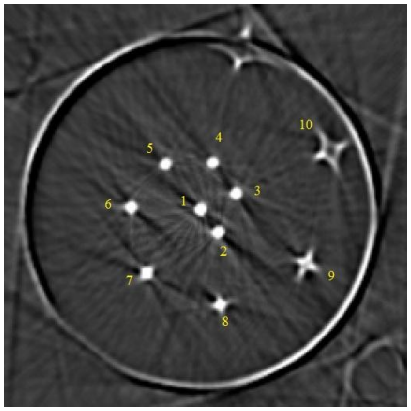

Figure 6-10: Slice from spatial resolution phantom. Phantom was reconstructed with the extreme resolution setting. The reconstruction of the wires in the spiral pattern was observed to degrade with radial distance from the centre of the projection.

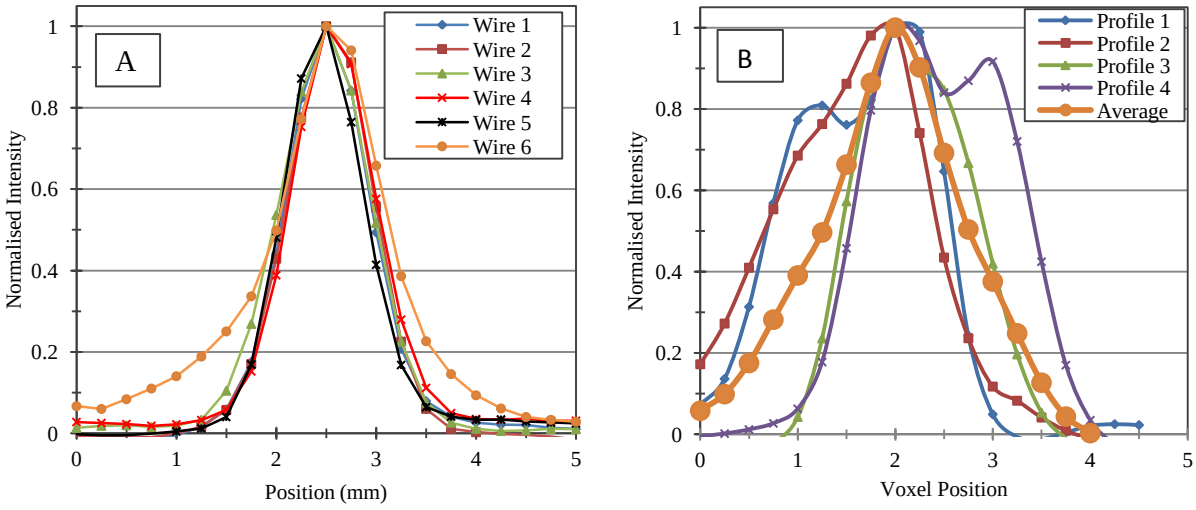

Figure 6-11: A) Measured PSF for the first 6 wires. The first 5 wires have a similar shaped profile, whilst for beam 6 the streaking artefact starts to influence the shape of the profile. B) The measured profile across wire 7. Lines are used to aid the eye.

Figure 6-12 A shows the MTF for positions 1 – 9. The dashed line has been added to aid the eye in finding the 50 % modulation value. Profiles at positions 1 - 5 show a general agreement with each other with position 6 showing a small decrease in modulation. The MTF measured at positions 7 – 9 show a significant change in modulation. Figure 6-12 B shows the 50 % modulation values, calculated via linear interpolation, against the distance from the centre of the phantom. The line pairs per millimetre measurable at a 50 % modulation are within ± 0.02 lp/mm until a radial distance of 12.5 mm. At increased radial distances the spatial resolution decreases.

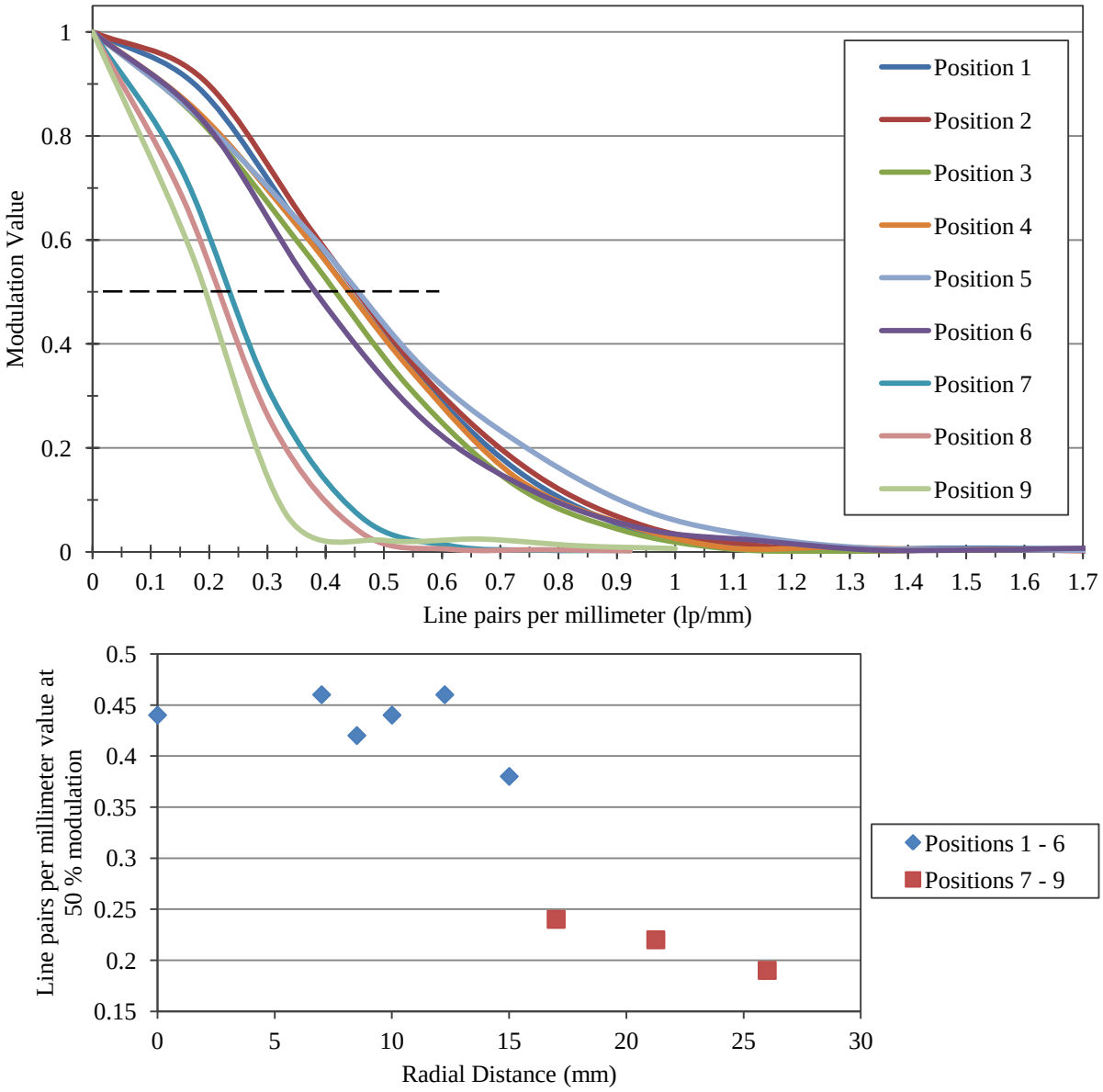

Figure 6-12: MTF for positions 1 – 9 (A) and the line pairs per millimetre measurable at a 50 % modulation as a function of radial distance (B). A dashed blue line has been added to A in order to aid the eye in determining the 50 % modulation values. The line pairs per millimetre values in B were determined via linear interpolation. Positions 1 – 6 and 7 – 9 have been separated due to the profiles at position 7 – 9 being affected by streaking artefacts.

6.4.3 Discussion and Comparison to 2D Projection Measurements

The PSF decreases in size as the reconstruction setting is changed from low to extreme indicating an increase in spatial resolution. The increase in spatial resolution with a decreasing voxel size is expected, because the point spread function is reconstructed with less blurring using smaller voxels. The low reconstruction resolution PSF was effected by an inability to resolve two wires close to each other (see Figure 6-8 A). Figure 6-13 shows the normalised profile measured across the wires at both positions 1 and 2 for the low resolution setting. The profile used for MTF measurements (shown in Figure 6-9 A) was not an average profile found via multiple profiles arranged in a spoke pattern, but a single profile which was not influenced by neighboring wires. Since this profile was not an average, the used profile may not be an accurate representation of the PSF.

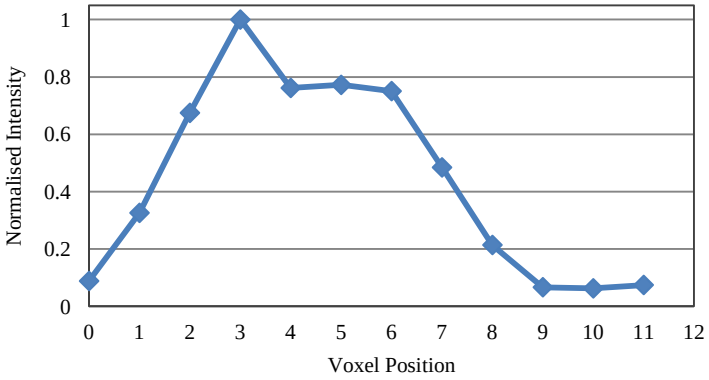

Figure 6-13: Profile across both wires at position 1 and 2 for the low resolution reconstruction settings. The profile highlights the inability to resolve the two wires into two separate PSF.

The MTF calculated for the different resolution settings show the expected increase in spatial resolution as the resolution is changed from low to extreme. However, Figure 6-9 A shows that the number of points in the FWHM was only equal to 5 or greater for the extreme resolution setting. For the other resolution settings, the FWHM contained less data points. As described in the introduction, calculation of the MTF requires a minimum of 5 – 6 pixels across the FWHM. Therefore the observed MTF could potentially be affected by a lack of data points.

The 50 % modulation value for the extreme resolution setting (0.44 lp/mm) will not be sufficient to meet the suggested criterion[67] (spatial resolution within 1 mm^3). To meet this criterion, the 50 % modulation value is required to be greater than 0.5 lp/mm.

Figure 6-12 A and B show that the spatial resolution does not vary with radial distance out until an approximate radial distance of 12.5 mm. At a distance of 15 mm the spatial resolution measurable with a 50 % modulation value drops to 0.38 lp/mm. The 50 % modulation values decreased significantly beyond 15 mm (wire positions 7 – 9) and is most likely related to the streaking artefact and does not potentially show a true decrease in spatial resolution. Therefore no conclusion could be drawn over the

trend of the MTF beyond 15 mm. To determine a trend at radial distances greater than 15 mm, a phantom needs to be developed that addresses the streaking artefacts observed for wires at positions 7 – 10.

Streaking artefacts were caused by the wires being totally opaque. This is similar to streaking observed when metallic objects are scanned in x-ray CT. Good practice when measuring spatial resolution in x-ray CT is to measure a high contrast object without saturating the CT number range[176]. In optical CT, the wire causes a saturation of the reconstructed attenuation coefficient. To avoid this, an optical fiber could be used, similar to the method presented by Papadakis et al[145]. However, problems with the refractive index matching between a fiber and the surrounding material may still exhist, but this is not known from Papadakis et al[145] as no images of the of the spatial resolution phantom were shown in the manuscript. An alternative method of determining spatial resolution could use the edge spread function across the edge of a thin gel finger of low to medium opacity in a clear gel. However, there would be potential diffusion issues of the opaque tint from the finger toward the clear gel which could influence the shape of the edge spread function.

The central axis offset is a known source of error in the measurement of the spatial resolution[63] and was checked before the measurements. The wall artefacts observed in Figure 6-10 are due to misalignments in the placement of the reference and wire phantom in the holder instead of a misalignment in the central rotation axis offset. As described in section 6.2.3, a more robust and reproducible PORP holder is required to eliminate this error.

Papadakis et al[145] measured the reconstructed spatial resolution on an in-house built cone beam optical CT scanner. The in-house scanner's CCD was different to the CCD used in this work. The distance between the CCD and the position of the spatial resolution measurement was not communicated[145]. The presented optical CT's spatial resolution was 1.1 lp/mm at 10 % modulation[145]. At the centre of the reconstruction for the optical CT in this work, the spatial resolution at 10 % was 0.83 lp/mm. The difference between these 10 % modulation values could be caused by the different CCDs (more specifically, different pixel size of the CCDs) and different distances between the CCD and the centre of the reconstruction.

The method of measuring and analysing the spatial resolution for 2D and 3D is not dissimilar. In each method a sharp, high contrast object is used to measure the MTF. Comparison between 2D and 3D spatial resolutions is difficult because a decrease in the spatial resolution between 2D projections and 3D reconstructions is expected due to the Vista™ Recon program averaging a region of 4 x 4 pixels in a projection into a single value prior to reconstruction[133]. With the 2D method, time is saved due to not acquiring a large number of images and reconstructing the data. The higher spatial resolution for the 2D projections could potentially offer improved sensitivity for quality assurance purposes.

6.5 Investigation of Scatter Contribution in Reconstructions

Stray light has been observed to influence the reconstructed voxel values for profiles measured across both scattering[130,131,133] and absorbing phantoms[133,136].

In section 5.6, the measured projection profiles across a dye phantom were observed to increase in measured attenuation as collimating cardboard was added to the entrance and/or exit of the specimen tank. This section uses the same window collimation configurations to investigate the influence of scattered light on a reconstruction of a uniform phantom. Similar to section 5.6, the measurements are not designed to calculate a quantitative correction, but are used to show the magnitude and source of stray light.

6.5.1 Method

Collimator configurations used to evaluate stray light in reconstructed data were described in detail in section 5.6.1. Briefly:

- Light not originally incident on the CCD that is scattered toward the CCD was reduced by collimation at the entrance window of the specimen tank (i.e. the window closest to the light source).
- Light scattered in the tank was reduced by collimation at the exit window of the tank (i.e. the window closest to the CCD).
- Both forms of stray light were reduced by collimation at the entrance and exit windows of the tank. This geometry approximates a fan beam geometry, measures the least scatter and is known as the *reference geometry*. All comparisons were relative to the reference geometry.
- No collimation was applied to either the entrance or exit windows of the tank. This is known as the *cone beam geometry* and is predominately used when evaluating dosimeters.

The window width of the collimation at the exit and entrance window was 11 and 18 mm respectively. These widths were equivalent in pixel size due to the diverging nature of the cone beam geometry as the distance from the CCD was increased.

The phantom measured was an absorbing solution of water and blue dye (fractional concentration of dye: 1×10^{-5} %). The reference phantom was a non-tinted container of water. 342 projection images of both the reference and data phantoms were acquired. These were reconstructed in the Vista™ Recon program using a Hamming filter (A = 0.540, B – 0.460) to form a 256 x 256 x 256 voxel volume with a size of 0.5 mm^3.

10 pixel wide profiles were acquired across the diameter of the reconstructed phantom for six slices (Figure 6-14 A). The slice position was selected so that the profiles were in the centre of the collimator opening (Figure 6-14 B). The comparison of the profile was limited to the inner 150 voxels inside the phantom (voxel position -75 to 75 – shown by black lines in Figure 6-14 A). This was ~1 cm inside the edge of the phantom and therefore avoided wall artefacts.

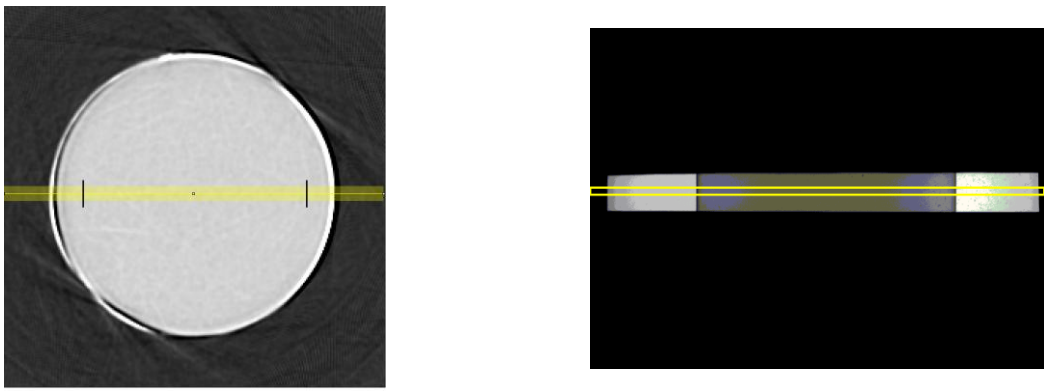

A B

Figure 6-14: Profile acquisition for cone beam geometry. A 10 pixel wide profile acquired over the diameter of the phantom (A). Lines have been added to display the position of the evaluated profiles in Figure 6-15. This region of interest was collected for 6 slices with positions corresponded to the centre of the collimator opening (B).

6.5.2 Results

Figure 6-15 shows the ratio of the profiles relative to the reference geometry. The ratio of the profiles measured when collimation is applied to either the entrance or exit window only is ~1. The full cone beam geometry shows a reduction in attenuation coefficient relative to the reference geometry.

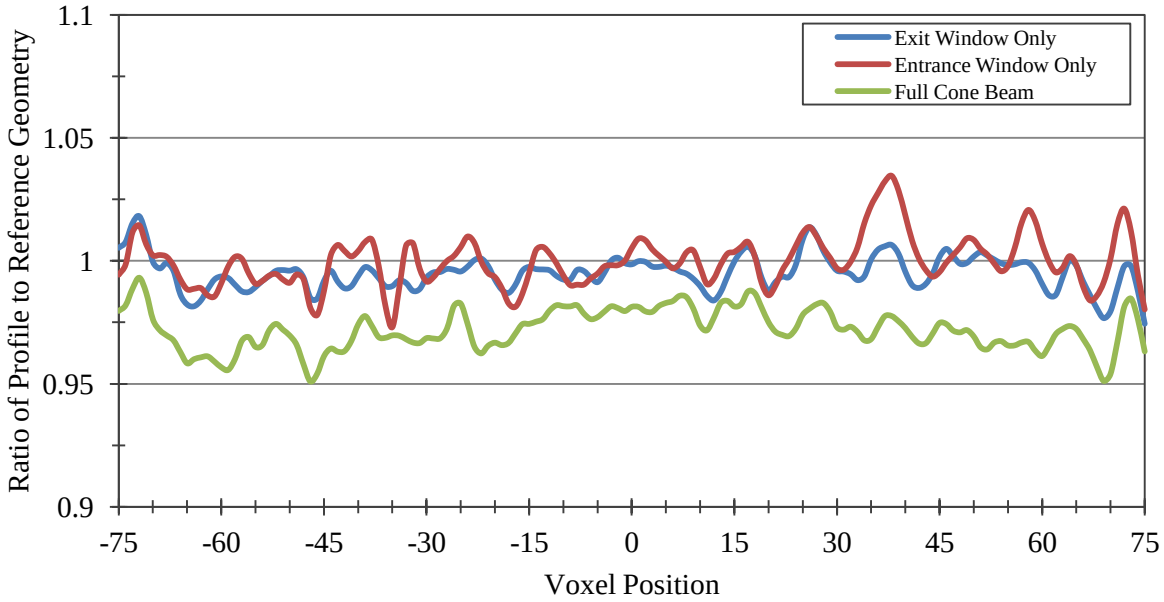

Figure 6-15: Profiles for different window combinations across an absorbing phantom (water and dye solution, fractional concentration of dye 1 x 10^{-5} %). Collimation of the exit or entrance specimen tank window results in a reduction of the scatter down to approximately the same level as the reference beam geometry. When no collimation was used, the measured attenuation coefficient was less than the attenuation coefficient measured in the reference geometry. This is consistent with the increase in light intensity observed for profiles measured from 2D projections with the same collimator configuration.

6.5.3 Discussion

Figure 6-15 shows a decrease of approximately 2.5 – 4 % in the measured attenuation coefficient relative to the measured attenuation coefficient in the reference geometry. The decrease is especially noticeable for the full cone beam geometry which has no collimation. This decrease is most likely related to increased light scatter. As described in section 5.6.3, the impact of scattered light in a high light intensity image (i.e. acquisition of an undyed phantom) is not expected to be as significant relative to when the light intensity reaching the CCD is low (i.e. acquisition of a tinted phantom). Scattered light will cause an increase in measured light intensity especially in a low light intensity image. This reduces the measured optical density and consequently the attenuation coefficient.

The observed ratio of the profiles measured with collimation at either the entrance or exit demonstrates that collimating the light source at either the entrance or exit is a suitable method for reducing scatter. Similar to section 5.6, collimation only at either the entrance or exit results in a similar profile indicating that the two sources of scattering described have a similar magnitude.

The collimation of light using windows to block areas of a projection is similar to the method used by Gore et al[63], with the main difference being the use of a vertical window as opposed to the horizontal window used in this work. Scatter contribution was measured using small pin holes across the projection[138]. The results show that low angle scatter is dominant and that blocking large areas of the projection does not significantly improve the uniformity of the reconstruction[138]. Additionally, Olding et al[82] pointed out that the use of collimating windows to attenuate light affects the normalisation of projections images used by the Vista™ Recon software.

The differences observed for the window collimation combinations used in this work is notable only when large areas of the projection are moved. Removing large areas of the projection is a compromise on the size of a dose distribution in the gel that can be evaluated and may not be practical in clinical measurements.

While the use of collimating windows is able to qualitatively identify scattered light, methods such as those presented by Jordan and Battista[138] and Olding et al[133,144] are superior for the quantitative calculation of scattered light and corrections needed by projections to account for stray light.

6.6 Summary of Investigations

The work presented in this chapter investigated the reconstructed optical density, uniformity, spatial resolution and influence scatter has on the reconstructed attenuation coefficient.

The range of attenuation coefficients with a linear response to opacity is between 0.094 – 0.68 cm^{-1} and 0.085 – 0.58 cm^{-1} for the orange and red light sources respectively. The accuracy of this technique was within 10 % and between 10 – 25 % of baseline values for the orange and red light source

respectively. Non-uniformities in the PORPs limited their effectiveness in measuring the accuracy of the reconstructed attenuation coefficient. The signal to noise ratio of the measured attenuation coefficients was high indicating a high level of precision. A similar value of net OD was measured for the attenuation coefficient range and the dynamic range of the CCD indicating the observed attenuation coefficient ranges were reasonable. The measured accuracy in the range of attenuation coefficients would not be sufficient for clinical gel dosimetry measurements. However, the accuracy issues are believed to be related to inadequacies in the PORPs (air bubbles, other non-uniformities) and limitations in the method of measuring the baseline attenuation coefficient. With improved manufacturing techniques, the measured accuracy of the PORPs relative to baseline values is expected to improve and PORPs could potentially be utilised for long term quality assurance of measured attenuation coefficients.

Comparison of profile and VOI uniformity measurement techniques on a tinted solution indicate a flat uniform phantom will have an agreement within 3 % between outer and central VOI. When applied to VOI calculated from PORP measurements, the PORPs do not appear to be uniform. However, closer inspection shows that uniformity measurements in the PORPs are limited by non-uniformities and inadequate refractive index matching. The VOI comparison methodology presented has the potential to improve uniformity measurement efficiency.

Both the attenuation coefficient comparison to baselines and uniformity measurements indicate that the accuracy, noise and uniformity of the PORPs can be improved through better quality control during manufacturing.

The spatial resolution was observed to improve as the reconstruction setting was changed from low to extreme resolution. The 50 % modulation value for the extreme resolution setting was 0.44 lp/mm. This is just below the spatial resolution criterion of 1 mm^3 (50 % modulation value greater than 0.5 lp/mm) suggested by Oldham et al[67]. The spatial resolution appears to be constant within a radial distance of 12.5 mm from the centre of the phantom. The observed decrease in spatial resolution at increased radial distances is thought to be related to the streaking artefacts caused by the opaque wires and is not a true reflection of the spatial resolution at this distance. The measured spatial resolution does not meet the Oldham et al[67] criteria, but still represents a level of accuracy that is smaller than clinical margins. Further investigation of the spatial resolution at larger radial distances with a more suitable phantom is needed. Additionally, optimisation of the CCD to rotation axis and lens system is required.

Scattered light in the full cone beam geometry lowers the measured attenuation coefficient in the reconstruction by approximately 4 %. Collimation of either the entrance or exit specimen tank window was observed to reduce the amount of scattered light by a similar magnitude. Full collimation (i.e., collimation at both the entrance and exit window of the specimen tank) reduces the influence of scatter. Collimation of the specimen tank windows has been shown to improve the accuracy of the

measured attenuation coefficient. However, clinical use of collimating windows will limit the physical size of the irradiated volume acquired by the optical CT. So this strategy is limited by the size of the treatment field to be investigated.

The accuracy of the measured attenuation coefficient relative to baseline attenuation coefficients and spatial resolution were sub-optimal with limitations in the PORP uniformity also observed. Inspection of the PORPs showed non-uniformities in the phantoms and refractive-index mismatches between the phantom and surrounding liquid were the main source of uncertainty. Similar to the 2D measurements, spatial resolution could be improved via optimisation of the scanner geometry. Artefacts caused by refractive index mis-matches influenced the measured uniformity, however the principle behind the VOI method was validated by measurements in a purely absorbing solution.

7. SUMMARY AND CONCLUSION

A 3D dosimeter and evaluation system requires careful consideration prior to purchasing for use in a clinical setting. This was investigated in the present work for a radiation sensitive gel evaluated using an optical CT scanner. The commissioning of the evaluation system must include characterisation in terms of influences of choice of gel on accuracy and precision. Results from characterisation measurements must be collected for use as baseline values for ongoing optical CT scanner quality assurance (QA). The evaluation system requires a separate characterisation to assess the overall impact of the scanner characteristics and parameters on a dosimetric distribution. Different optical CT evaluation systems are available for 3D dosimetry purposes (see section 2.3.4). Each system has a different configuration which needs to be assessed to determine appropriate characterisation tests. In this thesis, the Vista™ Cone Beam Optical CT scanner (the scanner) has been assessed before introduction into a clinical setting. All evaluation procedures described in this thesis are appropriate for cone beam type optical CT scanners. However, some procedures will be appropriate for evaluation of other types of optical CT scanners.

This thesis has investigated:

- The influence that two band pass filters have on their respective light spectra, specifically looking at the shift in the peak wavelength, the effect of differential attenuation and sensitivity of the CCD to different wavelengths.
- The light intensity variation as a function of time after initially switching on the scanner, for the orange and red light sources. The effect of such temporal variation on the acquisition and reconstruction of a uniform phantom.
- The reciprocity of the CCD detector and the impact on reconstructed images.
- Properties and suitability of PORPs for long term quality assurance of scanner stability.
- The dynamic range of attenuation coefficients reconstructed accurately compared to reference measurements acquired in a more controlled simple transmission geometry.
- The accuracy, noise and uniformity of attenuation coefficients over a large volume.
- The spatial resolution of the projection and reconstruction and the influence of charge integration time on the spatial resolution.
- The effect of stray light on the projection images and reconstructed volumes.

Other assessments required for the commissioning of a cone beam optical CT scanner include a validation of scanner geometry and evaluation of geometrical distortion (see section 2.6). These assessments have been previously presented by Olding et al[133].

Characterisation of the Scanner Setup

The light source can have an influence on the achievable accuracy of the dosimeter and evaluation system. Depending on the type of dosimeter the attenuation coefficient change per unit of absorbed dose will vary as a function of wavelength, where the attenuation coefficient is a property of the sample and has units of cm^{-1}. Matching the peak wavelength of the light source with the largest attenuation coefficient change per absorbed dose of the dosimeter improves dosimetric accuracy and precision. The spread of the light source surrounding a peak wavelength, as characterised by the FWHM, also has an impact on accuracy due to differential attenuation. This is caused by the dependence on wavelength of a dosimeter's attenuation coefficient and is compounded by a non-uniform light intensity across the light source spectrum. This is then further compounded by the quantum efficiency of the detector as a function of wavelength. This work investigated the impact of the light source spectra on the measured accuracy by evaluating: i) the change in attenuation coefficient per absorbed dose at the peak wavelength when a band pass filter is used, ii) the variance of the attenuation coefficient change per absorbed dose over the wavelengths of the FWHM, and iii) the change in quantum efficiency of the detector over the FWHM of the spectra.

For the orange light source, the peak wavelength was measured to be 598 nm and 595 nm without and with the addition of a band pass filter respectively. Using a Fricke gel attenuation curve, the shift in peak wavelength caused an apparent change in dose response of ~ 3 %. The FWHM narrowed from 17.5 to 11 nm with the addition of a filter. The variance of the measured attenuation coefficient change per absorbed dose across the FWHM reduced from 21 to 10.5 % for the unfiltered and filtered light respectively. The variation of the quantum efficiency of the detector across the FWHM of the orange light source reduced from 4.8 % to 3 % for the unfiltered and filtered light source respectively. The main function of the orange filter was to narrow the wavelength spectrum and reduce the effects of differential attenuation.

For the red light source, the peak unfiltered wavelength was 642 nm and the filtered wavelength was 635 nm. The change in the peak wavelength caused the attenuation coefficient change per absorbed dose to increase by 16 % for PRESAGE^{TM}, which results in a reduction in the uncertainty of the measured attenuation coefficient. The band pass filter narrowed the FWHM from 23 to 11 nm. This caused the variation in the attenuation coefficient change per absorbed dose across the FWHM to reduce from 46 to 7.9 % for the unfiltered and filtered light source respectively. The variation in the quantum efficiency of the detector reduced from 8.0 % to 3.7 % with the addition of the filter. The red filter was used to narrow the FWHM of the wavelength spectrum and better match the light spectrum to the maximum dose response of the dosimeter.

The addition of a filter reduces the intensity of light measured. This can be corrected for by changing the CCD light collection settings and is not considered an influence on dose accuracy.

After turning on the scanner, the intensity of the orange and red light sources as a function of time stabilised after 2 hours. The stabilisation of the light source reduces the uncertainty in the reconstructed attenuation coefficient. The results are consistent with measurements by Olding et al[82]. The use of an unstable light source to evaluate a uniform phantom demonstrated the importance of an appropriate warm-up time. A reference uniform volume was reconstructed from projection images acquired with a 2 hour warm-up time. Comparisons to this profile showed that using the scanner straight away to acquire pre and post irradiation scans will significantly influence the accuracy of the reconstructed attenuation coefficient. Using a cold scanner to measure either the pre or post-irradiation projection data set (and a warm scanner to measure the other projection images) will result in an accurate, yet noisier reconstruction.

The reciprocity of the CCD is the relationship between collected charge and light intensity. The characterisation of this relationship is important because the optical density calculation method used in this thesis is based on a reciprocal relationship. Measurement of an attenuation coefficient will be affected by a non-proportional response to light intensity. The reciprocity of the CCD was measured by keeping the light source constant and varying the charge integration time. The results indicated that the CCD response was close to, but not perfectly, linear. Therefore different initial light intensities through a dosimeter will result in a different measured optical density. To investigate this further, multiple data sets of the same uniform phantom, each reconstructed from projection images acquired with different charge integration times, were used to evaluate the influence a non-reciprocal CCD has on the reconstruction of a uniform sample. The results indicate that a high level of attenuation coefficient accuracy may be maintained by keeping the range of pixel values between ~5000 and 64000.

The polyurethane opacity reference phantoms (PORPs) used in this work were developed by a colleague for use in the optical CT scanner[177]. To use the PORPs in this work, the baseline attenuation coefficient and scattering properties of the PORPs were assessed. The baseline attenuation coefficient of each PORP was measured in the scanner (section 4.7) for both the orange and red light source. A range of 0 – 1.8 cm^{-1} and 0 – 1.5 cm^{-1} was observed for the orange and red light source respectively. The baseline attenuation coefficients were measured over a 3 year period with an uncertainty of ± 8.0 % observed. Positioning of the PORPs in the scanner caused the largest uncertainties in the measured attenuation coefficient. A more robust position device could reduce uncertainties in the measured value.

Characterisation of the scanner demonstrated large degrees of variation in the measured attenuation coefficient if the scanner was not allowed sufficient warm-up time, an inappropriate light and filter combination was selected or the pixel values in projection images were outside the reciprocal range. Uncertainty in measured attenuation coefficients could be reduced by allowing a minimum of 2 hours warm-up time, selecting an appropriate filter and light source for the given dosimeter to be assessed and ensuring that the pixel range was between ~5000 and 64000.

Assessment of Projections and 3D Reconstructed Images

Absorbance profiles of uniform absorbing solutions and PORPs were compared to modelled profiles. The absorbing solutions and PORPs exhibited an absorbance curvature similar to the model at the centre of the phantom. The absorbing solution profiles showed good agreement across the entire profile whilst the PORP profiles were affected by a refractive index mismatch. From the results it was determined that the PORPs could be used for measurement of attenuation coefficients provided the measurement was restricted to the centre of the phantom.

The dynamic range of attenuation coefficients was assessed by the comparison of the reference attenuation coefficient of individual PORPs to the measured attenuation coefficients from 2D projection images (section 5.3) and 3D reconstructions (section 6.2). It is acknowledged that the evaluation method is one part of the overall uncertainty involved with 3D dosimetry, and that many other factors can affect the dosimetric accuracy (see section 2.4)

The attenuation coefficient measured from 2D projections had a high uncertainty, which limited the use of 2D measurements in ongoing quality assurance. The 3D reconstructed values showed a similar range of attenuation coefficients but with a reduced uncertainty in the measured value relative to 2D data. It is recommended that 3D reconstructed data be used for ongoing QA of measured attenuation coefficient accuracy despite the additional time required over single 2D projections.

The range of attenuation coefficients exhibiting a proportional response was between 0.1 – 0.68 cm^{-1} and 0.1 – 0.58 cm^{-1} for the orange and red light sources respectively. The range is large compared to the result from Olding et al[133] due to a difference in the diameter of the phantoms used to measure the attenuation coefficient. The accuracy of the attenuation coefficients measured with the orange and red light source was low relative to the baseline measurements. Differences could be attributed to manufacturing defects in the PORPs causing streaking artefacts and uncertainties in the baseline attenuation coefficient measurements. The SNR ratio in these regions indicates that a noise level below 1 % is achievable.

The uniformity of the reconstruction was used to check the accuracy and noise of the reconstructed PORP images over a large volume. The mean and standard deviation of the reconstructed attenuation coefficient was measured for five volumes of interest (VOI), with four VOIs being toward the outer part of the reconstructed phantom and the fifth VOI in the centre. The outer four VOIs were compared to the central VOI for accuracy of attenuation coefficient. The SNR was calculated for each VOI to assess noise. For the attenuation coefficient regions described above, the VOI showed an agreement in attenuation coefficient values within 5 % between the outer and central VOI and a noise level for most VOI below 1 %. Some outliers were observed but were attributable to streaking artefacts caused by air bubbles in the PORPs.

Spatial resolution of the scanner was investigated in 2D projections and 3D reconstructions (sections 5.4 and 6.4 respectively). The spatial resolution measured in 2D and 3D could not be compared directly due to a change in the CCD and detector to central axis distance between measurements in 2D and 3D.

The 2D measurements were used to determine the variation in spatial resolution for the diameter of the PORP parallel and perpendicular to the CCD – light source axis. As the CCD to measurement point increased, the spatial resolution proportionally increased. From modulation transfer function (MTF) curves, a value greater than 50 % was measured at spatial resolutions of 0.5 lp/mm for distances less than ~ 46 cm. This is the minimum distance the edge of the dosimeter furthest to the CCD should be to achieve a sub mm spatial resolution with the scanner set-up used. Comparison to 2D measurements by Olding et al[133] indicate that a newer camera system and optimisation of the focusing and lens system can significantly improve the spatial resolution.

Blooming of the CCD pixels was observed for long charge integration times and has two significant and different effects on the spatial resolution: i) the 50 % modulation value of a MTF curve decreases, ii) the 50 % value increases, but the measured position of an edge response function shifts. The two different effects are due to how much of the charge is spilt over from one pixel to a neighbouring pixel. A small overflow of charge causes the edge spread function to become shallower, which lowers the MTF curve. When a high amount of blooming occurs, the spill over in charge is high enough to cause saturation of the neighbouring pixel, but will not change the next neighbouring pixel by the same magnitude. Therefore the edge response function sharpens, causing an increase in the MTF, but the actual position of the edge is not accurate because it has been shifted by one pixel.

The 3D spatial resolution was evaluated for the *low*, *medium*, *high* and *extreme* reconstruction settings in the Vista™ Recon software, with a 50 % modulation value calculated at 0.04, 0.12, 0.29 and 0.44 lp/mm. The extreme reconstruction setting's 50 % modulation value was not quite sufficient to meet the Oldham et al[67] criterion for sub-mm spatial resolution which requires 50 % modulation at 0.5 lp/mm. The result was compared to 2D projection measurements from Olding et al[133] which showed that their 50 % modulation value from projection images was much larger and satisfied the Oldham et al criterion. A smaller reconstructed modulation value could be attributed to a binning of pixels during reconstruction, which therefore down-samples the projection image, and a difference of the aperture settings (i.e. f-stop) within the lens.

Overall, the spatial resolution was found to be sub-optimal for evaluations requiring spatial accuracy greater than 1 mm^3. Results from Olding et al[133] indicate further investigation of the lens system, in particular the f-stop, is required to optimise spatial resolution.

The spatial resolution of the optical CT scanner is only a small part of the overall gel dosimetry system. Dosimeter factors, such as diffusion, could potentially have a larger impact on the achievable spatial resolution[54,75-81,87,92,96,97].

The primary source of scattered light was investigated in 2D and 3D via blocking light either entering and/or exiting the specimen tank. Blocking the entrance window reduced the amount of light not originally incident on the CCD which is then scattered toward the detector. Blocking the exit window reduced the stray light originating inside the specimen tank. The measured amount of scatter from the 2D projections was approximately 4 %. Stray light was observed to reduce the reconstructed attenuation coefficient, which is consistent with observations in the literature[37,63,130-132,135]. The reduction in scatter observed when either the entrance or exit was collimated was similar in magnitude. This indicates that light not originally incident on the CCD which was scattered toward the detector and stray light from inside the specimen tank were similar in magnitude. The results were not used to quantify a scatter correction, which requires a more detailed analysis and has previously been presented in the literature[133,138,144].

The results from the characterisation of the 2D projection images and 3D reconstructed volumes showed the PORPs were influenced by a refractive index mismatch and the spatial resolution was sub-optimal for gel dosimetry and could be influenced by blooming in the CCD. PORP measured attenuation coefficient uniformity was within 5 % over a large volume. Uncertainty in the measured attenuation coefficient could be reduced by better matching the refractive index of the liquid surrounding the PORPs to the refractive index of the PORPs and ensuring the pixel intensity values be kept between the suggested values determined from reciprocity measurements (~5000 – 64000). Spatial resolution could be improved by increasing the distance between the CCD and axis of rotation and optimisation of the lens f-stop. Uniformity measurements were observed to improve if the refractive index was better matched between the phantom and surrounding material as is the case with blue absorbing dye and water solutions.

The characterisation methods presented in this thesis can be used as a guideline for development of commissioning and ongoing scanner quality assurance protocols.

Limitations of the study

The major limitations of the measurements presented in this work were:

- Non-uniformities in the PORPs and refractive mismatches between the PORPs and the surrounding solutions
- The reproducibility of the samples in the holder
- Use of optically opaque metallic wire in 3D spatial resolution measurements causing streaking artefacts in the reconstructed images.
- Insufficient knowledge of the influence of f-stop on collected light prior to measurements.

The limitations associated with the method for measuring baseline attenuation coefficient and the influence of the manufacturing process on PORP accuracy, noise and uniformity has been previously discussed.

The PORP holder was designed to hold a number of PORPs for imaging. During the collection of projection images, the PORPs are either lopsided or the rotation of the holder causes some of the PORPs to move. This causes wall artefacts in the reconstructed images. A more robust method of holding the phantoms is required to eliminate this artefact.

The use of a metallic wire for spatial resolution measurements from a 3D reconstruction causes streaking artefacts. An improved measurement is expected using an optical fibre provided no large differences in refractive index are observed.

The f-stop value has been shown to affect the light intensity and spatial resolution measured by the CCD[133]. At the time of measurement the f-stop was not optimised. Optimisation of the f-stop could potentially improve the presented results.

Conclusion

This study has set out to assess the following issues associated with 3D dosimetry using gels and optical evaluation. As discussed in chapter 2, key areas of study were:

- Light intensity as a function of time
- Spectral output compatibility with 3D dosimeters
- Projection and reconstruction attenuation coefficient accuracy and dynamic range
- Projection and reconstruction spatial resolution
- Effect of scatter on the projection and reconstructed image
- Cone beam geometry validation
- Geometrical distortion

The wavelengths of the orange and red light sources were observed to match well to the peak absorbance of Fricke and PRESAGE^{TM} dosimeters. The light source intensity was observed to decrease as a function of time with a stabilisation of the intensity at approximately 2 hours. Incorrect warm-up procedures were observed to have a significant impact on attenuation coefficient accuracy. 2D projection and 3D reconstructed attenuation coefficient accuracy and range relative to values measured in a controlled configuration, were observed to be superior for 3D reconstructions. It is recommended that ongoing attenuation coefficient accuracy QA be performed using 3D reconstructed data despite the additional time required. QA using 2D projections, whilst potentially more efficient is not sufficiently sensitive. Uniformity of the reconstructed attenuation coefficient was shown to be within 3 % over a large volume. Spatial resolution was measured in 2D projections and 3D reconstructions with the results sub-optimal for evaluations requiring spatial accuracy greater than 1 mm^3. Additionally, blooming in the CCD was observed to influence spatial resolution with the major influence being a change in the position of edges in a 2D projection, and subsequently the inaccurate reconstruction of these edges in 3D. Stray light was observed to reduce the reconstructed attenuation coefficient by approximately 4 %.

Cone beam geometry validation and geometrical distortion have been previously reported extensively in the literature and were not investigated further in this study.

Table 7-1 contains a set of suggested tests based on these measurements and some suggested procedures from existing literature. The tests form the basis for characterisation and ongoing quality assurance of a cone beam optical CT scanner. The tests require measurements over a period of time to verify the frequency with which ongoing QA should be performed. Performance of ongoing quality assurance on an optical CT scanner will hopefully allow 3D dosimetry to be performed quicker and with reduced uncertainties.

Table 7-1: Suggested characterisation and ongoing QA measurements

Characterisation Test	***Suggested Frequency***	***Suggested tests***
Calibration of the geometry	Commissioning and when any component is moved or changed	Suggested tests in Modus Med document[156]
f-stop optimisation	Commissioning and when any component is moved or changed	Olding et al[133]
Wavelength Verification	Commissioning, when the light source is changed and annually	Section 4.2
Variation in light source after turning on scanner	Commissioning, when the light source is changed and annually	Section 4.3
CCD reciprocity	Commissioning, when the CCD is changed and annually	Section 4.5
Spatial Distortion	Commissioning, Annual	Olding et al[133]
Attenuation coefficient		
• Accuracy and noise in a uniform reconstruction	Commissioning	Section 6.2 + 6.3
• Constancy of attenuation coefficient reconstruction over time	Monthly until stability assured	Section 6.3
• Inter-day Reproducibility	Commissioning	See section 5.3 for measurements in this work, but suggest using 3D in commissioning work
Spatial Fidelity of scanner	Commissioning, Monthly until stability assured	Section 5.4 + 6.4
Calibration curve: attenuation coefficient to dose	Commissioning, Monthly until stability assured	

Evaluation of a 3D dosimeter using a cone beam optical CT scanner in optimal measurement conditions would enable uncertainties to be minimised. Ideal conditions for evaluation would be: stable light intensity over the evaluation time, CCD settings selected so that blooming was not present, the CCD response to light intensity would be linear and high reconstructed attenuation coefficient accuracy. In the case of small field measurements the region of interest should be placed near the centre of the field of view where uniformity and spatial resolution is best and allows a narrowing of the entrance and exit windows to minimise scatter. A summary of these uncertainties for both a typical situation and in optimal conditions is presented in Table 7.2.

Table 7-2: Uncertainties for both typical and optimal measurement conditions

Source of uncertainty	*Typical or Worst Case*	*Optimal*
Light Source	Polychromatic light source giving rise to differential attenuation. Potentially up to an 8 – 10 % variation in measured attenuation coefficient (Based on this work)	Using a LED and filter combination with a narrow FWHM.
Light intensity stability	If warm up not performed correctly then can see up to ~ 13 % differences over a 5 minute period	< 1% (Light source warmed up 2 hours)
CCD response to light intensity	2 % variation in attenuation coefficient shown in this work	Optimising gain and shutter settings to restrict to linear range.
Light scatter in evaluation equipment	Measured attenuation coefficient ~4 % lower in cone beam geometry relative to narrow window geometry	Minimal light scatter in narrow window geometry for small fields
Uniformity over a large volume	± 5 % over a large volume sample	< 5 % for small fields positioned in the centre of field
Spatial Resolution	50 % modulation of 0.44 lp/mm – extreme setting in Vista Recon Resolution degrades away from central rotation axis	50 % modulation of 0.44 lp/mm – extreme setting in Vista Recon For small fields locate ROI near axis of rotation for best resolution

Future Considerations

Future work will involve improving the design and manufacture of new long term standards having the required properties for use as long term QA tools. This includes elimination of non-uniformities such as bubbles and the use of optical contrast that is purely light absorbing. The improved phantoms would then be used to characterise attenuation coefficient accuracy, noise and uniformity in an ongoing capacity.

Clinical fields will typically be smaller and as such have less scatter, a larger dynamic range and smaller variation in the spatial resolution off axis. The characterisation methods in this thesis used large uniform samples. In this respect some observations could be considered worst case scenarios.

Clinical use of different dose formulations need to be assessed for their individual dose response curves relative to the dynamic range of the optical CT. Typically the chemical composition of the dose formulation can be adjusted to tailor the response to the dynamic range.

8. REFERENCES

1. *ICRU Report 50: Prescribing, Recording and Reporting Photon Beam Therapy*. 1993.
2. *ICRU Report 62: Prescribing, Recording and Reporting Photon Beam Therapy (Supplement to ICRU Report 50)*. 1999.
3. *ICRU Report No. 83: Prescribing, Recording, and Reporting Phonton-Beam Intensity-Modulated Radiation Therapy (IMRT).* Journal of the ICRU, 2010. **10**(1).
4. Emami, B., et al., *Tolerance of normal tissue to therapeutic irradiation.* International Journal of Radiation Oncology Biology Physics, 1991. **21**(1): p. 109-22.
5. Bentzen, S.M., et al., *Quantitative Analyses of Normal Tissue Effects in the Clinic (QUANTEC): An Introduction to the Scientific Issues.* International Journal of Radiation Oncology Biology Physics, 2010. **76**(3, Supplement 1): p. S3-S9.
6. Bhandare, N., et al., *Radiation Therapy and Hearing Loss.* International Journal of Radiation Oncology Biology Physics, 2010. **76**(3, Supplement 1): p. S50-S57.
7. Dawson, L.A., et al., *Radiation-Associated Kidney Injury.* International Journal of Radiation Oncology Biology Physics, 2010. **76**(3, Supplement 1): p. S108-S115.
8. Deasy, J.O., et al., *Radiotherapy Dose-Volume Effects on Salivary Gland Function.* International Journal of Radiation Oncology Biology Physics, 2010. **76**(3, Supplement 1): p. S58-S63.
9. Gagliardi, G., et al., *Radiation Dose-Volume Effects in the Heart.* International Journal of Radiation Oncology Biology Physics, 2010. **76**(3, Supplement 1): p. S77-S85.
10. Jackson, A., et al., *The Lessons of QUANTEC: Recommendations for Reporting and Gathering Data on Dose-Volume Dependencies of Treatment Outcome.* International Journal of Radiation Oncology Biology Physics, 2010. **76**(3, Supplement 1): p. S155-S160.
11. Jeraj, R., et al., *Imaging for Assessment of Radiation-Induced Normal Tissue Effects.* International Journal of Radiation Oncology Biology Physics, 2010. **76**(3, Supplement 1): p. S140-S144.
12. Kavanagh, B.D., et al., *Radiation Dose-Volume Effects in the Stomach and Small Bowel.* International Journal of Radiation Oncology Biology Physics, 2010. **76**(3, Supplement 1): p. S101-S107.
13. Kirkpatrick, J.P., A.J. van der Kogel, and T.E. Schultheiss, *Radiation Dose-Volume Effects in the Spinal Cord.* International Journal of Radiation Oncology Biology Physics, 2010. **76**(3, Supplement 1): p. S42-S49.
14. Lawrence, Y.R., et al., *Radiation Dose-Volume Effects in the Brain.* International Journal of Radiation Oncology Biology Physics, 2010. **76**(3, Supplement 1): p. S20-S27.
15. Marks, L.B., et al., *Radiation Dose-Volume Effects in the Lung.* International Journal of Radiation Oncology Biology Physics, 2010. **76**(3, Supplement 1): p. S70-S76.
16. Marks, L.B., R.K. Ten Haken, and M.K. Martel, *Guest Editor's Introduction to QUANTEC: A Users Guide.* International Journal of Radiation Oncology Biology Physics, 2010. **76**(3, Supplement 1): p. S1-S2.
17. Marks, L.B., et al., *Use of Normal Tissue Complication Probability Models in the Clinic.* International Journal of Radiation Oncology Biology Physics, 2010. **76**(3, Supplement 1): p. S10-S19.
18. Mayo, C., et al., *Radiation Dose-Volume Effects of Optic Nerves and Chiasm.* International

Journal of Radiation Oncology Biology Physics, 2010. **76**(3, Supplement 1): p. S28-S35.

19. Mayo, C., E. Yorke, and T.E. Merchant, *Radiation Associated Brainstem Injury.* International Journal of Radiation Oncology Biology Physics, 2010. **76**(3, Supplement 1): p. S36-S41.
20. Michalski, J.M., et al., *Radiation Dose-Volume Effects in Radiation-Induced Rectal Injury.* International Journal of Radiation Oncology Biology Physics, 2010. **76**(3, Supplement 1): p. S123-S129.
21. Pan, C.C., et al., *Radiation-Associated Liver Injury.* International Journal of Radiation Oncology Biology Physics, 2010. **76**(3, Supplement 1): p. S94-S100.
22. Rancati, T., et al., *Radiation Dose-Volume Effects in the Larynx and Pharynx.* International Journal of Radiation Oncology Biology Physics, 2010. **76**(3, Supplement 1): p. S64-S69.
23. Roach Iii, M., et al., *Radiation Dose-Volume Effects and the Penile Bulb.* International Journal of Radiation Oncology Biology Physics, 2010. **76**(3, Supplement 1): p. S130-S134.
24. Viswanathan, A.N., et al., *Radiation Dose-Volume Effects of the Urinary Bladder.* International Journal of Radiation Oncology Biology Physics, 2010. **76**(3, Supplement 1): p. S116-S122.
25. Werner-Wasik, M., et al., *Radiation Dose-Volume Effects in the Esophagus.* International Journal of Radiation Oncology Biology Physics, 2010. **76**(3, Supplement 1): p. S86-S93.
26. Schreiner, L.J. *Dosimetry in modern radiation therapy: limitations and needs*. 2006: IOP Publishing.
27. Thomas, B., *IMRT: a review and preview.* Physics in Medicine and Biology, 2006. **51**(13): p. R363.
28. Williamson, J.F., *Brachytherapy technology and physics practice since 1950: a half-century of progress.* Physics in Medicine and Biology, 2006. **51**: p. R303-R325.
29. Phillips, M.H., et al., *Stereotactic radiosurgery: a review and comparison of methods.* Journal of Clinical Oncology, 1994. **12**(5): p. 1085-1099.
30. Ost, P., et al., *Volumetric arc therapy and intensity-modulated radiotherapy for primary prostate radiotherapy with simultaneous integrated boost to intraprostatic lesion with 6 and 18 MV: a planning comparison study.* International Journal of Radiation Oncology Biology Physics, 2011. **79**(3): p. 920-926.
31. Metcalfe, P., T. Kron, and P. Hoban, *The Physics of Radiotherapy X-rays and Electrons*. 2007.
32. Gillis, S., et al., *An inter-centre quality assurance network for IMRT verification: Results of the ESTRO QUASIMODO project.* Radiotherapy and Oncology, 2005. **76**(3): p. 340-353.
33. Moran, J. and P. Xia, *QA-QC of IMRT: American Perspective*, in *Image-Guided IMRT*. 2006, Springer Berlin Heidelberg. p. 129-141.
34. Ting, J.Y. and L.W. Davis, *Dose verification for patients undergoing IMRT.* Medical Dosimetry, 2001. **26**(2): p. 205-213.
35. Jordan, K. *Review of recent advances in non gel dosimeters*. 2006: IOP Publishing.
36. Jordan, K., *Recent advances in non gel tissue equivalent dosimeters.* Journal of Physics: Conference Series 3 - Third International Conference on Radiatherapy Gel Dosimetry, 2009. **164**(1): p. 012041.
37. Oldham, M., et al., *Optical- CT gel-dosimetry 1: Basic investigations.* Medical Physics, 2003. **30**(4): p. 623- 634.
38. Gore, J., Y. Kang, and R. Schultz, *Measurement of radiation dose distributions by nuclear magnetic resonance (NMR) imaging.* Physics in Medicine and Biology, 1984. **29**(10): p. 1189-1197.

39. Adamovics, J. and M.J. Maryanski, *New 3D radiochromic Solid Polymer Dosimeter from Leuco Dyes and a Transparent Polymeric Matrix.* Medical Physics, 2003. **30**(6): p. 1349.

40. Fong, P.M., et al., *Polymer gels for Magnetic resonance imaging of radiation dose distributions at normal room atmosphere.* Physics in Medicine and Biology, 2001. **46**: p. 3105-3113.

41. Maryanski, M.J., et al., *NMR relaxation enhancement in gels polymerized and cross-linked by ionizing radiation: a new approach to 3D dosimetry by MRI.* Magnetic Resonance Imaging, 1993. **11**(2): p. 253-8.

42. Hilts, M., et al., *Polymer gel dosimetry using x-ray computed tomography: a feasibility study.* Physics in Medicine and Biology, 2000. **45**: p. 2559-2571.

43. Trapp, J.V., et al., *An experimental study of the dose response of polymer gel dosimeters imaged with x-ray computed tomography.* Physics in Medicine and Biology, 2001. **46**: p. 2939-2951.

44. Trapp, J.V., et al., *Attenuation of diagnostic energy photons by polymer gel dosimeters.* Physics in Medicine and Biology, 2002. **47**: p. 4247-4258.

45. Mather, M.L., et al., *Ultrasound absorption in polymer gel dosimeters.* Ultrasonics, 2003. **41**: p. 551-559.

46. Mather, M.L., et al., *Investigation of ultrasonic propeties of PAG and MAGIC polymer gel dosimeters.* Physics in Medicine and Biology, 2002. **47**: p. 4397-4409.

47. Mather, M.L., A.K. Whittaker, and C. Baldock, *Ultrasound evaluation of polymer gel dosimeters.* Physics in Medicine and Biology, 2002. **47**: p. 1449-1458.

48. Adamovics, J. and M.J. Maryanski, *Characterisation of PRESAGE^{TM}: A new 3-D Radiochromic solid polymer dosemeter for ionising radiation.* Radiation Protection Dosimetry, 2006. **120**(1-4): p. 107-112.

49. Guo, P., J. Adamovics, and M. Oldham, *PRESAGE - A Promising New Material for 3D Dosimetry.* International Journal of Radiation Oncology Biology Physics: Proceedings of the American Society for Therapeutic Radiology and Oncology 47 th Annual Meeting, 2005. **63**(Supplement 1): p. S206.

50. Maryanski, M.J., Y.Z. Zastavker, and J.C. Gore, *Radiation dose distributions in three dimensions from tomographic optical density scanning of polymer gels: II. Optical properties of the BANG polymer gel.* Physics in Medicine and Biology, 1996. **41**: p. 2705-2717.

51. Kelly, R.G., K.J. Jordan, and J.J. Battista, *Optical CT reconstruction of 3D dose distributions using the ferrous-benzoic xylenol (FBX) gel dosimeter.* Medical Physics, 1998. **25**(9): p. 1741-1760.

52. Tarte, B.J., P.A. Jardine, and T. van Doorn, *Laser-scanned agarose gel sections for radiation field mapping.* International Journal of Radiation Oncology Biology Physics, 1996. **36**(1): p. 175-179.

53. Tarte, B.J., et al., *Development of a CCD array imaging system for measurment of dose distributions in doped agarose gels.* Medical Physics, 1997. **24**(9): p. 1521-1525.

54. Maryanski, M.J., et al., *Magnetic resonance imaging of radiation dose distributions using a polymer-gel dosimeter.* Physics in Medicine and Biology, 1994. **39**: p. 1437-1455.

55. Ibbott, G., et al., *Three-dimensional visualisation and measurement of conformal dose distributions using Magnetic Resonance Imaging of Bang Polymer Gel Dosimeters.* International Journal of Radiation Oncology Biology Physics, 1997. **38**(5): p. 1097-1103.

56. De Deene, Y., *Review of quantitative MRI principles for gel dosimetry.* Journal of Physics: Conference Series 3 - Third International Conference on Radiatherapy Gel Dosimetry, 2009. **164**(1): p. 012033.

57. Jirasek, A. and M. Hilts, *An overview of polymer gel dosimetry using x-ray CT*. Journal of Physics: Conference Series 3 - Third International Conference on Radiatherapy Gel Dosimetry, 2009. **164**(1): p. 012038.

58. Mather, M.L. and C. Baldock, *Ultrasound tomography imaging of radiation dose distributions in polymer gel dosimeters: Preliminary study.* Medical Physics, 2003. **30**(8): p. 2140-2148.

59. DeJean, P., et al. *Initial experience with a commercial cone beam optical CT unit for polymer gel dosimetry I: Optical dosimetry issues*. 2006: IOP Publishing.

60. DeJean, P., et al. *Initial experience with a commercial cone beam optical CT unit for polymer gel dosimetry II: Clinical potential*. 2006: IOP Publishing.

61. Doran, S.J., et al., *A CCD-based optical CT scanner for high-resolution 3D imaging of radiation dose distributions: equipment specifications, optical simulations and preliminary results.* Physics in Medicine and Biology, 2001. **46 (2001)**: p. 3191-3213.

62. Doran, S.J. and N. Krstajic. *The history and principles of optical computed tomography for scanning 3-D radiation dosimeters*. 2006: IOP Publishing.

63. Gore, J.C., et al., *Radiation dose distributions in three dimensions from tomographic optical density scanning of polymer gels: I. Development of an optical scanner.* Physics in Medicine and Biology, 1996. **41**: p. 2695-2704.

64. Krstajic, N. and S. Doran, *Initial Characterization of fast laser scanning optical CT apparatus for 3-D dosimetry*. Journal of Physics: Conference Series - 5th International Conference on Radiotherapy Gel Dosimetry (DOSGEL 2008), 2008.

65. Krstajic, N. and S.J. Doran, *Focusing Optics of a parallel beam CCD optical tomography apparatus for 3D radiation gel dosimetry.* Physics in Medicine and Biology, 2006. **51**(8): p. 2055-2075.

66. Oldham, M., *Optical-CT scanning of Polymer Gels.* Journal of Physics: Conference Series - 3rd International Conference on Radiatherapy Gel Dosimetry, 2004. **3**: p. 122-135.

67. Oldham, M., et al., *High Resolution gel-dosimetry by Optical-CT and MR scanning.* Medical Physics, 2001. **28**(7): p. 1436-1445.

68. Wolodzko, J.G., C. Marsden, and A. Appleby, *CCD imaging for optical tomography of gel radiation dosimeters.* Medical Physics, 1999. **26**(11): p. 2508-2513.

69. Baldock, C., et al., *Polymer gel dosimetry*. Physics in Medicine and Biology, 2010. **55**(5): p. R1.

70. Fricke, H. and S. Morse, *The Chemical Action of Rontgen rays on dilute ferrosulfate solutions as a measure of dose.* Am J Roentgenol. Radium Ther, 1927.

71. Madsen, E.L. and G.D. Fullerton, *Prospective tissue-mimicking materials for use in NMR imaging phantoms.* Magnetic Resonance Imaging, 1982. **1**(3): p. 135-141.

72. Appleby, A., E.A. Christman, and A. Leghrouz, *Imaging of spatial radiation dose distribution in agarose gels using magnetic resonance.* Medical Physics, 1987. **14**(3): p. 382-384.

73. Olsson, L.E., et al., *Ferrous sulphate gels for determination of absorbed dose distributions using MRI technique: basic studies.* Physics in Medicine and Biology, 1989. **34**(1): p. 43-52.

74. Schreiner, L.J., *Review of Fricke gel dosimeters.* Journal of Physics: Conference Series 3 - Third International Conference on Radiatherapy Gel Dosimetry, 2004: p. 9-21.

75. Baldock, C., et al., *Experimental determination of the diffusion coefficient in two-dimensions in ferrous sulphate gels using the finite element method.* Australasian Physical & Engineering Sciences in Medicine, 2001. **24**(1): p. 19-30.

76. Harris, P.J., A.R. Piercy, and C. Baldock, *A method for determining the diffusion coefficient in Fe(II/III) radiation dosimetry gels using finite elements.* Physics in Medicine and Biology, 1996. **41**: p. 1745-1753.

77. Pedersen, T.V., D.R. Olsen, and A. Skretting, *Measurement of the ferric diffusion coefficient in agarose and gelatine gels by utilization of the evolution of a radiation induced edge as reflected in relaxation rate images.* Physics in Medicine and Biology, 1997. **42**: p. 1575-1585.

78. Rae, W.I.D., et al., *Chelator effect on ion diffusion in ferrous-sulfate-doped gelatin gel dosimeters as analyzed by MRI.* Medical Physics, 1996. **23**(1): p. 15-23.

79. Olsson, L.E., et al., *MR imaging of absorbed dose distributions for radiotherapy using ferrous sulphate gels.* Physics in Medicine and Biology, 1990. **35**(12): p. 1623-1631.

80. Olsson, L.E., et al., *Diffusion of ferric ions in agarose dosimeter gels.* Physics in Medicine and Biology, 1992. **37**(12): p. 2243-2252.

81. Schultz, R.J., et al., *Dose-response curves for Fricke-infused agarose gels as obtained by nuclear magnetic resonance.* Physics in Medicine and Biology, 1990. **35**(12): p. 1611-1622.

82. Olding, T. and L.J. Schreiner, *Cone beam optical computed tomography for gel dosimetry II: image protocols.* Physics in Medicine and Biology, 2011. **56**: p. 1259-1279.

83. Kron, T., P. Metcalfe, and J.M. Pope, *Investigation of the tissue equivalence of gels used for NMR dosimetry.* Physics in Medicine and Biology, 1993. **38**: p. 139-150.

84. Taylor, M., et al., *The effective atomic number of dosimetric gels.* Australasian Physical & Engineering Science in Medicine, 2008. **31**(2): p. 131-138.

85. Keall, P.J. and C. Baldock, *A theoretical study of the radiological properties and water equivalence of Fricke and Polymer gels used for radiation dosimetry.* Australasian Physical & Engineering Sciences in Medicine, 1999. **22**.

86. Baldock, C., et al., *Experimental procedure for the manufacture and calibration of polyacrylamide gel (PAG) for magnetic resonance imaging (MRI) radiation dosimetry.* Physics in Medicine and Biology, 1998. **43**: p. 695-702.

87. De Deene, Y., et al., *Three-dimensional dosimetry using polymer gel and magnetic resonance imaging applied to the verification of conformal radiation therapy in head-and-neck cancer.* Radiation and Oncology, 1998. **48**: p. 283-291.

88. Jirasek, A., K.B. McAuley, and M. Lepage, *How Does the Chemistry of Polymer Gel Dosimeters Affect their Performance?* Journal of Physics: Conference Series - 5th International Conference on Radiotherapy Gel Dosimetry (DOSGEL 2008), 2009. **164**.

89. Whitney, H.M. and J.C. Gore. *Measurement of particle size in polymer gel dosimeters using spectrophotometry*. 2006: IOP Publishing.

90. Oldham, M. and L. Kim, *Optical-CT gel-dosimetry 2: Optical artifacts and geometrical distortion.* Medical Physics, 2004. **31**(5): p. 1093-1104.

91. Taylor, M., et al., *Systematic variations in polymer gel dosimeter calibration due to container influence and deviations from water equivalence.* Physics in Medicine and Biology, 2007. **52**: p. 3991.

92. De Deene, Y., et al., *The fundamental radiation properties of normoxic polymer gel dosimeters: a comparison between a methacrylic acid based gel and acrylamide based gels.* Physics in Medicine and Biology, 2006. **51**(3): p. 653.

93. Taylor, M., et al., *Electron Interaction with Gel Dosimeter: Effective Atomic Numbers for Collisional, Radiative and Total Interaction Processes.* Radiation Research, 2009. **171**: p. 123-126.

94. Novotny Jr., J., et al., *Energy and dose rate dependence of BANG-2 polymer-gel dosimeter.* Medical Physics, 2001. **28**(11): p. 2379-2386.

95. Maryanski, M.J., C. Audet, and J.C. Gore, *Effects of crosslinking and temperature on the dose response of a BANG polymer gel dosimeter.* Physics in Medicine and Biology, 1997. **42**: p. 303-311.

96. De Deene, Y. and et al., *On the accuracy of monomer/polymer gel dosimetry in the proximity of a high-dose-rate 192 Ir source.* Physics in Medicine and Biology, 2001. **46**(11): p. 2801.

97. Vergote, K., et al., *On the relation between the spatial dose integrity and the temporal instability of polymer gel dosimeters.* Physics in Medicine and Biology, 2004. **49**(19): p. 4507.

98. De Deene, Y., et al., *An investigation of the chemical stability of a monomer/polymer gel dosimeter.* Physics in Medicine and Biology, 2000. **45**(4): p. 859.

99. De Deene, Y., et al., *A basic study of some normoxic polymer gel dosimeters.* Physics in Medicine and Biology, 2002. **47**: p. 3441-3463.

100. Baldock, C. *Historical overview of the development of gel dosimetry: a personal perspective*. 2006: IOP Publishing.

101. Senden, R.J., et al., *Polymer gel dosimeters with reduced toxicity: a preliminary investigation of the NMR and optical dose response using different monomers.* Physics in Medicine and Biology, 2006. **51**(14): p. 3301.

102. Jirasek, A. *Experimental investigations of polymer gel dosimeters*. 2006: IOP Publishing.

103. De Deene, Y., et al., *Dose-response stability and integrity of the dose distribution of various polymer gel dosimeters.* Physics in Medicine and Biology, 2002. **47**: p. 2459-2470.

104. Heard, M., J. Adamovics, and G.S. Ibbott. *Measurement of a 200 MeV proton beam using a polyurethane dosimeter*. 2006: IOP Publishing.

105. Venning, A.J., et al., *Radiological properties of normoxic polymer gel dosimeters.* Medical Physics, 2005. **32**(4): p. 1047-1053.

106. Adamovics, J., et al. *PRESAGE™ - Development and optimization studies of a 3D radiochromic plastic dosimeter - PART 2*. 2006: IOP Publishing.

107. Adamovics, J., K. Jordan, and J. Dietrich. *PRESAGE™ - Development and optimization studies of a 3D radiochromic plastic dosimeter – Part 1*. 2006: IOP Publishing.

108. Adamovics, J. and M.J. Maryanski, *OCT Scanning Properties of PRESAGE - A 3D Radiochromic Solid polymer Dosimeter.* Medical Physics, 2004. **31**(6): p. 1906.

109. Sakhalkar, H., et al., *A comprehensive evaluation of the PRESAGE/optical-CT 3D dosimetry system.* Medical Physics, 2009. **36**: p. 71.

110. Guo, P.Y., J.A. Adamovics, and M. Oldham, *Characterisation of a new radiochromic three-dimensional dosimeter.* Medical Physics, 2006. **33**(5): p. 1338-1345.

111. Mostaar, A., et al., *A basic dosimetric study of PRESAGE: the effect of different amounts of fabricating components on the sensitivity and stability of the dosimeter.* Physics in Medicine and Biology, 2010. **55**: p. 903.

112. Skyt, P.S. and et al., *Effect of irradiation and storage temperature on PRESAGE TM dose response.* Journal of Physics: Conference Series, 2010. **250**(1): p. 012100.

113. Brown, S., et al., *Radiological properties of the PRESAGE and PAGAT polymer dosimeters.* Applied Radiation and Isotopes, 2008. **66**(12): p. 1970-1974.

114. Doran, S., *The History and principles of optical computed tomography for scanning 3-D radiation dosimeter: 2008 update.* Journal of Physics: Conference Series - 5th International Conference on Radiotherapy Gel Dosimetry (DOSGEL 2008), 2008.

115. Krstajic, N. and S.J. Doran, *Characterization of a parallel-beam CCD optical-CT apparatus for 3D radiation dosimetry.* Physics in Medicine and Biology, 2007. **52**: p. 3693-3713.

116. Oldham, M. *3D Dosimetry by Optical-CT scanning*. 2006: IOP Publishing.

117. Lepage, M. and J.C. Gore, *Contrast Mechanisms in magnetic resonance imaging.* Journal of Physics: Conference Series 3 - Third International Conference on Radiatherapy Gel Dosimetry, 2004: p. 78-86.

118. Bosi, S.G., P. Naseri, and C. Baldock. *Initial Investigation of a novel phantom for simulating optical scattering of dosimetric gels*. 2006: IOP Publishing.

119. Van Doorn, T., et al., *A fast, high spatial resolution optical tomographic scanner for measurement of absorption in gel dosimetry.* Australasian Physical & Engineering Science in Medicine, 2005. **28**(2): p. 76-85.

120. Conklin, J., et al., *Fast laser optical CT scanner with rotating mirror and Fresnel lenses.* Journal of Physics: Conference Series - 4th International Conference on Radiotherapy Gel Dosimetry, 2006. **56**: p. 211-213.

121. Krstajić, N. and S.J. Doran, *Fast laser scanning optical-CT apparatus for 3D radiation dosimetry.* Physics in Medicine and Biology, 2007. **52**(11): p. N257.

122. Jirasek, A., D. Rudko, and D. Wells, *A prototype fan-beam optical CT scanner for polymer gel dosimetry.* Journal of Physics: Conference Series - 5th International Conference on Radiotherapy Gel Dosimetry (DOSGEL 2008), 2009. **164**(1): p. 012025.

123. Jordan, K., et al., *Optical Cone Beam Tomography with Low Pressure Sodium Light*, in *DOSGEL 2001*. 2001: Brisbane, Australia.

124. Adamovics, J., J. Dietrich, and K. Jordan, *SU-FF-T-239: Enhanced Performance of PRESAGE-Sensitivity, and Post-Irradiation Stability.* Medical Physics, 2005. **32**: p. 2004.

125. De Deene, Y. and et al., *The influence of cooling rate on the accuracy of normoxic polymer gel dosimeters.* Physics in Medicine and Biology, 2007. **52**(10): p. 2719.

126. *IAEA-TRS 398: Absorbed Dose Determination in External beam Radiotherapy: An Internation Code of Practice for Dosimetry based on Standards of Absorbed Dose to Water*. 2000, International Atomic Energy Agency.

127. IEC, *Medical Electrical Equipment: medical electron accelerators in the range 1 MeV to 50 MeV - Guidelines for functional performance characteristics*. 1989, International Electrical Commission (IEC).

128. Bayreder, C., et al., *Basic investigations on the performance of a normoxic polymer gel with tetrakis-hydroxy-methyl-phosphonium chloride as an oxygen scavenger: Reproducibility, accuracy, stability, and dose rate dependence.* Medical Physics, 2006. **33**(7): p. 2506-2518.

129. Grebe, G., et al., *Dynamic arc radiosurgery and radiotherapy: Commissioning and verification of dose distributions.* International Journal of Radiation Oncology Biology Physics, 2001. **49**(5): p. 1451-1460.

130. Bosi, S.G., et al., *Modelling optical scattering artefacts for varying pathlength in a gel dosimeter phantom.* Physics in Medicine and Biology, 2009. **54**(2): p. 275.

131. Bosi, S.G., et al., *Initial investigation of a novel light-scattering gel phantom for evaluation of optical CT scanners for radiotherapy gel dosimetry.* Physics in Medicine and Biology, 2007. **52**(10): p. 2893.

132. Islam, K.T.S., et al., *Initial evaluation of commercial optical CT-based 3D gel dosimeter.* Physics in Medicine and Biology, 2003. **30**(8).

133. Olding, T., O. Holmes, and L.J. Schreiner, *Cone beam optical computed tomography for gel dosimetry I: scanner characterization.* Physics in Medicine and Biology, 2010. **55**: p. 2819-2840.

134. Xu, Y., C.-S. Wuu, and M.J. Maryanski, *Performance of a commercial optical CT scanner and polymer gel dosimeters for 3D dose verification.* Physics in Medicine and Biology, 2004. **31**(11): p. 3024-3033.

135. Xu, Y., C.-S. Wuu, and M.J. Maryanski, *Determining optimal gel sensitivity in optical CT scanning of gel dosimeters.* Medical Physics, 2003. **30**(8): p. 2257-2263.

136. Jordan, K. and J. Battista, *Linearity and image uniformity of the Vista™ optical cone beam*

scanner. 2006, IOP Publishing. p. 217.

137. Jordan, K. and J. Battista. *Small, medium and large optical cone beam CT*. 2006: IOP Publishing.

138. Jordan, K. and J.J. Battista, *Scatter Measurements for optical cone-beam computed tomography*. Journal of Physics: Conference Series - 5th International Conference on Radiotherapy Gel Dosimetry (DOSGEL 2008), 2008.

139. Olding, T., O. Holmes, and L.J. Schreiner. *Scatter corrections for cone beam optical CT*. 2009: IOP Publishing.

140. Al-Nowais, S. and S.J. Doran. *CCD-based optical CT scanning of highly attenuating phantoms*. 2009: IOP Publishing.

141. Doran, S.J., et al., *Optical CT scanning of PRESAGE TM polyurethane samples with a CCD-based readout system.* Journal of Physics: Conference Series 3 - Third International Conference on Radiatherapy Gel Dosimetry, 2004. **3**(1): p. 240-243.

142. De Deene, Y. *On the accuracy and precision of gel dosimetry*. 2006: IOP Publishing.

143. Guo, P., J. Adamovics, and M. Oldham. *Quality assurance in 3D dosimetry by optical-CT*. 2006: IOP Publishing.

144. Olding, T., O. Holmes, and L.J. Schreiner, *Development of a Quality Assurance Scattering Phantom for Cone Beam Optical CT.* Journal of Physics: Conference Series - 5th International Conference on Radiotherapy Gel Dosimetry (DOSGEL 2008), 2008.

145. Papadakis, A., et al., *Three-dimensional radiation dosimetry with optical projection tomography.* Journal of Physics: Conference Series - 5th International Conference on Radiotherapy Gel Dosimetry (DOSGEL 2008), 2009. **164**.

146. Chhajed, S., et al., *Influence of junction temperature on chromaticity and color-rendering properties of trichromatic white-light sources based on light-emitting diodes.* Journal of Applied Physics, 2005. **97**(5): p. 054506.

147. Thomas, A., et al., *Commissioning and benchmarking a 3D dosimetry system for clinical use.* Medical Physics, 2011. **38**(8): p. 4846-4857.

148. Babic, S., J. Battista, and K. Jordan, *Micelle hydrogels for three-dimensional dose verification.* Journal of Physics: Conference Series - 5th International Conference on Radiotherapy Gel Dosimetry (DOSGEL 2008), 2008.

149. Bero, M.A., W.B. Gilboy, and P.M. Glover, *Radiochromic gel dosimeter for three-dimensional dosimetry.* Radiation Physics and Chemistry, 2001. **61**(3-6): p. 433-435.

150. Brooks, R.A. and G.D. Chiro, *Beam hardening in X-ray reconstructive tomography*. Physics in Medicine and Biology, 1976. **21**(3): p. 390.

151. Thomas, A., M. Pierquet, and M. Oldham. *Achieving accurate radiochromic optical-CT imaging when using a polychromatic light source*. 2010: IOP Publishing.

152. Mullikin, J.C., et al., *Methods for CCD Camera Characterization.* Image Acquisition and Scientific Imaging Systems, 1994. **SPIE vol 2173**: p. 73-84.

153. *Vista Optical CT Scanner Axis of Rotation Offset - Revision 2*, Modus Medical Devices Inc (London, Canada).

154. *Datasheet: SONY ICX204AL*.

155. Wilson, J. and J. Hawkes, *Optoelectronics: an introduction*. 3rd Edition ed. 1998: Prentice Hall.

156. *Vista Optical CT Scanner calibration*, Modus Med Devices Inc (London, Canada).

157. Zuurmond, K., *Calibration Procedure for the Optical CT*, in *College of Science, Engineering and Health*. 2008, RMIT University: Melbourne.

158. Bass, M., et al., *Handbook of Optics, Third Edition Volume I: Geometrical and Physical Optics, Polarized Light, Components and Instruments(set)*. 2009: McGraw-Hill.

159. Radon, J., *On the Determination of Functions from Their Integral Values along Certain Manifolds.* Medical Imaging, IEEE Transactions on, 1986. **5**(4): p. 170-176.

160. Feldkamp, L.A., L.C. Davis, and J.W. Kress, *Practical cone-beam algorithm.* J. Opt. Soc. Am. A, 1984. **1**(6): p. 612-619.

161. Hsieh, J., *Computed Tomography, Second Edition*. 2009: SPIE Press.

162. Curry III, T.S., J.E. Dowdey, and R.C. Murry Jr, *Christensen's Physics of Diagnostic Radiology*. 4th ed. 1990: Lippincott Williams & Wilkins.

163. Lenk, R. and C. Lenk, *Practical lighting design with LEDs*. IEEE Press series on power engineering. 2011: Wiley.

164. Sakhalkar, H. and M. Oldham, *Fast, high-resolution 3D dosimetry utilizing a novel optical-CT scanner incorporating tertiary telecentric collimation.* Medical Physics, 2008. **35**: p. 101.

165. Martínez Verdú, F.M., J. Pujol Ramo, and P. Capilla Perea, *Testing the reciprocity law in digital photography.* 2003.

166. Healey, G.E. and R. Kondepudy, *Radiometric CCD camera calibration and noise estimation.* IEEE Transactions on Pattern Analysis and Machine Intelligence, 1994. **16**(3): p. 267-276.

167. Campbell, W.G., A. Jirasek, and D. Wells, *Preliminary investigations with a photodiode-based fan-beam optical CT scanner.* Journal of Physics: Conference Series, 2010. **250**(1): p. 012024.

168. Guo, P., J. Adamovics, and M. Oldham. *Simple 3D validation experiments for PRESAGE™/optical-CT dosimetry*. 2006: IOP Publishing.

169. Shamir, J., *Non-Ideal Optical Systems*. Optical Systems and Processes. 1999: SPIE Press.

170. Babic, S., J. Battista, and K. Jordan, *Three-dimensional dose verification for intensity-modulated radiation therapy in the radiological physics centre head-and-neck phantom using optical computed tomography scans of ferrous xylenol-orange gel dosimeters.* International Journal of Radiation Oncology* Biology* Physics, 2008. **70**(4): p. 1281-1291.

171. Babic, S., et al., *Three-dimensional dosimetry of small megavoltage radiation fields using radiochromic gels and optical CT scanning.* Physics in Medicine and Biology, 2009. **54**: p. 2463-2481.

172. *VistaRecon User's Guide*, Modus Med Devices Inc (London, Canada).

173. *AAPM Report 83: TG-66 - Quality Assurance for computed tomography simulators and the computed tomography-simulation process*. 2003.

174. Nickoloff, E.L., *Measurement of the PSF for a CT scanner: appropriate wire diameter and pixel size*. Physics in Medicine and Biology, 1988. **33**: p. 149.

175. Miller, F.P., A.F. Vandome, and M.B. John, *Cutoff Frequency*. 2010: VDM Verlag Dr. Mueller e.K.

176. Keat, N., *Comparison of assessment techniques for CT scanner spatial resolution measurement*. 2005, Centre for Evidence-based Purchasing: www.pasa.nhs.uk/cep.

177. McDermott, L. and K. Zuurmond, *Personal Communication*. 2009.